Measurement of Magnetic Turbulence Structure and Nonlinear Mode Coupling of Tearing Fluctuations in the Madison Symmetric Torus Reversed Field Pinch Edge

by

SAEED ASSADI

A thesis submitted in partial fulfillment of the

requirements for the degree of

Doctor of Philosophy

(Nuclear Engineering and Engineering Physics)

at the

UNIVERSITY OF WISCONSIN-MADISON

1992

Measurement of Magnetic Turbulence Structure and Nonlinear Mode Coupling of Tearing Fluctuations in the Madison Symmetric Torus Reversed Field Pinch Edge

Saeed Assadi

Under the Supervision of

Professor Gilbert A. Emmert (Nuclear Engineering and Engineering Physics)

and

Professor Stewart C. Prager (Physics)

at the University of Wisconsin-Madison

The linear and nonlinear magnetohydrodynamic (MHD) stability of current-driven modes are studied in the MST reversed field pinch. The measured low frequency ($f < 35$ kHz) magnetic fluctuations are consistent with the global resistive tearing instabilities predicted by 3-D MHD simulations. At frequencies above 35 kHz, the magnetic fluctuations were detected to be localized and externally resonant. Discrete dynamo events, "sawtooth oscillations", have been observed in the experimental RFP plasmas. This phenomenon causes the plasma to become unstable to $m = 1$ tearing modes. The modes that may be important in different phases of these oscillations are identified. These results then assist in nonlinear studies and also help

to interpret the spectral broadening of the measured data during a discrete dynamo event.

Three-wave nonlinear coupling of spectral Fourier modes is measured in the MST by applying bispectral analysis to magnetic fluctuations measured at the plasma edge at 64 toroidal locations and 16 poloidal locations, permitting observation of coupling over 8 poloidal and 32 toroidal modes. Comparison to bispectra predicted by resistive MHD computation indicates reasonably good agreement. However, during the crash phase of the sawtooth oscillation the nonlinear coupling is strongly enhanced, concomitant with a broadened k-spectrum. During the sawtooth formation, the plasma is undergoing a purely diffusive process. The dynamo only occurs during the sawtooth crash. High frequency activity prior to a sawtooth crash is found to be caused by nonlinear frequency (small-scale) mode coupling. Growth rate and coupling coefficients of the toroidal mode spectra are calculated by statistical modeling. Temporal evolution of the edge toroidal mode spectra has been predicted by transfer function analysis and results are promising. The driving sources of electrostatic fields have been found to be different than for the magnetic fields. The characteristics of the tearing modes can be altered by external field errors and the addition of impurities to the plasma.

Approved:

Date

Professor Stewart C. Prager
Department of Physics

Date

Professor Gilbert A. Emmert
Nuclear Engineering and Engineering Physics

Acknowledgements

I would like to thank my advisors, Professor Gilbert A. Emmert and Professor Stewart C. Prager, for their support and guidance during the course of this research and the years spent searching for a suitable thesis project. I would also like to thank Professor J.D. Callen, Professor J.C. Sprott and professor S. Hokin for their suggestions and support.

This work would have been impossible without the efforts of John Laufenberge, Jim Morin, chief enginner Tom Lovell and Professor R. Dexter. My thanks to all of hourly workers who provided vital support for this work and in the general maintenance of MST. I would like to thank Glenn Fleet, the master of computers Larry, Paul, and Berent for their endless dedication.

Many of the features of the main diagnostics used in this thesis were materialized after lengthy discussions in the plasma physics hallways with my fellow graduate students and postdocs. I am especially indebted to Dr. A. F. Almagri, Dr. D. Kortbawi, Dr. M. LaPointe, Dr. K. Sidikman and Dr. J. Sarff.

To the Chicos: you are the best. To all those who spent hours on the Terrace discussing whatever, I will fondly remember those times.

Finally, I wish to acknowledge the love and support of my family. They never pushed or pulled me into this, They have just been at my side. I would like to

express my appreciation to Professor Amir Assadi and (soon to be Dr.) Fariba Assadi-Porter for their love and patience. And to the Lamb, thank you for the love and support throughout these years and I hope to have many more years to explain to you just what it is I do for a living.

This work has been supported by the United States Department of Energy. Computers were provided by AT&T and National Science Foundation.

TABLE OF CONTENTS

III. EXPERIMENTAL APPARATUS AND DIAGNOSTICS

IV. STATIONARY TIME SERIES AND SPECTRAL ANALYSIS

V. EXPERIMENTAL RESULTS AND DISCUSSIONS

Chapter 1

Introduction

The status of fusion research would be greatly enhanced by improved understanding of energy and particle confinement. A ubiquitous feature of plasmas is the presence of nonthermal fluctuations composed of a spectrum of frequencies and wave numbers. The difficulty of evaluating the relevance of the turbulent processes to transport is viewed as the leading obstacle to this understanding. The plasma turbulence is marked by density, temperature, and electromagnetic fluctuations. These fluctuating quantities and the correlations among them are postulated as a major candidate for the observed anomalous plasma transport. This is abetted by the nonlinear character of the problem and the lack of experimental data with which to compare theoretical and computational results. This lack of experimental results becomes clearer when one considers that spectral analysis of experimental magnetic turbulence requires hundreds of magnetic sensors with the necessary resolution in order to be able to compare with the computational results. Understanding the origin of the spatial and temporal structure of the spontaneously occurring fluctuations remains a daunting goal of nonlinear plasma physics. Nonlinear interactions between spatial Fourier components are a key determinant of the wave vector ($\mathbf{k}$) spectrum of the fluctuations. It is generally presumed

that coupling of three spatial components, satisfying the sum rule $\mathbf{k_1} + \mathbf{k_2} = \mathbf{k_3}$, is the dominant nonlinear interaction. Higher order coupling (4-wave and up) is assumed to be small in most theoretical treatments of fluctuations. In fusion plasmas nonlinear interactions are important since the resulting spectra might determine macroscopic behavior, such as dynamo effects (magnetic field generation) and sawtooth oscillations. Fluctuation spectra have been measured in numerous plasma confinement experiments [1]. However, to our knowledge direct observation of nonlinear interactions in k-space, the subject of this thesis, has not heretofore been obtained.

The reversed field pinch plasma configuration is an excellent vehicle for the study of nonlinear interactions. The dominant magnetic fluctuations in reversed field pinches (RFPs) are tearing modes. Tearing fluctuations are relatively large scale oscillations predicted by resistive magnetohydrodynamics (MHD). They are believed to underlie sawtooth oscillations and disruptions in tokamaks [2], the dynamo effect [3], sawtooth oscillations in RFPs [4], and perhaps, transport in reversed field pinches.

The purpose of this thesis is to measure magnetic turbulence. We present a comprehensive survey of the magnetic fluctuation amplitude, phase, spatial correlation in the toroidal and poloidal directions, mode numbers and associated helical modes. We have directly measured the three-wave coupling of such magnetic fluctuations in the edge of the MST reversed field pinch (RFP) experiment. In the RFP, tearing fluctuations

over the wave number range which we examine appear to be intermediate between fully developed turbulence and isolated coherent modes. The results of nonlinear mode coupling in frequency and wavenumber space and energy cascading are presented. Next, we compare the measurements with the three-wave mode coupling of tearing fluctuations calculated by a three-dimensional, nonlinear, resistive MHD code. Finally, we present the correlation between electrostatic and magnetic fluctuations. The effect of the insertion of a movable limiter and impurities on the magnetic fluctuation spectra and rotational speed of the coupled modes is also presented.

This chapter is divided into four sections. First, a brief description of a reversed field pinch is presented. The second section discusses the objective of the thesis research. Section Three presents the thesis outline. Section Four describes the organization of this thesis.

I-1) Brief Description of a Reversed Field Pinch

The purpose of this section is to highlight the general characteristics of reversed field pinches.

The reversed field pinch is an axisymmetric, toroidal magnetic configuration. The plasma is confined by a toroidal magnetic field and a poloidal magnetic field

generated by toroidal plasma current. Unlike the tokamak [5], the ratio of toroidal current to the toroidal magnetic field is relatively high in an RFP. The stability of RFPs are mainly achieved through strong shear in the magnetic field and a conducting wall, which appear to suffice even at relatively high β [β= plasma pressure/magnetic field energy density]. These differences may lead to a more efficient reactor in terms of heating, reactor size, and utilization of the externally applied magnetic field.

Experiments have demonstrated spontaneous self-generation and sustainment of the reversed toroidal field at the edge, which contributes to the strong shear necessary for the stability of the RFPs.

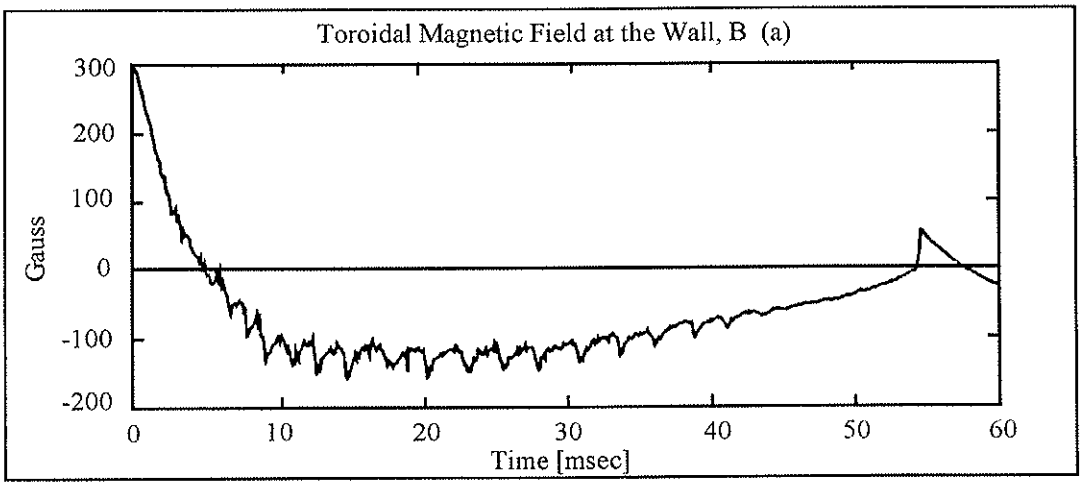

Figure 1-1) Self-generation and sustainment of toroidal field measured at the edge of MST. Sawtooth oscillations are observed.

astrophysical dynamo [7], and paramagnetic effects (magnetic profile modifications) [8]. The paramagnetic effect alone cannot cause reversal; hence dynamo action is essential for the existence of the RFP state. The dynamo is most likely the dissipative dynamical process by which the plasma relaxes through resistive reconnection to the minimum energy "Taylor" state (Taylor, 1974) [9]. Experimental RFP states are not fully relaxed, but are close enough to exhibit much of the macroscopic features of the minimum energy "Taylor" state. For example, reversal of the toroidal magnetic field, B_t , at the wall is shown above in Figure (1-1). Another example is reduction of magnetic fluctuation during reversal is presented in Figure (1-2).

RFP equilibria are typically expressed in terms of the normalized edge magnetic fields. This is accomplished by the F-θ diagram (reversal parameter, $F = B_\phi(a)/\langle B_\phi \rangle$, pinch parameter, $\theta = B_\theta(a)/\langle B_\phi \rangle$) which conveniently displays relaxation toward the Bessel Function Mod

el (BFM)[1] (Figure 1-3). Several review articles [9,10,11] exist and should be referred to for additional background on reversed field pinches.

---

1) Due to the large aspect ratio, R/a, of many RFP experiments, toroidal curvature effects are small, so the RFP can often be approximated as a periodic circular cylinder. Using this approximation, the solutions to $\nabla \times \mathbf{B} = \lambda \mathbf{B}$ are known as the Bessel Function Model (BFM).

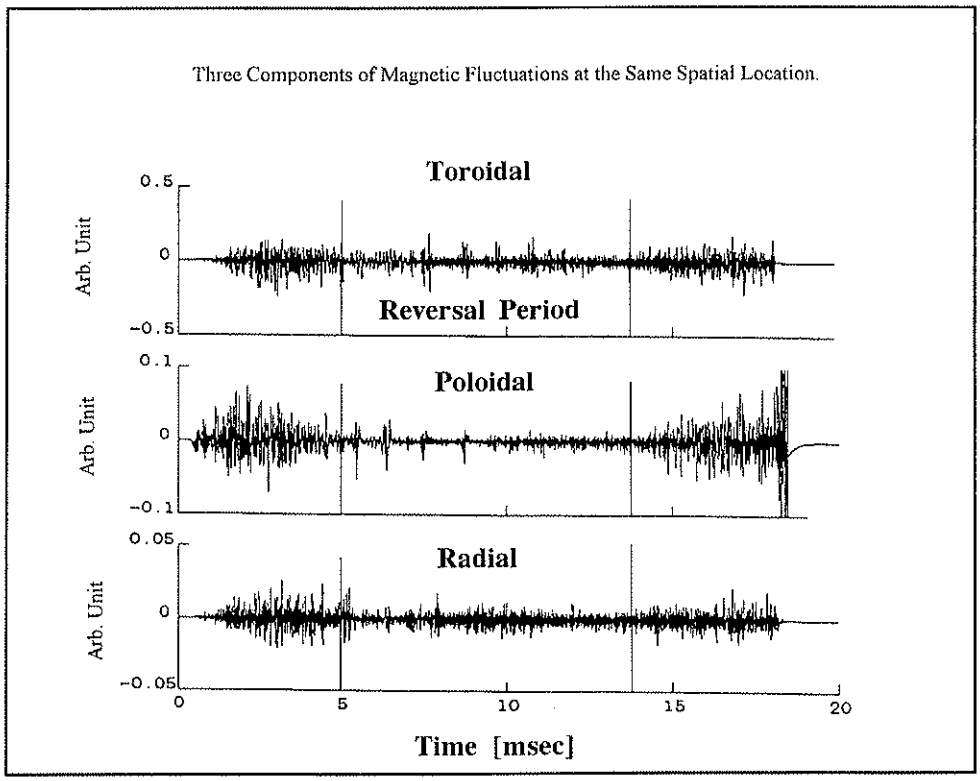

Figure 1-2) Magnetic fluctuations measured in early MST plasma show a relatively quiescent period when the toroidal field is reversed at the wall. Vertical lines indicate the beginning and end of reversal.

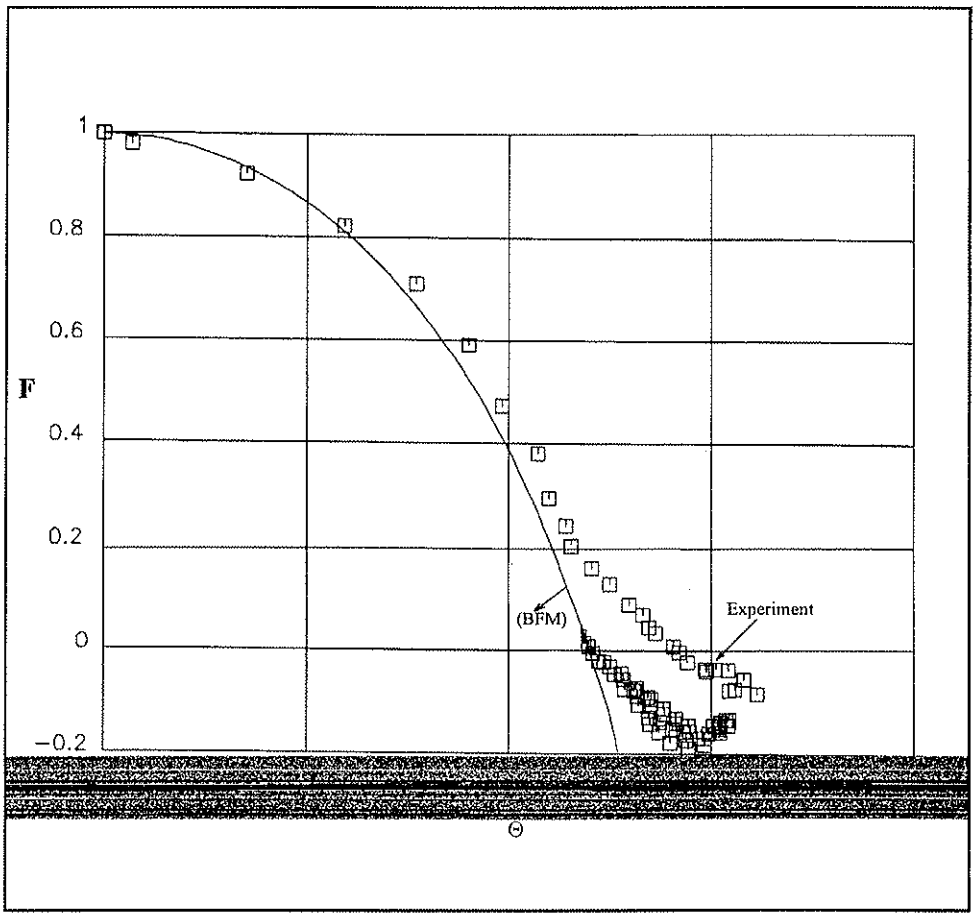

Figure 1-3) The F-θ curve for the BFM model and the experimental results from the MST.

I-2) Objective of Thesis Research

The dynamics of plasma systems have been studied either by a hydrodynamic fluid description or the more detailed kinetic description. In the first case, the MHD equations of motion are used and, in the second case, the Boltzmann equation is used. The common feature of these two sets of equations is nonlinearity, although they describe the plasmas from different standpoints. The nonlinear character of the equations introduces difficulties in the mathematical treatment. In order to simplify the mathematics one may restrict oneself to small variations in time and space of the quantities studied. This approximation and the neglect of the product of varying quantities results in a linear system. Having the above logic in mind, I will present the linear treatment of the experimental edge magnetic fluctuations obtained on MST and compare them with the computational results of a resistive MHD code [12,13]. Then, I use advanced signal processing to obtain the first order nonlinear effect (three-wave coupling) and compare this with the computational 3-D resistive MHD results using the same technique.

I-3) Thesis Outline

In this thesis, I study both linear and nonlinear mode analysis and compare the experimental results with resistive MHD models to describe macroscopic phenomenon in the MST reversed field pinch. For the RFP, MHD models have accounted for the observed magnetic fluctuation energy spectrum [12] and resistive MHD codes have successfully simulated the RFP sustaining "dynamo" [12,14,15]. The thesis addresses a range of issues as follows,

1) The general characteristics of the magnetic fluctuation are treated such as: i) power spectrum; ii) magnitude of the fluctuation amplitudes of B_θ, B_ϕ, and B_r; iii) coherence structure as a function of frequency. The MST magnetic fluctuation results are compared to measurements obtained on ZETA [16], OHTE [17], ETA-BETA-II [18], HBTX1A [19], and ZT-40M [20]. This verifies the general features associated with the RFPs, such as the reduction of the magnetic fluctuations during the reversal period. MST is about twice the size of the other devices, and has a higher plasma current and Lundquist number. This will help determine whether the increase in the size of the device could justify the development of the next generation reversed field pinches.

2) I will compare the measured low frequency coherent magnetic mode structures I have obtained on the MST with 3-D resistive MHD computational results [21,22,23],

and also with measurements made on HBTX1A [24] and OHTE [25]. I have measured the toroidal (n) and the poloidal mode numbers (m). Determination of the dominant modes, in particular the m=0 and the m=1 mode amplitudes and phase, are compared with the numerical results given by Caramana, Nebel and Schnack [26], who conjecture that the driving source of the m=0 mode is the unstable m=1 mode .

3) The relaxation of the pinch configuration to a minimum energy state, as proposed by Taylor [27], has been observed in RFP's: The departure from the fully relaxed state has been associated with finite pressure, toroidal effects, and energy throughput coupled to fluctuations [28,29]. I will present the relation between the nonlinear mode coupling of magnetic fluctuations and the departure from this relaxed state [30,31] by having studied the sawtooth phenomenon observed on MST.

4) To a first approximation turbulent fluctuations can be regarded as the linear superposition of statistically independent waves. However, linear analysis is not able to explain how finite unstable wavenumber and frequency waves could generate a broadband turbulent spectrum. To obtain an understanding of the mechanics of this phenomenon, I have measured nonlinear effects. To first approximation in the nonlinear effects, I have investigated the quadratic wave coupling. The bi-spectral analysis [32,33], which is the third-order spectral correlation, has been used to measure quadratic frequency coupling and quadratic wavenumber coupling. I have compared the edge

magnetic fluctuation measurements of the MST with results from nonlinear, 3-D, resistive MHD computation.

5) I present measurements of magnetic fluctuations as a function of the Lundquist number, $S=\tau_r/\tau_a$, (where τ_r is the resistive diffusion time and τ_a is the Alfven transit time). Comparison of this scaling with the nonlinear turbulence analysis for tearing fluctuations made by Strauss [34] and An et al. [35], resistive interchange instabilities made by Robinson and Hender [36], computational studies by Schnack et al. [22], and also the experimental results of OHTE [37], are made.

6) To understand the characteristics of the phase-locked modes observed on the MST, I have studied the effect of a movable limiter and impurity injection on the magnetic fluctuation spectra and the rotational speed of the coupled modes. I also present the measurement of the cross correlation between electrostatic and magnetic fluctuations to gain insight into the driving source of electromagnetic turbulence.

I-3) Organization of This Thesis

This thesis has been organized into 5 chapters. Chapter 2 contains an introduction to RFP instabilities. and presents a summary of the experimental and computational understandings of the linear and nonlinear mode analysis. The MST reversed field pinch, and the diagnostics unique to this research are discussed in Chapter 3. The experimental methods are presented in Chapter 4. Chapter 5 contains the data obtained during this research investigation. Characteristics of the plasmas investigated, comparison of experimental and computational linear mode analysis, nonlinear mode coupling and energy cascading, cross correlation of electrostatic and magnetic fluctuations, and the effect of a limiter and impurities on the phase-locking of the modes are also given in this chapter. A summary and discussion of the results along with suggestions for the future work are presented in Chapter 6.

A note about Thesis References and PLPs:

Throughout this thesis, I refer to the internal reports (PLPs) of the University of Wisconsin Plasma Physics Group and the Ph.D. theses from the University of Wisconsin-Madison. Copies of the PLPs and theses are available upon request from:

Physics Department, Plasma Section. University of Wisconsin-Madison ,

1150 University Avenue, Madison, WI 53706.

References:

1) A.J. Wootton et al., Phys. Fluids B, **2**, 2879 (1990).

2) See, for example, G. Bateman, MHD Instabilities, The MIT Press, 1978.

3) See, for example, H.R. Strauss, Phys. Fluids, **27**, 2580 (1984); A.Y. Aydemir and D.C. Barnes, Phys. Rev. Lett., **52**, 930 (1984).

4) R.B. Watt and R.A. Nebel, Phys. Fluids, **26**, 1168 (1984).

5) H.P. Furth, Nuclear Fusion, **15**, 487 (1975).

6) E.J. Caramana and D.A. Baker, Nuclear Fusion, **24**, 423 (1984).

7) H.K. Moffatt, Magnetic Field Generation in Electrical Conducting Fluids. (Cambridge University Press, Cambridge 1978).

8) S.C. Prager and L. Turner, Phys. Fluids **28**, 1155, (1985).

9) J.B. Taylor, Reviews of Modern Physics **58**, 741 (1986).

10) A.B. Bodin, and A.A. Newton, Nuclear Fusion **20**, 1255 (1980).

11) H.Dreicer, Physica Scripta **T212**, 435 (1982)

12) D.D. Schnack, D.C. Barnes, Z. Mikic, D.S. Harned, and E.J. Caramana, J. Compt. Phys., **70**, 330 (1987).

13) E. Zita, Private Communication.

14) see, for example, P. Kirby, Physic Fluids **31**, 625, (1988).

15) A.Y. Aydemir, D.C. Barnes, E.J. Caramana,A.A. Mirin, R.A. Nebel, D.D. Schnack, and A.G. Sgro, Phys. Fluids **28**,898 (1985).

16) D.C. Robinson, M.G. Rusbridge, and P.A.H. Saunder, Plasma Physics **10**,1005 (1968).

17) P.L. Taylor, R.J. LaHaye, P.S. Lee, M.J. Schaffer, T. Tamano, Plasma Behavior in OHTE (1984).

18) V. Antoni and S. Ortolani, Plasma Physics **25**, 799 (1983).

19) H.A.B. Bodin, et al., "Results from HBTX1A Reversed Field Pinch Experiment", Plasma Physics and Controlled Nuclear Fusion Research 1982 (9th Int. Conf. Baltimore, 1982), Vol. **1**, IAEA, Vienna 641 (1983).

20) R. G. Watt and R.A. Nebel Physics Fluids **26**, 1168 (1983).

21) R.A. Nebel, E.J. Caramana, D.D. Schnack. Physics Fluids B, **1**, 1671 (1989).

22) J.A. Holmes, Carreras, P.H. Diamond, V.E. Lynch. Physics Fluids, **31**, 1166 (1988).

23) D.D. Schnack, E.J. Caramana and R.A. Nebel Physics Fluids, **28**, 321 (1985).

24) J.W. Johnson, Plasma Physics **23**,187, (1981).

25) G.L. Jackson, J.S. DeGrassie, M.S. Schaffer, T.S. Taylor and K.W. Gentle, Magnetic Field perturbations in plasma devices, (1988).

26) E.J. Caramana, R.A. Nebel, D.D. Schnack, Phys. Fluids. **26**,1305.

27) J. B. Taylor, Physical Review Letters **33**,1139, (1974).

28) D.C. Robinson, From Particles to Plasmas, Addison Wesley (1988).

29) H. Y. Tsui, A.A. Newton and M. G. Rusbridge, Controlled fusion and Plasma Heating, 13th European Conference Schliersee Vol. **10**C, part 1, 340 (1986).

30) H.Y. Tsui, J. Cunnane, D.E. Evans Controlled Fusion and Plasma Physics,14th European Conference, Madrid. Vol. **11**d, Part 11,P.511 (1987).

31) J.B. Eggen, and W. Schuurman (1986), Controlled Fusion and Plasma Heating, Proc. 13th Euro. Conf.. Schliersee. FRG. Vol. **10**C, Part 1, P.356 (1986).

32) Y. Kim, J. Beall, and E. Powers, Phys. Fluids **23**, 258 (1980).

33) Y. Kim and E. Powers, IEEE Trans. Plasma Sci. **7**, 120 (1979).

34) H. R. Strauss Phys. Fluids **29**, 3008 (1986).

35) T. C. Hender and D.C. Robinson, 9th International Conference in Plasma Physics and Controlled Nuclear Fusion Research, Baltimore, Vol.**3**, 417, (1983).

36) Z.G. An and P.H. Diamond, Eleventh int. Conf. on plasma Physics and Controlled Nuclear Fusion Research, **vol. ii**, 663, (1987).

37) R. LaHaye, M.J. Schaffer, Nuclear Fusion **27**, 2576, (1984).

Chapter II

Review of RFP Magnetic Turbulence

II-1) Introduction

A laboratory plasma not in thermodynamic equilibrium contains free energy available to drive collective motion of the plasma; this energy can be dissipated via radiation of electromagnetic waves or it can be converted into a violent motion of the plasma (i.e. plasma instability). There are basically two ways by which a plasma can deviate from thermodynamic equilibrium. The first is by localizing in space with locally non-uniform thermodynamic quantities such as density, pressure, temperature or some other thermodynamic quantity. The second is by having a velocity distribution deviating from the Maxwell-Boltzmann distribution. I am mainly concerned with the measurement of the macroscopic (magnetohydrodynamic-MHD) instabilities. These are low frequency phenomena described by a simple macroscopic fluid model and which concern the plasma as a whole.

Measurements of the plasma pressure and magnetic pressure reveal a relatively high beta. These stable high β discharges $\beta \sim (P/B^2/2\mu_o)$ attributed to the large gradients in the pitch of the magnetic field lines. The condition for stability against pressure driven modes concerning toroidicity is given by the Mercier criterion [1],

$$(1-q^2)\frac{dp}{dr}+\frac{B_\phi^2}{32\pi}\left[\frac{1}{q}\frac{dq}{dr}\right]^2 \geq 0, \qquad (1)$$

where p is the plasma pressure and q is the safety factor defined as:

$$q(r)=\frac{r}{R}\frac{B_\phi}{B_\Theta}. \qquad (2)$$

MHD predicts the occurrence of pressure driven resistive interchange fluctuations. In experiments, the pressure gradient appears to be largest in the outer part of the plasma. Thus, resistive interchange fluctuations might arise in the vicinity of the reversal surface. The RFP has the advantage of possessing high shear throughout the plasma compared to tokamak plasmas, so that equation (1) is satisfied. The ideal stability analysis, as developed by Newcomb [2], shows that RFPs are susceptible to current driven instabilities. This analysis involves the energy integral, $W(\zeta)$. An instability arises whenever a trial radial displacement function (ζ) makes the energy integral negative. The radial locations r_s for which the radial displacement is large is given by $q(r_s) = m/n$, where m and n are poloidal and toroidal mode numbers respectively. The surfaces that correspond to these unstable modes are called resonant surfaces.

A comparison of q profiles for a tokamak and RFP is given in Fig. (2-1). The RFP is characterized by the presence of many closely spaced unstable modes (Figure

2-1); this is unlike the Tokamak configuration in which there are at most one or two widely separated resonance surfaces.

Large scale MHD activities have been observed in RFP experiments [3,4,5]. These activities are believed to be the manifestation of m=1 tearing modes. The m=1 tearing modes have been linked to relaxation and dynamo effects [6,7,8] and may be responsible for the anomalous losses [7,9].

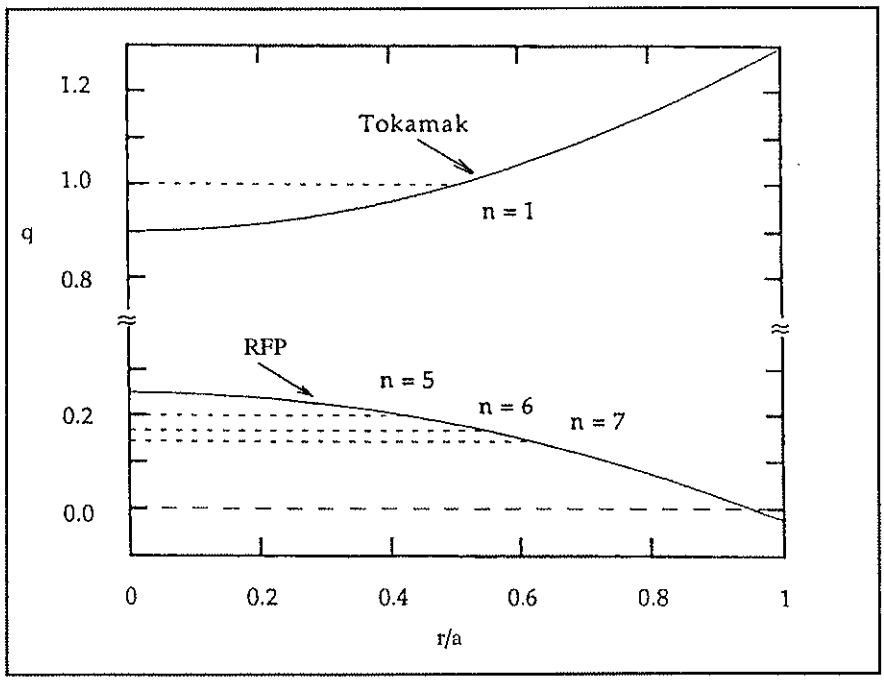

Figure 2.1) Comparison of q profiles for RFP's and Tokamaks.

For this reason, the RFP provides a unique opportunity to study the nonlinear interactions of tearing modes, the generation of the associated turbulence,and effects associated with it. In this chapter we will continue with a brief discussion of the various nonlinearities in RFPs and the description of the numerical code used to generate data for comparison with the MST results.

II-2) Tearing Instabilities

Although the classic paper on resistive MHD instabilities was published over two decades ago (Furth, Killeen and Rosenbluth 1963), the topic is still under development. Recently there has been emphasis on nonlinear development of tearing modes. In this section, we briefly present the physics of tearing modes which provides the basis in my thesis research.

Tearing modes are examples of resistive MHD instabilities. Other examples of resistive versions of the ideal MHD instabilities are kinks and interchange instabilities, but tearing modes are the most important in the RFP. In toroidal plasma devices, specifically in RFPs, "sawtooth-like" oscillations are attributed, at least partly, to the onset or saturation of a tearing instability. Tearing instabilities are also thought to be important in tokamak disruptions, Mirnov oscillations, sawtooth oscillations, and also in solar flares and other astrophysical phenomena.

A detailed mathematical treatment of tearing instabilities [10], is impractical here. However, we will very briefly outline the linear theory of tearing instability. In ideal MHD the magnetic field lines and the plasma are constrained to move with each other; i.e., the magnetic field lines are 'frozen' to the plasma. The curl of Ohm's law, ($\mathbf{E} + \mathbf{v} \times \mathbf{B} = \mathbf{J}/\sigma$), combined with Faraday and Ampere's laws give

$$\frac{\partial \boldsymbol{B}}{\partial t} = \nabla \times (\boldsymbol{v} \times \boldsymbol{B}) + \frac{1}{\mu_o \sigma} \nabla^2 \boldsymbol{B} \qquad (1)$$

The component of **B** in the x-z plane may be described in terms of Euler potentials; we set $\alpha = \psi(x,z)$ and $\beta = y$ so that $\mathbf{B} = \nabla\alpha \times \nabla\beta$. This implies

$$\boldsymbol{B} = \nabla\psi \times \boldsymbol{e}_y + B_y \boldsymbol{e}_y \qquad (2)$$

For $\sigma = \infty$, the above equation reduces to $\partial\mathbf{B}/\partial t = \nabla\times(\mathbf{v} \times \mathbf{B})$, which implies that the field lines move with the perpendicular fluid velocity $\mathbf{v}_\perp$. The second term in equation (1) represents the slippage of the magnetic field lines when resistivity is introduced. The unperturbed magnetic field is assumed to be of the form $B_x = 0$, B_y = constant, $B_z = B_o f(x)$, with $f(x) \rightarrow \pm 1$ at $x \rightarrow \pm\infty$ and with $f(x) \approx x/L$ for $|x| << L$.

The length L characterizes the variation in the magnetic field across the neutral layer. We can Fourier transform in the y- and z- directions. From ordering near x=0, together with $\nabla \bullet \mathbf{B} = 0$, We require that $\mathbf{k}$ satisfy $\mathbf{k} \bullet \mathbf{B}_1 = 0$ at $x = 0$. Here, we assume $k_y = 0$, $k_z \neq 0$. In toroidal geometry the pitch of the tearing mode is opposite to that of the magnetic field at the rational surface. (i.e., for $q = m/n$ the tearing mode varies as $e^{(-im\theta - n\phi)}$), this being the appropriate form for $\mathbf{k} \bullet \mathbf{B}_o \propto (mq-n) = 0$ at the rational surface $q = m/n$. The equation of motion is

$$\rho \frac{d\boldsymbol{V}}{dt} = -\nabla P + \boldsymbol{J} \times \boldsymbol{B} \tag{3}$$

The plasma is assumed to be incompressible, $\nabla \bullet \mathbf{v} = 0$. Also small amplitude wave motion is assumed; ($\psi = \psi_o + \delta\psi$) and we assume ψ varies with z as exp [ikz]. This allows one to linearize the curl of the equation of the fluid motion and equation (2) above to get two coupled second order differential equations for $\delta\psi$.

At this stage it is appropriate to rely on a semi-quantitative argument. The system is separated into a resistive layer about x=0 where resistivity is important; the regions above and below this layer satisfy ideal MHD. The growth rate ω_i and the resistive layer width (W) along the x-axis are derived from boundary layer theory.

$$\omega_i \approx \frac{(\Delta' L)^{4/5}}{\tau_R} S^{2/5} \tag{4}$$

$$(\frac{W}{L})^5 \approx \frac{\Delta' L}{S^2} \tag{5}$$

where $\tau_R = \mu_\omega \ \sigma L^2$, the resistive time scale, $S = \tau_R/\tau_A$, the Lundquist number, and τ_A is the Alfven time. The quantity Δ' characterizes the properties of the resistive layer when viewed as a surface separating two ideal MHD regions. There is a discontinuous change in the derivative of the x-component of the field ($\delta\psi \equiv B_x$, $d\delta\psi/dx$ changes by $\Delta' \delta\psi$). The quantity Δ' is defined as

$$\Delta' = \left(d\ln\frac{\delta\psi}{dx} \right)_+ - \left(d\ln\frac{\delta\psi}{dx} \right)_- \tag{6}$$

The fact that S is large (order 10^6) for RFPs implies that the width W is much smaller than the characteristic length L, and the growth time $(\omega_i)^{-1}$ is shorter than the resistive time scale τ_R.

II-3) Review of Numerical Simulations of Nonlinear Dynamics in RFP's.

This section presents a brief review of numerical simulations of nonlinear dynamics in RFP's.

Robinson [11] in 1978 showed that current driven resistive instabilities in the RFP could be stabilized and MHD stable RFP equilibria could exist. However, profile maintenance against transport was not addressed. Caramana et al. [12] have studied the nonlinear single helicity reconnection of the RFP using 3-D resistive nonlinear MHD equations. Essentially the full set of nonlinear MHD equations were used to follow the evolution of single helicity resistive tearing modes. They have concluded that there are two processes in the evolution of single helicity tearing modes. The off-axis current gradient drives the plasmas unstable during the first reconnection, resulting in peaking of the on-axis current; this moves the reversal surface outward. Then, the second reconnection where the resonant surface is restored takes place, the q on axis increases above its initial value, and the plasma approaches the minimum energy state (Taylor state [13]). Transport was not included in the simulation and the effect of the nonlinear interaction of modes with different helicities was not considered.

Schnack and Killeen [14], using 2-D MHD simulations, have found that global

reconnection could occur for modes with m=1 poloidal mode number. Subsequently, Schnack et al. [15,16], have found nonlinear coupling between different helicity modes using the 3-D nonlinear MHD code. The m=0 and m=2 modes are nonlinearly produced from m=1 mode couplings and change the n-spectrum of the m=1 mode. This occurs because energy is drained away by the m=0 and m=2 modes. The effect of multiple helicities is the generation of a stochastic region about the resonance regions. For large values of pinch parameter $\theta > 1.6$, they conjecture that the m=0 island (resonant on the reversal surface) may overlap with the m=1 island and make the entire discharge stochastic. Nebel et al. [17] have asserted that the m=0 modes have very little effect on field reversal when they consider a few linearly m=1 unstable modes.

Kusano and Sato [18], have used a topological argument to show that both m=1 and m=0 modes are required for the field reversal. They asserted that depending on the departure from the Taylor relaxed state, the contributions of different modes change. Nonlinear reconnection of m=0 becomes dominant when the percent excess energy, W^* is less than 8%, where W^* is given by

$$W^* = \frac{W_m - W_{BFM}}{W_{BFM}}, \tag{7}$$

where W_m is the total magnetic energy of the initial state, and W_{BFM} is the

magnetic energy of the BFM minimum energy state which has the same helicity as the initial state.

To elucidate the nonlinear dynamics, Holmes et al. [9] performed a statistical turbulence calculation. They fixed the mean profiles, and hence did not specifically study the reversal process. They took a broad spectrum of modes to interact nonlinearly. They identified two processes. First, the toroidal mode spectrum broadens, resulting in a radial spread of turbulence from the center to the reversal surface when the poloidal mode number is one. Second, the unstable m=1 modes are stabilized via an energy cascade to small scales; the energy transfer is in the radial direction. The m=1 spectral broadening is mediated by an m=0 energy sink; they back-couple to keep m=1 and generate a high n spectrum. Similarly, the cascade to small scales is mediated by the nonlinearly driven m=2 modes. Their coupling transfers the energy to a higher poloidal mode spectrum.

Ho and Craddock [19] further investigated the energy flow using a 3D MHD code. They have identified the conversion of the poloidal magnetic energy to toroidal magnetic field energy by the dynamo. They predicted that, at high pinch parameter θ, the dynamo can be alternatively dominated by quasilinear and nonlinear processes in a quasiperiodic fashion. They have identified the m=0 modes as being crucial to produce the nonlinear dynamo whereas quasi-linearly, the m=1 modes can reverse

the axial field by themselves.

II-4) Computational MHD Model

The computational model used to generate data to compare with our experimental results is described in this section. We used the initial value code DEBS [20,21]. This code has been employed by Sidikman to generate the three components of the **B** field in real space. The code uses a semi-implicit method for solving the time-dependent, nonlinear, 3-D MHD equations in a periodic cylinder [7-8]. The pressureless resistive MHD equations which are solved, written in dimensionless form, are

$$\frac{\partial \boldsymbol{A}}{\partial t} = S\,(\boldsymbol{V}\times\boldsymbol{B}) - \eta\,\boldsymbol{J} \tag{8}$$

$$S\frac{\partial \boldsymbol{V}}{\partial t} = -S\,\boldsymbol{V}\cdot\nabla\boldsymbol{V} + S\boldsymbol{J}\times\boldsymbol{B} + \nu\,\nabla^2\boldsymbol{V} \tag{9}$$

where $\mathbf{B}= \nabla \times \mathbf{A}$, $\mathbf{J} = \nabla \times \mathbf{B}$ and $\mathbf{V}$ is the velocity. The chosen gauge is

$$\frac{\partial \boldsymbol{A}}{\partial t} = -\boldsymbol{E} \qquad (10)$$

where **E** is the electric field. Nonlinear MHD systems evolve on time scales that are long compared to those associated with the fastest normal modes of the plasma; for this reason the nonlinearities are treated pseudospectrally, while time is advanced using the semi-implicit method [22]. The magnetic field is normalized to the on-axis magnetic field strength at t = 0, time to τ_R (resistive diffusion time $\tau_R = 4\ \pi\ a^2\ /\ c^2\ \eta_c$). The subscript c denotes a characteristic value. Velocity is normalized to the Alfven velocity ($V_A = B_c\ /\ (4\ \pi\ \rho_c)^{0.5}$), lengths to the minor radius a, and resistivity to the on-axis resistivity, η_c. The viscosity is added for numerical stability [23]. In order to model the experiment, there is a need for hundreds of runs to generate an ensemble of statistically independent fluctuations. The code is typically 12,000,000 words in length and requires tens of Cray CPU hours per run [24]. Although the total number of time steps required to follow resistive evolution is greatly reduced by the code, such a large number of runs is unrealistic. Hence, rather than starting the code each time from the beginning, we simulate the experiments by starting with the equilibrium to which the code is known to evolve, but with random initial perturbation profiles. Initial phases of all fluctuation components are random, subject to the constraint $\nabla \circ \mathbf{B_1} = 0$. This reduced the required

CRAY time to 20-30 minutes per run.

The modes considered are $-2 < m < 2$, $-42 < n < 42$ and there are 127 radial grid points. However, the time-space representation of the magnetic field components will be used for the spectral analysis of nonlinear mode coupling.

Certain assumptions that have gone into the computation are worthy of note. First, the code does not contain plasma pressure. This assumption of a zero-beta model approximates the experimental observation that RFPs have low β. This is consistent with the force free relaxed state chosen for the equilibrium representation. Second, density profiles are not evolved. Third, the Lundquist number in the computation is two orders of magnitude smaller than that in the experiment. Fourth, viscosity is time independent.

References:

1. C. Mercier, Nucl. Fusion **1**, 47, (1960).
2. A.W. Newcomb, Ann. Phys., 232, (1960).
3. I.H. Hutchinson, M. Malacarne, P. Noonan, and D. Brotherton-Ratcliffe, Nuclear Fusion **24**, 59 (1984).
4. R.G. Watt and R.A. Nebel, Physic Fluids **26**, 1168 (1983).
5. S. Assadi, A. Almagri, J. Beckstead, E. Hotta, D. Kortbawi, S. Prager, J. Sarff, and C. Sprott, Bull. Am. Phys. Soc. **1**, 265(1988).
6. E.J. Caramana, R.A. Nebel, and D.D. Schnack, Phys. Fluids **26**, 1305 (1987).
7. H. R. Strauss, Phys. Fluids **27**, 2580 (1984).
8. Z. G. An, P.H. Diamond, R. D. Hazeltine, J.N. Leboeuf, M.N. Rosenbluth, R.D. Sydora, T. Tajima, B.A. Carreras, L. Garcia, T.C. Hender, H.R. Hicks, J.A. Holmes, V.E. Lynch, and H.R. Strauss, in Plasma Physics and controlled Nuclear Fusion Research, 1984, Proceedings of the 10th International Conference, London (IAEA, Vienna, 1985), Vol. **2**, 231.
9. J.A. Holmes, B.A. Carreras, T.C. Hender, H.R. Hicks, V.E. Lynch,Z.G. An, and P.H. Diamond, Phys. Fluids **28**, 261 (1985).
10. See, for example, G. Bateman, MHD Instabilities, The MIT Press, (1978).

11. D.C. Robinson, Nuclear Fusion **18**, 939 (1978).

12. E.J. Caramana, R.A. Nebel and D.D. Schnack, Phys. Fluids **26**, 1305 (1983).

13. J.B. Taylor, Reviews of Modern Physics, **58**, 3, (1986).

14. D.D. Schnack and J. Killeen, J. Comp. Phys. **35**, 110 (1980).

15. D.D. Schnack, E.J. Caramana, and R.A. Nebel Phys. Fluids **28**, 224, (1985).

16. R.A. Nebel, E.J. Caramana and D.D. Schnack, Phys. Fluids **B1**, (1989).

17. R.A. Nebel, E.J. Caramana, and D.D. Schnack, Phys. Fluids **B1**, 1663 (1989).

18. K. Kusano and T. Sato, Nuclear Fusion **27**, 821 (1987).

19. Y.L. Ho and G.G. Craddock, Phys. Fluids **B1**, 721 (1991).

20. D.D. Schnack, D.C. Barnes, Z. Mikic, D.S. Harned, E. J. Caramana, and R.A. Nebel, Computational Phys. Communication. **43**,17 (1987).

21. D.D. Schnack, D.C. Barnes, Z. Mikic, D.S. Harned, and E.J. Caramana, J. Compt. Phys. **70**, 330 (1987).

22. D.S. Harned and D.D. Schnack, J. Comput. Phys. **65**, 57 (1986).

23. J. W. Eastwood and W. Arter, Phys Fluids **30**, 2774 (1987).

24. K. L. Sidikman, "Self-consistent Field Errors Effects in Reversed Field Pinch Plasma" Ph.D. Thesis, University of Wisconsin-Madison, 1990.

CHAPTER III

Experimental Apparatus and Diagnostics

The Madison symmetric Torus (MST) is a toroidal reversed field pinch device for plasma physics and fusion research. A brief description of the unique design features of this device is discussed in section III-1. In section III-2 the diagnostics developed for the purpose of this research thesis is presented.

III-1) Description of MST Device

The Madison Symmetric Torus, MST, is a toroidal reversed field pinch device which commenced operation in June, 1988. The MST is a large RFP with a minor radius of 52 cm and a major radius of 150 cm. The shell thickness "t" of 5 cm corresponds to a poloidal magnetic soak-in time, defined by $\tau=2\mu_0 t^2/\eta$, of about 60 msec. The parameters of the device are listed in Table III-1. The MST is shown on Figure (III-1). The design of MST was heavily concerned with minimizing field errors due to gaps, portholes, DC and primary windings. The vacuum system of the MST is unconventional: it is used as the toroidal field winding and the stabilizing conducting shell, as shown in Fig. (III-2).

The conducting shell has two cuts, toroidal (ϕ) and poloidal (θ). The toroidal gap is a cut the long way around the torus, allowing the toroidal magnetic

field to enter the shell. The poloidal gap is a cut in the short way around the torus allowing the poloidal magnetic field to enter the shell.

Ohmic heating and field generation are provided by a 2.0 Volt-second laminated iron core transformer, which links the plasma to the 20 turn primary winding. The pulsed current to this winding is supplied by a 5 KV capacitor bank.

The poloidal field windings are composed of three separate sets of windings around the iron core [1,2,3,4,5] as shown in Fig. (III-3). First, the reversed DC bias winding enables a 2.0 volt-second flux swing by reverse biasing the iron core. It carries 8000 ampere-turns of dc current for 3 to 10 seconds. The bias winding has been distributed along the iron core in such a way to trap most of the magnetic flux inside the iron and minimize the dc field in the plasma volume [6]. Second, the continuity winding carries the wall current from one side of the poloidal gap to the other side by topologically excluding the iron core. This winding provides a low impedance path for the surface currents flowing on the inside surface of the shell. Third, the poloidal field (PF) winding carries the pulsed current which provides the flux swing; it is tightly wound around the continuity winding; the distribution of the PF winding is optimized to match the plasma image current flowing on the inside surface wall of the torus and the flange, through the holes, to the outside surface of the flange and the continuity winding.

The toroidal field is produced by the poloidal current in the conducting shell. This shell is used as a one turn secondary to a 1/2 Volt-second transformer. This results in small toroidal field ripple, easy diagnostic access, and maintenance. The primary of the toroidal field transformer is connected to a 450 Volt, 1/2 Farad electrolytic capacitor bank.

Pumping is done through a manifold connected to the bottom of the vessel by 193 1.5" diameter holes rather than a few large pumping ducts. The main pumping system are three Sargent-Welch 1500 l/s turbomolecular pump, one Cryogenic pump and one Sargent-Welch 800 l/s turbomolecular pump. Vacuum pressure and quality were monitored on a Bayard-Alpert ionization gauge and a quadruple gas analyzer.

Table III-1 MST PARAMETERS

Major radius	R= 150 cm
Minor radius	a= 52 cm
Shell thickness	t= 5 cm
Plasma Current	I_p <600 KA
Toroidal field	B_θ< 0.12 T
Line ave. density	$\langle n_e \rangle = 2.x\ 10^{13}\ cm^{-3}$
Base Pressure	4×10^{-7} Torr
Ion Temperature	250 eV.
Electron temperature	200 eV.
β~10%	

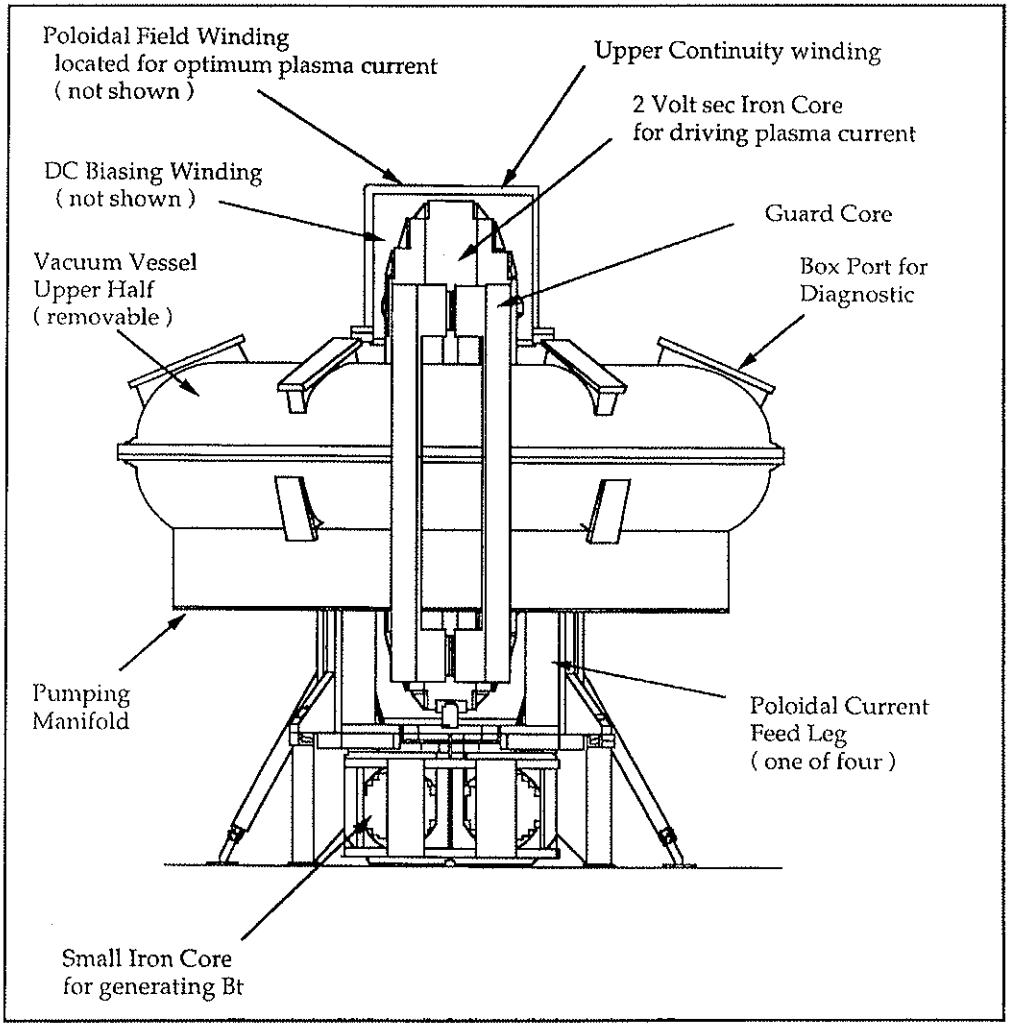

Figure III-1) Side view of the Madison Symmetric Torus (MST).

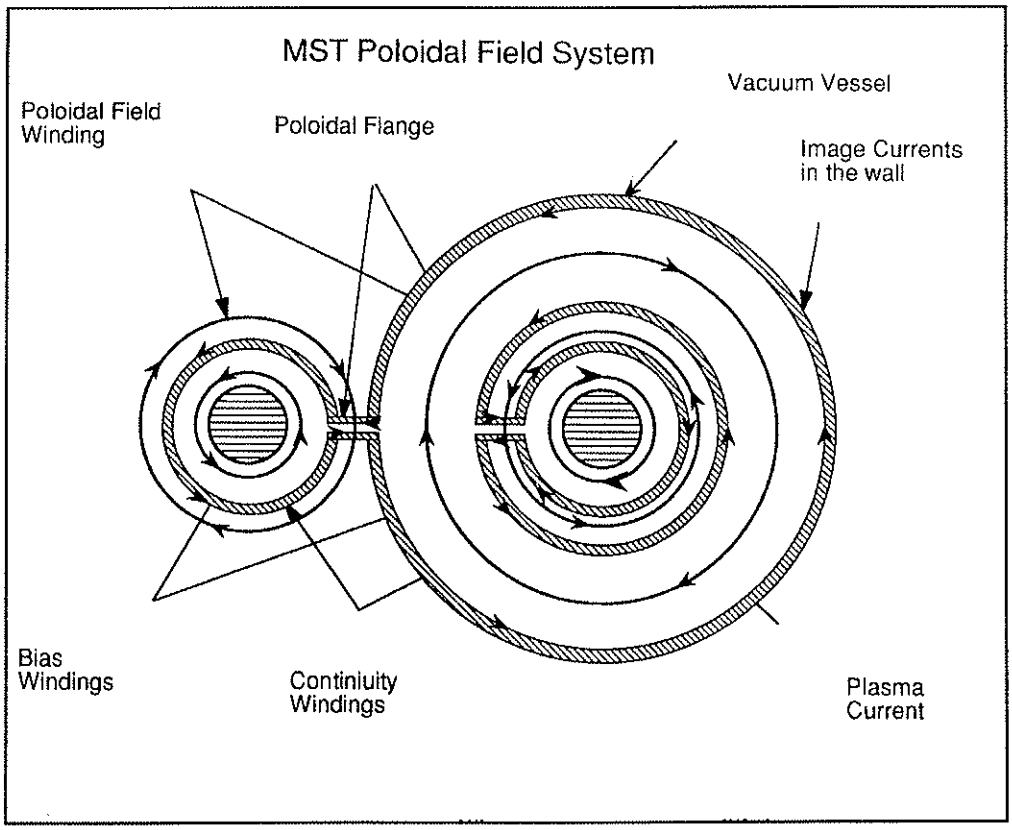

Fig. III-2) Poloidal field system of MST.

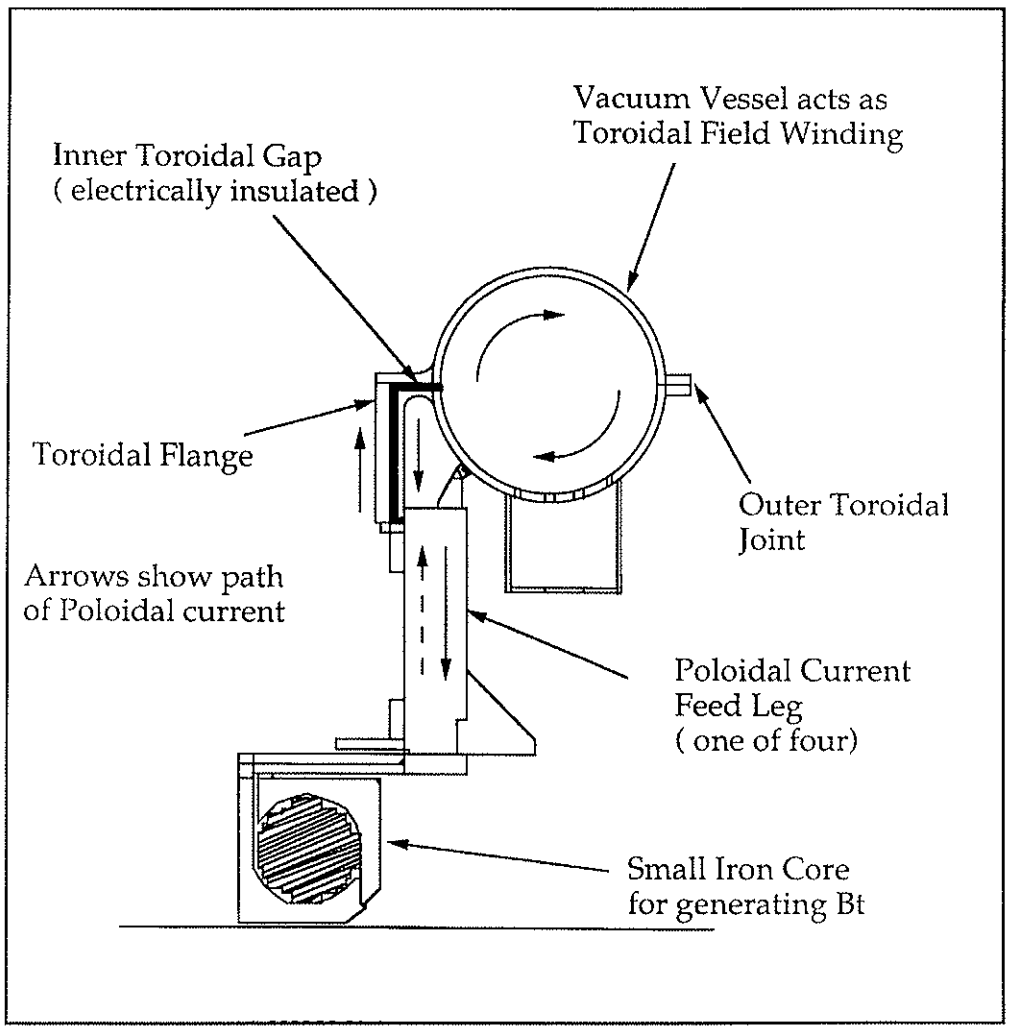

Fig. III-3) Toroidal Field system of MST.

III-2) Diagnostic Description

Magnetic sensors are commonly used to measure the magnetic properties of plasma experiments [7-9]. Probes consist of copper wire coils encased in a nonconducting heat shield and one or more layers of conducting material such as graphite, stainless steel or a thin layer of silver paint as an electrostatic shield. Magnetic sensors are used both inside and outside the plasma to measure the equilibrium and fluctuating field in MST.

Since magnetic fluctuation coherence measurements are frequency dependent, a technique has been developed to calibrate the magnetic coils-amplifier system to measure the magnetic fluctuation signals for a wide frequency range. The frequency-dependent effect of the electrostatic shielding and the self-inductance effect of the coils are taken into account over the entire bandwidth. The technique may also be used to take into account the eddy currents present in the vacuum vessel walls.

a) Magnetic Probes

The magnetic probes have been developed for general use, as well as specifically for this thesis research. Ease of access and minimization of the cost have been the primary goal.

I have developed four types of magnetic sensors during this research. (1) two poloidal and one toroidal fixed array of tri-axial sensors installed at the inside edge of the device, (2) a dense array of 32 toroidal and 16 poloidal coils, (3) a multi-purpose movable probe consisting of 8 radial coils and two ion saturation current probes, and (4) a large number of tri-axial movable coil sets.

1) Fixed Poloidal and Toroidal Arrays:

The fixed coil sets consist of three orthogonal magnetic sensors (Figure III-4), oriented to measure the magnetic field in poloidal, toroidal and radial directions.

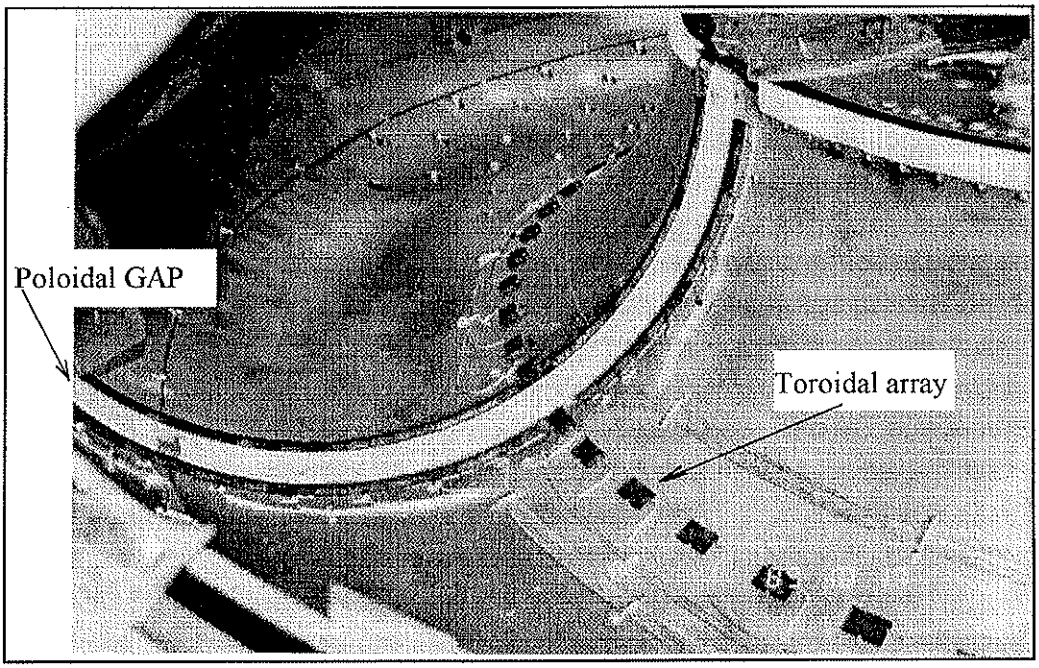

Figure III-4) View of toroidal and gap coils. Each toroidal coil set is encapsulated in a graphite box as an electrostatic and heat shield.

The five turn coils are wound on machinable ceramic of an "H" cross section using 32 gauge HML coated wire. Typical coil resistance is $\approx 1\Omega$ and typical effective coil areas are 1.5 Cm^2. The coils are installed inside a ceramic heat shield case which also acts as structural support (Figure III.5).

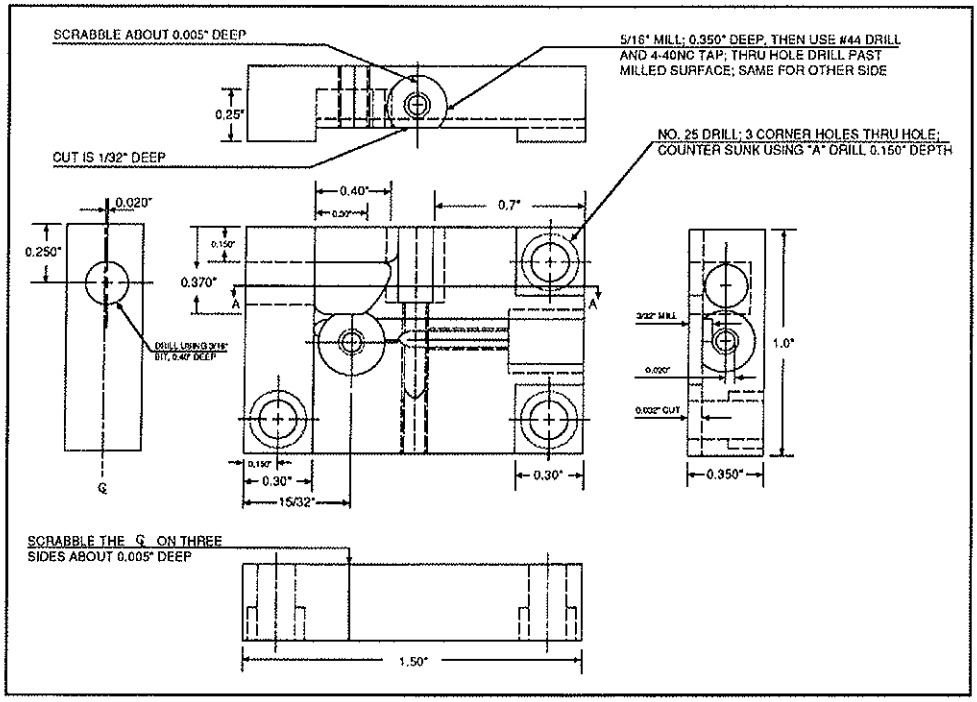

Figure III-5) Schematic drawing of a fixed coil set which are installed on inside wall of MST.

These encapsulated coil forms are mounted on the inside of MST as shown in Figures (III.6) and (III.7). The electrostatic and heat deposition shield is a 3/32" graphite box. The twisted coil leads are inserted inside a teflon heat shield and covered by 3/16 inch aluminum tube. The curvature formed aluminum tubes are formed to the curvature of MST and mounted to the inside of the vacuum vessel. The vacuum seal is made at two toroidal location at breakout trees. Vacuum feedthrough BNC connects the sensor leads to the outside. There are 64 fixed coil sets in the toroidal direction. The two poloidal fixed arrays have 16 and 8 coil sets.

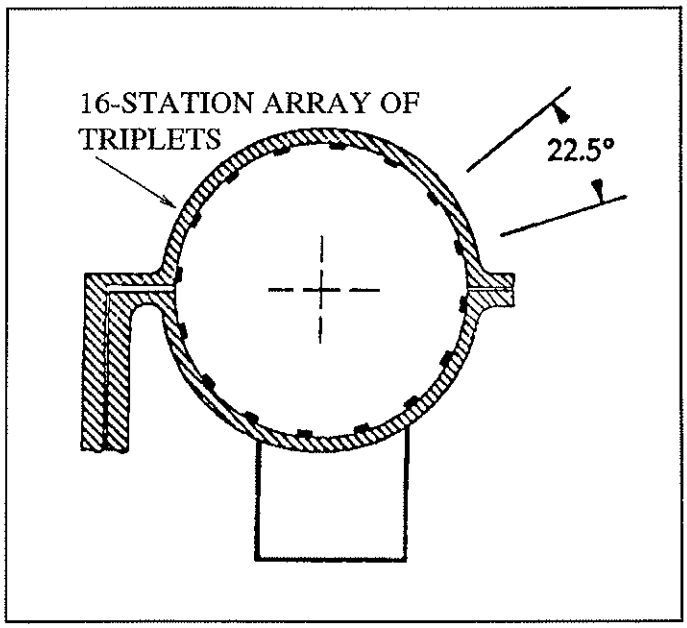

Figure III-6) Poloidal view of the location of fixed array at ϕ=180 degrees.

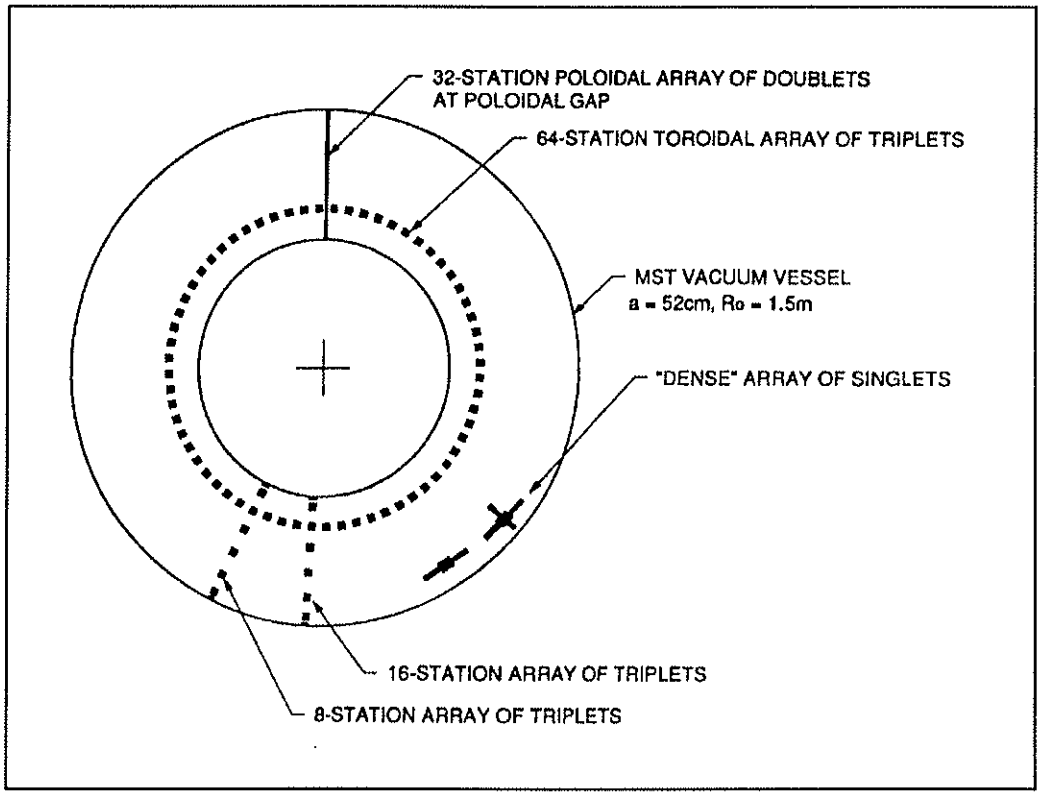

Figure III-7) Top view of MST showing the location of magnetic sensors.

2) Dense Array:

I have designed two dense arrays. These closely-spaced magnetic sensors have been designed to not only measure low frequency ($f < 250$ kHz) magnetic fluctuations but also high frequency ($f < 5$ MHz) magnetic fluctuations. There are four modules in the toroidal direction and two in the poloidal direction. Each module has eight coils separated one centimeter from one another. The coils are wound on hollow low conductance graphite "H" forms with 38 gauge HML coated wire. The typical 25 turn coils have a resistance of 6.9Ω and area ≈ 1.4 cm^2. The coils are encased in 0.005" open ended (in the direction of magnetic pickup) stainless steel tube formed to the curvature of the MST. Structural support and electrostatic shielding is provided by machinable ceramic which are thinly silver painted on the inside. These forms are in the shape of the inside curvature of the MST and mounted to graphite blocks as shown in Figure (III-8). Each graphite block acting as a router of the coil leads is attached to the inside vacuum vessel. The vacuum seal is made with a breakout pot and vacuum feed through BNC connectors.

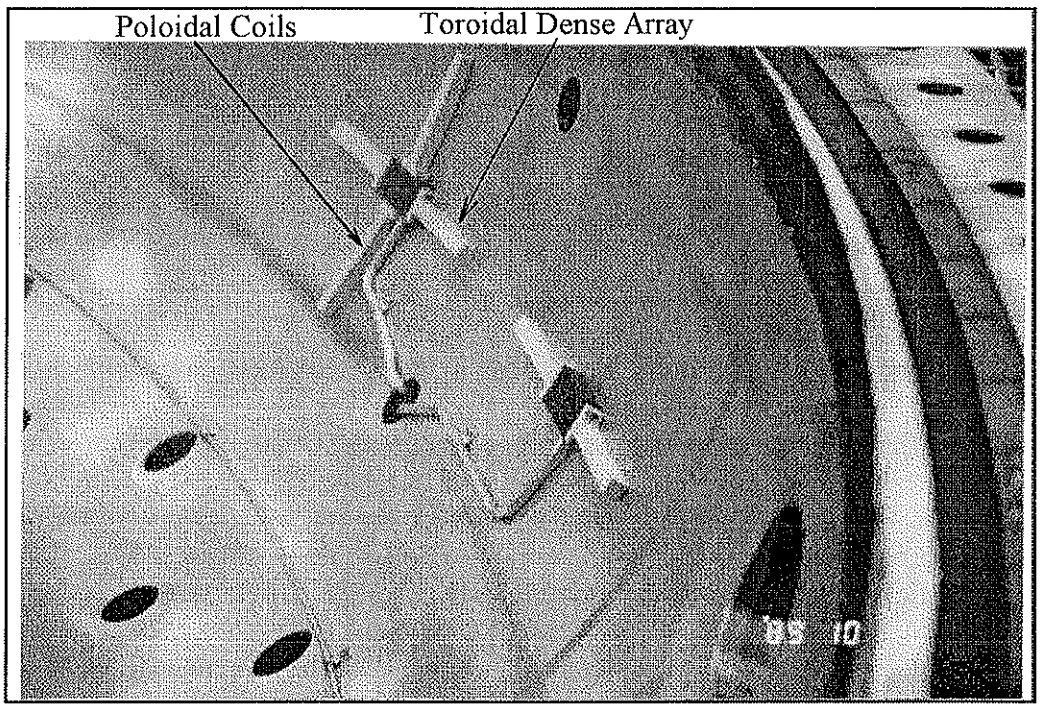

Figure III-8) View of dense array, 16 coils in poloidal direction and 32 coils in toroidal direction. The silver electrostatic coated coils are covered with ceramic particle shield.

3) Movable Forked Probe:

The movable forked probe developed for the experiments described in this thesis was motivated by trying to determine whether the source of magnetic fluctuations was related to electrostatic fluctuations.

As Figure (III-9) shows, there are 4 radial coils 1.2 cm apart. The specifications of the radial coils are similar to the dense array discussed above with the difference that there is a tungsten wire running through the center of the radial coils. The tungsten wire is used to measure the ion saturation current. The magnetic field generated via the current drawn by the ion saturation probe is perpendicular to the axis of B_r coils and does not alter the magnetic fluctuations measurement. Bench test after the construction of the probe has verified that.

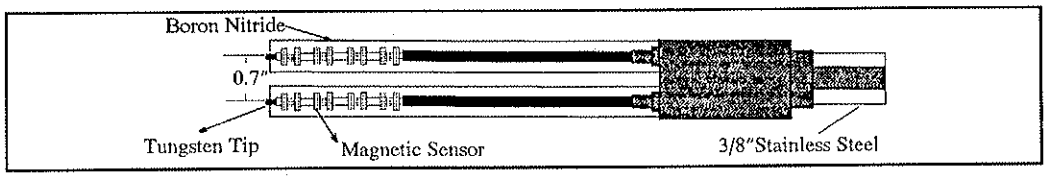

Figure III-9) Schematic of the "forked" probe. Each tine is a Boron Nitride particle shield. Electrostatic shield is provided by silver painting the inside wall.

4) Tri-axial Coil Sets:

Throughout this thesis project and the previous research done on the Octupole, a noncircular RFP machine and the diverter noncircular RFP device, about 100 tri-axial movable probes were made to measure the radial profile of the fluctuating and equilibrium fields. The probes consist of three orthogonal magnetic coils wound on a three dimensional "H" cross section machinable ceramic forms. A typical set was made from 42 to 54 gauge Teflon coated wire (20 turn transverse coils and 60 turn radial coils). Coil resistance varied from 8Ω to 60Ω depending on the type of the wire and the length of the probe. The coils were mounted on a ceramic cup. Structural support and electrostatic shielding is provided by a stainless steel tube (0.005" thick wall, 3/16" outside diameter). A boron nitride sheath is used for particle shielding and heat deposition. These sheaths are machined from a solid 1/4" boron nitride rods (0.10" thick wall, and < 1/4" O.D.). The tube containing the coils is inserted into this sheath (Figure III-10).

The main body of the probe is a 1/4" outer diameter, 0.20" thick seamless stainless steel tube. The vacuum seal is made at the back end of the probe with spatially designed breakout pot and vacuum feedthrough BNC connectors.

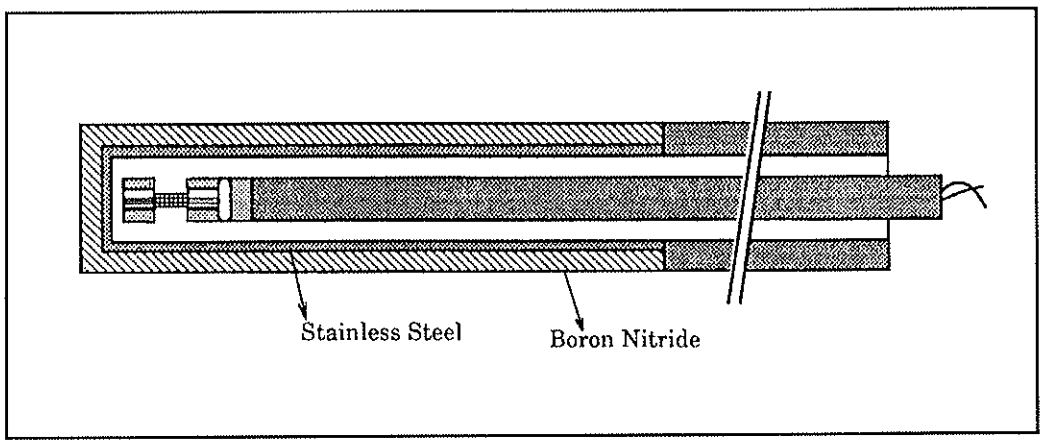

Figure III-10) Assembly drawing for a tri-axial magnetic probe used in this research showing the coils inside the electrostatic shield. The vacuum seal is made on the main probe body and is not shown.

III-3) Standard Calibration:

The output of a magnetic sensor is given by

$$V = -\frac{d\Phi}{dt} = \frac{d}{dt}\int \boldsymbol{B}\cdot\boldsymbol{ds} = -A_{eff}\frac{d<B>}{dt} \qquad (1)$$

where Φ is the magnetic flux linked by the coil, **B** is the magnetic field at the coil, **ds** is the element of the coil area, A_{eff} is the effective area of the coil, and $< B >$ is the average magnetic field over the coil area. Ideally, $A_{eff} = NA$ where A is the geometric area of the coil and N is the number of loops. Attenuation of

signals due to the thickness of the electrostatic shielding, tension of wire on the coil form, and imprecision in winding deviates the A_{eff} from such a simple relation. As mentioned previously, the effective areas are calibrated as a function of frequency. This is accomplished with a Helmholtz coil set that produces a known magnetic field. Coils are calibrated from 1 kHz to 250 kHz. At low frequencies, (10 kHz < f < 100 kHz), A_{eff} can be represented by a frequency independent constant A_{eff}. For frequencies above 100 kHz calibration curve is used.

The detailed list of MST diagnostics is given in Table III-2. The magnetic sensors designed for this thesis are listed in this table. There are 354 magnetic coils designed, built and installed for this research experiment.

Table III-2) MST DIAGNOSTICS

1 TOROIDAL ARRAY OF MAGNETIC SENSORS; 64 x 3 COILS.
1 POLOIDAL ARRAY OF MAGNETIC SENSORS; 16 x 3 COILS.
1 POLOIDAL ARRAY OF MAGNETIC SENSORS; 8 x 3 COILS.
1 PARTIAL ARRAY OF 32 CLOSELY SPACED TOROIDAL COILS.
1 PARTIAL ARRAY OF 16 CLOSELY SPACED POLOIDAL COILS.
1 MOVABLE PROBE OF 6 x 4 COILS.
1 MOVABLE PROBE OF 8 x 3 COILS.
6 MOVABLE PROBES OF TRI-AXIAL COILS.

Array of 40 soft x-ray detectors.
Array of 32 visible light detectors.
Microwave interferometer for $\langle n_e \rangle$.
Thompson scattering for T_{eo} & N_{eo}.
Fast ion gauge.
CXA
Bolometer.
Optical diagnostics

References

1) Y. Ho, R.N. Dexter, D.W. Kerst, T.W. Lovell, S.C. Prager, J.C. Sprott, The design of MST Reversed Field Pinch, University of Wisconsin Report PLP 956, Nov. 1985.

2) R.N. Dexter, D.W. Kerst, T.W. Lovell, S.C. Prager, J.C. Sprott, Fusion Technology in 19, 131 (1991).

3) D.W. Kerst, primary system, University of Wisconsin Report PLP 972, March 1986.

4) A.F. Almagri, S. Assadi, J. Beckstead, G. Chartas, D.J. Den Hartog, Y. Ho, R.N. Dexter, D.W. Kerst, T.W. Lovell, S.C. Prager, J.S. Sarff, W. Shen ,C. Spragins, J.C. Sprott, The design of MST Reversed Field Pinch, University of Wisconsin Report PLP 1022, Nov. 1987.

5) D.W. Kerst, Primary system connection, University of Wisconsin Report PLP 955, Oct. 1985.

6) A.F. Almagri, "The Effects of Magnetic Field Errors on Reversed Field Pinch Plasma" Ph.D. Thesis, University of Wisconsin-Madison (1990).

7) R. H. Lovberg, Plasma Diagnostic Techniques, edited by R. H. Huddlestone and S.L. Leonard (academic Press, NY, 1965).

8) W. Botticher, Plasma Diagnostics, edited by R.H. Huddlestone and S. L. Leonard (academic Press, NY, 1965).

9) S. L. Leonard, Plasma Diagnostic Technique, edited by R. H. Huddlestone and S. L. Leonard (Academic Press, NY, 1965).

Chapter IV

Stationary Time Series and Spectral Analysis

Analysis of magnetic fluctuation data on the MST relies on the use of the Fast Fourier Transform (FFT) algorithm [1] for both speed of the calculation and to derive the frequency dependence of the measured quantities. In this chapter, I will present a brief introduction to the theory of stationary time series and spectral analysis, including bi-spectral analysis used to measure nonlinear coupling.

IV-1) Introduction

If a stationary time series is Gaussian, and therefore linear, the second moment (auto- and cross-power spectra) contains all the useful information present in the series, (e.g. information about the possible presence of harmonics). If the series is non-linear, the second order spectra will not adequately characterize the series. For instance, the second order properties of a bi-linear time series are similar to those of a linear time series model. As such, second order spectral analysis will not necessarily show up any features of non-linearity (or non-Gaussian) present in the

series. It is essential, therefore, to perform higher order spectral analysis on the series in order to detect departures from linearity and "Gaussianity". The simplest form of higher order spectral analysis is bi-spectral analysis. The basic concepts of digital linear analysis relevant to the magnetic fluctuations are given in section IV-2. Wavenumber and frequency spectra are given in section IV-3. The estimation of the coupling coefficient and a brief description of bi-spectral analysis is given in section IV-4. The temporal evolution of the wavenumber spectrum via energy cascading is introduced in section IV-5.

IV-2) Basic Concepts

Let $B_1(t)$ and $B_2(t)$ denote two fluctuating magnetic signals which are digitized and then Fourier transformed to $B_1(\omega)$ and $B_2(\omega)$. The RMS amplitude spectrum is given by

$$\tilde{B}(\omega) = \{\frac{1}{T} C(\omega)^2 \langle \mid \dot{B}(\omega) \mid^2 \rangle\}^{1/2} \qquad (4.1)$$

where <···> represents an ensemble average over hundreds of data records of duration T, $C(\omega)$ is the complex frequency calibration (amplitude and phase) and $B(\omega) = B(\omega) / \omega$. The discrete form of the above equation is

$$\tilde{B}_n = \{ C_n^{\,2} \langle \mid \dot{B}_n \mid^2 \rangle \}^{1/2}. \qquad (4.2)$$

The magnetic fluctuation amplitude in a specific frequency range is simply given by summing over the limited number of the frequency steps. This is different from the standard Blackman and Tukey [2] [3] method .

The cross power spectrum is computed from $P_{12}(\omega) = B_1(\omega)^* B_2(\omega)$ where * denotes complex conjugation. Since $P_{12}(\omega)$ is in general complex, it may be expressed via its real and imaginary parts.

$$P_{12}(\omega) = C_{12}(\omega) + iQ_{12}(\omega) \equiv |P_{12}(\omega)| e^{i\theta_{12}(\omega)} \tag{4.3}$$

where the real part $C_{12}(\omega)$ is called the co-spectrum, and the imaginary part, $Q_{12}(\omega)$, is called the quad-spectrum. $|P_{12}(\omega)| = |B_1(\omega)| |B_2(\omega)|$ is called the cross-amplitude spectrum and $\theta_{12}(\omega) = \theta_1(\omega) - \theta_2(\omega)$ is named the cross-phase-spectrum. Preservation of the phase information in the form of a phase difference is being used to measure the wavenumber of waves/modes present in the plasma. The phase spectrum can be interpreted as the phase shift each spectral component undergoes in traveling a distance Δr between the two spatial points at which $B_1(t)$ and $B_2(t)$ are being measured. This phase shift $\theta_{12}(\omega)$ (and poloidal & toroidal mode numbers m,n) are given by the dot product of the wave-vector **k** and the distance of travel Δ**r**:

$$\theta_{12}(\omega) = \bar{k}(\omega) \cdot \overline{\Delta r} \tag{4.4}$$

$$m(\omega) = r\, k_\theta(\omega) \tag{4.5}$$

$$n(\omega) = R k_z(\omega) \tag{4.6}$$

where r is the minor radial position and R is the major radial position. The azimuthal phase velocity is given by

$$V_{ph} = \frac{2\pi f}{k_\theta} \equiv \frac{2\pi R \Delta\theta f}{\theta_{12}(f)}. \tag{4.7}$$

The coherency spectrum is defined in terms of the (auto-) cross-power spectrum as

$$\gamma_{12}(\omega) = \frac{|P_{12}(\omega)|^2}{[P_{11}(\omega) P_{22}(\omega)]^{1/2}} \tag{4.8}$$

where $0 \leq |\gamma_{12}| \leq 1$.

The cross-amplitude spectrum is normalized by the auto-power spectrum of both $B_1(t)$ and $B_2(t)$ and can be interpreted as the degree of the cross-correlation between $B_1(t)$ and $B_2(t)$ at each frequency. If the coherency is zero at a particular frequency then the two magnetic fluctuating signals are called incoherent at that frequency. If, on the other hand, the coherency is 1, the two signals are fully coherent. Due to background noise and discreteness of the signals an intermediate value for coherency exists. If the two signals are spatially separated by a distance Δx, then the

coherence length of an exponentially decaying coherence is defined as $L(\omega) = \Delta x / (\ln\gamma)$. The cross correlation is defined as:

$$R_{12} = \frac{\int_{-\infty}^{\infty} f_1(t) f_2(t+\tau)\, dt}{[\langle \int_{-\infty}^{\infty} f_1^2(t)\, dt \rangle \langle \int_{-\infty}^{\infty} f_2^2(t)\, dt \rangle]^{1/2}} \tag{4.9}$$

where

$$\int_{-\infty}^{\infty} f_1(t) f_2(t+\tau)\, dt = \int_{-\infty}^{\infty} F_1(\omega)\, F_2^*(\omega)\, e^{j\omega\tau}\, d\omega\,. \tag{4.10}$$

Error estimates of the above statistical quantities are derived by Bendat and Piersol [4]. The estimates of the square coherence (γ^2) errors is given as:

$$\epsilon(\gamma_{12}^2) = \frac{\sqrt{2}(1-\gamma_{12}^2)}{\sqrt{N}\,|\gamma_{12}|}\,. \tag{4.11}$$

The error in the coherency (γ^2) is inversely proportional to the number of terms in the ensemble (N). The error in the coherence is also inversely proportional to the coherence itself as expected, since the causal relation for two similar signals is easier to determine. The random error in relative phase determination is similar to coherence error:

$$\epsilon(\gamma_{12}^2)=\frac{(1-\gamma_{12}^2)^{1/2}}{|\gamma_{12}|\sqrt{2N}}. \qquad (4.12)$$

IV-3) The Wavenumber-Frequency Spectrum

While the dispersion relation for linear waves in a stationary state can be deterministic (for a given ω there is a unique value of k), this is not the case for the turbulent state: instead, the power at a given frequency band ω to ω + Δω may be distributed broadly in wavenumber space due to nonlinear wave coupling. The dispersion relation is broadened and must be described by the joint wavenumber-frequency power spectrum S(k,ω). The S(k,ω) spectra contain complete information on the second order space-time relationship of a stationary process. As noted earlier, the frequency spectra can easily be obtained from a single probe, but wavenumber information would require simultaneous measurement of fluctuations in at least two spatial locations. One method is a spatial Fourier decomposition of spatially distributed probes to obtain the wavenumber spectrum. This straightforward method has the disadvantage of limited wavenumber resolution and can be potentially expensive. An alternative method has been developed by Beall [5] to calculate a local wavenumber-frequency spectrum using a fixed probe pair separated by Δx. In this

technique, it is assumed that fluctuations consist of a superposition of a finite number of sinusoidal oscillations in time and space. It is also assumed that the amplitudes and phases of the oscillations are slowly varying over time. The power and average wavenumber spectra can be calculated as described in the previous section. The local wavenumber and frequency spectrum $S_L(k,f)$ can be estimated by

$$S_L(m\Delta k, l\Delta f) = \langle S_j(x, l\Delta f)\, I_{m\Delta k}[k_j(l\Delta f)] \rangle \qquad (4.13)$$

where m = number of wavenumber bins, l = number of frequency bins, Δk= wavenumber resolution, Δf = frequency resolution = 1/T and $I_{m\,\Delta k}[k_j(l\,\Delta f)] = 1$ for $(m-1/2)\,\Delta k < k_j\,(l\,\Delta f) \le (m+1/2)\Delta k$ and $I_{m\,\Delta k}[k_j(l\,\Delta f)] = 0$ elsewhere and the sample jth realization is given by equation (4.13) as

$$S_j(x, l\Delta f) = B_{1j}^*(x, l\,\Delta f)\, B_{1j}(x, l\,\Delta f) \equiv H_j(\Delta x \to 0, l\Delta f). \qquad (4.14)$$

Note that $< H_j\,(\Delta x, l\,\Delta f) >$ is another way of defining the cross-power spectrum, and the discrete wavenumber (m Δk) are bounded by $(-\pi / \Delta x)$ and $(\pi / \Delta x)$ and the wavenumber resolution Δk is given by the number of segments chosen in the interval $(-\pi / \Delta x)$ and $(\pi / \Delta x)$. The resolution (i.e., number of wavenumber bins) must be chosen appropriately so as to have a sufficient number of realizations falling into the

wavenumber bins of interest to provide good statistics. For easier visualization we will, in the following , use the notation k = m Δk and f = l Δf .

From the local wavenumber frequency spectrum $S_L(k, f)$, the frequency spectrum $S_L(f)$ and the local wavenumber $S_L(k)$ can be estimated by

$$S_L(f) = \sum_k S_L(k,f) \equiv \langle S_j(x, l\,\Delta f) \rangle, \tag{4.15}$$

$$S_L(k) = \sum_f S_L(k,f). \tag{4.16}$$

The frequency spectrum ($S_L(f)$) can also be obtained directly from the temporal Fourier transform using Equation (4.14).

The frequency spectrum of magnetic fluctuations in transition to turbulence falls off rapidly toward higher frequencies. Thus by analogy with random variable theory it is useful to define a normalized $S_L(k, f)$ spectrum, called the conditional spectrum $S_L(k \mid f)$ as

$$S_L(k \mid f) = \frac{S_L(k,f)}{S_L(f)}. \tag{4.17}$$

The conditional spectrum $S_L(k|f)$ enhances the frequency components with low power.

In situations where random nonlinear interactions are present the dispersion relation (k(f) versus f) is no longer deterministic. However, an average statistical dispersion estimate, $< k(f)>$, can be written.

$$< k(f) > = \sum_k S_L(k|f). \tag{4.18}$$

The broadening of the spectrum is defined by

$$< \sigma_k^2(f) > = \sum_k (k - < k(f) >)^2 S_L(k|f). \tag{4.19}$$

The wavenumber broadening for a given frequency f_o is related to the distribution of the $S_L(k , f)$ spectrum at frequency f_o. It has been shown by Beall et al. [5] that, in a spatially homogeneous medium, the local $S_L(k , f)$ spectrum is equal to the conventional wavenumber spectrum. It should also be noted that, just as the sampling interval must be short enough to avoid aliasing in the frequency domain, so must the probe separation be small enough such that $\pi/\Delta x$ is greater than the highest wavenumber of any significant spectral component.

IV-4) Bi-spectral Analysis

In this section auto- and cross- bi-spectrum are introduced. These powerful statistical concepts have been used in a number of investigations as data analysis tools, notably by Hasselman, Munk and McDonald, [6] on ocean waves, Lii, Rosanblatt and Van Atta [7] on turbulence, Helland and Lii [8] on the energy transfer in grid-generated turbulence, Ritz, Powers and Bengtson [9] on the three wave coupling and energy cascading in plasmas. The focus here is on the statistical properties of auto- and cross-bispectra, and how to estimate them from finite data lengths.

There are two different approaches to obtaining quadratic wave coupling in a self-excited fluctuation spectrum.

(1) " Multi-windows bispectrum estimation" method. A good reference is by David J. Thomson of AT&T Bell Laboratories. Briefly, this method has proven to be useful when the process is of evolutionary nature or the number of data points are not sufficient (spatial Fourier decomposition of the modes are coarse). Here, a multiple-window method for computing consistent estimates of the bispectrum from a short segment of the process is used. In multi-window methods the information in a narrow band is summarized by the coefficient of its expansion in the Slepian sequence [10] (Discrete Prolate Spheroidal Sequences). Bispectrum estimates are then formed either

by averaging what are effectively complex demodulates over time, or by averaging products of such expansions centered at frequencies f_1 , f_2 and $f_1 \pm f_2$ over a 3-dimensional element of the frequency domain (wavenumber domain). Either choice reduces to the weighted average of products of the expansion coefficients.

(2) The second method which I mostly follow is based on the digital time series analysis technique. A review of the concepts of cumulant spectra [11], [12], [13], which measure the extent of joint dependence of the spectral components, is not given here and the reader is encouraged to refer to the above references. First, we define the power spectrum, S(k), which is familiar from the last section as a second order cumulant spectra and then the bispectrum B(k,l) is the third-order cumulant spectra:

$$S(k) = E[B_k B_k^*] \tag{4.20}$$

$$B(k,l) = E[B_k B_l B_{k+l}^*], \tag{4.21}$$

where E[...] is defined as

$$E[B(\times)B(\times+\chi_1)B(\times+\chi_2)] = \int_{-1/2}^{1/2}\int_{-1/2}^{1/2} B(k_1,k_2)\, e^{i2\pi(k_k\chi_1+k_l\chi_2)}\, dk_1\, dk_2$$

The definition of the B(k,l) clearly shows how the bispectrum measures the statistical dependence between three waves [14]. That is, if waves present at k_1, k_2, and $k_1 \pm k_2$ are spontaneously excited independent waves, each wave can be characterized by statistically independent random phases. Thus, the summation of the three spectral component phases will be randomly distributed over $(-\pi,\pi)$. When a statistical averaging process denoted by the expectation operator (4.22) is carried out, the bispectrum will vanish due to the random phase mixing effect. On the other hand, if the three spectral components are nonlinearly coupled to each other, the total phase of the three waves will not be random, though phases of each wave are randomly changing for each realization. Consequently, the statistical averaging will not lead to a zero value of the bispectrum.

The bispectrum satisfies the following symmetry relations:

1) $B(k, l) = B(l, k) = B^*(-k , -l)$;

2) $B(k, l) = B(-k-l, l) = B(k, -k-l)$.

Let's consider a simple example of *single* three-wave coupling with wavenumber k_1, k_2, and k_3 ($k = 1$, $l = 2$), satisfying the resonance conditions for wavenumbers and frequencies.($k_3 = k_1 \pm k_2$, $\omega_3 = \omega_1 \pm \omega_2$). Then the general quadratic nonlinear relation is

$$B_3 = \sum_{k_3=k_1\pm k_2} A_{2,1} B_2 B_1 + \epsilon, \tag{4.23}$$

where the quantity ε denotes any error associated with the measurement. For a simple three-wave coupling with zero imperfection then Eq. 4.23 will reduce to:

$$B_3 = A_{2,1} B_2 B_1 . \tag{4.24}$$

The "goodness" of equation (4.24), which is in a quadratic regression form, may be measured by the quadratic correlation coefficient [15], b(k,l), called the bi-coherence spectrum:

$$b^2(k,l) = \frac{|B(k,L)|^2}{E[\,|B_k B_l|^2\,]\,E[\,|B_m|^2\,]} \tag{4.25}$$

where m = k ± l. The Equation (4.25) is basically the measure of the coherence between the three waves due to the wave coupling and it is analogous to the linear coherence spectrum which measures the degree of linear correlation between two signals on a spectral basis [16]. The bi-coherence spectrum is bounded by $0 \le b \le 1$. This can be shown by employing Schwarz' inequality. The bi-coherence spectrum is close to unity when the resonant wave $k_m = k_k \pm k_l$ is excited by the waves at k_k and k_l . On the other hand b(k,l) = 0 implies an absence of coherence for the

interaction and thus suggests that the waves k_m, k_k and k_l are spontaneously excited independent modes. The quantity $b^2(k, l)\, S(k)$ corresponds to the power of the wave at k_m due to the coupling of the waves at k_k and k_l. That is, $B(k_m) = B_{unc} + A_{k,l}\, B_k\, B_l$ is decomposed into an uncoupled, B_{unc}, part and a part which is generated by three wave coupling, described by a coupling coefficient $A_{k,l}$. The bi-coherence $b^2(k, l)=A_{k,l}$ enters as the nonlinear coefficient and measures the fraction of the power at k_m due to the three-wave coupling in a single three-wave interaction. Note that $A_{k,l}$ is given by

$$A_{k,l} = \frac{E[B_k^* B_l^* B_{k+l}]}{E[|B_k B_l|^2]}. \tag{4.26}$$

This value of $A_{k,l}$ minimizes the mean-square error $E[\,|\,\varepsilon\,|^2\,]$ of the quadratic model of single three-wave coupling (Eq. 4.24).

In the more general case of multiple interacting waves, the spectrum can contain numerous modes coupled by previous interactions. In this case the number of coupled pairs (k_k , k_l) which can contribute to the bispectrum in equation (4.20) then exceeds a single triad and the bi-coherence can no longer be considered as a fractional power measure. In general, the bi-coherence is viewed as a phase coherence measure between coupled waves.

IV-5) Energy Cascading and Estimation of the Coupling Coefficients

A brief description of the estimation of the nonlinear coupling coefficients and of the resulting amount of energy cascading between waves for a fully turbulent system is given in this section. This method was initially introduced in plasma physics by Ritz et al. [17].

Suppose the time evolution of the wave coupling spectrum in the simplest variant of a wave-wave coupling could be described by linear plus a quadratic nonlinear terms in the form:

$$\frac{\partial B(k,t)}{\partial t} = (\gamma_k + i\,\bar{\omega}_k)\,B(k,t) + \frac{1}{2}\sum_{k_1,k_2,k} \Lambda_k^Q(k_1,k_2)\,B(k_1,t)\,B(k_2,t) \quad 4.27$$

where γ_k is the growth rate, ω_k is the dispersion relation, $\Lambda_k{}^Q$ is the coupling coefficient. Then the spatial Fourier spectrum B(k = k_1 + k_2, t) of the magnetic fluctuations is defined by

$$B(x,t) = \sum_k B(k,t)\,e^{ikx}. \qquad (4.28)$$

Then the computation of the linear (γ_k , ω_k) and the three-wave coupling $\Lambda_k{}^Q$ [k_1 , k_2] coefficients from the raw fluctuating time series data via spectral anal-

ysis model of figure IV-1 is facilitated.

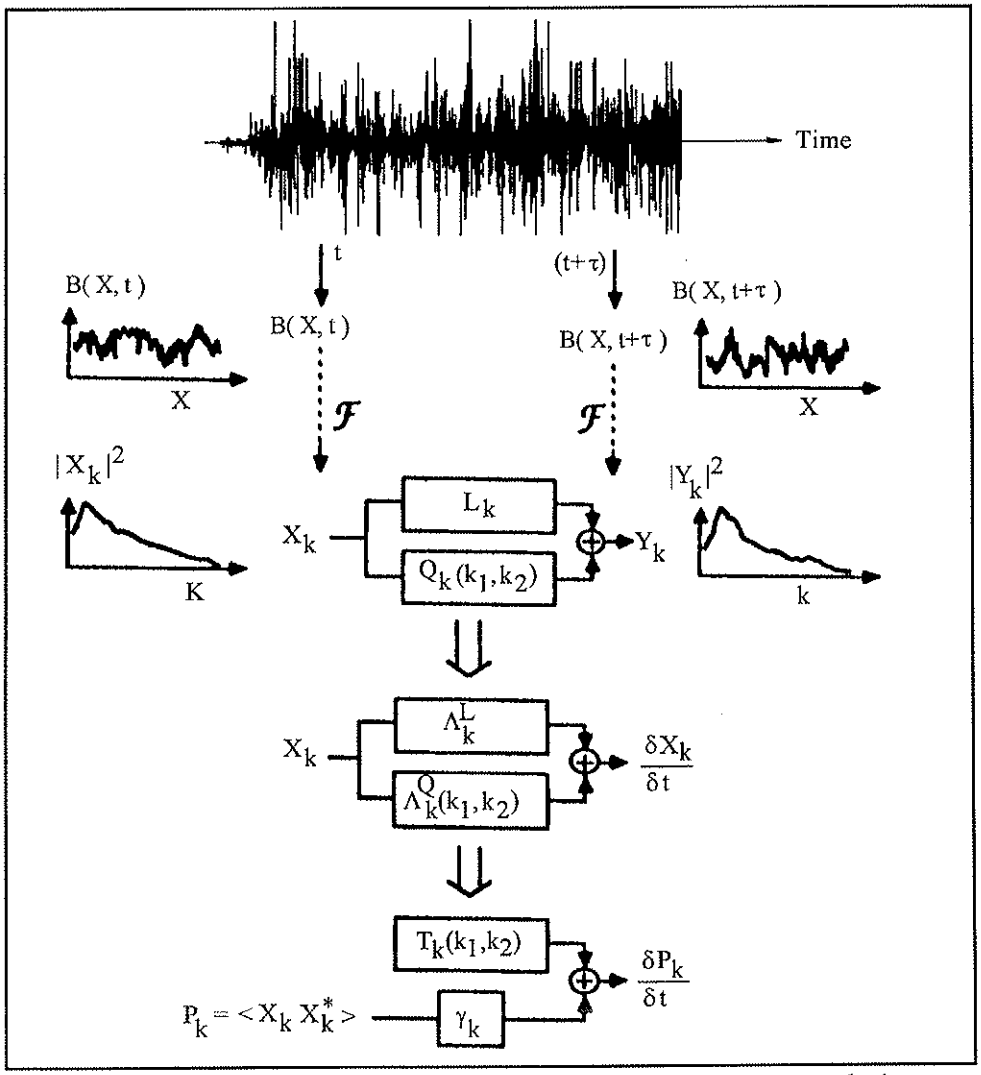

Figure IV-1) Schematic representation of the measurement technique as described by Ritz, et al.

In plasmas the turbulence system can be very complicated. It should be noted that Fig. (IV-1) only represents the linear plus the quadratic nonlinear coupling. We assume that four wave coupling and higher-order processes are much weaker than three-wave coupling.

Definitions

γ_k = Linear growth rate.
ω_k = Mean dispersion relation.
L_k = Linear transfer function.

$Q_k (k_1,k_2)$ = Quadratic transfer function.

$\Lambda_k^L = \gamma_k + i< \omega_k >$ = Linear coefficient coupling.

$\Lambda_k^Q (k_1,k_2)$ = Quadratic coupling coefficient.

$T_k (k_1,k_2)$ = Power transfer function.

The fast Fourier transform of the measured spatial magnetic fluctuations at two different times results in the wavenumber spectra X_k and Y_k. Following the recipe given by Ritz et al. we obtain two coupled equations:

$$< Y_k X_k^* > = L_k < X_k X_k^* > + \frac{1}{2} \sum_{k_1,k_2,k} Q_k^{k_1,k_2} < X_k^* X_{k_1} X_{k_2} > \qquad (4.29)$$

$$< Y_k X_{k_1'}^* X_{k_2'}^* > = L_k < X_k X_{k_1'}^* X_{k_2'}^* > + \frac{1}{2} \sum_{k_1,k_2,k} Q_k^{k_1,k_2} < X_{k_1}^* X_{k_2}^* X_{k_1'}^* X_{k_2'}^* > \qquad (4.30)$$

with $k = k_1 + k_2 = k'_1 + k'_2$

The fourth order moment $< X_{k1} \; X_{k2} \; X_{k'1}^* \; X_{k'2}^* >$ can be approximated by the square of second-order moments $< |X_{k1} \; X_{k2}|^2 >$, as suggested by Millionshchikov [18] for weak turbulence, by neglecting terms with $(k_1 \; , k_2) \neq (k'_1 \; , k'_2)$. Hence Equation (4.30) becomes

$$< Y_k X_{k_1'}^* X_{k_2'}^* > = L_k < X_k X_{k_1'}^* X_{k_2'}^* > + \frac{1}{2} \sum_{k_1,k_2,k} Q_k^{k_1,k_2} < | X_{k_1}^* X_{k_2}^* |^2 > . \qquad (4.31)$$

Equations (4.29) and (4.31) can be solved iteratively to find the transfer functions (defined in Chapter 5).

The quantities in the angular brackets can be calculated from the procedure given in the last two sections, i.e. $< X_{k1} \; X_{k'1}^* >$ the is auto-power spectrum; $< Y_{k1} \; X_{k'1}^* >$ is the cross power spectrum; $< X_k \; X_{k'1}^* \; X_{k'2}^* >$ is the auto-bispectrum; and

$< Y_k \; X_{k'1}^* \; X_{k'2}^* >$ is the cross-bispectrum.

The growth rate γ_k, the dispersion relation ω_k, and the coupling coefficient Λ_k^Q can be calculated from the transfer functions.

References:

1. M.B. Priestley, Spectral Analysis and Time Series , Academic Press, (1981).

2. R.B. Blackman and J.W. Tukey, The Measurement of Power Spectra, New York: Dover, (1959).

3. D.E. Smith, E. J. Powers and G. S. Caldwell, IEEE Trans. on Plasma Science **2** 261, (1974).

4. Bendat, J.S., Piersol, A.G., Random Data Analysis and Measurement Procedures, Wiley-Intersience, John Wiley and Sons, NY, (1986).

5. Beall, J.M. et. al. Journal of Applied Physics, **53**, 3933 (1982).

6. Hasselman, K., Munk, W., McDonald, G. "Bi-spectra of Ocean Waves", in Proc. Sym. Time Series Analysis, John Wiley, 135-139 (1963).

7. Lii, K.S., Rosenblatt, M. and Van Atta, C., J. Fluid Mech. **77**, 45, (1976).

8. Helland, K.N., Lii, K.S., and Rosenblatt, M. "Bi-spectra and Energy Transfer in Grid-Generated Turbulence", in Development in Statistics. Vol. **2,** Academic Press, 125-155, (1979).

9. Ritz, Ch. P., Powers, E.J., and Bengtson, R.D., Phys. Fluids **B1**, 153, 1989.

10. Slepian D., Bell System Tech. J., **57**, 1371, (1978).

11. Brillinger, D.R., and Rosenblatt, M. " Asymptotic Theory of Estimate of K^{th} Order Spectra", in Spectral Analysis of Time Series. John Wiley, (1967).

12. Harris, B. (Ed.) " Computation and Interpretation of the kth Order Spectra", in Spectral Analysis of Time Series. John Wiley, (1967).

13. Brillinger, D.R., "Time Series", Holt, (1975).

14. Kim, Y.C. and Powers, E.J., Phys. Fluids, **2**, 1452 (1978).

15. Jenkins, G.M. and Watts, D.G., Spectral Analysis and Its Application, Holden-Day, (1968).

16. Kim, Y.C., and Powers, E.J., IEEE Trans. Plasma Sci.; **PS-5**, 31 (1977).

17. Ritz, Ch. P., Powers, E.J. and Bengtson, R.D., Phys. Fluids **B1**, 153 (1989).

18. Millionshchikov, M.D., "Dokl. Akad. Nauk SSSR" **32**, 611 (1941).

Chapter V

Experimental Results and Discussion

Magnetic fluctuations are associated with self-reversal, sustainment and plasma transport in the reversed field pinch (RFP) . Though the mechanism is not well understood, fluctuations are thought to mediate both, through their role in energy and helicity transport. The prime objective of this research has been to determine the behavior of the edge magnetic fluctuations measurements and to compare them with predictions of MHD computation. Edge magnetic fluctuations in MST have been measured with fixed magnetic coil arrays at the wall and with insertable probes. Spatial mode spectra from full arrays at the wall are compared with two-point correlation measurements. In contrast to tokamaks, relative magnetic fluctuations are large, B_1 / B_o ~ 1-3%. The dominant fluctuations occur at frequencies f<35 kHz, and have been identified as global modes with poloidal mode number m = 1, and toroidal mode number n ~ 2R/a ~ 6. The short-wavelength, high frequency fluctuations (f > 35 kHz) represent only a small fraction of the total magnetic fluctuation power and correspond to modes locally resonant in the edge.

Three-wave nonlinear coupling of spatial Fourier modes is measured by applying bi-spectral analysis to magnetic fluctuations measured at the plasma edge at 64 toroidal locations and 16 poloidal locations, permitting observation of coupling

over 8 poloidal modes and 32 toroidal modes. Comparison to bi-spectral prediction of MHD computation indicates reasonably good agreement. However, during the crash phase of the sawtooth oscillations, the nonlinear coupling is strongly enhanced, concomitant with a broadening of the k-spectrum and frequency spectrum. In this chapter, I present initial results of energy cascading of toroidal modes. The results are promising; in particular, the computed linear and nonlinear transfer functions could be used to predict the linear and quadratic growth of the toroidal modes.

It is convenient to classify the wave interactions in a collisionless plasma as wave-wave or wave-particle interactions [1-3]. To understand the coupling mechanism, I designed a movable probe to measure simultaneously magnetic and electrostatic fluctuations. The coherence (γ^2) between fluctuating B_r and J_{sat} has been found to be small. Thus, a significant fraction of the measured particle fluctuations may have risen from sources other than radial convection with the magnetic field.

The effect of impurities and an insertable limiter on the magnetic fluctuation spectra and the rotational speed of the coupled modes show that the coherent coupled modes slow down and the fluctuation levels increase.

This chapter presents the measurements of the edge magnetic fluctuations on the MST reversed field pinch. The chapter is divided into eight sections. First, the

experimental parameters and diagnostic considerations are presented. In second experimental parameters and diagnostic considerations are presented. The second section also discusses the magnetic fluctuation types. Section Three presents the general characteristics of the measured edge magnetic fluctuations. Current and Lundquist number scaling of magnetic fluctuations are also presented in this section. Section Four presents the linear poloidal, toroidal and associated helical mode spectra. The fluctuation driven quantities such as parallel and perpendicular correlation length, global v.s. local mode spectra are also presented in this section. Section Five presents the measurements of nonlinear mode coupling. Section Six discusses the initial results of energy cascading associated with three-wave toroidal mode coupling. Section Seven presents the correlation of magnetic and electrostatic fluctuations. Section Eight discusses the effect of a material limiter and impurities on edge magnetic fluctuations and mode number spectrum.

V-1) Experimental Parameters and Diagnostic Consideration

Optimized parameters for the MST reversed field pinch are listed in Table 2-1. However, considerably lower plasma current, which is reproducible over hundreds of shots, have been utilized for the purpose of this thesis. For completeness, I include plasma current and magnetic Lundquist number scans of magnetic fluctuations in section V-3. The plasma parameters chosen for this thesis experiment are: plasma current I_p= 250 KA, electron line density $n_e \approx 0.7\times10^{13}$ cm^{-3}, central electron temperature $T_e \approx 200$ ev, single-turn loop voltage $V_l \approx 15$ V, reversal parameter $F = B_t(a)/\langle B_t \rangle \approx -0.15$, and pinch parameter $\Theta = B_p(a)/\langle B_t \rangle \approx 1.75$.

For the data presented, the dense-array is utilized for high frequency magnetic fluctuation measurements. Two fixed poloidal arrays ($\phi = 165^o$ & 180^o) and one toroidal array @ $\theta = 241^o$ were designed for spatial mode analysis and nonlinear mode coupling measurements. There is another poloidal array of coils at $\phi = 0^o$ (poloidal gap), but due to the size of the coils they were unsuitable for fluctuation studies. Measurements made at other poloidal and toroidal locations utilizing movable probes indicated no major difference in the characteristics of the magnetic fluctuations and resultant mode spectra. The persistent coherent modes are present in every discharge irrespective of varying plasma current, reversal and pinch parameters (i.e.

see section V-4); however, their characteristics are dependent on impurity levels and field errors (see section V-8).

V-2 Magnetic Fluctuation Types Considered

Before we present the results of edge magnetic fluctuations on MST, it is useful to review some of the macroscopic influences on the fluctuations due to impurities and field errors. The magnetic fluctuations with frequency from 1 kHz to 500 kHz have been measured externally by the closely arranged dense array of toroidal and poloidal extent. The measured frequency spectra of fluctuations are dominated by coherent phase-locked oscillations. These long-wavelength, low-frequency ($f < 35$ kHz), global magnetic oscillations greatly influence macroscopic behavior of the discharges. These oscillations are identified as MHD tearing modes [4]. These modes are rotating with respect to the laboratory frame and are sensitive to the impurity level (see V-8), and the structure of the equilibrium field [5,6]. In the presence of a non-axisymmetric error in the equilibrium magnetic field, the modes can cease rotation and become stationary or "locked" in the laboratory frame. In MST locked modes occur in response to field errors or high impurity levels. Locked discharges are drastically different from "normal" discharges. Premature discharge termination (Fig. V-2-1), higher error field at the poloidal and toroidal gaps, confine-

ment degradation, higher single-turn loop voltage, and higher impurity levels are characteristics of these locked discharges.

I will not consider the shots with locked modes in the linear and nonlinear analysis in this thesis. Figure V-2-2 presents the raw poloidal magnetic fluctuations for both "normal" and "locked discharges". The observed low frequency fluctuations in the "normal" discharges diminish when phase locking to the wall occurs. Other examples of locked discharges are given in the section V-8.

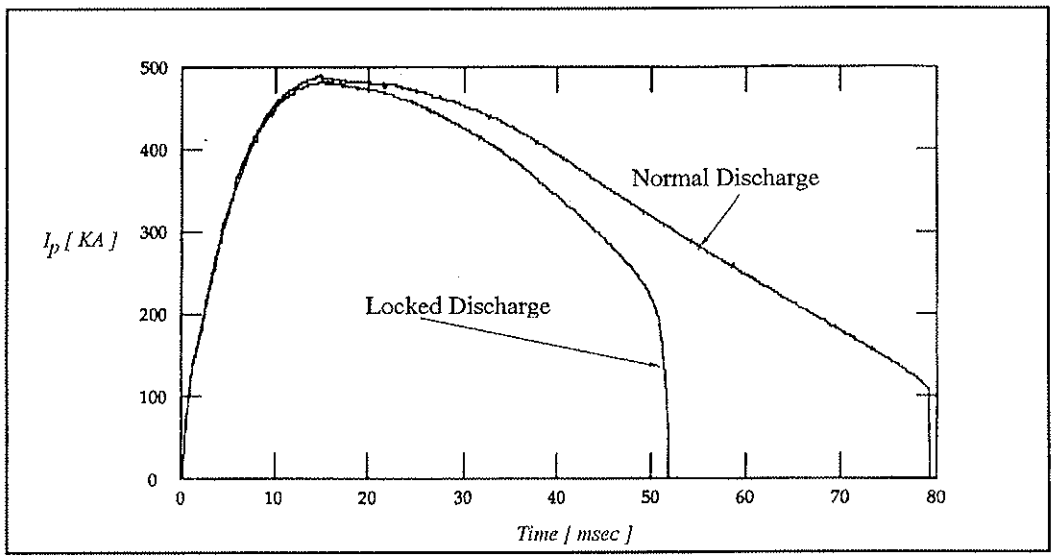

Figure V-2-1) The plasma current for two identical discharge, one is "normal", and longer the other is "locked", shorter and degraded.

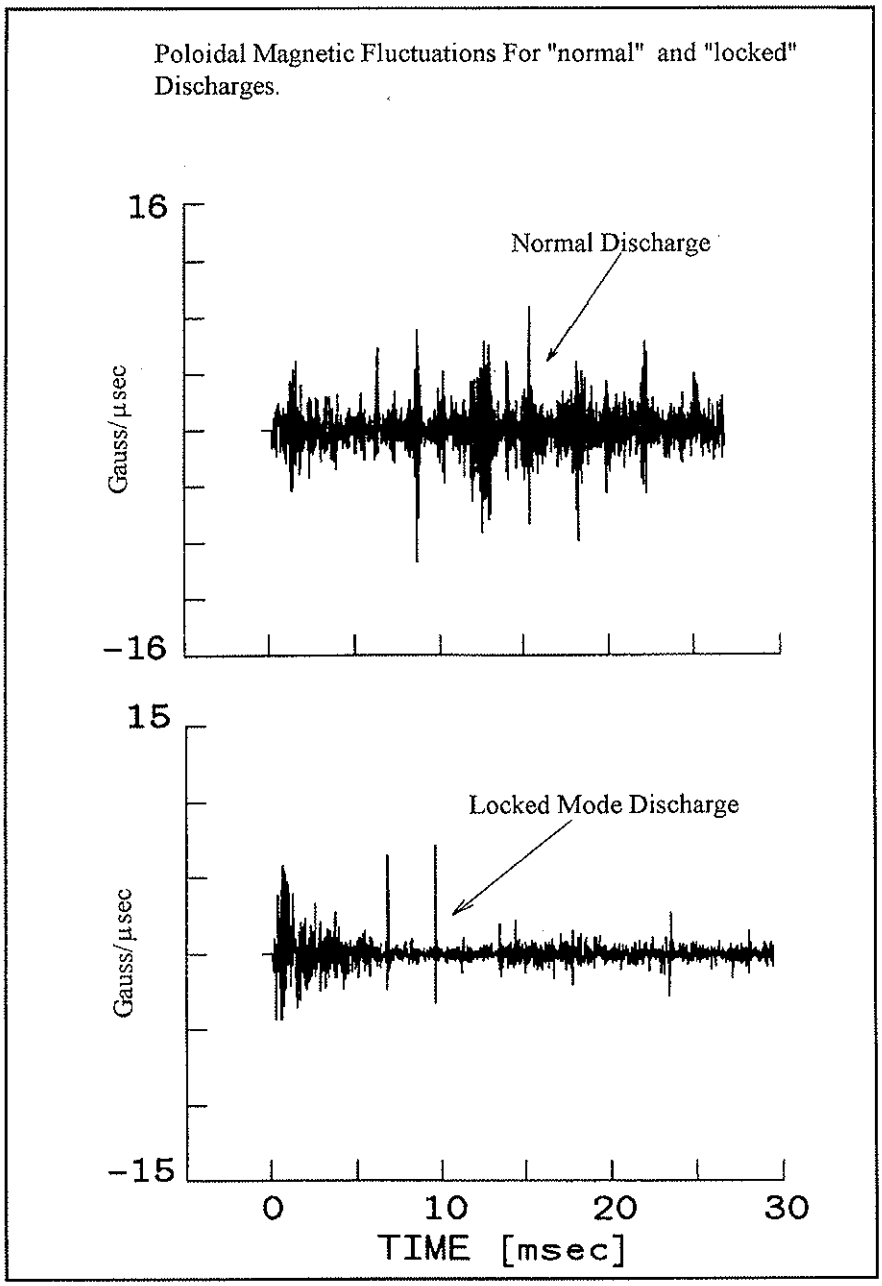

Figure V-2-2) Raw poloidal magnetic fluctuations measured. High fluctuations are present when discharges are "normal" (top Fig.). Mode locking occurs, in the bottom Fig. at 5.3 ms.

V-3) General Characteristics of Magnetic Fluctuations

In RFP's, even during relatively quiescent periods, a significant level of magnetic fluctuations exist. The three components of the edge magnetic fluctuations in the MST are shown in Fig. V-3-1. Periods of greatly reduced fluctuations are observed as the sustained reversal is achieved. The same phenomena has been observed on other RFPs [7,8,9,10,11]. It is widely accepted that the appearance and sustainment of a reversed toroidal magnetic field by the plasma requires such magnetic fluctuations, although the detailed mechanism by which self-reversal occurs is not yet established experimentally. The energy confinement in the RFP is also correlated with enhanced transport arising from the fluctuations. Detailed study of the fluctuations therefore offers the possibility of elucidating these vital topics.

V-3.1) General Features of Edge Magnetic Fluctuations in MST

The magnetic fluctuation measurements on MST show that more than 90% of the power is from low frequency ($f < 35$ kHz) oscillations, Figure V-3-2. Superimposed on these oscillations are high frequency fluctuations with small amplitudes. These low frequency, coherent fluctuations are present throughout the reversal of most discharges. The coherent oscillations can be seen clearly on the dB_p/dt signals, as shown in Figure V-3-3. Also present are sudden "bursts" of periodic nature as the plasma experiences "sawtooth-like" activities. This is signified

by a sudden increase in the average toroidal field. On the other hand, the high frequency magnetic fluctuations (f > 35 kHz) are broadband with no dominant peak. Figure V-3-4 shows the power spectrum of the 3 components of the fields. The data used to calculate the fluctuation power spectra are taken near the peak plasma current. The toroidal fluctuating field is twice the poloidal field which in turn is 3 times the radial component. This is consistent with $B_T/B_P \sim n/m$, (Figure V-3-5), derivable at the conducting boundary from $((\nabla\times\mathbf{B})|_r = \mathbf{j}_r = 0) \Rightarrow$

$$\frac{R}{r}\frac{|\tilde{B}_T|}{|\tilde{B}_P|} \leq \frac{n}{m}$$

if only one mode is present. When many modes are present, the right hand side represents an average value of n/m.

Excluding the coherent fluctuations with toroidal mode n~5-7 and m~1, the magnetic fluctuations of the MST can be characterized as broadband, monotonically decreasing with frequency.

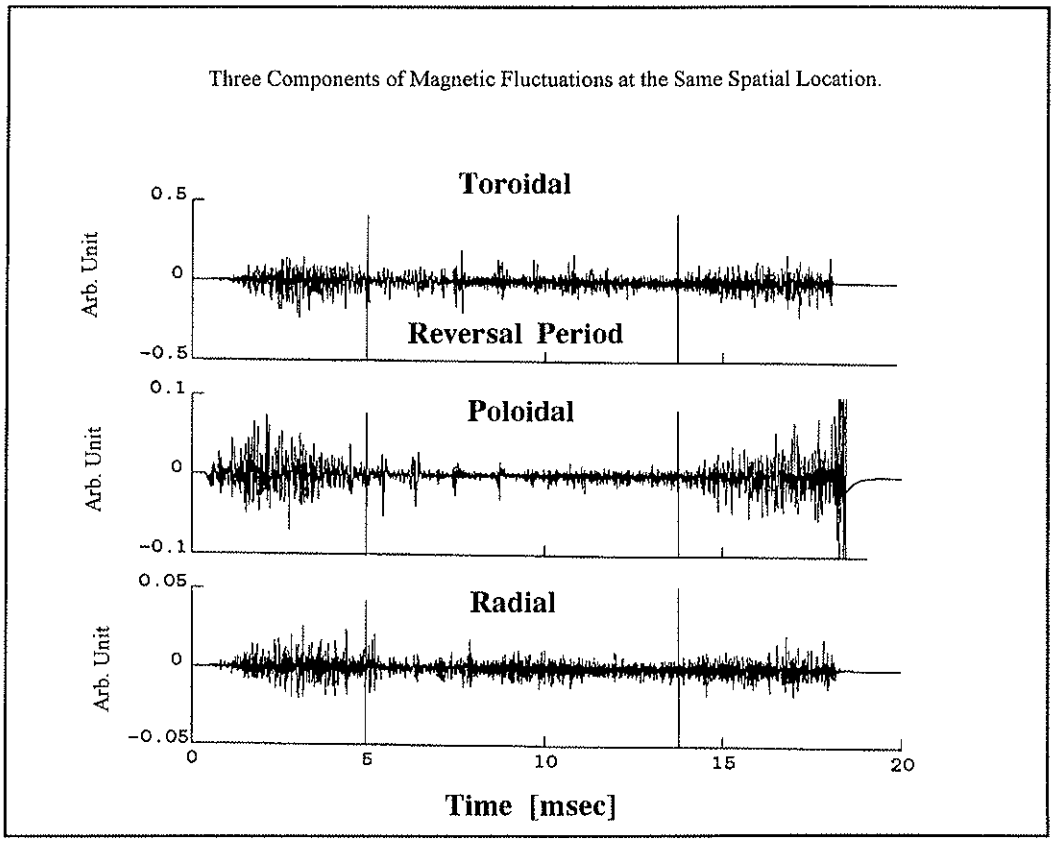

Figure V-3-1) Magnetic fluctuations measured in early MST plasma shows relatively quiescent period when the toroidal field is reversed at the wall. Vertical lines indicate beginning and end of reversal.

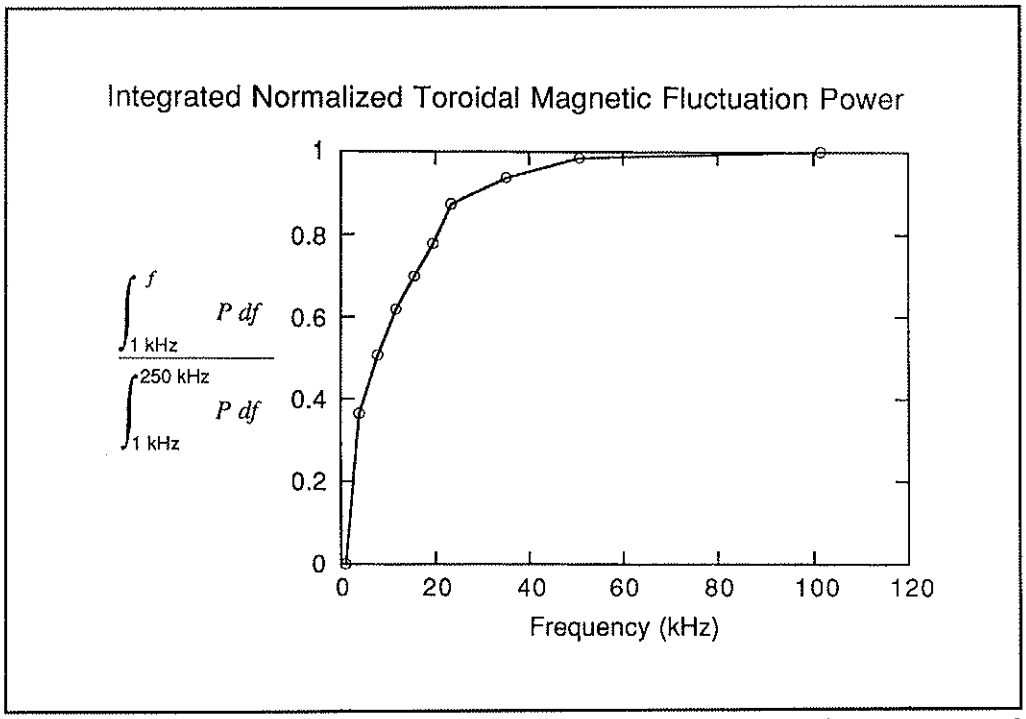

Figure V-3-2) More than 90% of magnetic fluctuation power is concentrated at frequencies below 35 kHz.

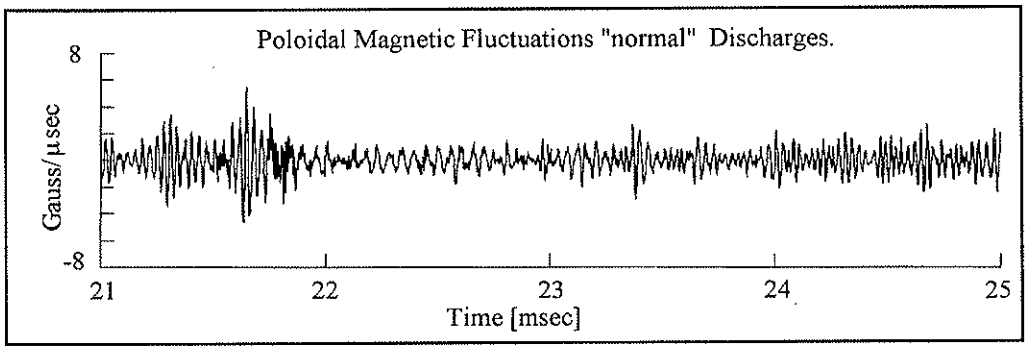

Figure V-3-3) Low frequency coherent oscillations are clearly seen on raw poloidal magnetic fluctuation signals.

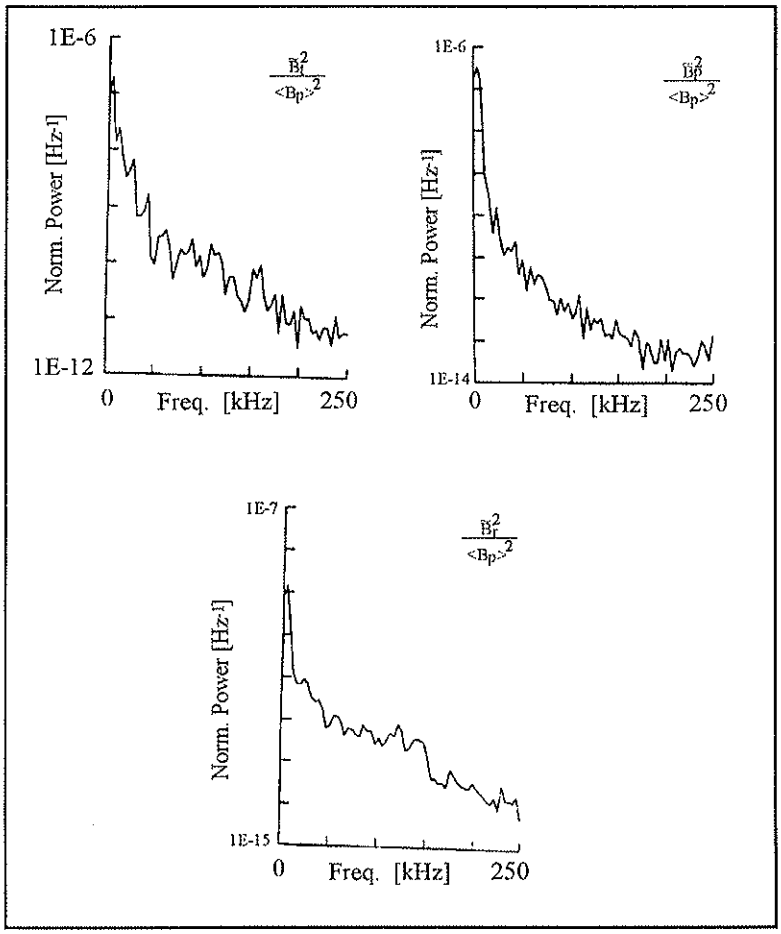

Figure V-3-4) The power spectrum of the 3 components of magnetic fluctuations.

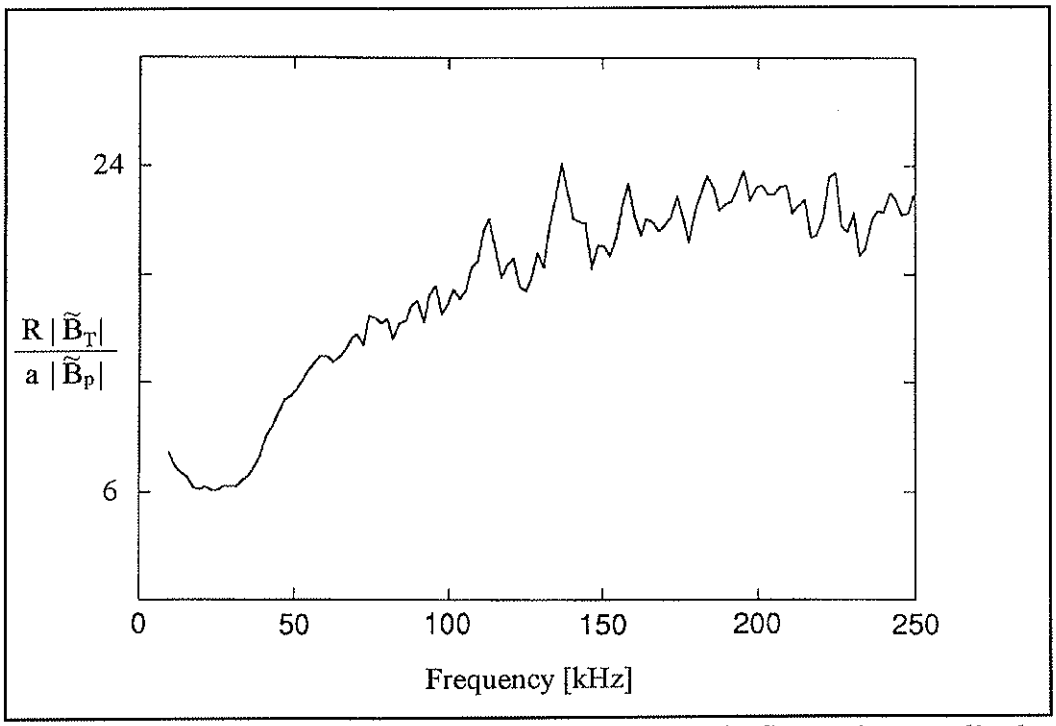

Figure V-3-5) Ratio of toroidal to poloidal magnetic fluctuation amplitudes measured at the edge which are proportional to n/m as a function of frequency.

V-3.1.1) Coherent Oscillations

The large scale, low frequency ($f < 35$ kHz) oscillations on arrays of discrete magnetic field pick-up sensors are accompanied by oscillations of approximately the same frequency on the SXR flux (Fig. V-3-6). Note that the SXR emissivity surfaces (Fig. V-3-6) show the formation of an m=1 island. The amplitude of these oscillations are sensitive to profile modifications and nonlinear mode coupling during a sawtooth-like phenomenon. The magnetic and soft x-ray perturbations have |n|~5-8,

and they are internally resonant, The helical structures of these coherent oscillations are consistent with resistive MHD simulation which predict $|n/m| \sim 2R/a \sim 6$ for MST. This will be discussed in more detailed in Section V-4. We should note that these oscillations are not evident in any of the line radiation diagnostics. This would suggest that, although there are perturbations in the current density and the plasma temperature, they have small effect on the plasma density.

The behavior of RFP magnetic fields and currents during the sawtooth-like oscillations is illustrated using a F-Θ diagram; see Fig. V-3-7. The locus of Taylor minimum energy Bessel Function Model (BFM) states is left of the diagram (i.e. at $\Theta < 1.7$). The minimum energy states have zero β_θ ($\mathbf{j}_\perp = 0$) and a flat λ-profile, where $\lambda = \mathbf{j}.\mathbf{B}/B^2$. The MST experiment operates to the right of the BFM due to both the finite β_θ and non-flat λ-profile. During these "sawtooth-like" oscillations, the discharge follows an almost closed trajectory in the F-Θ plane suggesting that the oscillations can be described as the recovery of an initial state from which the plasma departs periodically.

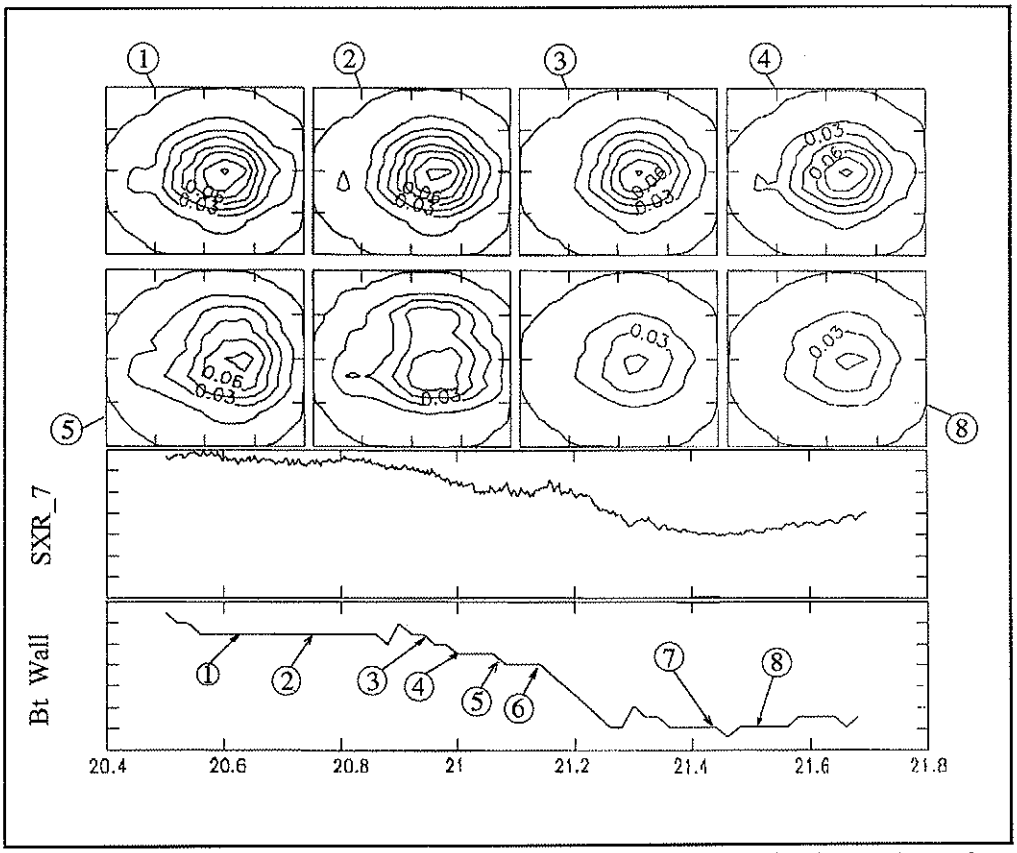

Figure V-3-6) Soft x-ray emissivity reconstructions show the formation of an m=1 island during a sawtooth crash. (courtesy of G. Chartas)

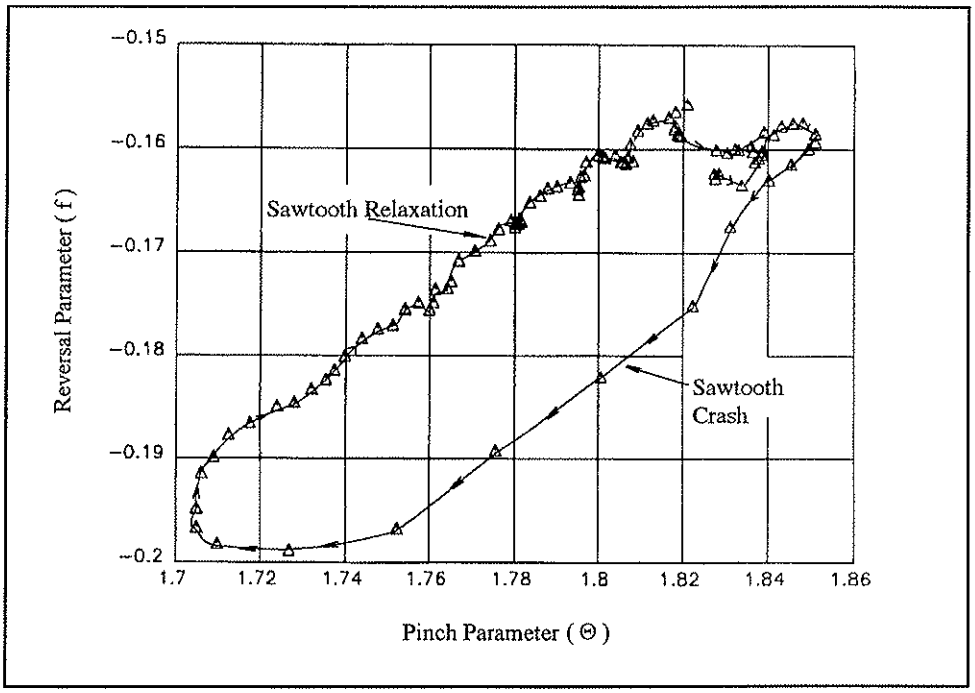

Figure V-3-7) F-Θ diagram during a sawtooth, (formation, evolution and crash).

V-3.2) Current Scaling of Magnetic Fluctuations

Edge magnetic fluctuations are measured on the MST by varying the plasma current from 200 KA to 480 KA. The normalized toroidal magnetic fluctuations are presented in Figure V-3-8 and the normalized poloidal component is shown in V-3-9. We have observed the reduction of the fluctuations for various frequency ranges as the plasma current has increased. The normalized toroidal and poloidal fluctuations have been calculated for the flat top region of the discharge.

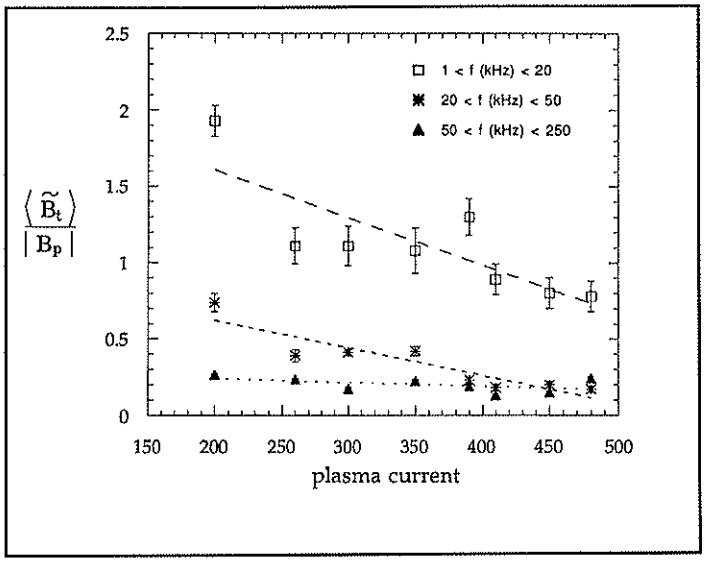

Figure V-3-8) Normalized toroidal magnetic fluctuations decreases as plasma current increases during the flat top region of the discharges.

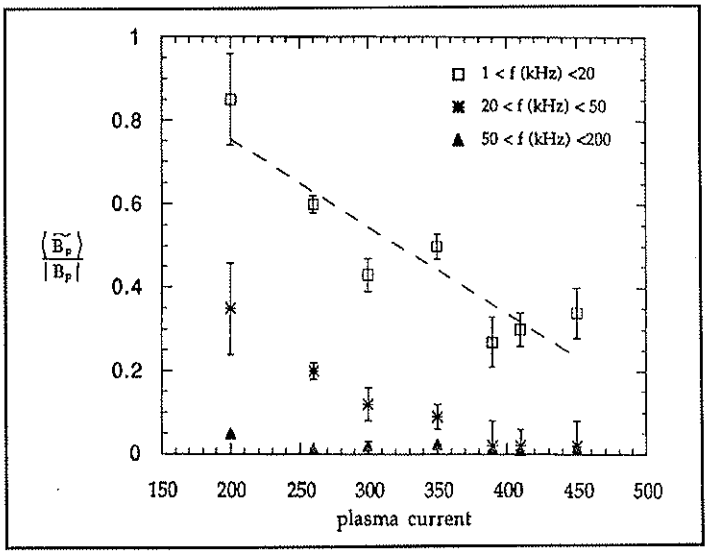

Figure V-3-9) Normalized poloidal magnetic fluctuations decrease as the plasma current increases during the flat top part of the discharge.

V-3.3) Magnetic Fluctuation Scaling with Lundquist Number

The scaling of the fluctuations with Lundquist number, (S) is important since it increases with plasma current. Hender and Robinson [12] in 1983 predicted for the resistive interchange mode that the fluctuating B_r is proportional to an inverse fractional power of Lundquist number. Struss [13] in 1986, using an approximate nonlinear turbulence analysis, predicted that radial magnetic fluctuations scale as $S^{-1/3}$. An et al. [14] were able to correlate S and fluctuating field. Nebel [15] found that the magnetic fluctuation is independent of Lundquist number for a limited S range. LaHaye [16] in 1984 obtained scaling of $S^{-0.54}$ for the normalized total fluctuating field from experimental data on OHTE (Fig. V-3-10). In MST we have varied S over a factor of 10. S is changed by varying the plasma current (magnetic field), with accompanying changes in density and temperature. Thus, it is not a single-parameter scan. The S value is computed from the central density and temperature, which is measured by Thomson scattering. It is seen in Fig. V-3-11 that fluctuations tend to decrease with S. However substantial scatter in the data might imply that other parameters are important. Fluctuation dependence on the value of S calculated from the measured conductivity temperature results in the same conclusion.

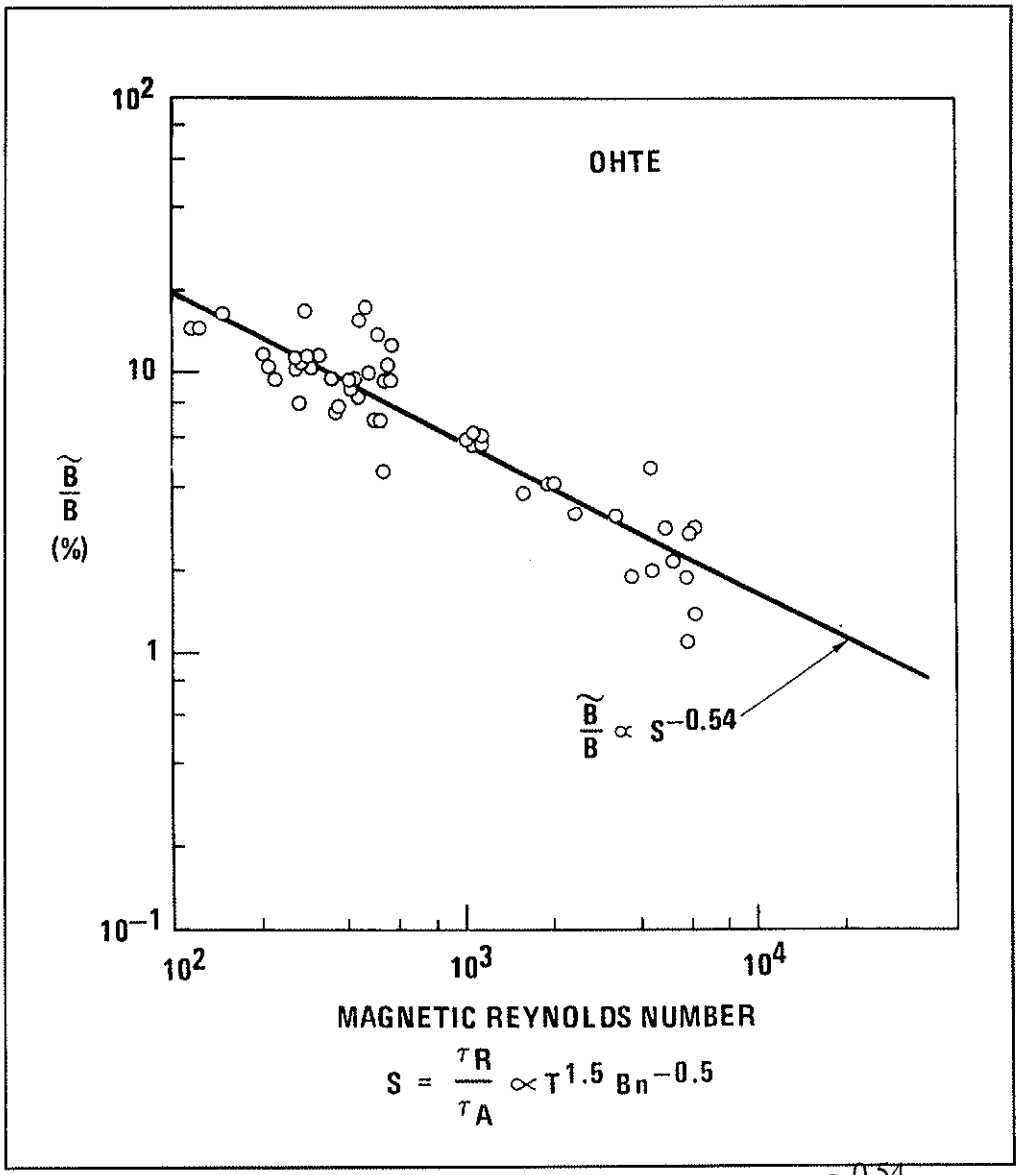

Figure V-3-10) Magnetic fluctuations on OHTE decrease as $S^{-0.54}$.

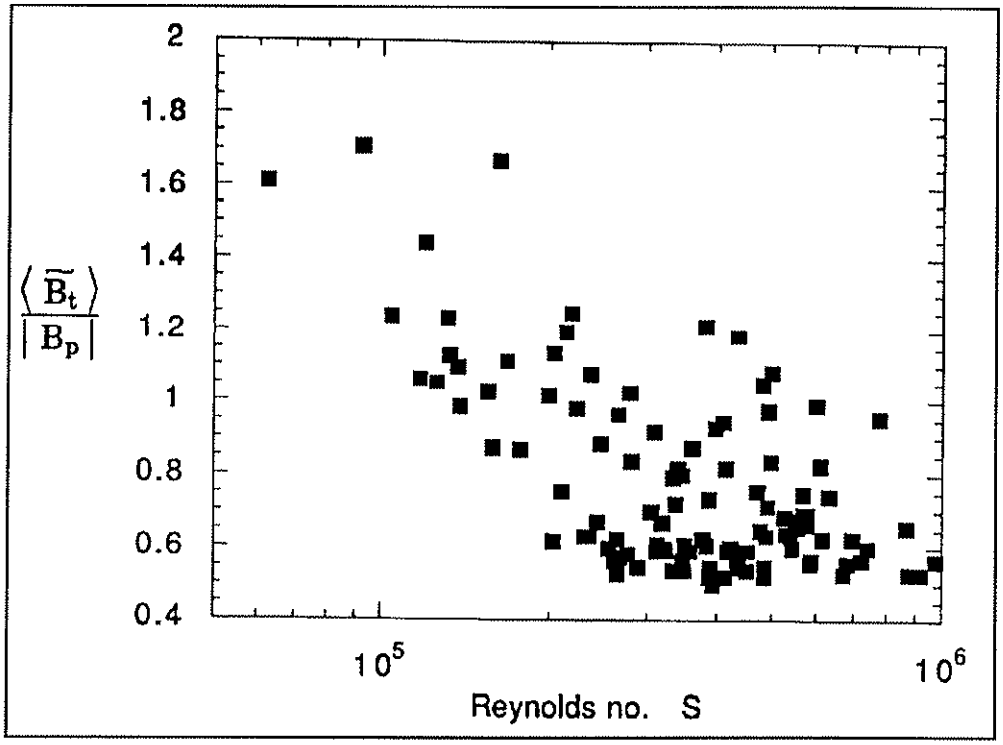

Figure V-3-11) There is no clear correlation between Lundquist number and edge magnetic fluctuations on MST.

V-4) Linear Mode Analysis

Before turbulence is addressed, the linear modes of the system are analyzed in order to gain prior insight. By linear analysis, I mean the amplitude of a single k_y component is simply given by a Gaussian profile in the "y" direction. The spectra are averaged over 100-400 ensembles to illustrate the trends, although variations from shot to shot occur in the details of the spectra. At the same time, the phase relative to the signal detected by a fixed coil provides both positive and negative propagation directions. It should be noted that the method presented here works well only when linear modes are varying in time. The frequencies below 1 kHz cannot be considered due to hardware filtering restrictions. Linear analyses were carried over a period long enough that the standard deviation in the source/sink term (Γ's) over a window was below the error Γ_E. Three important factors distinguish my techniques from those which are most frequently used. The first factor is that the two-point correlation measurements of toroidal and poloidal mode analysis were carried out using the multi-coil dense array. This method provides the flexibility of calculating modes at different frequency ranges by keeping the coherence between the selected coils constant. The second factor is that the most dangerous MHD instabilities [17,18,19] have poloidal modes $m < 2$ and toroidal modes, $n=2R/a$ in the RFP. This is the converse of the tokamak situation with dominantly $n\sim1$ and high m. This required a

large number of magnetic sensors in both toroidal and poloidal direction to be implemented. The third factor is that the majority of magnetic fluctuations in RFPs do not have the obvious periodicities in time which are commonly seen in tokamaks; in contrast, the fluctuations are stochastic. Consequently, the simple inspection method of raw data to distinguish the evolution of the modes is discarded. It is therefore necessary to adapt statistical forms of analysis in order to extract from the apparently random signal the required information.

Section V-4.1 identifies the high frequency localized turbulence. Section V-4.2 presents the measured global poloidal mode spectra (for the entire frequency range) using three different methods. Section V-4.3 presents the toroidal mode spectrum measurements and comparison with the results of 3-D MHD code. The calculated helical modes from the "associated cross-spectrum" of the experimental data are presented in section V-4.4.

V-4.1) Localized Edge Magnetic Fluctuations

In this section I will give detailed results of the measured high frequency mode spectra. Although the cross coherence among adjacent magnetic sensor pairs stays high, the rapid spatial drop off gives further evidence of global and localized modes at different frequencies. To investigate the correlation of oscillations as a

function of frequency, the coherence must be calculated. The coherence is a measure of the correlation of two signals at specific frequency intervals such that the correlation of each interval is linearly independent of the correlation at all other intervals. Figure (V-4-1) presents the square cross coherency γ^2. Here γ is the measured cross-coherence between two dense-array magnetic sensors, discussed in Chapter 4, for various coil separations. We see that the coherency is very sensitive to the fluctuation frequency. In the low frequency range ($f < 35$ kHz), coherency stays high. As the frequency increases to ≥ 35 kHz, the γ^2 falls by ~1/2 after 4 cm.

Another evidence that high frequency modes are localized is obtained from the spectral analysis. To calculate the high frequency mode structure we estimate the power-weighted wavenumber spectra from two spatially separated magnetic sensors. The method is discussed in Chapter 4. Figures V-4-2 and V-4-3 are the m and n spectra for $50 \text{ kHz} < f < 100$ kHz. The low frequency spectra is given in Section V-4.2 and V-4.3. The high frequency n-spectrum is shifted in the negative toroidal mode direction peaking at $n \sim -30$, whereas at low frequency it peaks at positive $n \approx 5\text{-}8$. However, the m-spectrum does not change sign and peaks at m~1-2. This is again an indication of locally resonant modes at high frequencies since $m/n < 0$ modes resonate in the edge reversal region where $q < 0$ ($q = m/n$).

Since the parallel correlation length is virtually in the poloidal direction in

RFPs, we speculate that the minimum energy required for the reconnection is for the smallest scale reconnections which are in the transverse direction, hence the sign of n rather than m change. Here, the positive ratio of poloidal mode number to toroidal mode numbers represents internally resonant modes.

The multi-coil dense array used in this experiment is well suited for toroidal and poloidal correlation decay measurements for the 0-4 MHz frequency range, although the hardware amplifier/filters bound the measurement to less than 250 kHz. One suitable estimate of the degree of relationship between two simultaneous samples of turbulence data is the absolute maximum of their cross-correlation function. A single coil is chosen as a reference (coil #1 in toroidal direction and coil # 33 in the poloidal direction) and cross correlated with successively more distant coils (Figure V-4-4). We see that the zero lag time correlations change sign as the separation from the reference coil increases. The result is a measure of the gross correlation decay with distance. This is another evidence of localized high frequency modes.

The cross-correlations are perhaps more clearly represented by the coherence length defined as $L_i(\omega) = -\Delta x_i / \ln(\gamma_{\Delta x}(\omega))$ where (Δx is the spatial coil separation, "i" is poloidal or toroidal). Figure V-4-5 displays the poloidal coherence length calculated for frequencies 30, 60 and 100 kHz. The decay is faster for the higher frequency cases. Figure V-4-5 shows the poloidal coherence length drops from 460

cm to 54 cm when the frequency increases from 30 kHz to 100 kHz. For the toroidal coherence length in Fig. V-4-6, this calculation was done for 10, 40 and 120 kHz. The toroidal coherence length decreases from 20 cm at 10 kHz to 6 cm at 120 kHz. A two-point exponential fit predicts a slower decay than the experimental results. This is perhaps due to collisions. The curves indicate that most of the high-power activity corresponds to low frequencies ($f < 35$ kHz). The poloidal coherence length is longer than the toroidal coherence length.

Poloidal coherence lengths are an indication of the spread in poloidal mode numbers at a given frequency, by the relation $\Delta m = \pi\ a\ /\ L_p$. Figure V-4-7 shows Δm versus frequency. A clearly broad m-spectrum exists as frequency increases. The same method is used to calculate Δn, as shown in the lower graph of Figure V-4-7; Δn is much broader than Δm, as we have seen in Figure V-4-2 and V-4 -3.

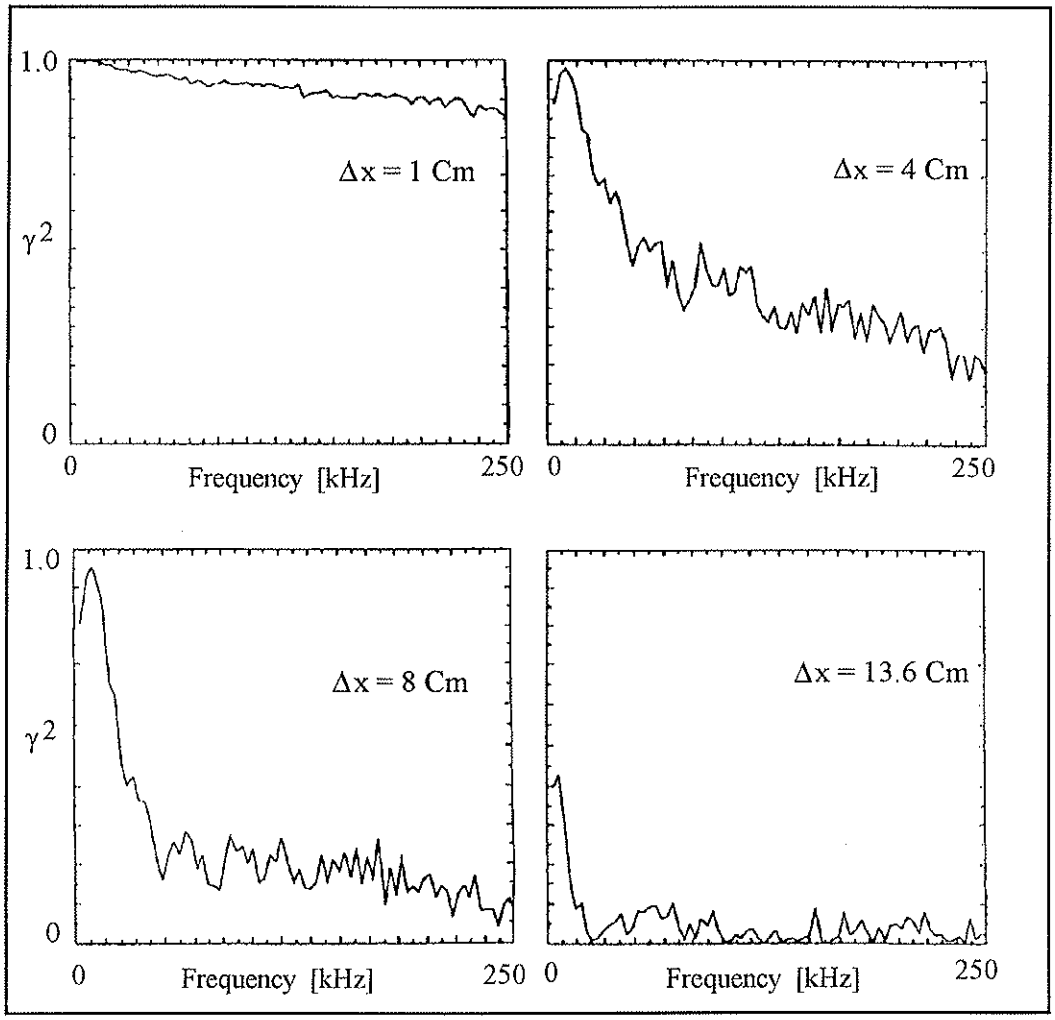

Figure V-4-1) The square cross-coherency between two magnetic fluctuation signals for four toroidal separations. The square coherency drops rapidly as coil separation increases.

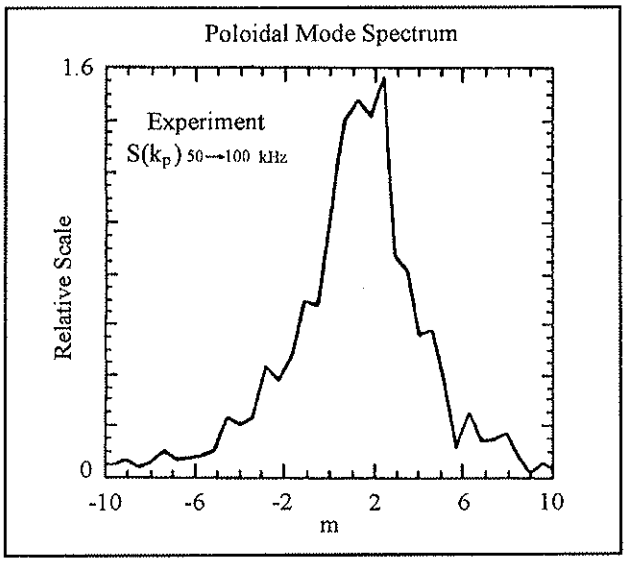

Figure V-4-2) Poloidal mode number spectra of magnetic fluctuations from 2-point phase shift measurements peaks at m~2 at high frequencies.

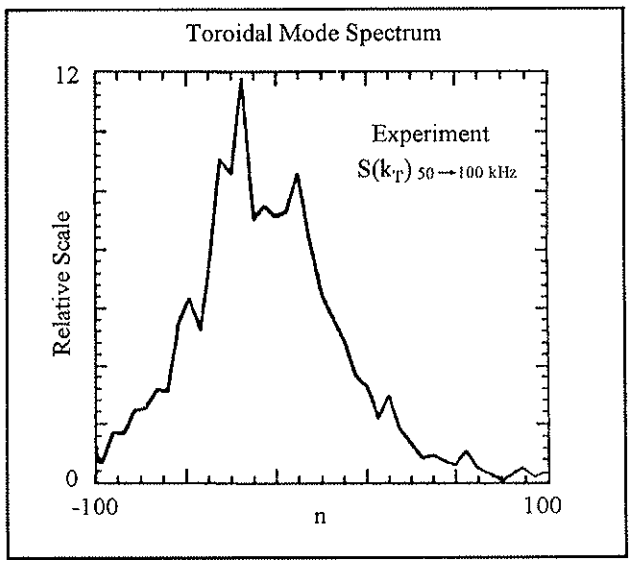

Figure V-4-3) Toroidal mode spectra of magnetic fluctuations from 2-point phase shift measurements peaks at n~-30.

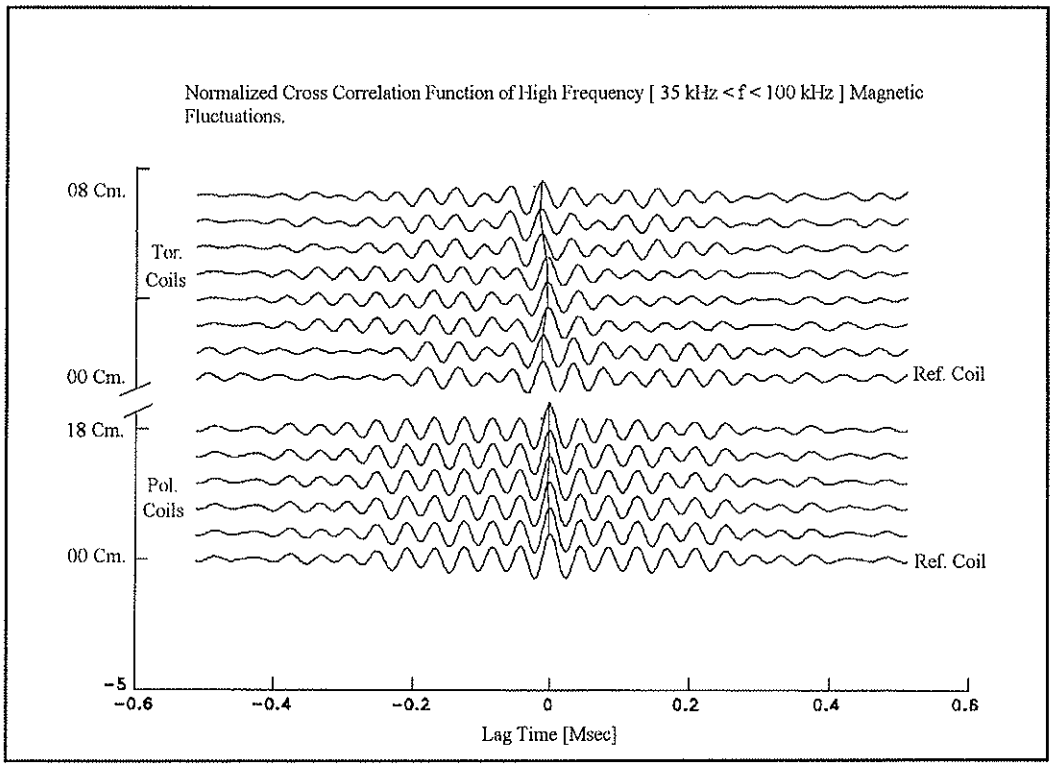

Fig. V-4-4) Normalized cross correlation function [35 kHz < f < 100 kHz] from edge magnetic fluctuation. The top figure shows the toroidal cross correlations. The bottom figure shows the poloidal cross correlations.

Note: Each curve represents an additional separation of 1 cm from the reference coil in the toroidal array and 3 cm in the poloidal array.

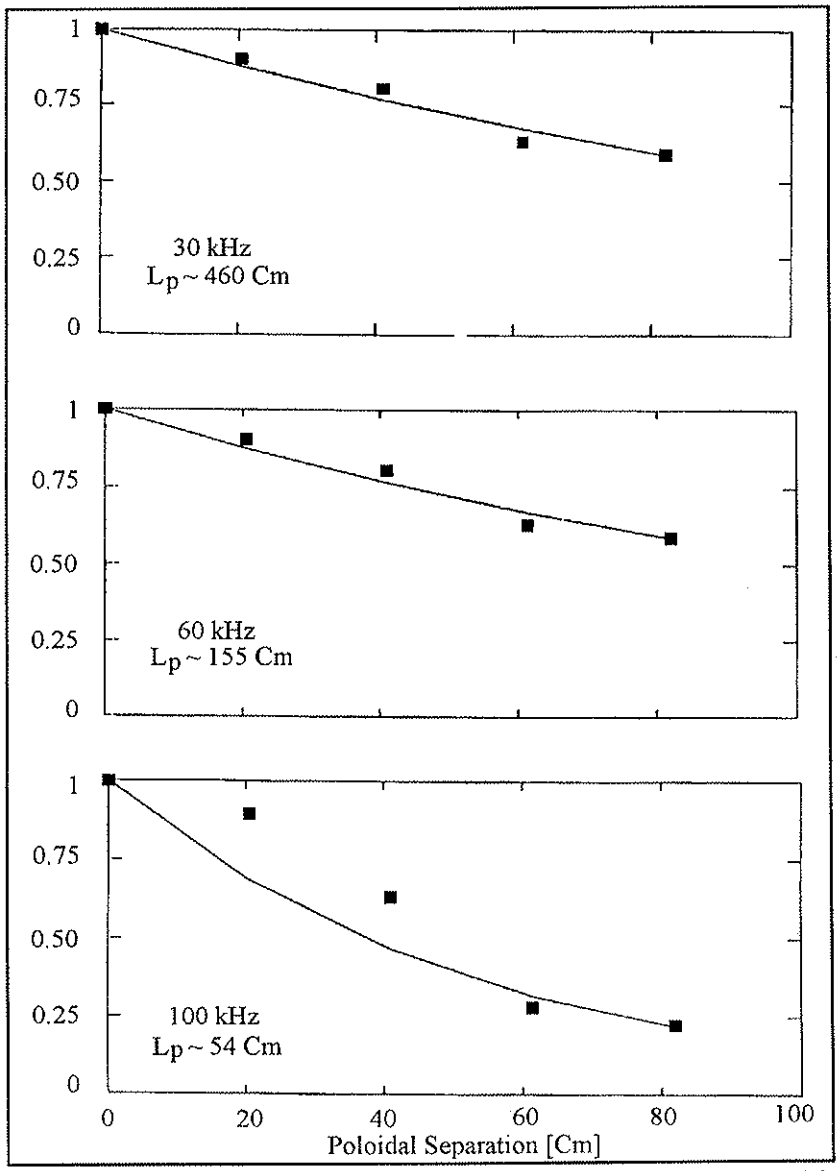

Figure V-4-5) Poloidal coherence length decreases with increasing frequency. The solid line represents the exponential fit between the first and the last point of the graph.

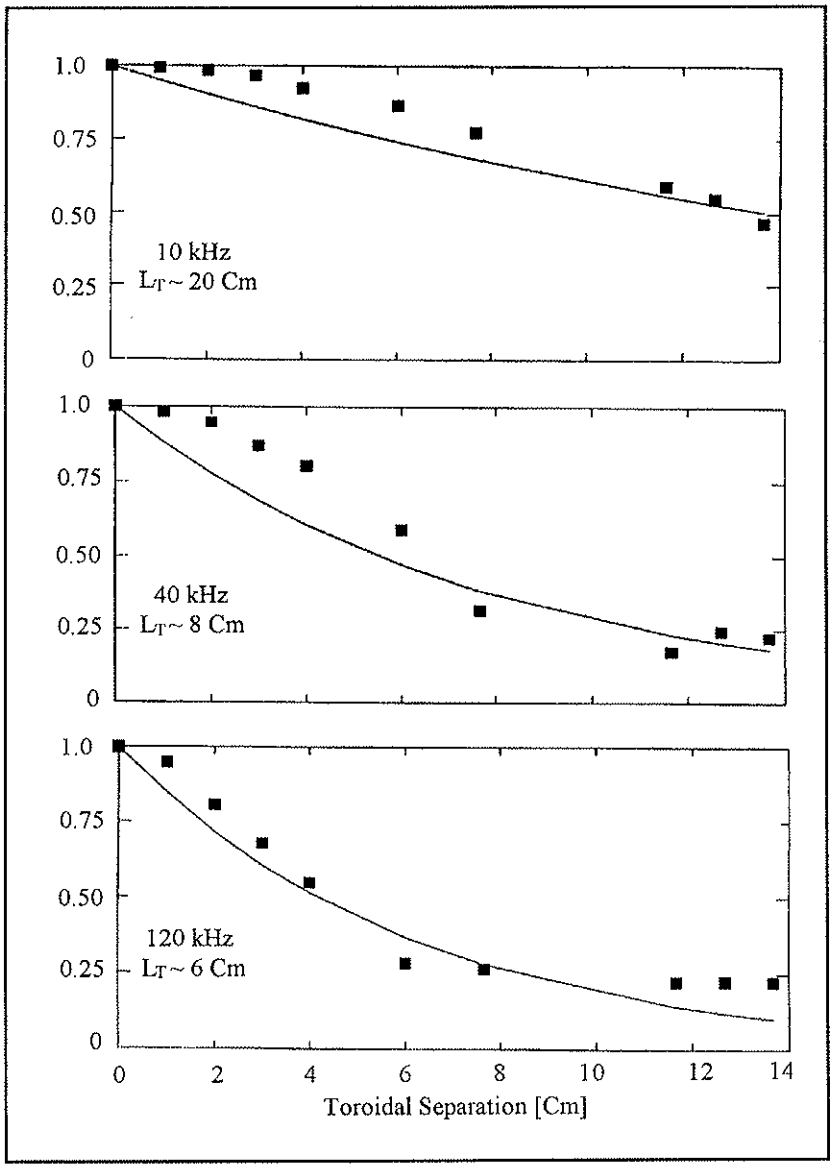

Figure V-4-6) The toroidal coherence length decreases slower than the exponential fit to the data represented by the solid lines. Clearly a decrease of L_T with frequency is seen.

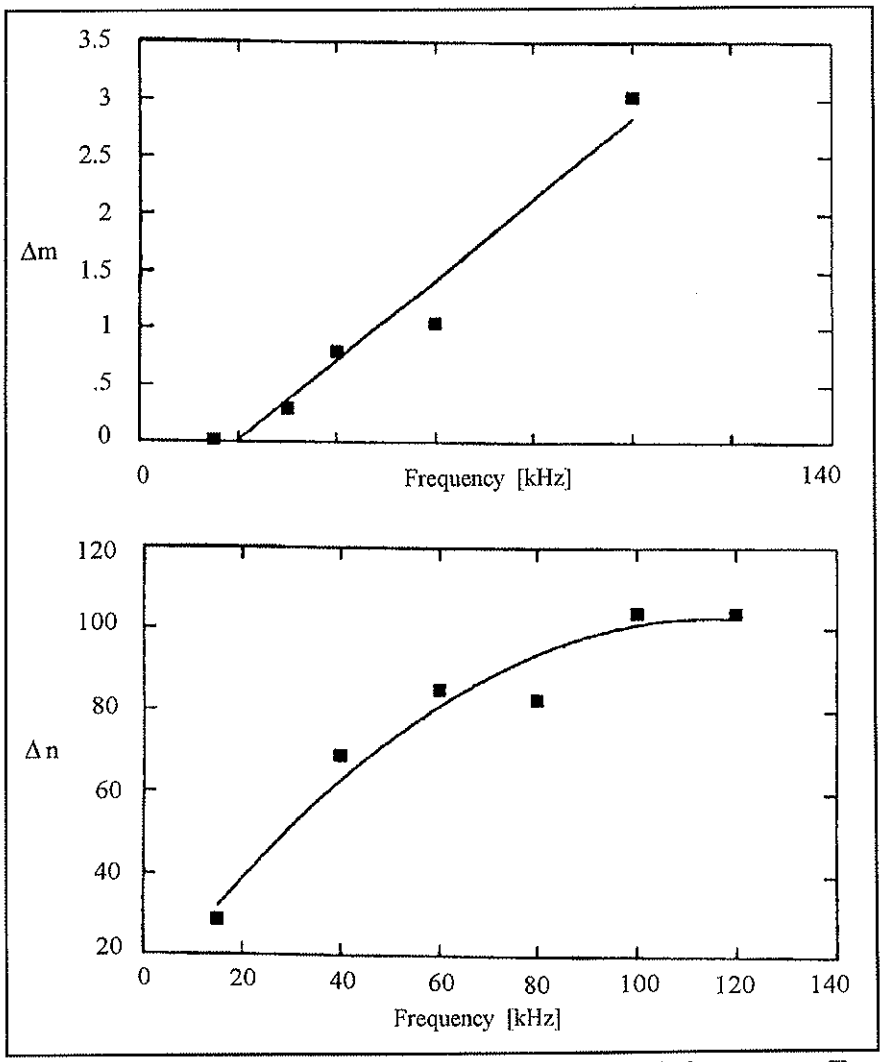

Figure V-4-7) Spread of mode number width with frequency. Top graph shows the spread in poloidal mode number from poloidal coherence. Bottom shows the spread of toroidal mode number.

V-4.2) Poloidal Mode Structure

In order to determine the structure of the magnetic fluctuations, we Fourier decompose the signals in the poloidal direction (θ) by forming the sums over 16 sensors:

$$C_m = \frac{2}{N}\sum_{k=1}^{N} \tilde{B}_k \, Cos(m\theta_k)$$

$$S_m = \frac{2}{N}\sum_{k=1}^{N} \tilde{B}_k \, Sin(m\theta_k)$$

$$A_m = \frac{1}{2}\sqrt{< |C_m|^2 + |S_m|^2 >}$$

where $m \leq k/2$ is the poloidal mode number and A_m is the amplitude in each Fourier mode. The resultant poloidal mode power spectra obtained from the internal coil array during the sustainment phase are plotted in Figures (V-4-8) through (V-4-11). The spectrum of poloidal magnetic fluctuations is dominated by m=1-2 with very rapid fall off at higher m's.

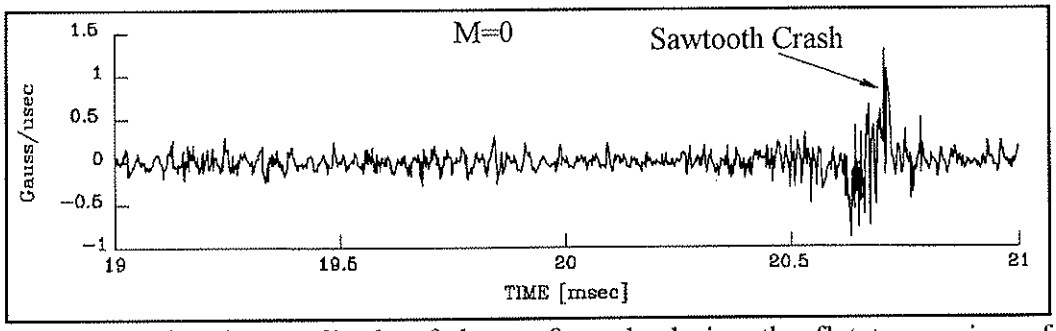

Figure V-4-8) The amplitude of the m=0 mode during the flat top region of discharge.

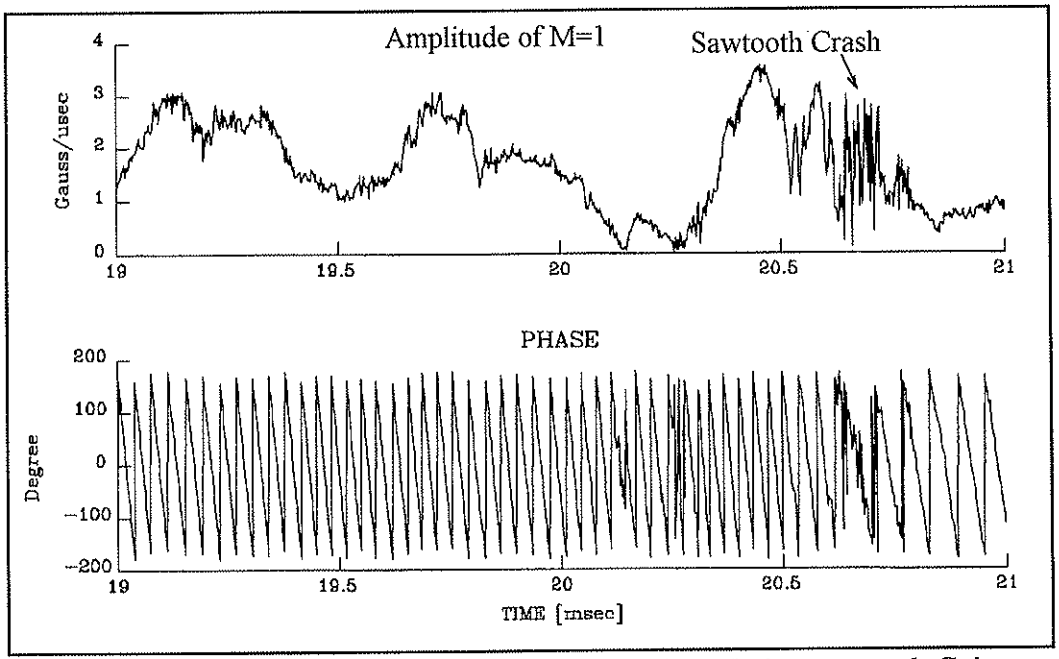

Figure V-4-9) The amplitude and phase of the m=1 mode is presented. Coherent oscillations are observed. The sawtooth crash induces impurities resulting in slowing down these oscillations.

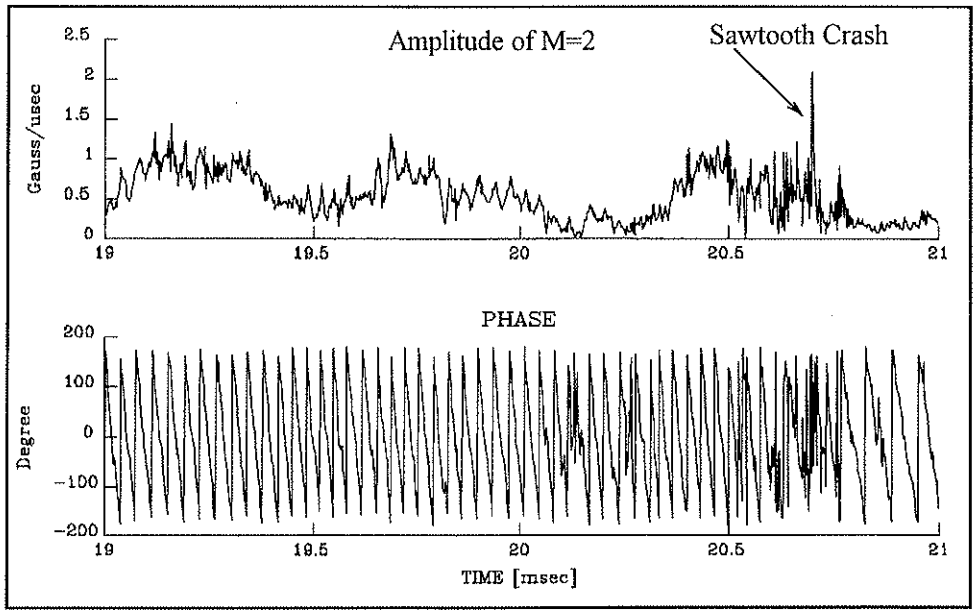

Figure V-4-10) Amplitude and phase of poloidal m=2 mode during a sawtooth event.

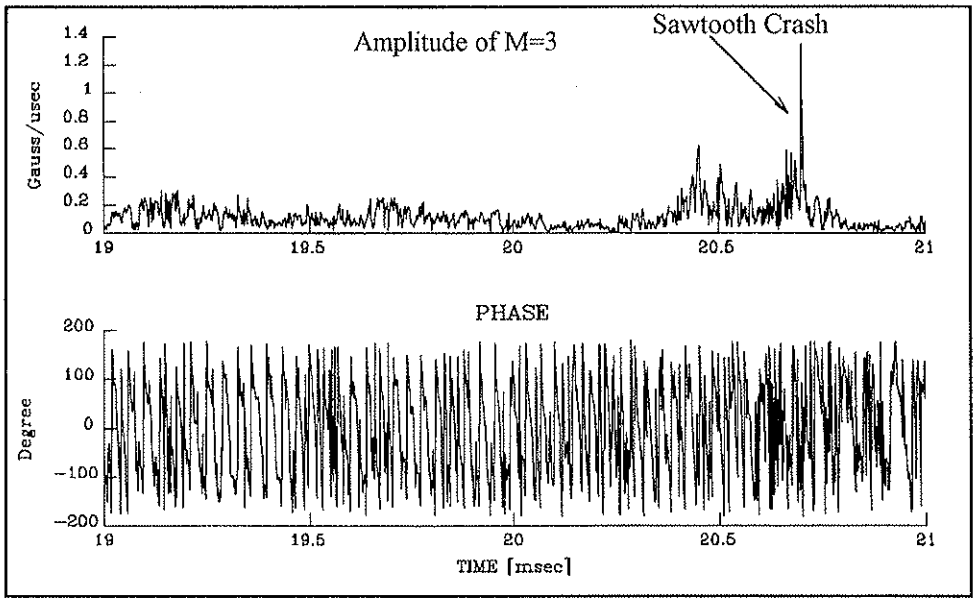

Figure V-4-11) The amplitude and phase of m=3 poloidal mode. We note the amplitude is small except during the sawtooth oscillation.

The above four graphs are obtained from 1-D Fourier decomposition applied to a single poloidal array; thus the mode numbers have been determined for all n (i.e. $A_m = \sum A_{mn}$ for all n). No information can be extracted on helical modes (m,n) from the above analysis. Helical modes have been estimated in section V-4.4. The amplitudes shown in Figures (V-4-8)-(V-4-11) are derived from the dB_θ /dt signals; no integration has been applied either analog or digitally. Although the frequency during a sawtooth oscillation is complicated, it remains constant prior and after a crash. This is apparent from the linear time dependence of the m= 1-2 phases. Away from the sawtooth, changes in the dB_θ/dt represents a true variation in the mode amplitudes, A_m. At the time of the sawtooth oscillation ($t \sim 20.6$ msec in the above case) the mode structure becomes quite complicated (see section V-5) as high mode numbers are generated. These high mode numbers are associated with high frequencies, 100-250 kHz, and severely alias the linear decomposition depicted above. For this reason, the temporal mode evolutions shown in Figs. (V-4-8)-(V-4-11) are not a sensible representation during the sawtooth crash. As such, the two point phase measurements have been adopted to obtain the spectra.

The second approach to the poloidal mode structure is to form a cross correlation coefficient among various coils. This is shown for B_θ in Figure V-4-12 using the coil at $\theta = 16$ degrees as reference detector. We observe a clear shift in the

peak of the cross correlation as θ advances from the reference coil. This shift in Figure V-4-13 indicates poloidal rotational asymmetry in the magnetic fluctuations. The nature of the fluctuations can be deduced from inspection of such cross-correlation with zero time delay ($\tau = 0$). To lowest order, disregarding the lack of rotational symmetry, the cross correlations predict the poloidal mode (e.g. the peak cross correlations sign changes once in this case shown so we see an $m = 1$ mode). Lack of symmetry indicates that the m=1 is distorted due to toroidicity. This is observed from an asymmetric cross-phase variation at $\theta \sim 16^{O}$ compared with that of $\theta \sim 173^{O}$ as shown in Figure V-4-14.

Poloidal coherence at lower frequencies is very high (≥ 0.8), indicating that $m = 1$ modes are low frequency. It is possible that other modes become important at higher frequencies (see Section V-5, on nonlinear frequency coupling).

To determine propagation and rotational effects, we examine the time-delayed cross correlation between the poloidal array coils. Fig. V-4-13 shows the results for fluctuating B_{θ}. As shown, the low frequency magnetic fluctuations are measured to have helical propagation. The phase velocity of such propagation is defined as $v_{\phi} = 2\pi f / k = 2\pi a / \Delta t = 3\times10^{4}$ m/sec . The rotation is in the direction of ion diamagnetic drift which is the direction of electron poloidal current flow inside the reversal surface. The rapid fall off with time (or distance, Fig. V-4-12) of the maximum value

of the time delayed correlation coefficient indicates the relative incoherence of the modes due to growth and decay rates of the same order of magnitude as the rotation.

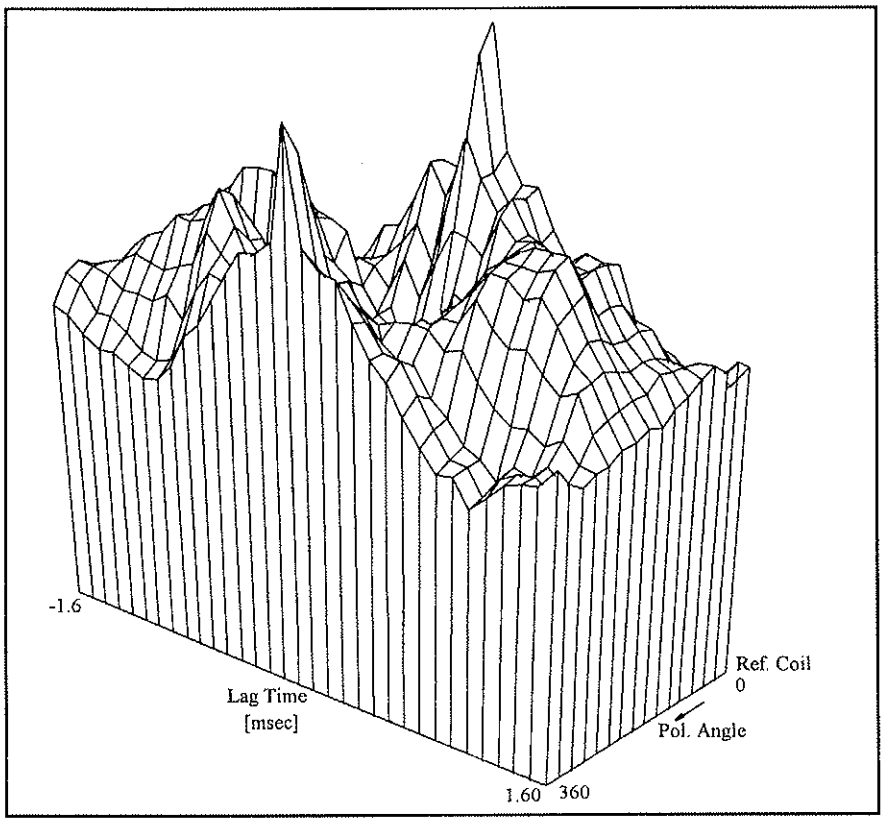

Figure V-4-12) Time-delayed normalized cross correlation function as a function of poloidal angle. Ensemble-averaged over the sustainment phase (digital filtered 1-35 kHz).

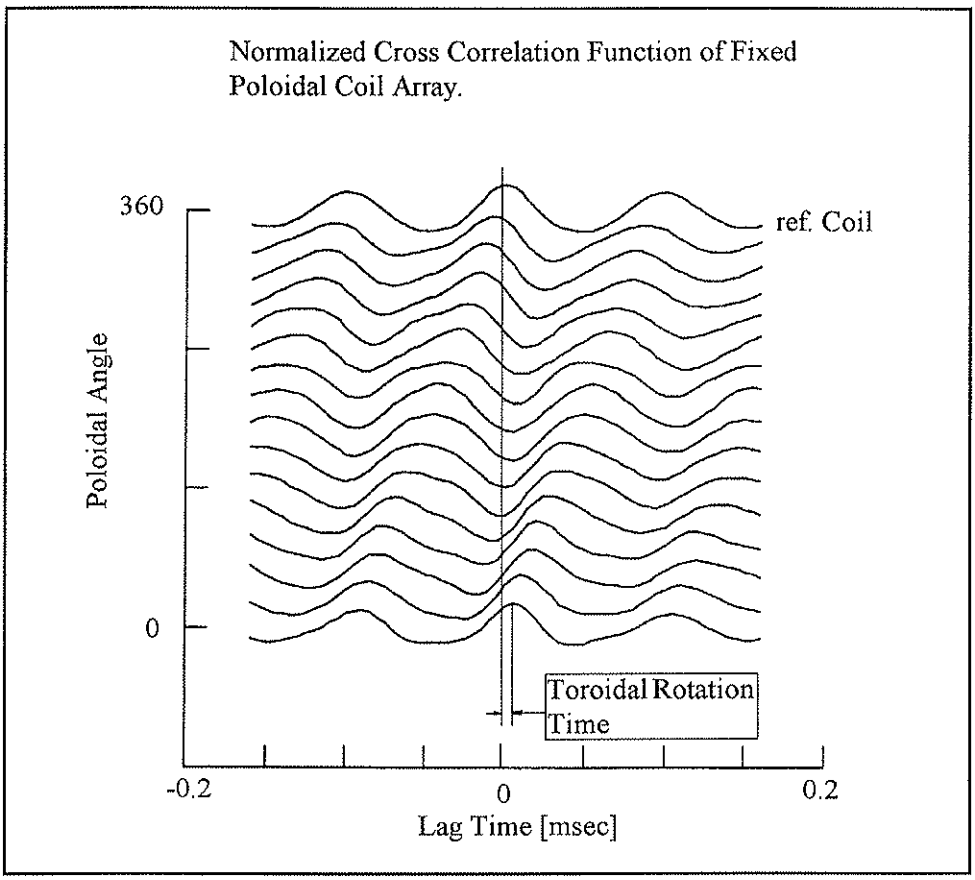

Figure V-4-13) 2-D plot of time-delayed cross-correlation function of B_θ of poloidal array indicates the poloidal and toroidal rotation

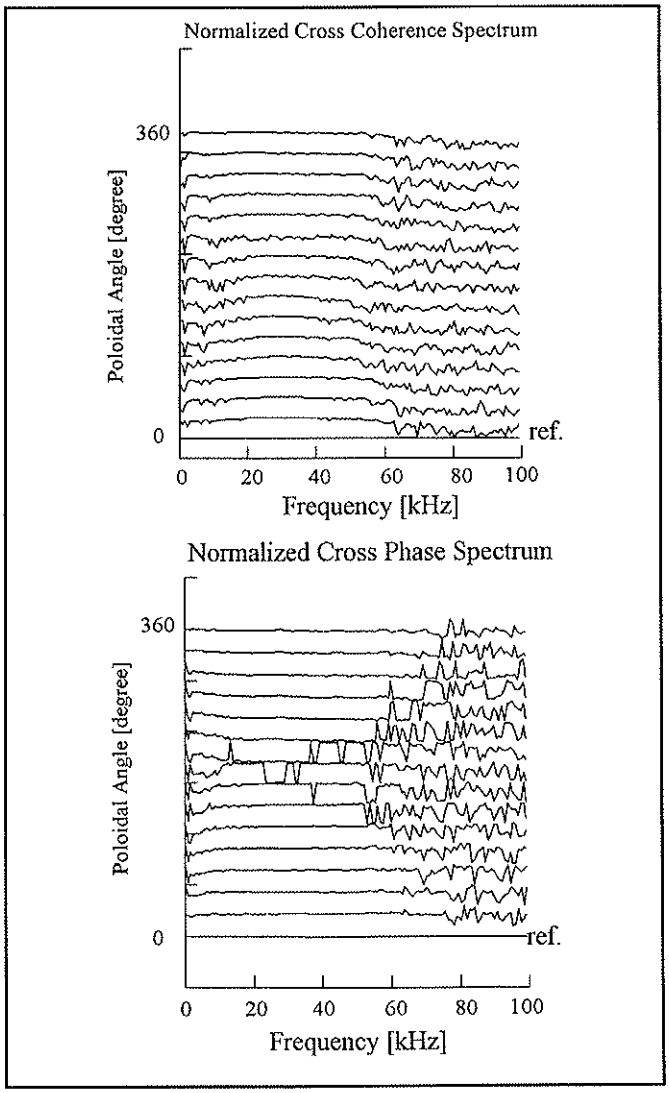

Figure V-4-14) Cross-coherence and cross-phase spectrum between poloidal coils.

The third approach to measure the poloidal mode spectra is given by the wavenumber-frequency spectrum $S(k,\omega)$. The two-point correlation technique presented in chapter 4 has been used to estimate the power weighted mode number spectrum by analyzing the turbulent time signals taken from two spatial points that are poloidally separated. Figure V-4-15 presents the experimental poloidal mode spectra. The computational spectra[1-2] (Fig. V-4-16) for similar aspect ratio as MST are nearly identical to experimental spectra at low frequency (10 kHz < f < 30 kHz). Figure V-4-16 has been obtained from one computational run by summing the energy of all toroidal modes of a given m. The initial value MHD code employed for comparison to the experiment solves the full compressible MHD equations for a periodic cylinder with an aspect ratio of 3, as in the experiment (a brief description is given in Chapter 2). The code was also run 256 times with random initial conditions to generate an ensemble of computational data. I have then applied the same 2-point correlation analysis to the computational data to obtain an ensemble averaged m-spectrum (Figure V-4-17). The single run (Fig. V-4-16) and the ensemble analysis, (Fig. V-4-10) are similar, since the k_θ-spectra is narrow, with most of the power concentrated at the lowest k_θ value.

---

1 * Courtesy of Dr. E. Zita.

2 * Data provided by Dr. K. Sidikman.

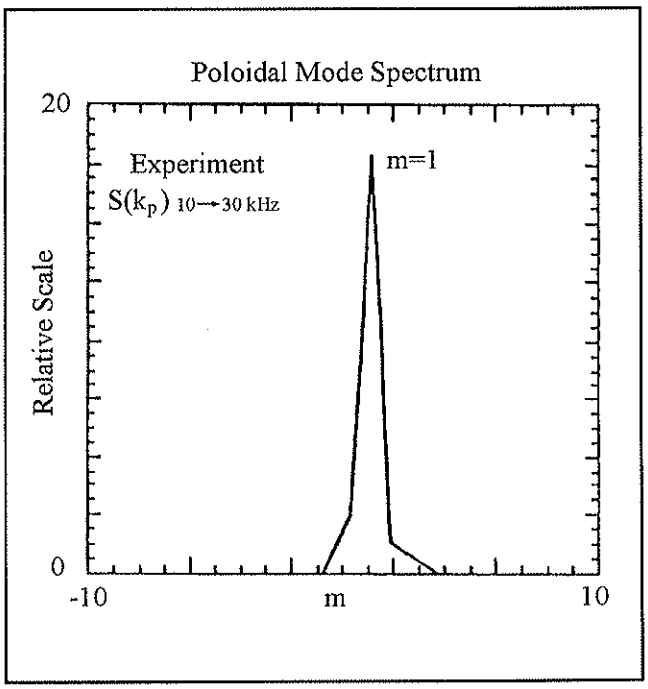

Figure V-4-15) Poloidal modes spectra seen in experiment are similar to those predicted by the nonlinear tearing simulation (see Figs. V-4-16 and V-4-17).

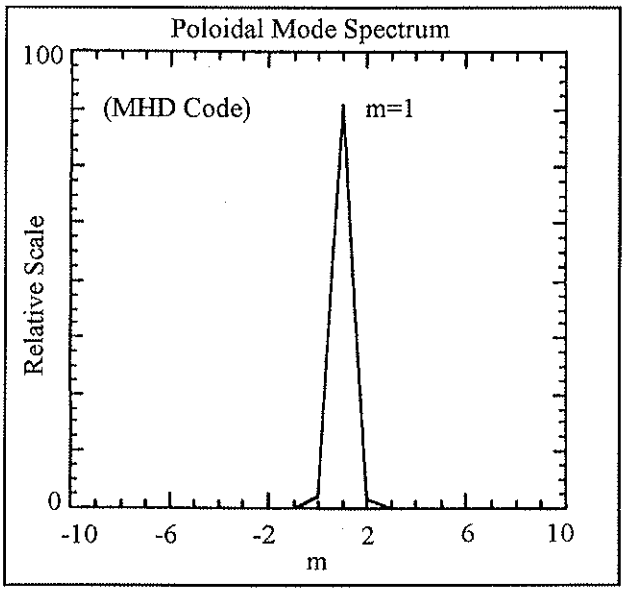

Figure V-4-16) Poloidal mode spectra of magnetic fluctuations, from 3D-MHD computation.

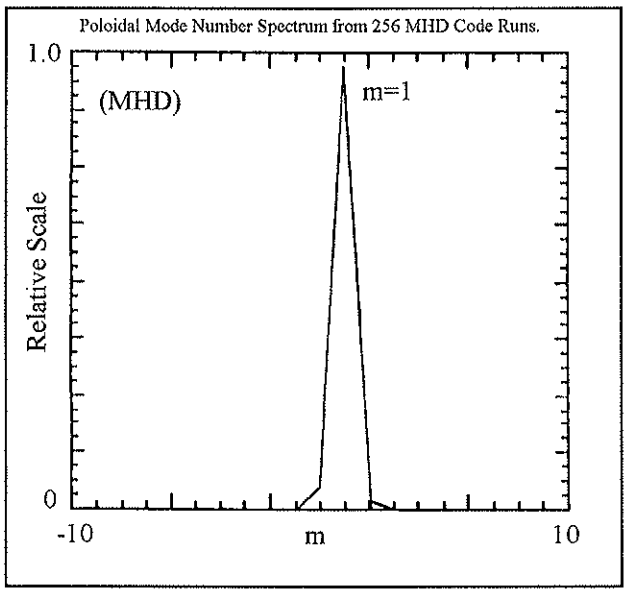

Figure V-4-17) Poloidal mode number spectra of magnetic fluctuations from an ensemble of 256 3D MHD computation runs, using 2-point technique.

V-4.3) Toroidal Mode Structure and Phase-locking

Using the internal magnetic sensors described in chapter 3, the helical mode evolution of the coherent m=1, n=5-8 modes can be determined. In this section, we will describe their evolution and phase locking mechanism, and compare the results obtained on the MST with the experimental results of OHTE, (Tamano et al. [20-22]) and TPE-1RM15 (Hattori, et al. [23]), and simulation studies by Kusano et al. [24], and by Schnack et al. [25].

We have utilized the 64-coil fixed array of tri-axial magnetic sensors to determine the time evolution of the toroidal mode structure. Figure V-4-19 shows the amplitude and phase evolution of the dominant n = 6 spectrum calculated by spatial Fourier transform for a given shot:

$$C_n = \frac{2}{N}\sum_{k=1}^{N} \tilde{B}_k \, Cos(n\phi_k)$$

$$S_n = \frac{2}{N}\sum_{k=1}^{N} \tilde{B}_k \, Sin(n\phi_k)$$

$$A_n = \sqrt{\frac{1}{2} < |C_n|^2 + |S_n|^2 >}$$

where $n \leq k/2 = 32$ is the toroidal mode number and A_n is the amplitude of each Fourier mode. Averaging is not necessary to obtain the n-spectrum using spatial Fourier decomposition. This is advantageous to see the detailed temporal mode evolution. We observe that fluctuations occur in bursts separated by quieter periods. One striking observation is "cyclic-like" behavior of the temporal evolution of the dominant modes (see section V-8). The time evolution of the ampltitude of selected toroidal modes are shown in Figures V-4-20 and V-4-21. From the poloidal array, the coherent helical modes are m = 1, and from the toroidal array, they have a modal structure in the range n= 5-8. The n=6-8 modes begin to grow at ~20.7 msec while the n>13 components stay relatively constant. As shown in section V-5, the n=13 mode is driven by nonlinear interaction of coherent helical (m=1,n=6) and (m=1,n=7) modes, but it is only shown here as a representative of the level of the higher n modes which do not make up the phased locked disturbance. The amplitudes shown in Figs. V-4-19 through V-4-21 are derived from the $dB\phi/dt$ signals; no integration has been applied either analog or digitally. As presented in the last section, the mode structure of sawtooth crash is quite complicated. Using 2-pt correlation techniques

and ensemble averaging of ~ 400 sawtooth events, I have shown in section (V-4.5) that the n-spectrum is strongly peaked prior to the crash with the dominant n's in the range 5-8. When the sawtooth crash occurs, the spectrum is broadened and extends out to n~100. The higher n's are primarily due to the higher frequencies, (see Section V-5.3). These high n numbers severely alias the linear Fourier decomposition described above. For this reason, the mode evolution shown in Figs. V-4-19 through V-4-21 are not reasonable representation during the sawtooth crash interval.

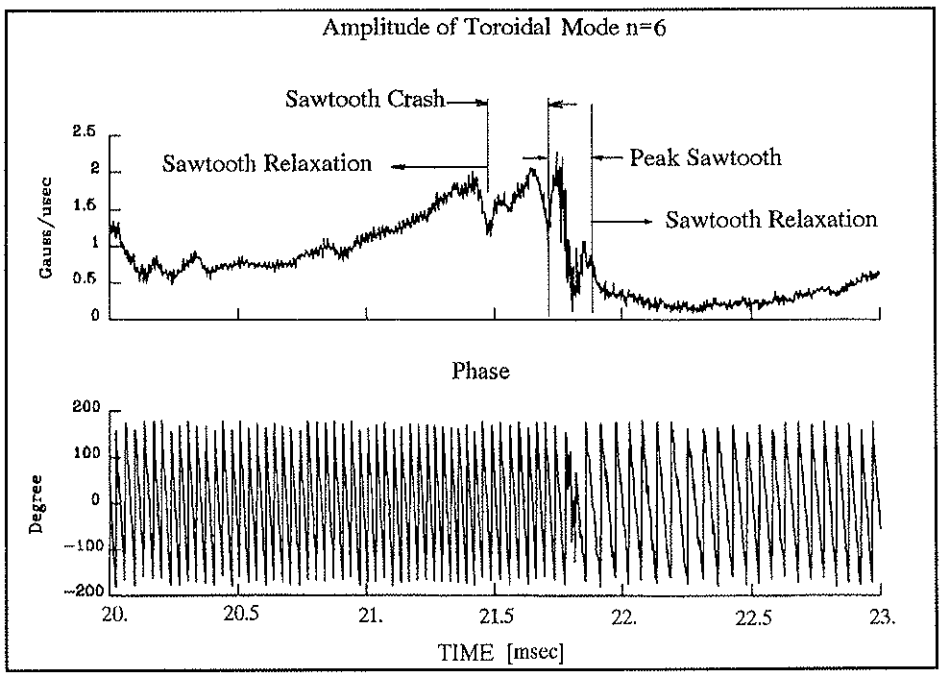

Figure V-4-19) The amplitude (top) and phase (bottom) of the n = 6 toroidal mode including a sawtooth event. Slowing down of rotating coherent mode after a sawtooth crash is shown.

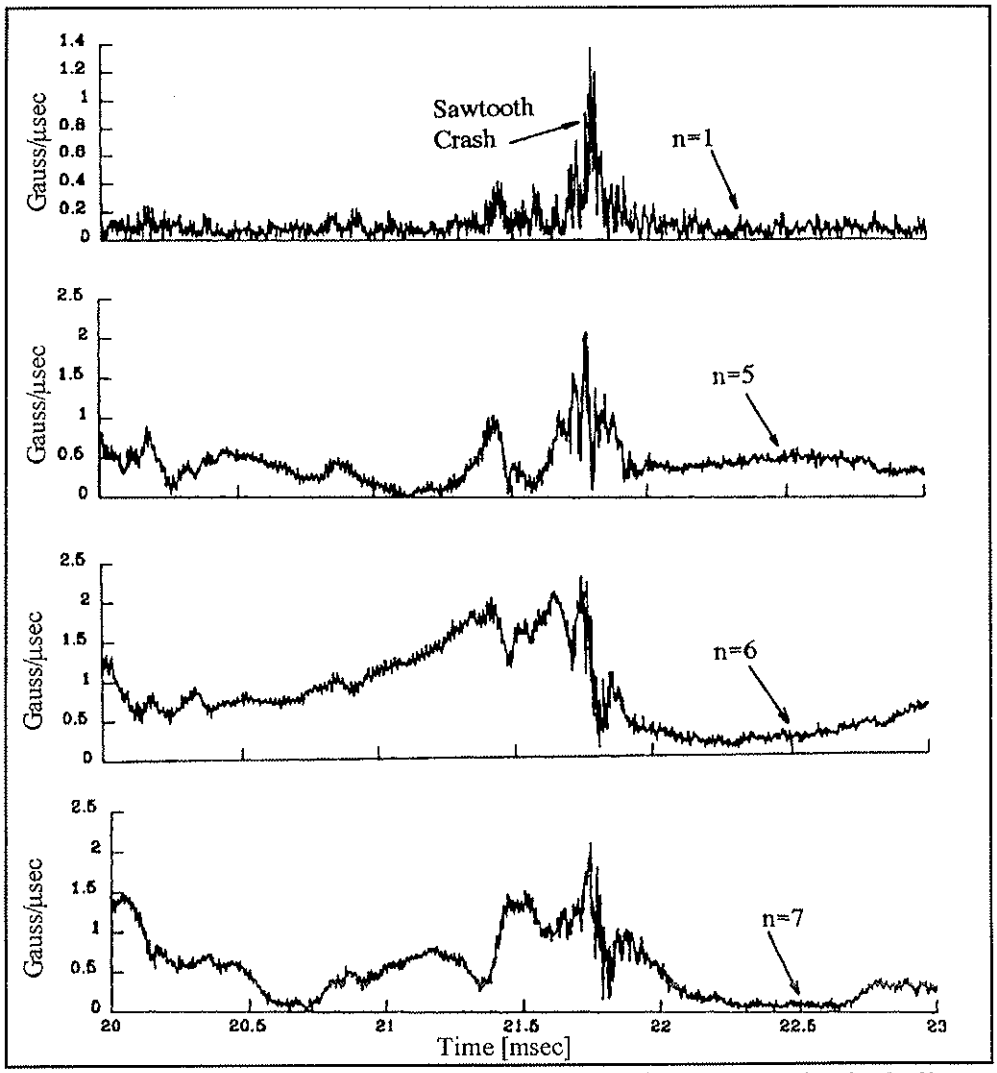

Figure V-4-20) The amplitude of the n = 1, 5, 6, and 7 modes including a sawtooth event.

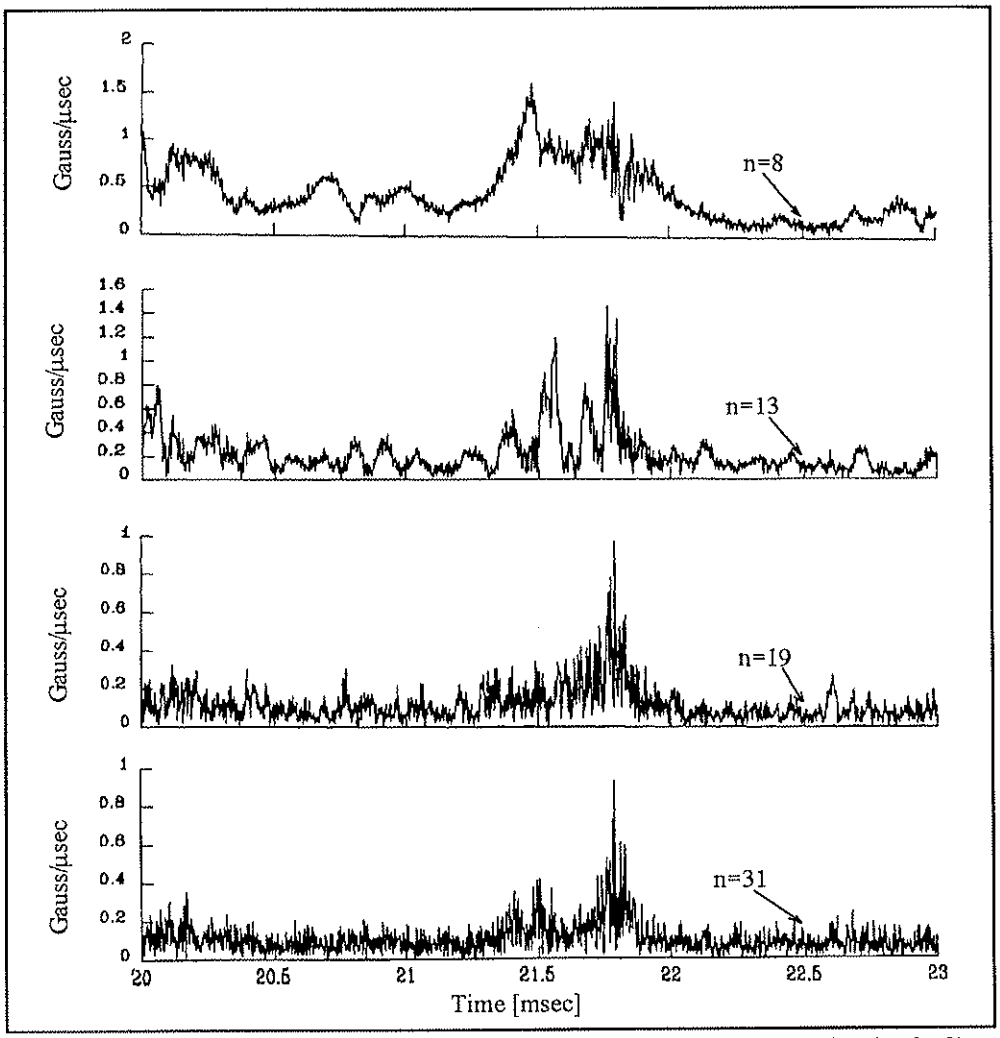

Figure V-4-21) The amplitude of the n = 8, 13, 19, and 31 modes including a sawtooth event.

The second approach is to form the cross-correlation of the magnetic fluctuations among the toroidal array to give the spatial evolution of the coherent modes. If the machine is completely toroidally symmetric, then ϕ is an ignorable coordinate and the cross-correlation between two angles ϕ_1 and ϕ_2 only depends on the phase difference $|\phi_1 - \phi_2|$. Figures V-4-22 and V-4-23 show the averaged spatial cross-correlation of 50 identical records over the sustainment phase of identical discharges. Coil 1 at $\phi=3^o$ is the reference point. In fact, the time evolution of the peak correlation is slightly nonlinear, indicating a slight toroidal asymmetry. This could be due to the poloidal gap or the presence of port holes. The number of peaks at $\tau = 0$ (Fig. V-4-23) represents the dominant mode, n = 6 and m = 1. The spatial auto-correlation of the reference coil has a rapidly decaying form indicating a fairly broad spectrum of toroidal wavelength. The observed toroidal mode structure can be divided into two distinct phenomena:

1) Low frequency coherent modes with n = 9-15, which are sometimes present, and rotate independently from one another.

2) Coherent modes with n ~ 5-8, which are phased-locked to each other and are present throughout the discharge. Their amplitude increases at the time of the reversal, where the toroidal field at the wall goes to zero, and phase-locking creates a local disturbance which rotates toroidally.

Propagation in the toroidal direction has been observed from time-delayed cross-correlation coefficient. Figure V-4-23 shows the rotation and the toroidal extent of constructive phase coupling of these mode. At the lower frequencies where the cross-phase spectrum is constant (Fig. V-4-24), the rotation is generally least ambiguous. The observed preferred rotation is in the direction of ion-diamagnetic drift direction with speed of ~3× 10^4 m/sec.

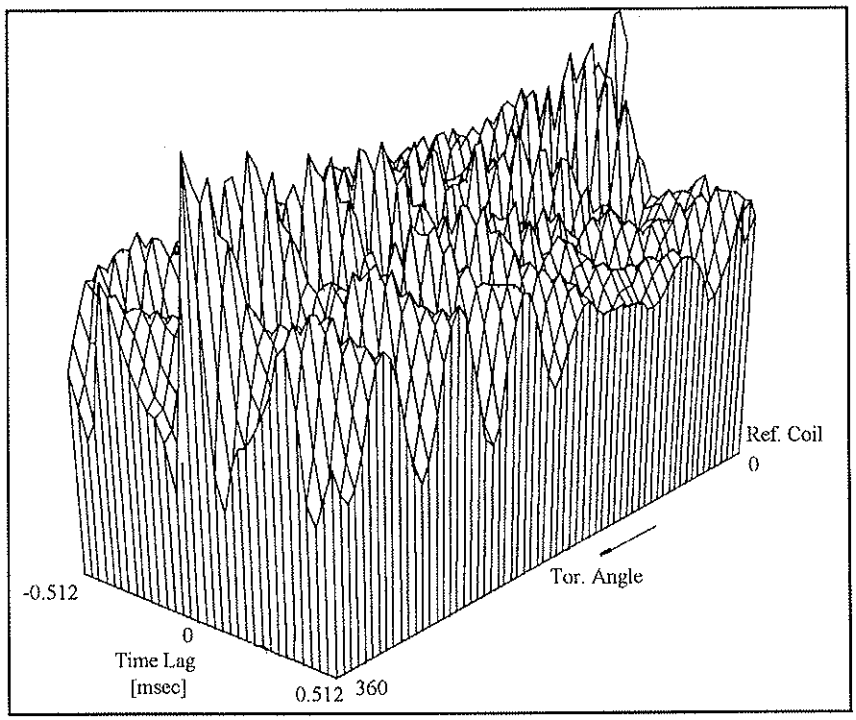

Figure V-4-22) Time-delayed cross-correlation coefficient as a function of ϕ. (filter 1-35 kHz), showing evidence of phased-locked modes as seen on z-axis oscillations v.s. tor. angle.

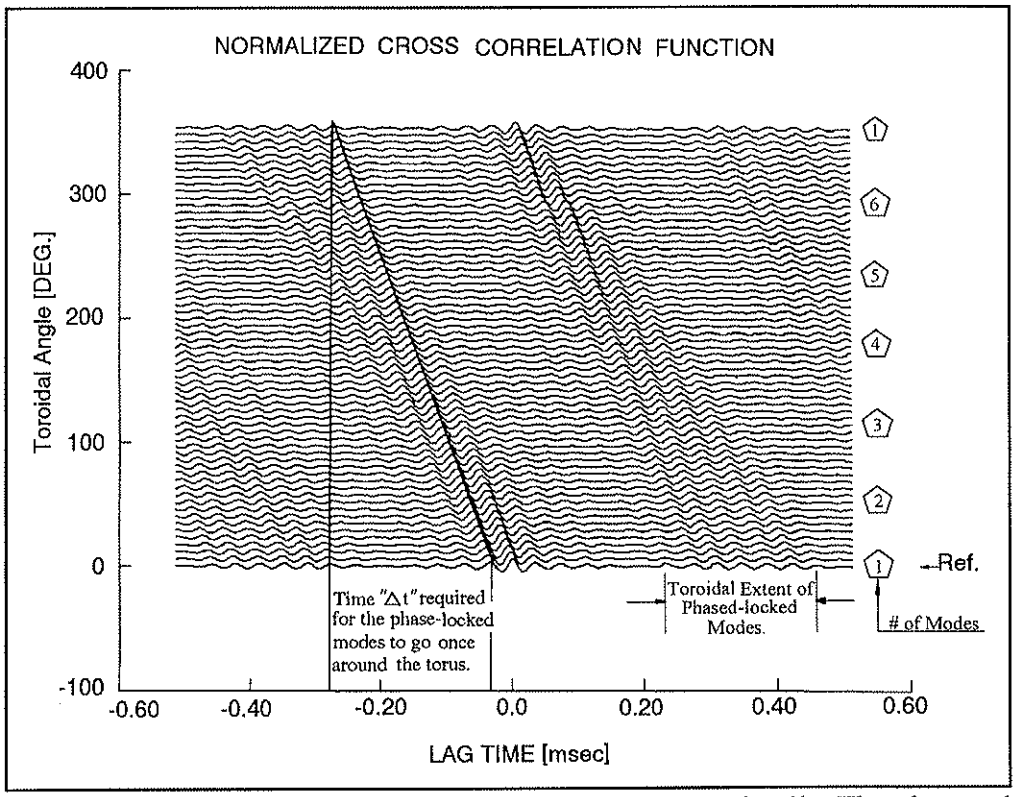

Figure V-4-23) Cross correlation of 63 toroidally located coils. The observed peaks are the result of the constructive addition of the coherent modes.

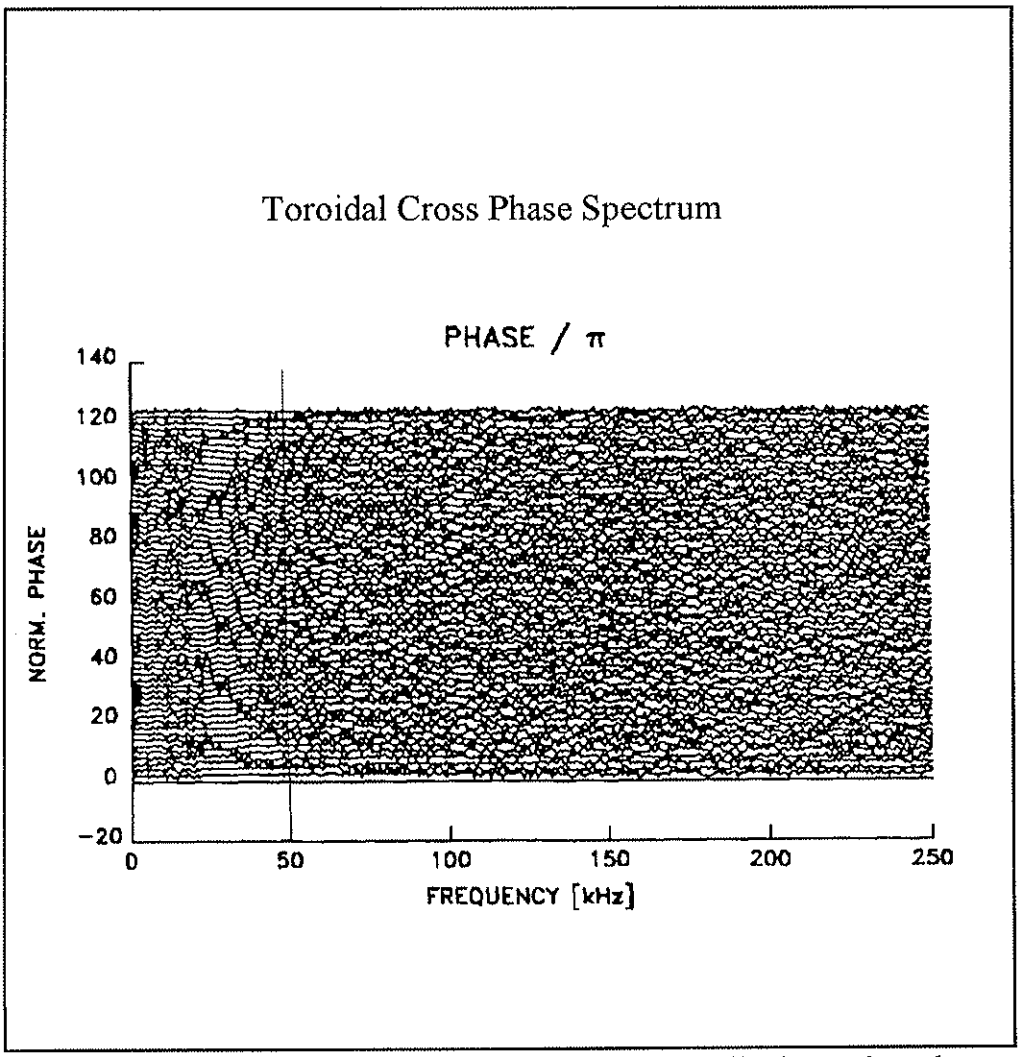

Figure V-4-24) Cross phase spectrum of the toroidal coils shows the coherent modes have frequencies below 50 kHz.

Kusano et al. [24] and Schnack et al. [25] using 3D MHD computations have numerically observed this phase locking mechanism in a simulation of the self-reversal and self-sustainment processes. Figure V-4-25 shows phase locking. Moreover, Kusano et al. mention that the location where the phase locking appears is coincident with the location at which the most unstable kink modes have the same phase in the pre-relaxed state. They associate this phenomena with the MHD relaxation process, since they can observe the phase locking with the perfectly conducting boundary condition when the system is very unstable. A similar mode was first observed experimentally on OHTE [20-22] with a thin shell and named the 'slinky mode'. There is a clear difference between the results on OHTE and on MST. In MST the "phase-locked" coherent modes are present throughout the reversal, whereas on OHTE they appear and disappear at will. MST results are shown in Fig. V-4-26 for comparison.

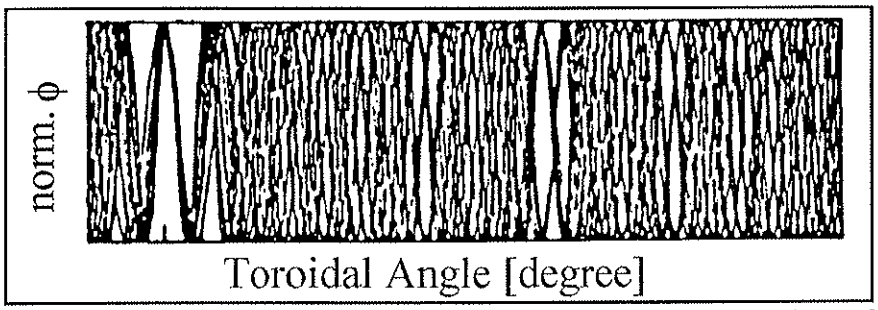

Figure V-4-25) Phases of resonant kink modes as a function of toroidal angle ϕ from Kusano et al. show constructive interference.

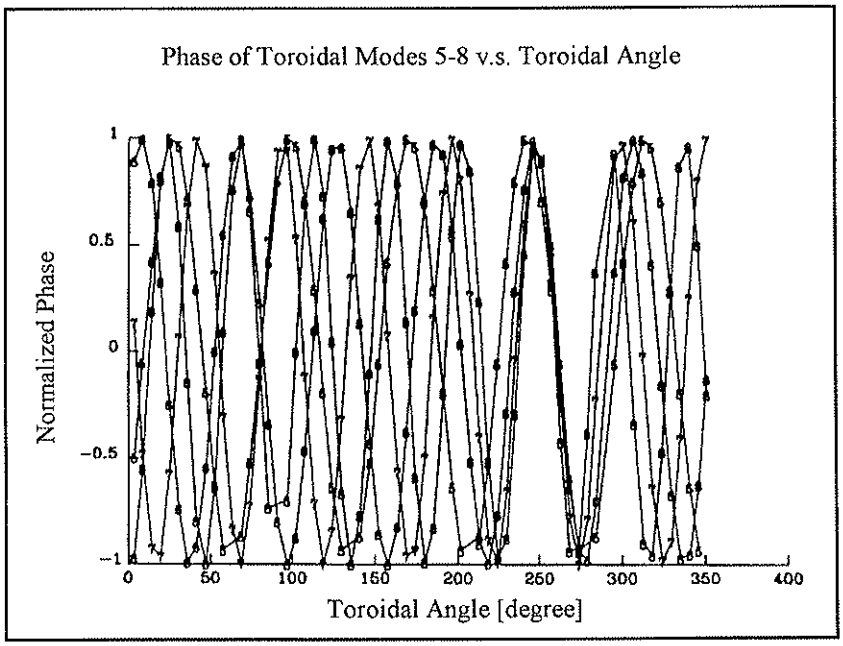

Figure V-4-26) Phases of resonant modes in MST as a function of toroidal angle ϕ.Phase locking at ϕ =240 deg. is exhibited.

The third approach to estimate the toroidal mode structure is to form the two-point correlation technique. The method used to calculate the mode number spectrum is discussed in some detail in chapter 4. Edge measurements in MST, shown in figure V-4-27, indicate low frequency n-spectra quite similar to that observed in smaller devices. The computational[1] spectra (Fig. V-4-28) for similar aspect ratio as MST are nearly identical to experimental spectra at low frequency (Fig. V-4-27), with the exception that the experimental spread in n exceeds that of the code. The difference might be attributed to the Lundquist number S, the ratio of the resistive diffusion time to the Alfven transit time. The experimental S is $\sim 10^6$ vs 3×10^3 in the code. The larger S of experiment yields greater nonlinear mode coupling. Figure V-4-28 has been obtained from one computational run as described in section V-4.2. The results of two point correlation method applied to 256 computational data yield Fig. V-4-29. In essence, this approach contains the same information as the single run results; however, it provides a statistically meaningful trend rather than a greater resolution.

It has long been known that the low frequency ($f < 35$ kHz) magnetic fluctuations observed in the RFP agree with predictions for nonlinear tearing mode fluctuations, as calculated from various 3D resistive MHD computations. In both

---

[1] * Courtesy of Dr. E. Zita.

experiment (Hutchinson et al.) and computation (Schnack et al., 1985; Holmes et al., 1988; Nebel et al., 1989), the dominant Fourier modes measured at the edge have poloidal mode number m=1 and toroidal mode number n~2R/a peaked such that a resonance close to the center is indicated. The modes are resonant within the reversal surface, but are global and non-zero over the entire cross section. I have verified that the mode spectra obtained from experimental and computational data are very similar.

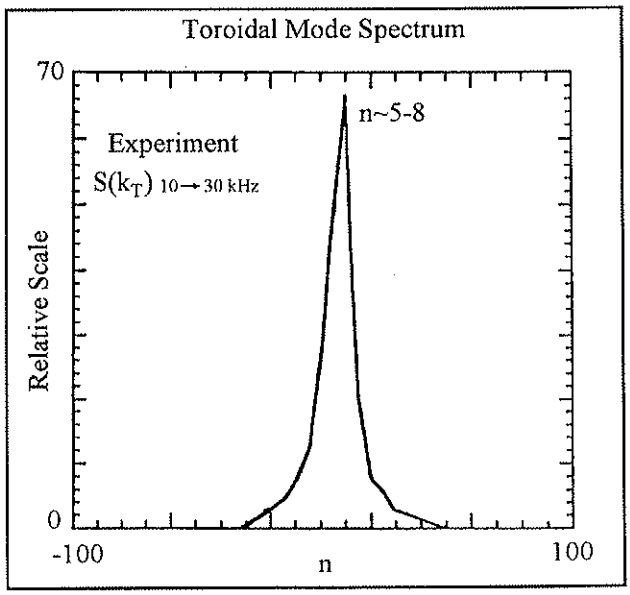

Figure V-4-27) Low frequency toroidal mode number spectra of magnetic fluctuations peaks at n ~ 5-8

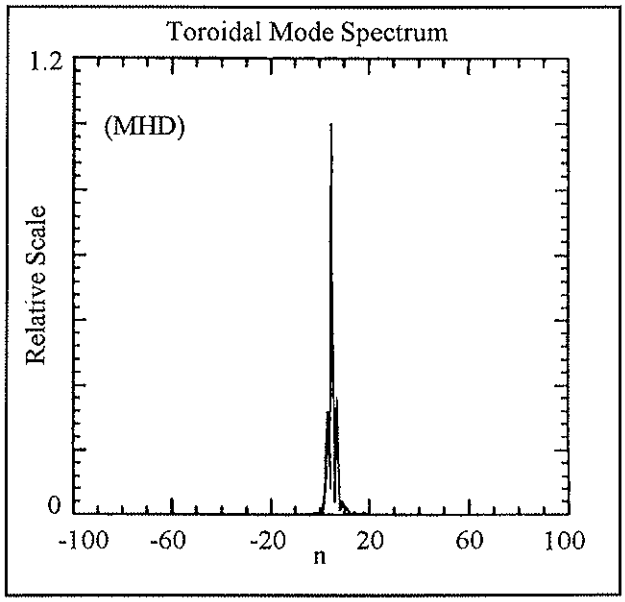

Figure V-4-28) Toroidal mode number spectra of magnetic fluctuations, from 3D MHD computation. $S=3\times10^3$, R/a=2.5.

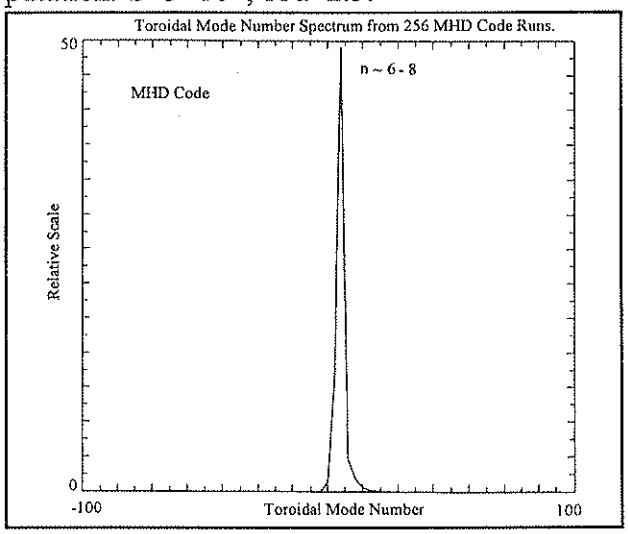

Figure V-4-29) Toroidal mode number spectra of magnetic fluctuations, from ensemble average of 256 MHD code runs, $S = 10^4$, R/a = 3.

V-4.4) Helical Mode Structure

Although the results of linear mode analysis presented above describe the general characteristics of the m & n spectra separately, they do not associate given m's with certain n's. In fact, we have calculated $a_n = \sum_{m=0}^{\infty} a_{nm}$ and $a_m = \sum_{n=0}^{\infty} a_{mn}$.

No information has been extracted on the helicity of the modes. In order to obtain the helical mode structure, a two-dimensional array of measurements is required to form 2-D helical Fourier components of the form exp[i(nθ + m ϕ)].

If we form the correlation matrix of the poloidal array ϕ_0=180° with toroidal array θ_0= 241° at zero time delay,

$$Q(\theta,\varphi) \equiv \langle B_1(\theta,\varphi_0=180^\circ)\, B_1^*(\theta_0=241^\circ,\varphi) \rangle, \qquad \text{(V.4.4.1)}$$

we obtain a two-dimensional measure of the statistical properties. In the case of ignorable θ and ϕ dependence, "Q" is sufficient to determine essentially completely the second-order statistics (i.e. power spectra, cross-correlations ,etc.). Fourier transform of "Q" is the two dimensional power spectra:

$$A_{mn} = \frac{1}{(2\pi)^2} \int\int \exp[-i(m\theta + n\varphi)]\, Q(\theta,\varphi)\, d\theta\, d\varphi\,, \qquad \text{(V.4.4.2)}$$

which is referred to as the associated spectrum [19] since it is a measure of the correlation between 'm' and 'n' components.

Figure V-4-20 shows the cross correlation between m=1, n=5-7 helical modes. The maximum cross correlation of m=1 helical modes are phase shifted from one another. This states that the (m=1, n=5) helical mode grows ahead of (m=1, n=6) which grows ahead of (m=1, n=7) modes.

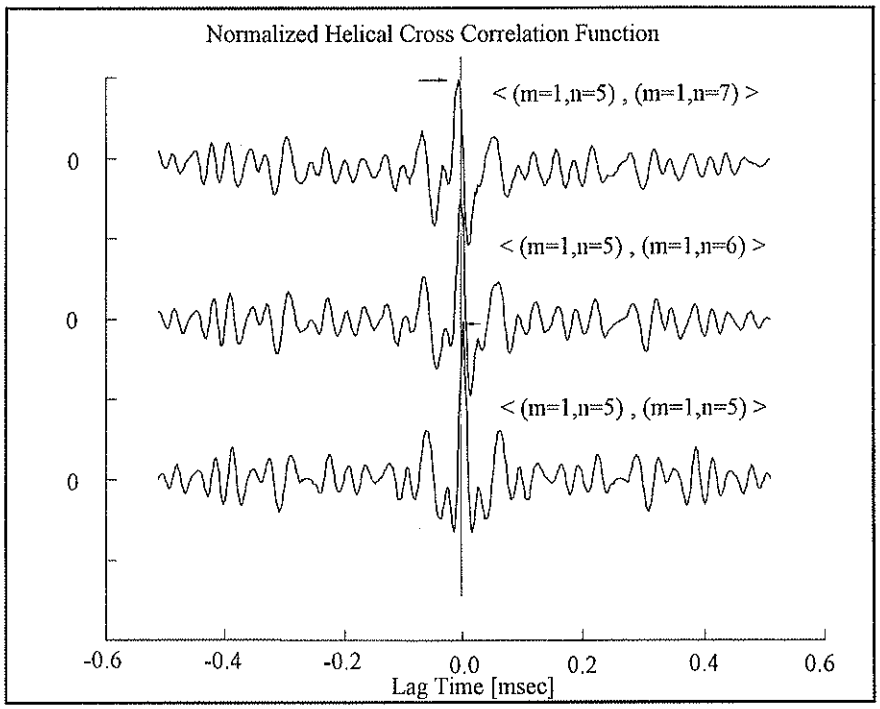

Figure V-4-30) The experimental result of the cross correlation of $B_{1\phi}$ helical modes m=1, n=5-7 .

The symmetry $A_{m,n}=A^{*}_{-m,-n}$ allows us to adopt the convention $m\geq 0$ and $-\infty < n < +\infty$ which is consistent with the sign convention of the experimental two-point correlation results discussed earlier. Then, the magnetic field lines inside the reversal surface have helicity corresponding to negative n, but at times I have assigned positive n as resonant inside the reversal. I will specifically state the proper sign of n when the convention changes. I only show $m\leq 3$ since the power is negligibly small for higher m.

The dominant feature of the helical spectrum, Figure V-4-31 is the m=1, $|\ n\ | \approx 6$ helical mode, although higher modes extend to $|\ n\ | \sim 15$. The MHD computational result of m=1, for all 'n' is given on Figure (V-4-25). Quantitatively, the helical mode spectra calculated from MHD simulation data and the experimental results agree. The discrepancies could be due to:

1) the Lundquist number for the theoretical data is $S=10^4$ whereas in the experiment S is $\sim 10^6$;

2) the MHD simulation solves the compressible, resistive MHD equations in a periodic cylinder with aspect ratio 3 whereas the experimental data was obtained in a toroidal device.

Note: The experimental result is normalized to the highest m=1 mode plus the statistical errors , ($|\ A_{1,6}\ | \leq (\ |\ A^2_{1,6} + \varepsilon^2_{1,6}\ |\ ^{1/2}$).

The m=2 spectrum is broader than m=1 spectrum and the maximum m=2 helical mode is less than 0.2 times of maximum m=1 helical mode. Experimental results are given on Figure V-4-33 and the MHD code result is presented on Figure V-4-34. It would be a mistake to conclude that all m=2 helical modes are representing independent modes. In fact, virtually all m=2 spectra has been risen from m=1 nonlinearly coupled helical modes (see section on nonlinear mode coupling).

The m=0 helical modes are symmetric in "n" as expected but the amplitudes are suspect. The m=0 helical mode spectrum is mainly generated by nonlinear interaction of helical m=1 modes. The frequency coupling of the two m=1 modes ($f_3=f_1-f_2$) results in an m=0 helical mode which could have frequency below 1 kHz, but as pointed out earlier, we are unable to measure f < 1 kHz magnetic fluctuations due to hardware restrictions. The experimental m=0 helical modes are given in Figure V-4-35 and the MHD code results are given in Figure V-4-36.

The Helical association spectrum of M=3 is shown on Figure V-4-37. The amplitude of these helical modes are very small . No statistical significance is given to this figure.

Note: that magnetic fluctuations cannot have a $B_{1\theta}$ component of m=0, n≠0 at the plasma edge due to $\nabla \times \mathbf{B_1} = 0$. Thus, I only present the $B_{1\phi}$ helically associated spectrum results in this thesis.

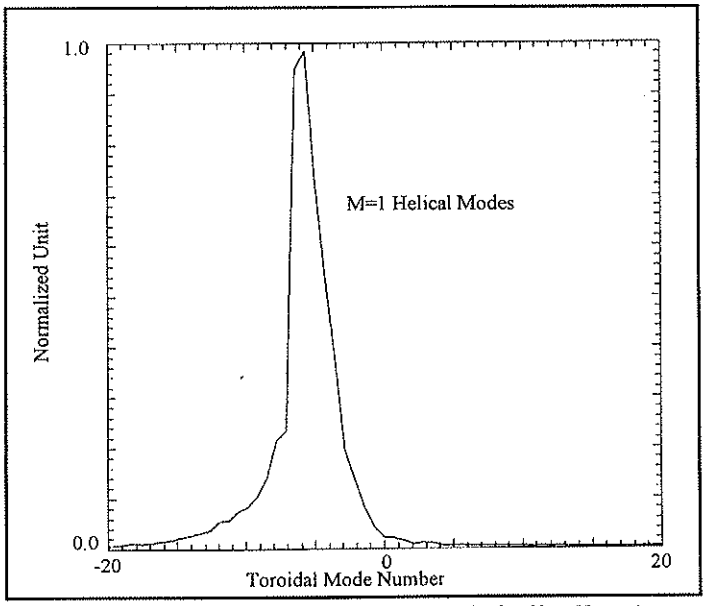

Figure V-4-31) Experimental M=1 helically Associated spectrum for $B_{1\phi}$.

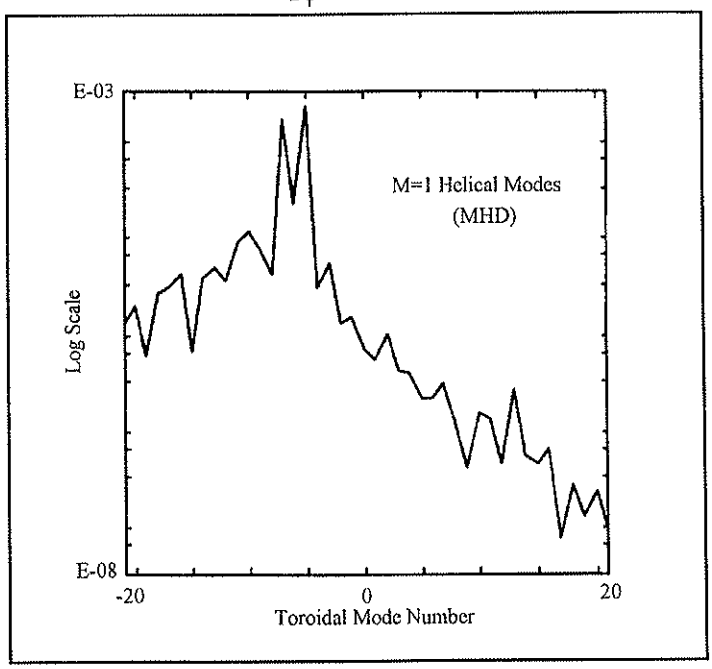

Figure V-4-32) M=1 helically Associated spectrum for $B_{1\phi}$, obtained from MHD code.

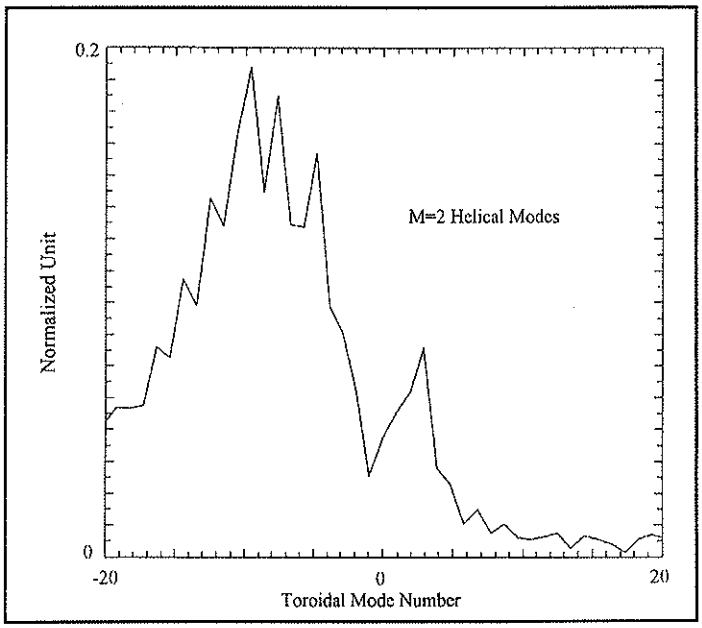

Figure V-4-33) Experimental M=2 helically associated spectrum of $B_{1\phi}$.

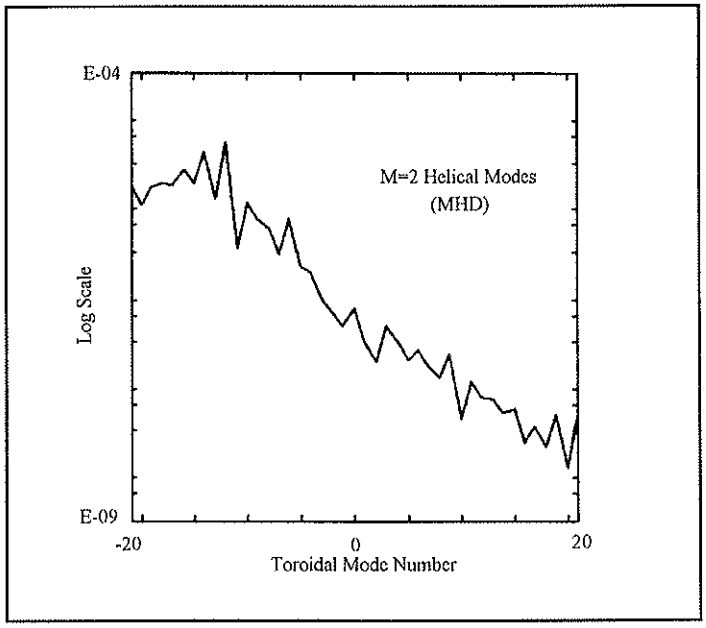

Figure V-4-34) M=2 Helically associated spectrum of MHD code.

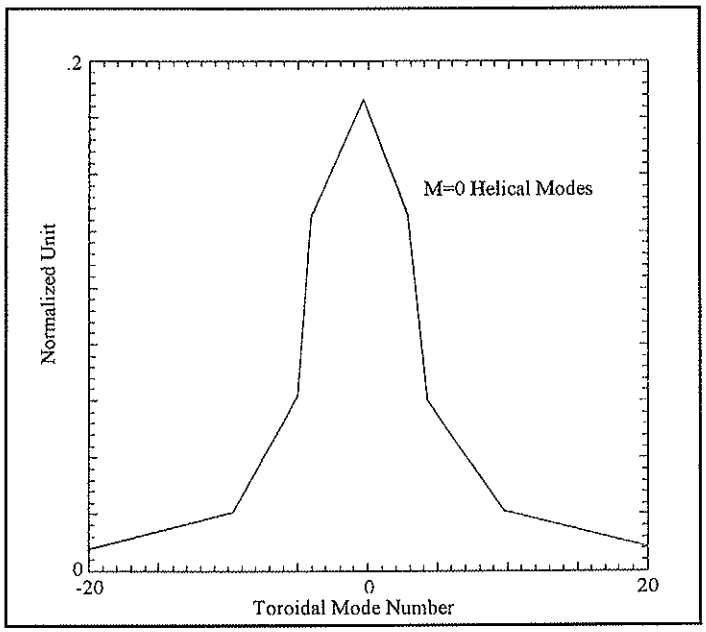

Figure V-4-35) Experimental M=0 helically associated spectrum of $B_{1\phi}$.

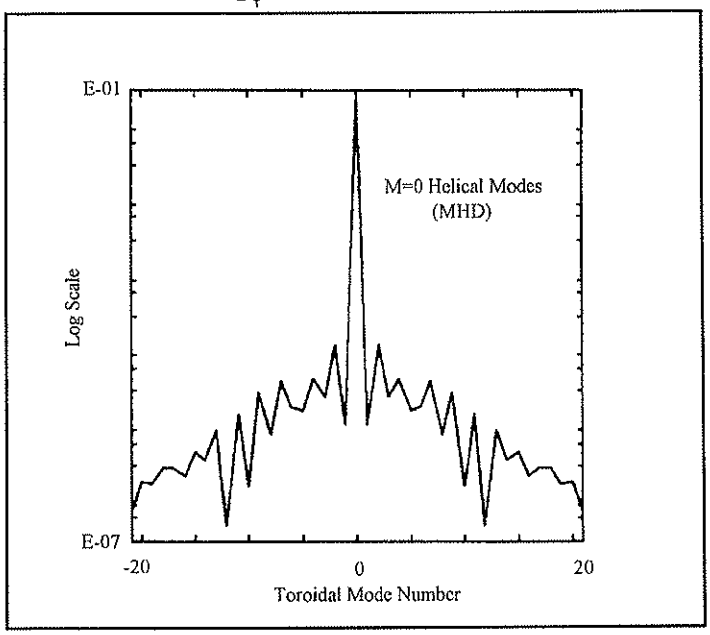

Figure V-4-36) M=0 associated spectrum for $B_{1\phi}$ of MHD code.

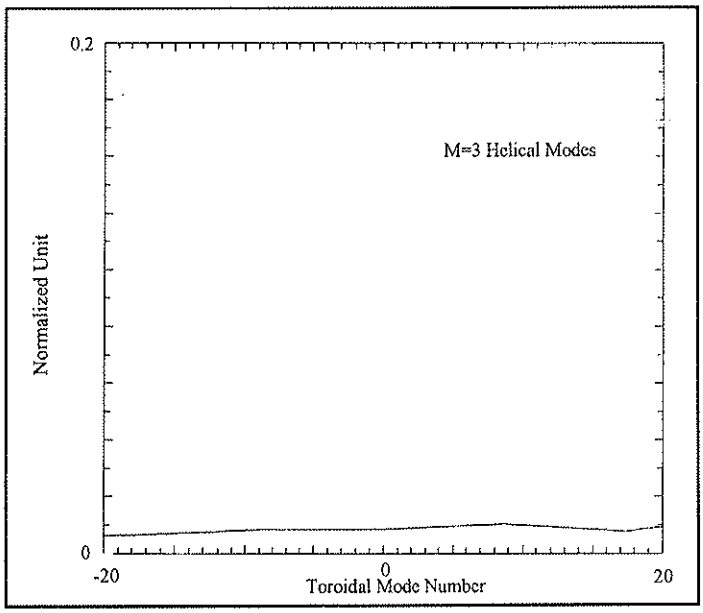

Figure V-4-37) The M=3 associated spectrum for experimental results of $B_{1\phi}$.

V.5) Measurement of Nonlinear Mode Coupling

Three-wave nonlinear coupling of spatial Fourier modes is measured in MST by applying bi-coherency spectrum analysis to magnetic fluctuations. The 64 tri-axial toroidal and tri-axial poloidal magnetic sensor arrays were used to measure wave-number coupling over 32 toroidal and 8 poloidal modes.

I have directly measured the three wave coupling of tearing fluctuations at the plasma edge. Comparison to bi-coherence predicted by MHD computation indicates reasonably good agreement. However, during the crash phase of the sawtooth oscillation the nonlinear coupling is strongly enhanced, concomitant with a broadened (presumably nonlinearly generated) k-spectrum. Three-wave nonlinear frequency coupling of magnetic fluctuations in the frequency domain is also measured for frequencies 1 kHz < f < 250 kHz. There is a substantial low frequency coupling.

In section (V.5.1), I will describe the measurement of magnetic fluctuations for the purpose of nonlinear spatial mode coupling and implementation of digital filtering to minimize the incoherent signals. The linear mode spectrum of the measured data and the MHD code data are also given in this section. In section (V.5.2), nonlinear frequency coupling is presented. Section (V.5.3) describes the nonlinear poloidal mode coupling at five different times during a sawtooth evolution,

and comparison with the bispectrum predicted by MHD computation. Section (V.5.4) describes the toroidal mode coupling at six different times during a sawtooth evolution. The quadratic coupling of the measured data prior to the sawtooth crash is compared with bispectra predicted by MHD computation in this section.

V-5.1) Data and Frequency Selection

Magnetic fluctuations measured in the MST revered field pinch with various waves exhibit different characteristics depending on the field errors, impurity level and the applied magnetic field. For the purpose of nonlinear mode coupling of this thesis research, the reversal parameter and the pinch parameter were chosen such that the commonly observed sawteeth oscillations were small. To simplify the presentation, I have divided the observations into six categories: (1) multi-coherent modes with small nonlinear coupling; (2) coherent nonlinear coupling of two modes (m=1,n), (m=1,n+1) to form (m=0,n=1); (3) turbulent region, broadened spectrum; (4) transition to relaxation via energy cascading to intermediate mode numbers (n~5-10) and small scale modes; (5) formation of n=5-10; (6) minimum nonlinear mode coupling. This classification is somewhat arbitrary.

In Figure V-5-1, the poloidal component of magnetic fluctuations is shown. The observed coherent oscillations are clearly disturbed by high frequencies when a sawtooth crash occurs.

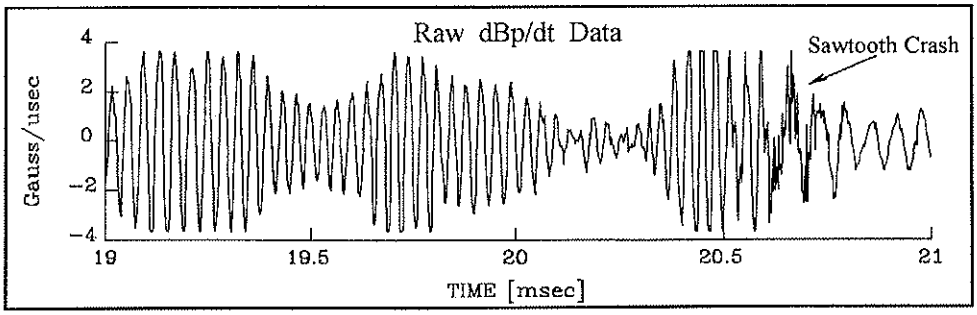

Figure V-5-1) Raw signal from poloidal magnetic pickup coil. The coherent oscillations can be seen clearly.

Clearly, numerical filtering is required to eliminate incoherent frequencies above 65 kHz (see Section V-5.2 for frequency selection logic). In figure V-5-2, raw toroidal magnetic fluctuations of 512 μsec duration and its digitally filtered version is shown.

The initial value MHD code employed for the comparison to experiment solves the full compressible MHD equations for a periodic cylinder with aspect ratio of 3, as in the experiment. The code includes 8 modes poloidally (azimuthally, $-2 \leq m \leq 2$, after aliasing effects are taken into account) and 128 modes toroidally (axially, $-42 \leq n \leq 42$). The zero-pressure code has been described extensively, and is commonly used to treat current driven tearing fluctuations in the RFP [26]. Brief description of the code is given in chapter 2. The main difference between the code

assumptions and the experimental conditions, given an MHD model, is the value of the Lundquist number (10^4 for the code and order 10^6 for the experiment). Also the code is for cylindrical system and does not include mode coupling arising from toroidicity.

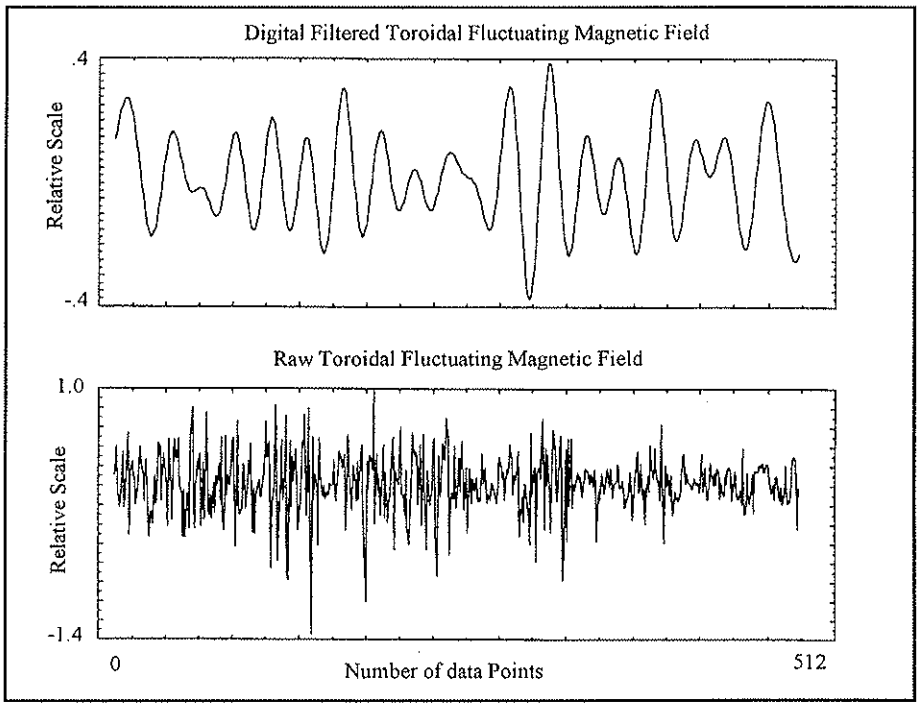

Figure V-5-2) Raw, (bottom) and digitally filtered (top) toroidal magnetic fluctuation signal. The coherent oscillations are only observable on the filtered signal.

The code was run 256 times with random initial conditions to generate an ensemble of computational data, as described in chapter 2. Experiment and the MHD

code results (both linear and nonlinear) are analyzed by the same spectral techniques. MST displays sawtooth oscillations, which have been observed in other RFP experiments [27]. Magnetically, these sawteeth oscillations suddenly deepen reversal, by decreasing the boundary toroidal magnetic field and increasing the total toroidal flux. I have found that during a sawtooth crash the nonlinear coupling changes dramatically. In this section, the results of linear mode analysis performed on both sawtooth and computational data is presented. The experimental data shown in this section are obtained at selected times during sawteeth oscillations. These data bins are marked by numbers on Figure V.5.3.

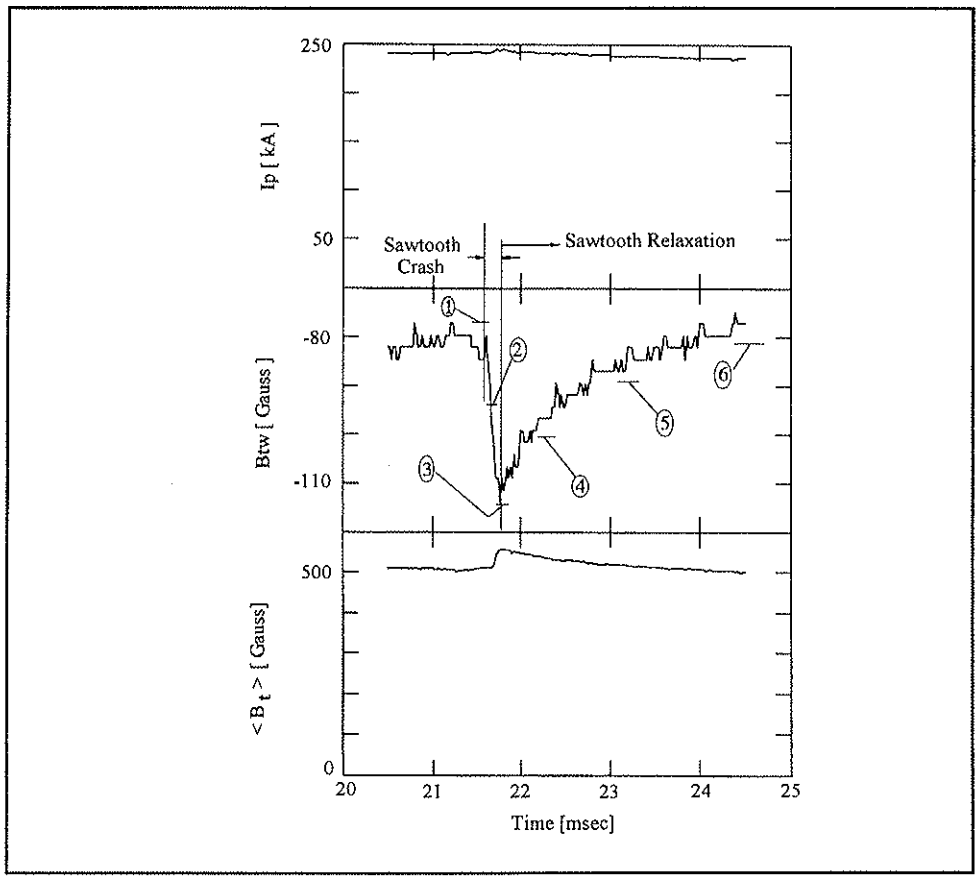

Figure V-5-3) Toroidal magnetic field measured at the wall for 5 msec duration (middle); plasma current, and average toroidal field are shown. Bin numbers are marked on the sawtooth .

Note: in Figure V-5-3 the horizontal length of the time markers indicate the duration of the time record of each sample of the ensemble.

Figure V-5-4 presents the statistical analysis results applied to the MHD computation data. The toroidal mode amplitudes are plotted in logarithmic scale. It is clear that the noise, corresponding to modes above n=42, are ten order of magnitude smaller than the amplitude of the tearing modes. This computational errors due to finite number of Fourier modes are negligible. On the other hand, the noise, corresponding to leakage of poloidal modes m > 3 are significant. When the bispectral analysis was used to compute the quadratic coupling of the numerical poloidal modes, where the number of Fourier components are small, the leakage of the m=1 mode generates a m=3 mode. The amplitude of this "error" mode was ~20%. This problem was alleviated by using the "sliding window" method of chapter (4). Figure V-5-5 and Figure V-5-6 show the results for the poloidal and toroidal amplitude spectra of the data incorporated in nonlinear mode analysis at two times. The top graphs can be directly compared to the MHD computation results of Figure V-5-3. Similarities to the linear analysis are astonishing, The presence of sawtooth, specifically point # 3 of Figure V-5-3 are plotted at the bottom graphs of Figures V-5-5 and V-5-6. Clearly, spectra have broadened during the crash phase. Thus, coupling is plausible. The mechanism underlying the broadening of the spectrums is the subject of the next two sections.

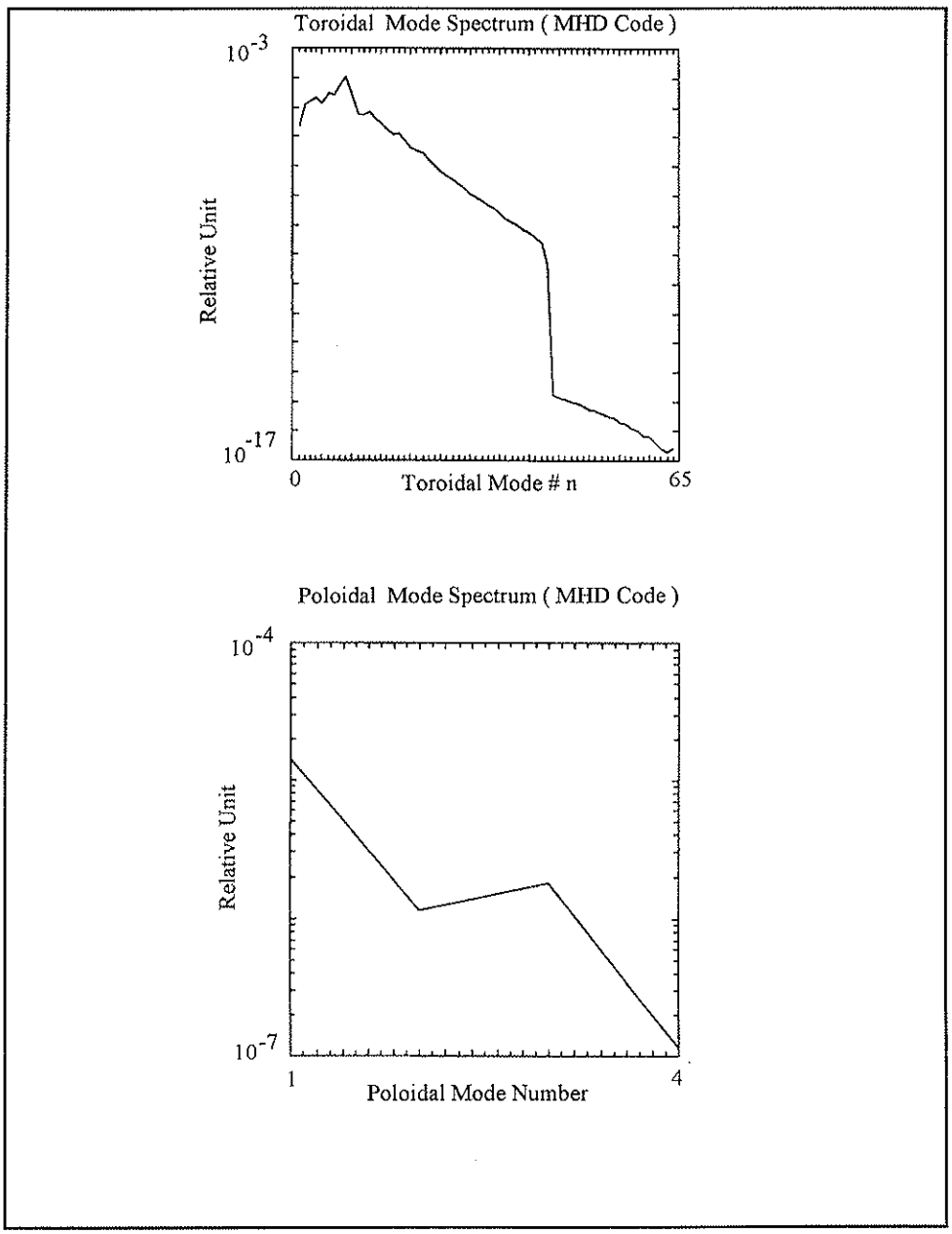

Figure V-5-4) Toroidal and poloidal mode spectra obtained from computational data. We observe an accurate toroidal spectrum and 10% error on the poloidal amplitude spectrum.

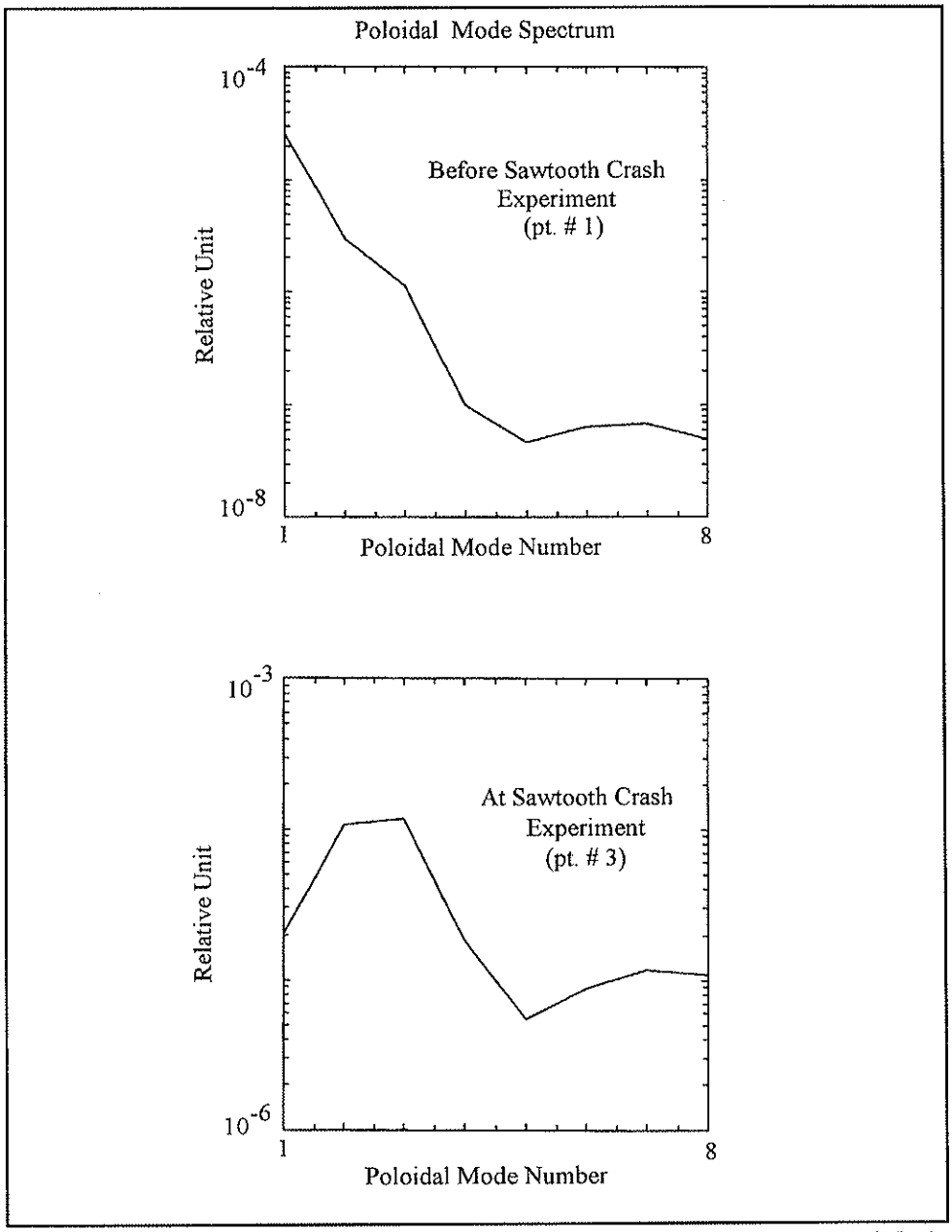

Figure V-5-5) Poloidal mode spectra obtained from measurements. Mode spectra is obtained from an ensemble of sawteeth oscillations. Bin #'s are associated with Fig. V-5-3.

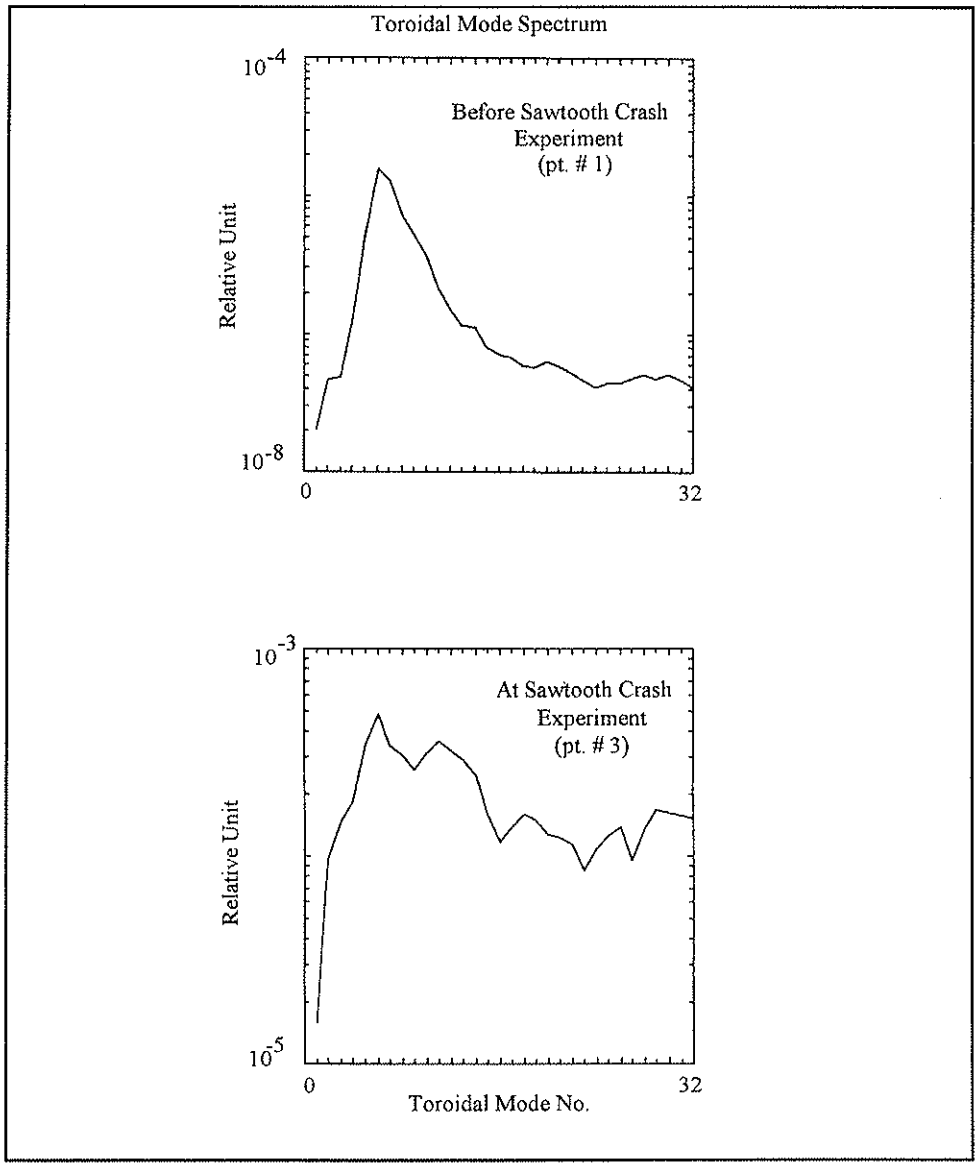

Figure V-5-6) Toroidal mode spectra obtained from measurements. Mode spectra is obtained from an ensemble of sawteeth oscillations. Bin #'s are associated with time markers on Fig. V-5-3.

V-5-2) Frequency Coupling

Graphical representation of three-wave coupling requires 3-dimensional or couture plots. I present my results in 3-D graphs but contour plots are also used to emphasize the range of coupled frequency or wavenumber. To assist the readers, a schematic of a contour plot is shown below in Figure V-5-7.

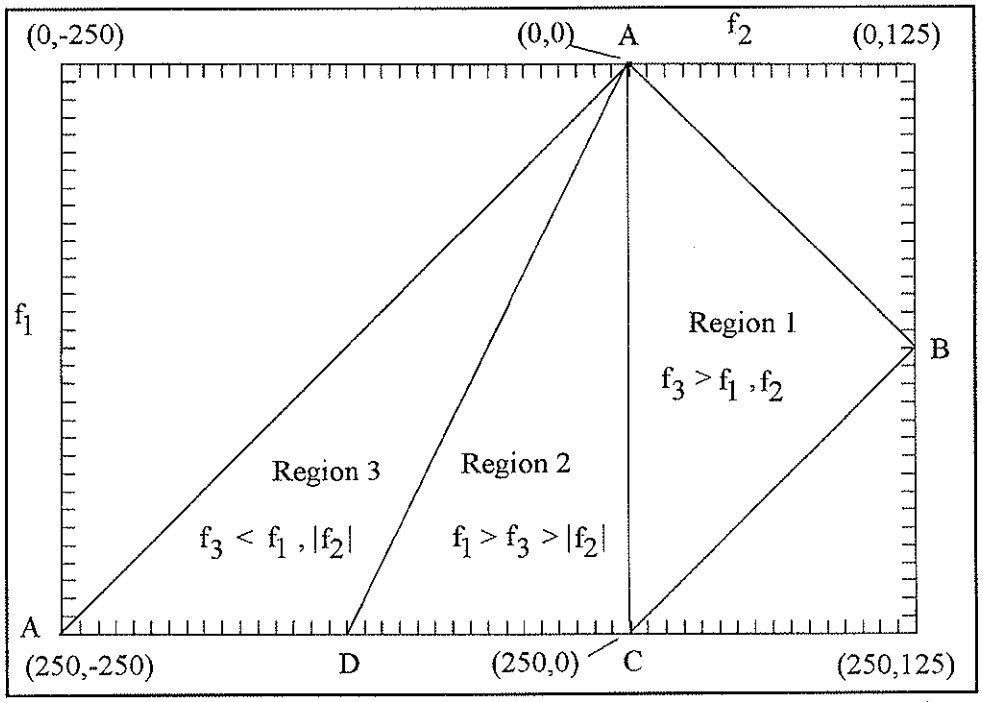

Figure V-5-7) schematic of three-wave coupling diagrams. Three regions are assigned for coupled frequencies (wave-numbers).

Considering the symmetries defined in chapter IV and resonance conditions $f_1 \pm f_2 = f_3$, where f_3 cannot exceed the Nyquist frequency (f_{Nyq}), the regions of coupling are divided into three regions, as shown in Figure V-5-7: region (1) represents coupling to small scales (high frequencies), region (2) shows the coupling to intermediate frequencies modes, region (3) represents couplings to low frequencies. I should emphasize the fact that the coupled modes along (A-A) line of Figure V-5-7 are f_1 , f_2 modes coupled to $f_1 - f_2 = f_3$ modes. These modes are m=0 dynamo modes. The block diagram of Fig. V-5-8 describes this process as given by Hattori [28]. Detailed discussion is given in Section V-5-5. Note an identical set of regions of Fig. V-5-7 can be shown in k-space to represent wave-number couplings.

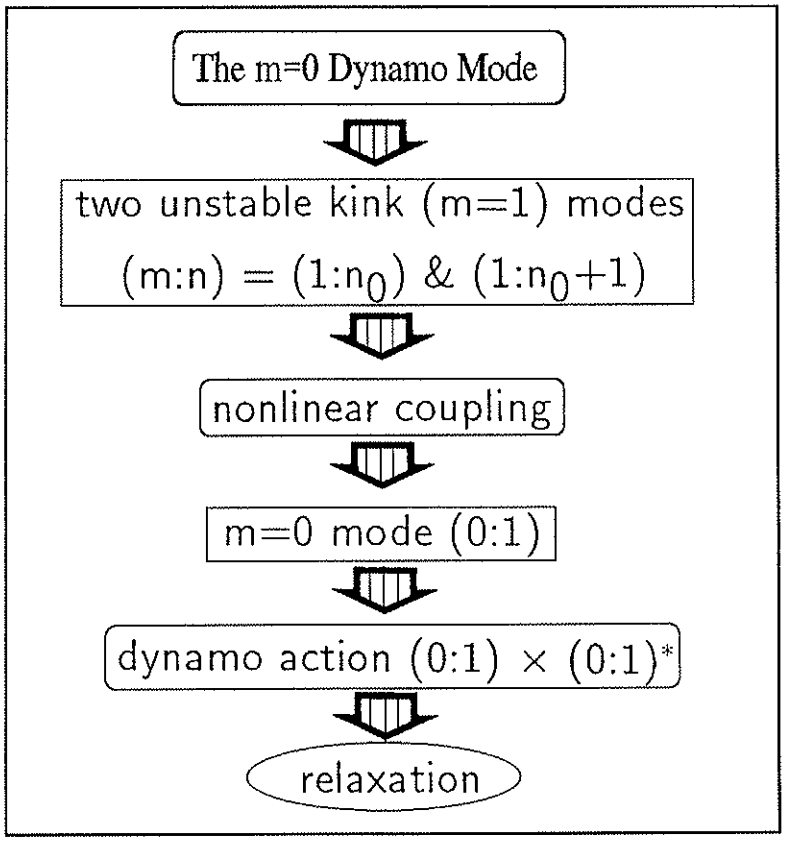

Figure V-5-8) Block diagram of m=0 dynamo mode coupling.

Figure V-5-9 shows the cross-power frequency spectra of coherent toroidal magnetic fluctuations measured from two adjacent coils of the toroidal array for bin number (5) of Figure V-5-3. Note, high frequency resolution and 400 ensembles have

suppressed the incoherent frequencies from the spectrum. The 3 dB point of the hardware filter is at 250 kHz; this restriction has eliminated the pickup of the higher frequencies, in fact the cross power of frequencies above 300 kHz are at noise levels (10 bit digitizers have three orders of magnitude of dynamic range).

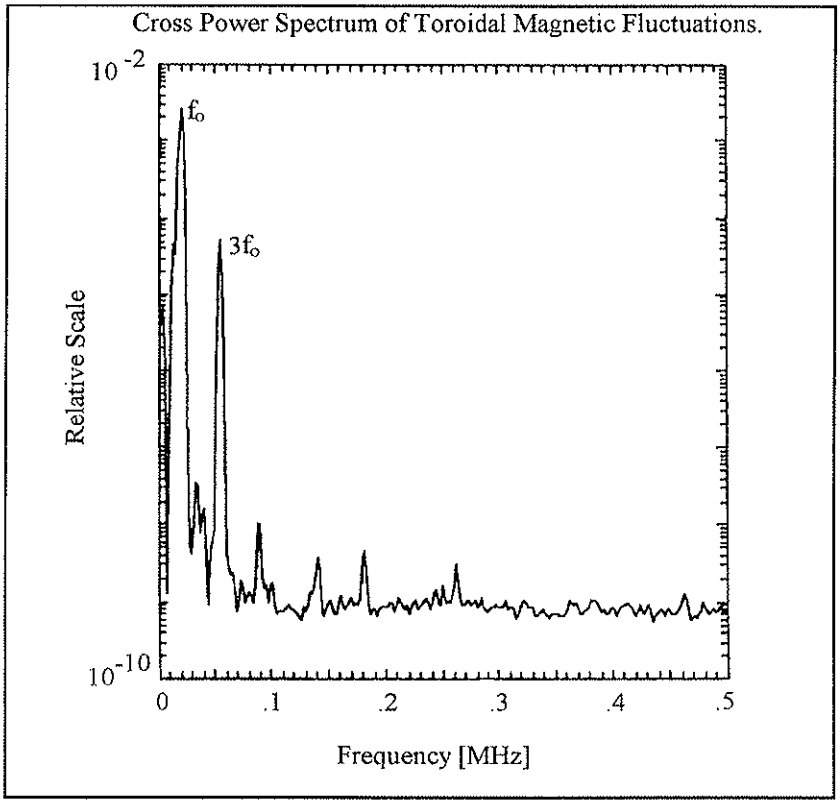

Figure V-5-9) Cross-power frequency spectra of toroidal magnetic fluctuations shows few "narrow" band coherent modes.

The experimental conditions and the mean equilibrium field are the same for all shots. As pointed out in section (V-3), 90% of power is below 35 kHz and background fluctuation measurements taken shows a continues spectrum with no independent coherent peaks. From the cross-power spectrum at the plasma edge, we can see the early emergence of a narrow but continuous band of dominant instability modes centered near f_o = 20 kHz (Fig. V-5-9). This center frequency, which will be used to identify the instability band is presuming the frequency of the most unstable m = 1 tearing modes. We speculate that the peak at $2f_o$ is associated with two m=1 modes coupled to m=2 mode. Hence, at $2f_o$, m = 2 nonlinearly stabilizes m=1 by dissipating energy to small scale fluctuations (i.e., the cross power amplitude of $2f_o$ is small). Whereas at $3f_o$, the second harmonic of the m=1 mode (odd mode number) has emerged and has higher amplitude than m=2. The amplitude of these "coupled" modes are ~20 times smaller in power than the fundamental modes. The frequency coupling results for five Bin numbers, (regions) of Figure V-5-3 in the form of 3-D plots are presented in Figures (V-5-10)-(V-5-14). The horizontal axes represents f_1 and f_2. The vertical axis represents bi-coherence corresponding to a value f_3 given by $f_3 = f_1 \pm f_2$ subject to the symmetries given in chapter IV. Note the bi-coherence plot of bin (1) which is prior to the sawtooth crash is given in Figure V-5-10. Figure V-5-14 has the smallest peaks on the bi-coherence diagram and its

spectrum is narrower than the frequency coupling of the sawtooth peak (bin #3) which is given in Figure V-5-13. The toroidal amplitude spectrum of the corresponding bin numbers 1, 3 and 6 are presented in Figures (V-5-15) through (V-5-17). Frequency coupling has been accompanied by wavenumber spectrum broadening.

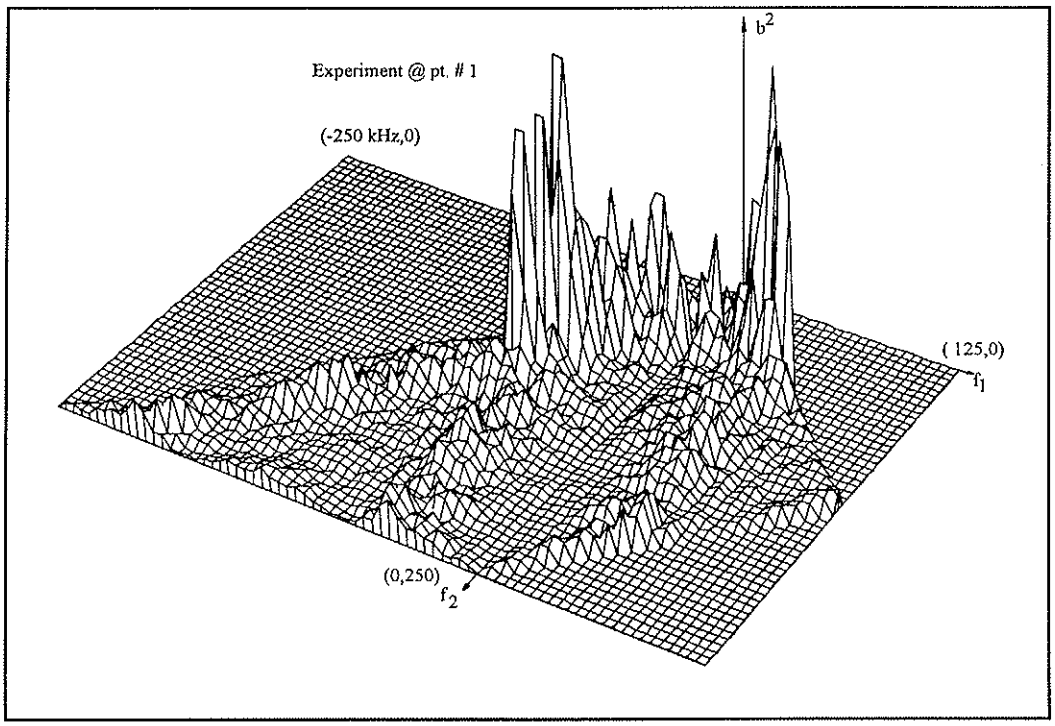

Figure V-5-10) *Frequency coupling. Bi-coherence,* $b^2(f_1, f_2, f_3)$, *obtained from the toroidal field component at* ***Bin # 1****. The vertical axis denotes the* b^2 at f_3, *corresponding to* $f_1 \pm f_2 = f_3$. *The large peaks indicate coupled frequencies associated with the onset of sawtooth crash.*

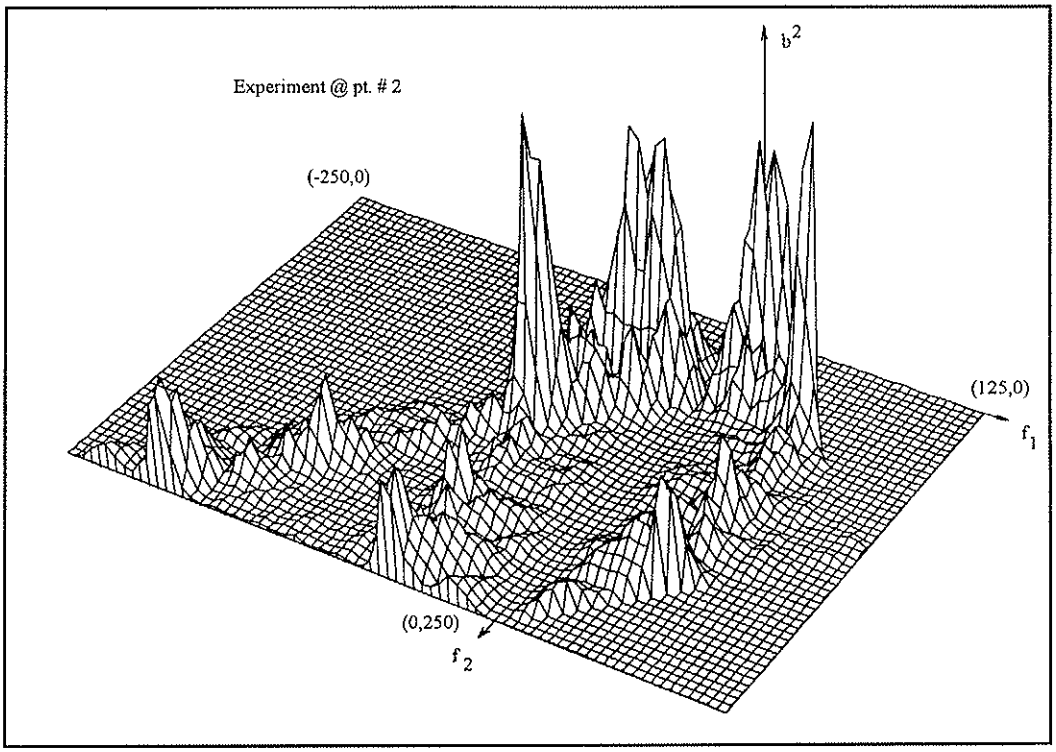

Figure V-5-11) *Frequency coupling. Bi-coherence,* $b^2(f_1, f_2, f_3)$, *obtained from the toroidal field component at* ***Bin # 2****. The vertical axis denotes the* b^2 at f_3, denotes the b^2, *corresponding to* $f_1 \pm f_2 = f_3$. *Frequencies associated with n=1 mode coupling (presumably m=0) is observed. The wavenumber couplings are shown in Fig. V-5-24.*

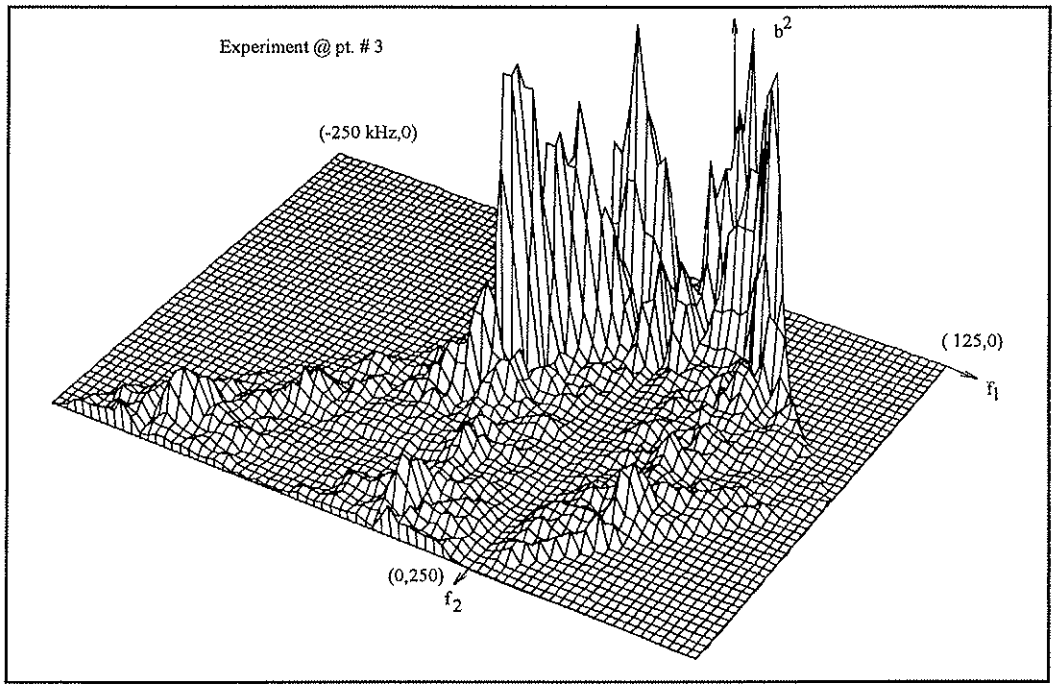

Figure V-5-12) *Frequency coupling. Bi-coherence,* $b^2(f_1, f_2, f_3)$*, obtained from the toroidal field component at* ***Bin # 3****. The vertical axis denotes the* b^2*, corresponding to* $f_1 \pm f_2 = f_3$ *. Broadband frequency coupling is observed.*

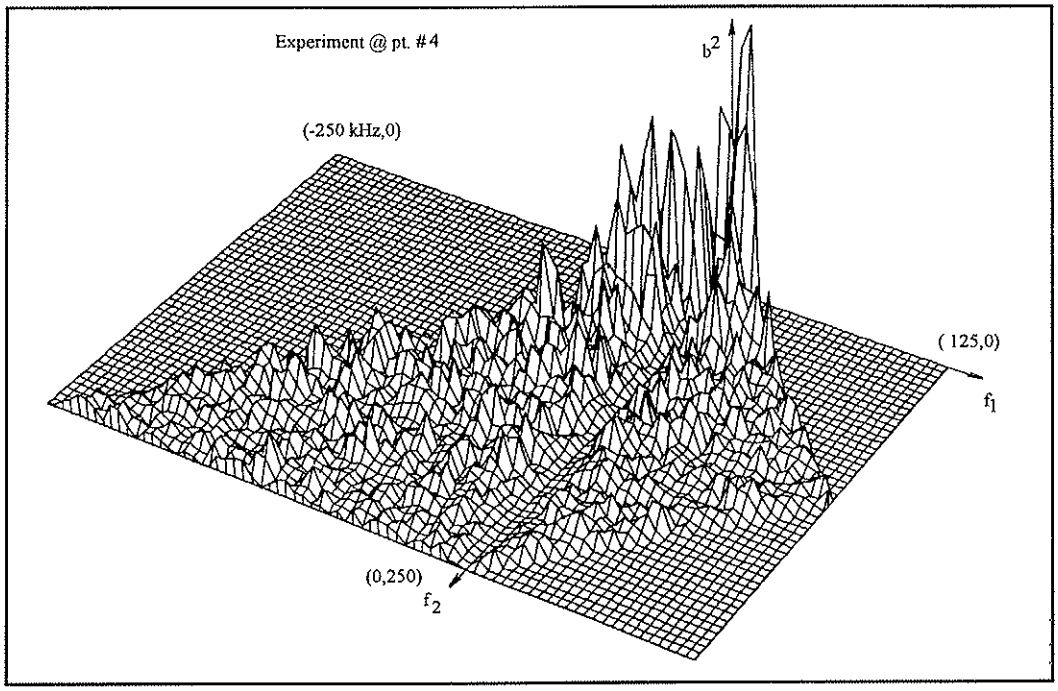

Figure V-5-13) *Frequency coupling. Bi-coherence,* $b^2(f_1, f_2, f_3)$, *obtained from the toroidal field component at* ***Bin # 4****. The vertical axis denotes the* b^2, corresponding to $f_1 \pm f_2 = f_3$. *Low frequency coupling is observed.*

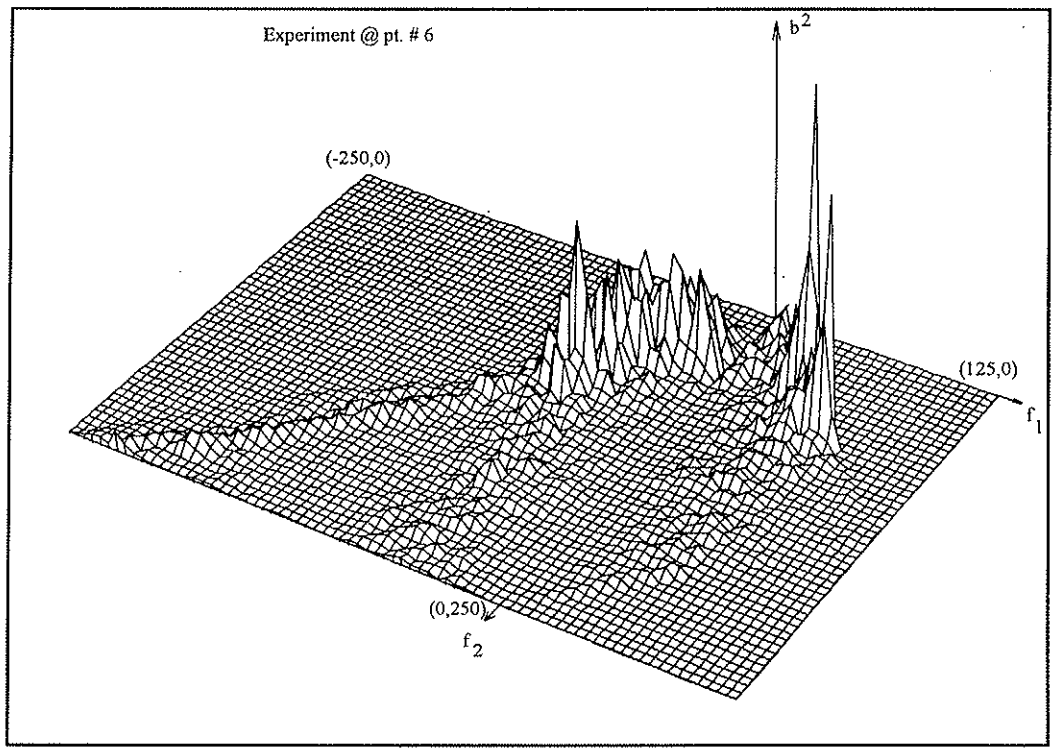

Figure V-5-14) *Frequency coupling. Bi-coherence,* $b^2(f_1, f_2, f_3)$, *obtained from the toroidal field component at* ***Bin # 6****. The vertical axis denotes the* b^2, *corresponding to* $f_1 \pm f_2 = f_3$. *Frequency coupling is small.*

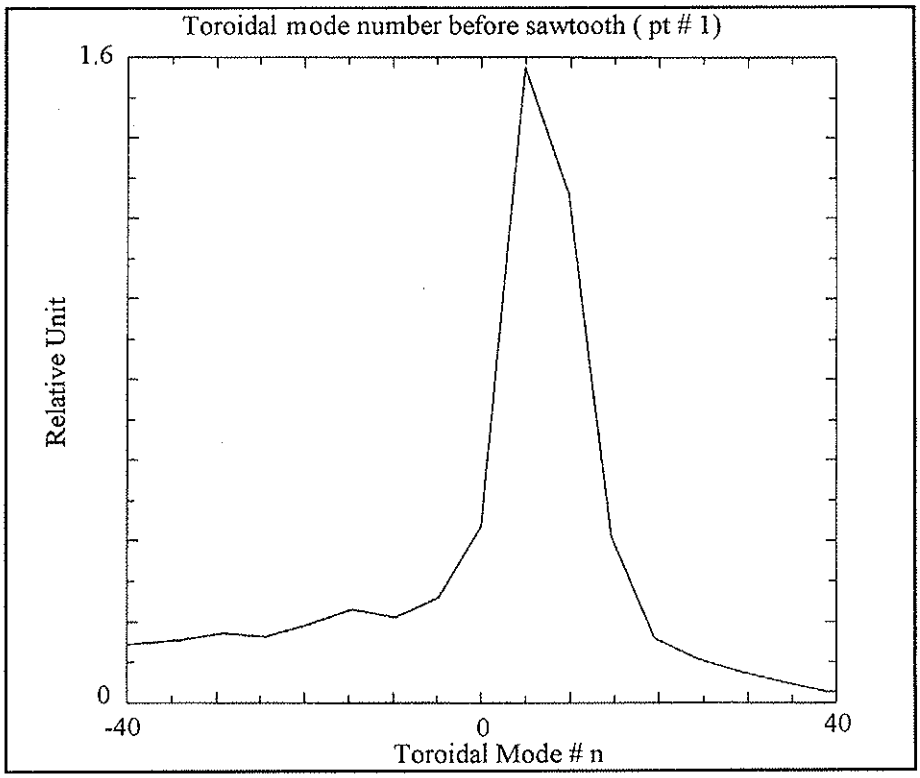

Figure V-5-15) Toroidal mode spectrum associated with **bin # 1** v.s. frequency. Peaking of n~5-8 is observed.

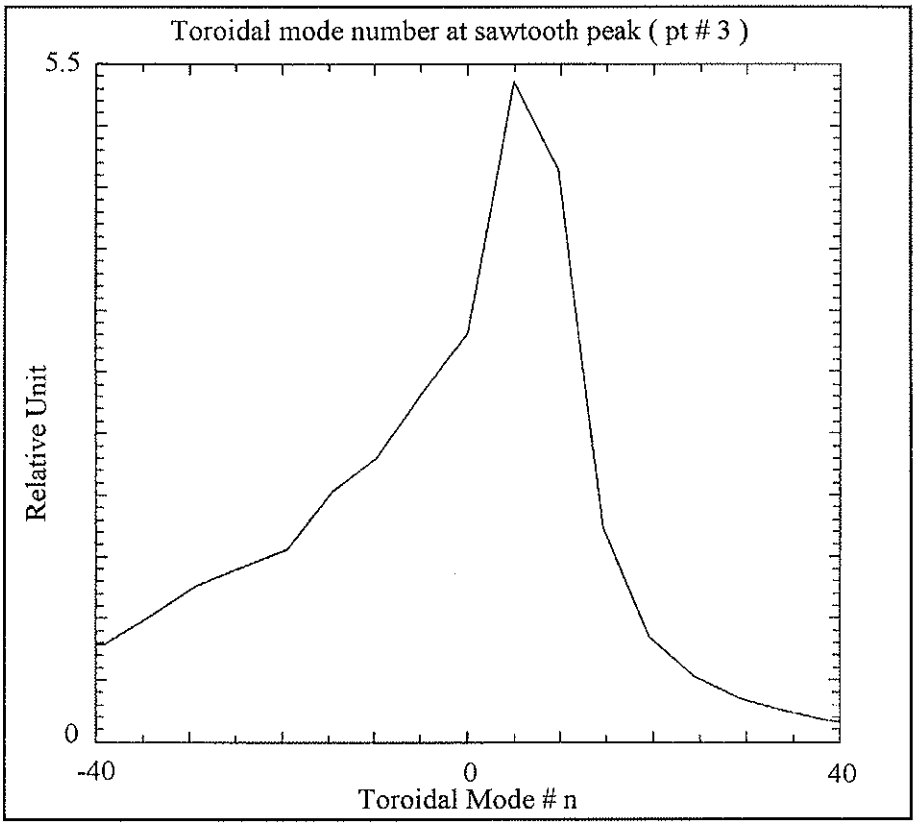

Figure V-5-16) Toroidal mode spectrum associated with **bin # 3** v.s. frequency. Broadening of k-spectrum at sawtooth crash time is observed.

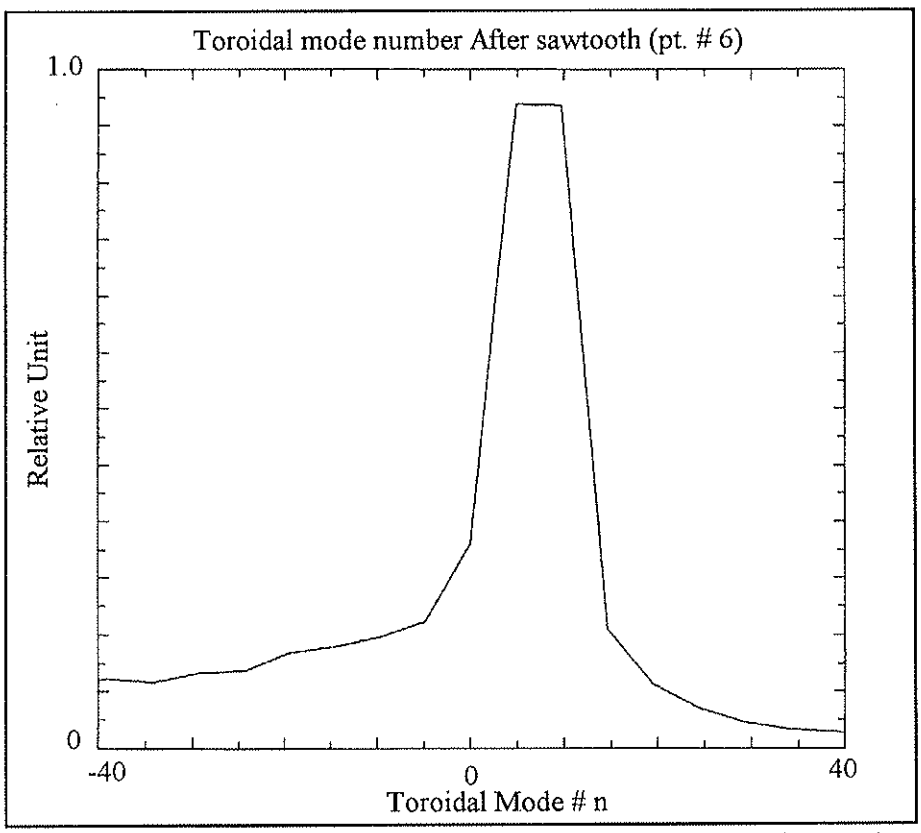

Figure V-5-17) Toroidal mode spectrum after sawtooth crash associated with **bin # 6** v.s. frequency is shown. Spectrum has narrowed.

V-5-3) Nonlinear Wavenumber Coupling

In this section, bispectral-analysis measurements in conjunction with power spectra and probability density functions are used to study the quantitative features of the nonlinear interactions which govern the energy redistribution and randomization process during sawteeth cycles. The experimental results, when compared with the same analysis performed on the data obtained from 3-D resistive MHD code, indicate that the basic nonlinear dynamics measured in the MST plasmas can be modeled by nonlinear resistive MHD computation.

Bispectral analysis and mode spectra presented in this thesis are the result of statistical analyses performed on 110 shots to study poloidal mode coupling, 404 shots for toroidal mode coupling and 256 independent 3-D MHD code runs for computational mode coupling.

(a) Poloidal Mode Coupling

The wavenumber and frequency spectra of the edge magnetic fluctuations have been presented earlier in this chapter. Note that the experimental conditions are the same for all shots in the ensemble (variations in plasma current is fixed within $\pm$ 3 kA, reversal parameter and pinch parameter are constant). The bin numbers are associated with a fixed percentage of a sawtooth period. The cross bi-coherence of

the non-reversed and the reversed part of the discharge, which are statistically independent, is chosen as an experimental estimation of statistical noise level, (~ 5%). This base line noise has been subtracted from the calculated bi-coherence.

Poloidal Bi-coherency at three different times in the sawtooth crash are presented in Figures (V-5-18)-(V-5-20). Shown in Figure (V-5-18) is a characteristic poloidal magnetic fluctuation bi-coherence spectrum, $b(m_1, m_2, m_3)$, in the early stage of sawtooth crash given by the (bin #1) of Figure V-5-3. The bi-coherency at the peak of the sawtooth crash (bin # 3) is given in Figure V-5-19. The bi-coherency during the relaxation phase (rise time) of the sawtooth (bin # 5) is shown in Figure V-5-20. The bicoherency results are presented in 3-D plots; the two horizontal axes represent m_1 , m_2 and the vertical axis corresponds to bi-coherence at values of m_3 given by $m_1 \pm m_2 = m_3$. We note that the bi-coherence shown in Figure V-5-20 has two dominant peaks, of comparable magnitude (Max. b^2 is 0.45), corresponding to $m_1 = m_2 = 1$, $m_3 = 2$, and $m_1 = -1$, $m_2 = 2$, $m_3 = 1$. The sign of the mode number indicate the sense of the rotation. There is also a small peak at slightly higher m values. The poloidal bi-coherence predicted by the MHD code is shown in Figure V-5-21 for direct comparison with the experiment. We note that the dominant peaks are identical with the experiment (shown in Fig. V-5-20), although peaks at higher mode numbers than $m_2 = 2$ cannot be resolved. As pointed out earlier, $|m| \leq 2$ had

been imposed in the code, but the finite number of Fourier component in conjunction with the windowing of the data has generated the fictitious peaks at these higher mode numbers. In both the experiment and the MHD model there is strong mode coupling between two |m| = 1 modes and an |m| = 2 mode. The direction of energy flow in k-space is not discernible from this analysis, although it has been predicted theoretically that unstable m = 1 modes would drive a stable m = 2 mode, which transfers energy to the small scale where it is dissipated [29].

The poloidal bi-coherence obtained from an array at one toroidal location includes contributions from all toroidal modes. This effect is more pronounced during the sawtooth crash when a large number of toroidal and poloidal modes exists. We find that during a sawtooth crash the nonlinear coupling changes dramatically. The data shown in Figure V-5-18 were obtained at the onset of the crash phase (time 1 in Figure V-5-3). The bi-coherence at the sawtooth crash is obtained from an ensemble average of sawteeth crashes of 110 different shots. There is a dramatic broadening in the number of modes involved in the nonlinear coupling. The dominant poloidal mode interaction is now coupling of two |m| = 2 modes to an |m| = 4 mode with the maximum b^2 of 0.42. The toroidal modes (see next section) now display strong nonlinear coupling over the entire range of resolvable n values from 1 to 32. Concurrent with the enhanced nonlinear interactions, we observe that the n-spectrum

of the fluctuation power is substantially broadened, as shown in the previous section, (similar broadening has been observed in TPE-1RM15 [30]). These results are consistent with the view that the broadened n spectrum arises from the nonlinear generation of high and low n modes, as opposed to generation from linear instabilities (for example arising from profile modification during the crash).

The bi-coherence at the peak sawtooth crash, (time 3 in Figure (V-5-3)) is shown in Figure (V-5-19). The dramatic broadening of the poloidal modes has subsided. The dominant interactions are now coupling of two $|m| = 1$ modes to an $|m| = 2$, ($m = -1$, $m = 2$) to $m = 1$ and ($m = -2$, $m = 2$) to $m = 0$ modes of comparable magnitudes with the maximum b^2 of 0.47. No information on energy cascading is available from this computation, since the bi-coherence presented is a snapshot measure of the sawtooth evolution.

It is safe to speculate from the bi-coherency snapshots that the nonlinear mode coupling is a result of a dual mode ("energy") cascading process, as computed by Holmes et al. [29]. The first process is coupling of $m = 1$ helical modes toward low and high n's generating global $m = 0$ perturbations, which are driven by $m = 1$ instabilities to large amplitudes (see next section on toroidal mode coupling), and back coupling to $m = 1$ modes to higher n's. The second process is the generation of large m and n modes.

During the crash phase of the sawtooth oscillation, (which is not modelled by the MHD computation employed here), the nonlinear couplings are strongly enhanced, simultaneous with broadening of the mode spectra.

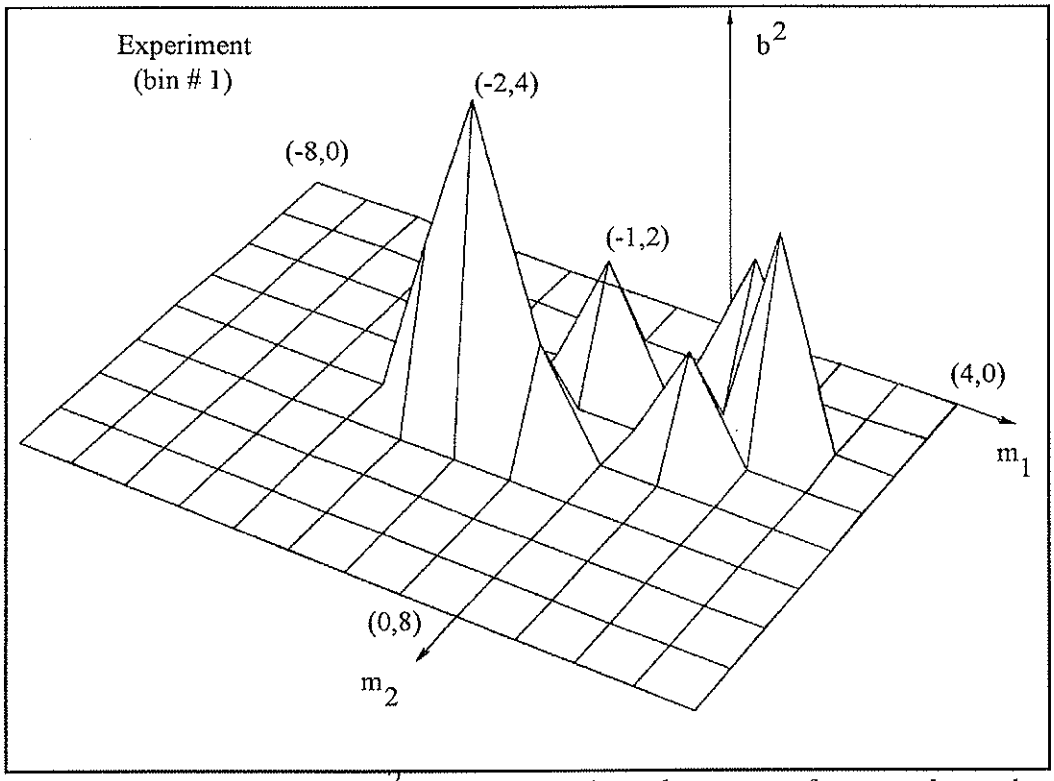

Fig V-5-18) Bi-coherence, $b^2(m_1, m_2, m_3)$ at the onset of sawtooth crash, obtained from the poloidal magnetic component from experiment. Max. b^2 is 0.52.

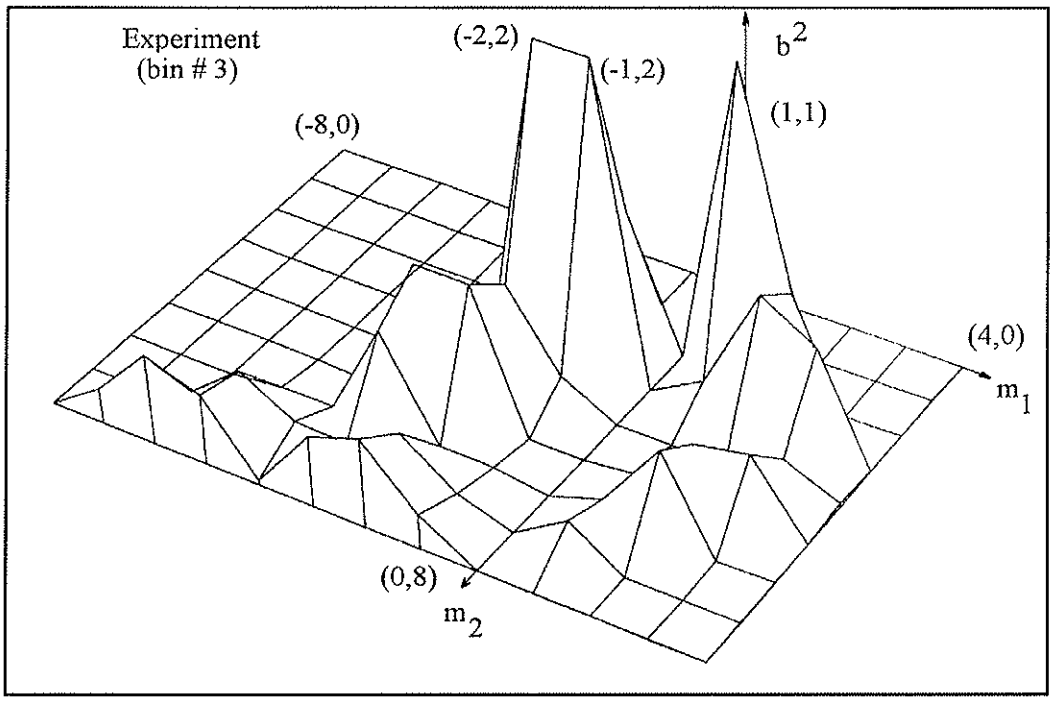

Figure V-5-19) Experimental bi-coherence at peak of sawtooth. Low poloidal mode couplings have been observed. Maximum b^2 is 0.47.

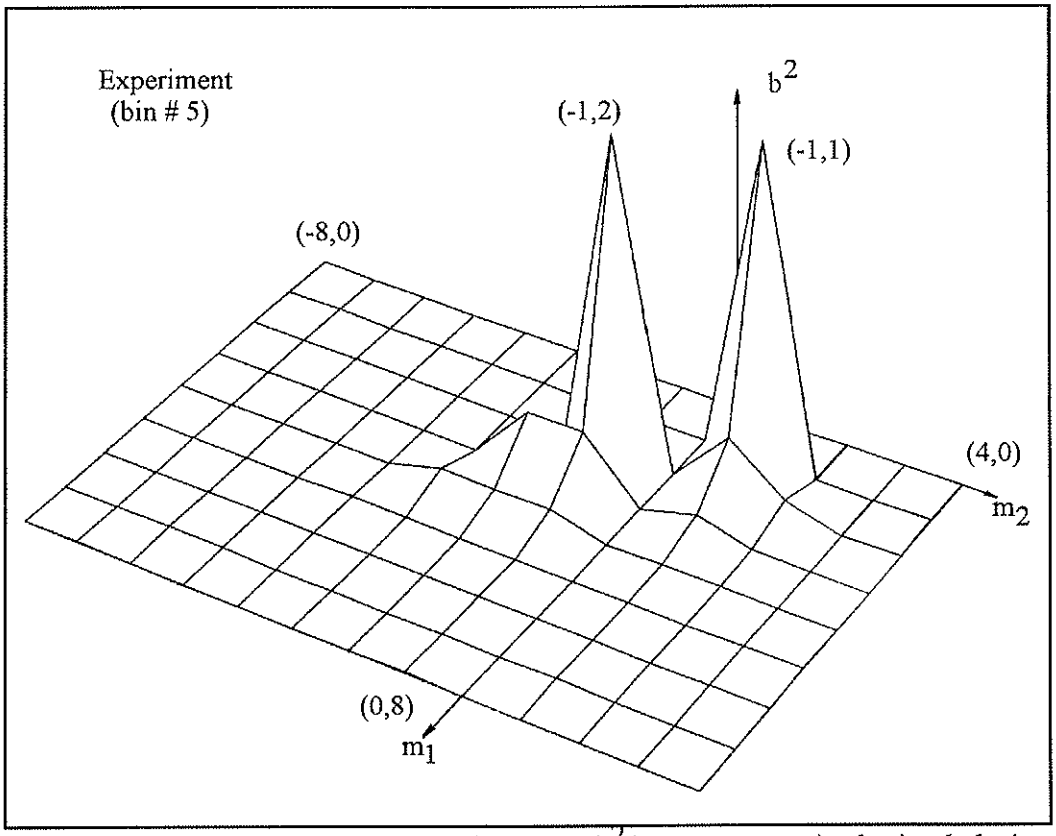

Figure V-5-20) Experimental bi-coherence, $b^2(m_1, m_2, m_3)$ obtained during sawtooth relaxation. Maximum peak is 0.45. b^2 is similar to MHD code results.

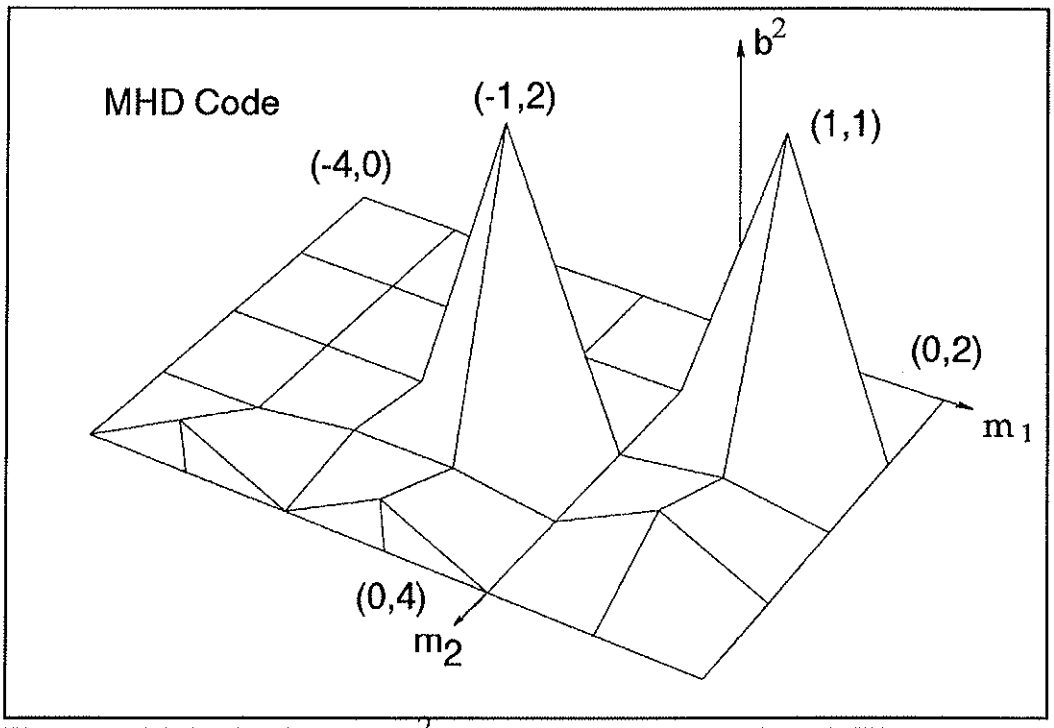

Figure V-5-21) Bi-coherence, $b^2(m_1, m_2, m_3)$ obtained from MHD code data. Max. $b^2 = 0.61$. MHD Results are similar to the experimental results, (Fig V-5-20).

Note that the peaks at |m|>2 are due to errors caused by finite Fourier components; the amplitudes of the main peaks are not affected by the errors of higher m's.

(b) Toroidal Mode Coupling

The coupling of toroidal modes obtained from the toroidal fixed coil array are displayed in Figures (V-5-22) through (V-5-31). The experimental bin number (5) is selected for comparison to MHD code results. Toroidal mode coupling involves a large number of modes. However, the experimental coupling is broader in n than theoretically predicted. This distinction is perhaps simply a feature of the different values of Lundquist number, S. One might expect that at the higher S values of the experiment, nonlinear energy transfer is enhanced and resistive energy dissipation is diminished. One feature which experiment and code share is that the dominant mode coupling occurs at intermediate n values. That is, n values of order unity are only weakly coupled to other modes and the coupling at n greater than 20 is also weak.

As shown in the previous section, interaction between adjacent instability modes (f_k, f_l) also generate a band of low-frequency fluctuations at $f_m = f_k - f_l$. Due to the fairly narrow band-width of the dominant helical instability modes (m =1, n = 5-8), the difference frequencies ($f_k - f_l$) produced via the interaction of any two modes in the band will be low (e.g., frequency coupling in Fig. V-5-10 does show f~ 1-10 kHz coupled modes due to difference wave-numbers). Thus, the modes with n = 5-8, which we know are coupled from observed constructive interference, do not couple through an n = 1 mode (except during a sawtooth crash, as discussed below).

For example, the n = 5 and n = 6 couple through n = 11 with higher probability than through the n = 1. The n = 11 can then couple to other modes, and so on. However, the coupling does not proceed strongly to n values as high as 32 (toroidal coherence length of n > 32 is shorter than the coil-spacing).

Figures V-5-22 through V-5-31 represent the nonlinear toroidal mode coupling throughout a sawtooth crash and formation cycle. The numbers given on these graphs are associated with the *bin number* of the analyzed data as shown in Figure V-5-3. The small amplitude (weak contours) in the bi-coherence plots indicate that interactions between n_k and n_l generate a weak mode at $n_k \pm n_l = n_m$. It is useful to note that any pair of fluctuations (n_k , n_l) with the same difference/sum in wavenumber can contribute to a particular fluctuation. In addition, due to the random initiation of instabilities in laboratory plasmas, the instantaneous spectrum of interacting waves may not always contain the same pair, and the relative amplitudes of any given pair will change from instant to instant and from shot to shot. Therefore, the amplitude, wavenumber, frequency and phase of the dominant low frequency (m = 1, n = 5-8) fluctuations produced by multiple interactions at any instant will vary in a random manner. The result is a broad band of coupled modes with smaller bi-coherence amplitude. To insure reproducibility from shot to shot, I have applied digital filters to 256 point data records to minimize the superimposed incoherent

signals. I have also limited the phase variations of the selected data by restricting the cross phase to ±2 degrees from shot to shot.

The 3-D plots are accompanied by contour plots to enhance the visualization of the basic interactions involved during the sawtooth oscillation. Shown in each contour plot are lines of constant $n_k + n_l = n_m$ corresponding to the basic interaction mechanism. Values of bi-coherency which fall along these lines can be interpreted as representing interactions between various pairs of waves with a sum toroidal mode equal to n_m (see Fig. V-5-7). However, the sign of the mode number indicates the sense of the rotation. The difference-mode interactions of the form $n_k - n_l = n_m$ are mapped into the negative (n_k, n_l) octant. Thus, the time evolution of $b^2(n_k, n_l)$ represented by different snapshots given at various bin numbers can indicate direction of the mode cascading. Spectral broadening based on two-point correlation measurements and power spectra has already confirmed the existence of nonlinear mode coupling (see section V-5-2).

The bi-coherency plots in Figure V-5-22 and V-5-23 provide a spectral map of the nonlinear interactions invoked at the onset of sawtooth crash (bin # 1). At this time there is a dramatic broadening in the number of helical modes involved in the nonlinear coupling. The toroidal modes display strong nonlinear coupling over the entire range of resolvable n values, from 1 to 32. Concurrent with the enhanced

nonlinear interactions, we observe that the n-spectrum of the fluctuation power is substantially broadened (see the toroidal mode spectra measurement in Section V-4.3). The dominant poloidal interaction (Fig. V-5-18) is now coupling of two $|m| = 2$ modes to an $m = |4|$ mode.

The bi-coherency plot in Figure (V-5-24) provides a contour map of nonlinear interactions involved at the mid-crash region (bin # 2). We observe a significant shift in toroidal mode interactions mediated by n = 1 coupling. Interactions between adjacent instability modes (n_k, n_l) also generate a band of low toroidal mode fluctuations via difference interactions such that $n_k - n_l = n_m$. The strong coupling of the m=1 helical modes by the m = 0, n = 1 (poloidal mode number m=0 is a speculation from the frequency coupling given in Fig. V-5-11) are driven to large amplitudes associated with bin # 3.

The bi-coherency plot at the peak of the sawtooth (bin # 3) is shown in Figure V-5-25. The back coupling of m = 0, n = 1 modes generated at bin # 2 time with large n modes redistributes the mode spectra among the m = 1-2 helical modes. The toroidal modes display strong nonlinear coupling over the entire range of resolvable n values with highest peaks at intermediate n modes.

The 3-D Fig. (V-5-26) and its contour plot (Fig. V-5-27) show the toroidal mode coupling as sawtooth recovery proceeds. We note that the m = 1 helical modes

grow and the nonlinearly generated toroidal modes are concentrated in the intermediate n's (schematic diagram (V-5-7)).

Coupling of toroidal modes (Fig. V-5-28) of bin # 5 are compared with the MHD code results (Fig. V-5-29). Toroidal mode coupling involves a large number of modes. However, the experimental coupling is broader in n than theoretically predicted. One feature which the experiment and code share is that the dominant mode coupling occurs at intermediate n values.

The 3-D figure (Fig. V-5-30) and its contour plot (Fig. V-5-31) present the bi-coherency plot of the toroidal mode coupling at the zero slope section of the sawtooth relaxation region (bin # 6). The narrow contour width in the intermediate mode coupling region indicates that only the dominant instability modes in the spectrum are interacting to produce high toroidal modes ($n > 11$). These modes presumably are the result of additive $m = 1$ helical modes, initiated by the nonlinear generation of stable $m = 2$ modes (the amplitude of the $m = 2$ mode does not grow as shown by its time evolution (Fig. V-4-10)).

In summary, I have measured directly the three-wave nonlinear coupling of magnetic fluctuations which are identified as tearing fluctuations. There is good agreement between the measurements of the k-space couplings and predictions of nonlinear MHD computation. The measured poloidal modes in the experiment

involves two |m| = 1 modes coupling to an |m| = 2 mode. Toroidal mode number coupling is much broader, involving tens of modes. These measurements add credibility to the nonlinear MHD theory used to describe magnetic reconnection in tokamaks and RFPs.

During the crash phase of the sawtooth oscillation, which is not modelled by the MHD computation employed here, the nonlinear couplings are strongly enhanced, simultaneous with broadening of the mode spectra. The rapid process of m = 1 spectral broadening toward large n is observed (bi-coherency at bin # 6) followed by the cyclic process of simultaneous broadening of the poloidal and toroidal mode spectra (bin # 1). However, the broadening of the spectrum is delayed by an unpredictable time until the next sawtooth crash (timing between sawtooth oscillations are not constant). The m = 1 spectrum is strongly affected by nonlinear interaction with the (m = 0,n = 1) mode during the crash (as seen in Fig. V-5-24). During this time we speculate the current profiles are steep and this causes the neighboring (m = 1, n = n_1) and (m = 1, n = n_1 + 1) modes to beat together to drive (m = 0, n = 1) and (m = 2, n = $2n_1$ +1) modes. The (m = 0, n = 1) mode back couples with the (m = 1, n = n_1 + 1) to drive (m = 1, n = n_1 + 2) resulting in the m = 1 spectrum broadening at peak sawtooth (bin # 3). Consequently, these high toroidal modes couple to form intermediate coherent modes (n = 6 - 11) as shown

by the coherency of (bin # 4). This cyclic process continues by bin # 5 results.

This is consistent with nonlinear coupling being the source of generation of spectral broadening during a crash (although bi-spectral analysis does not indicate causality).

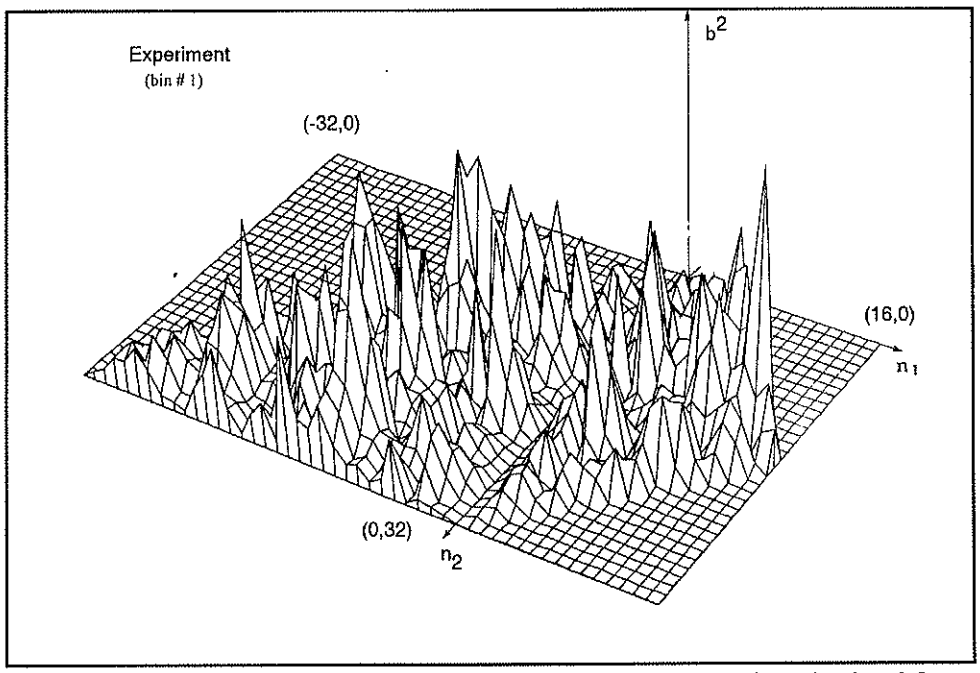

Figure V-5-22) Bi-coherence, $b(n_1,n_2,n_3)$, of toroidal modes obtained from the toroidal magnetic field component at the onset of a sawtooth. Maximum b^2 is 0.42.

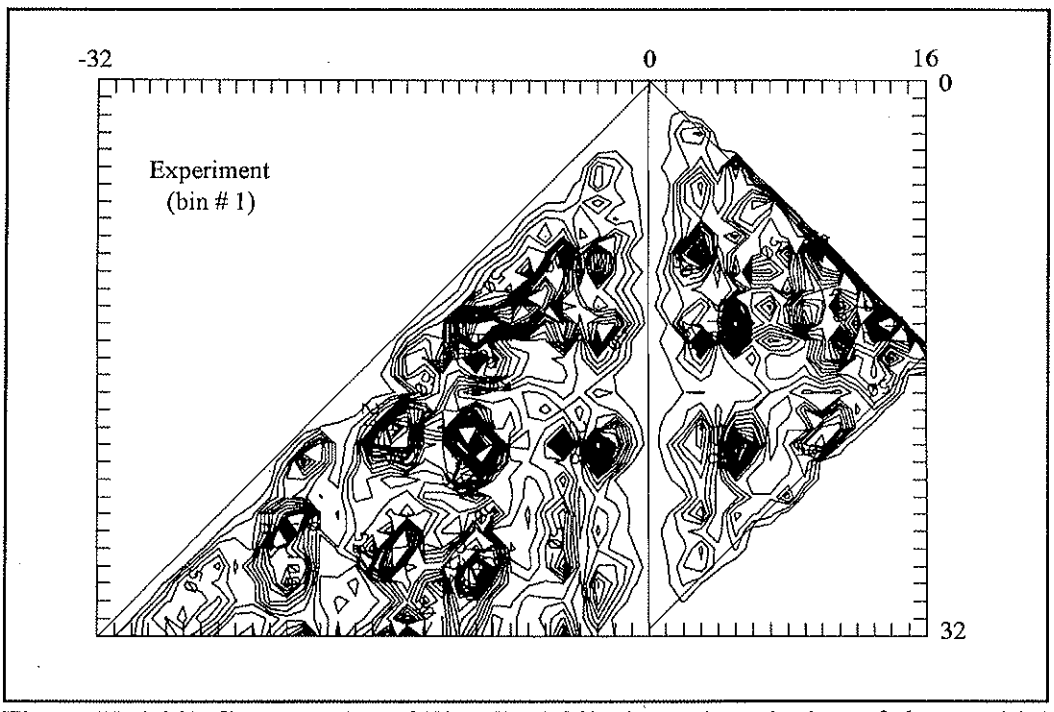

Figure V-5-23) Contour plot of Fig. (V-5-22) shows broadening of the toroidal mode spectrum.

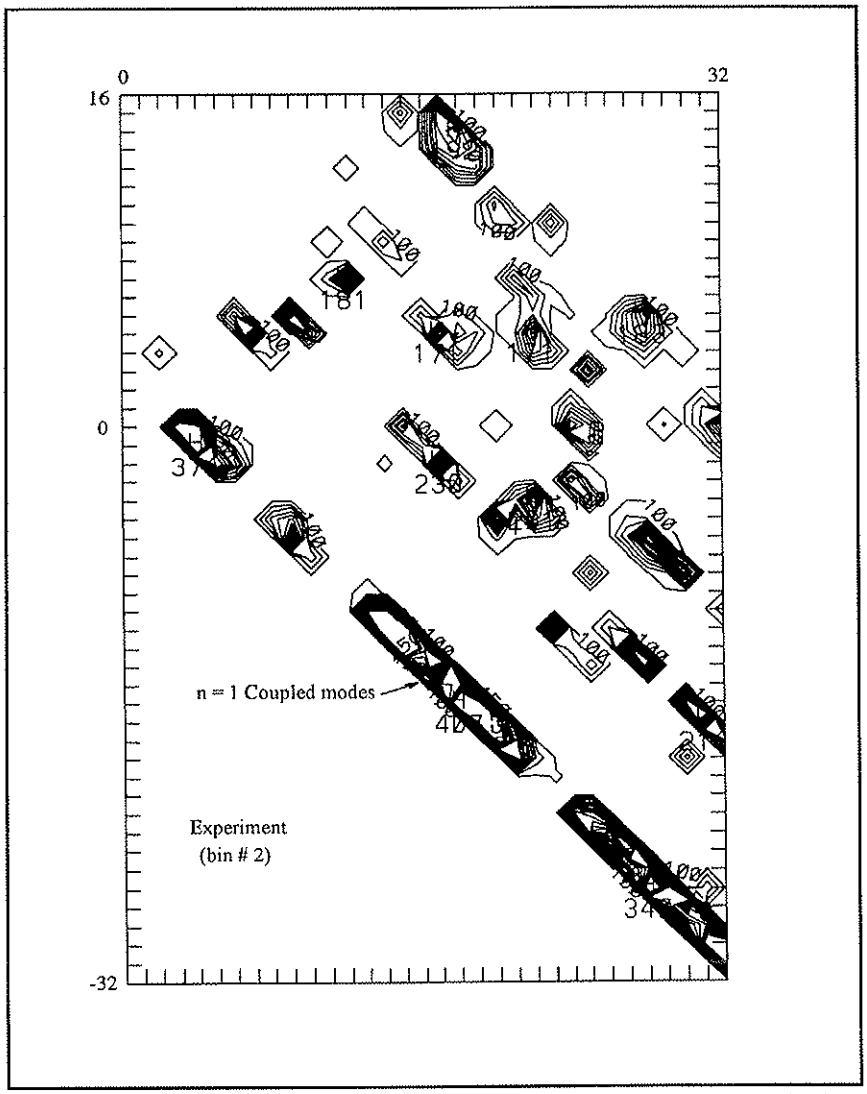

Figure V-5-24) Strong n=1 coupled modes are observed during the crash phase. Maximum b^2 is 0.4.

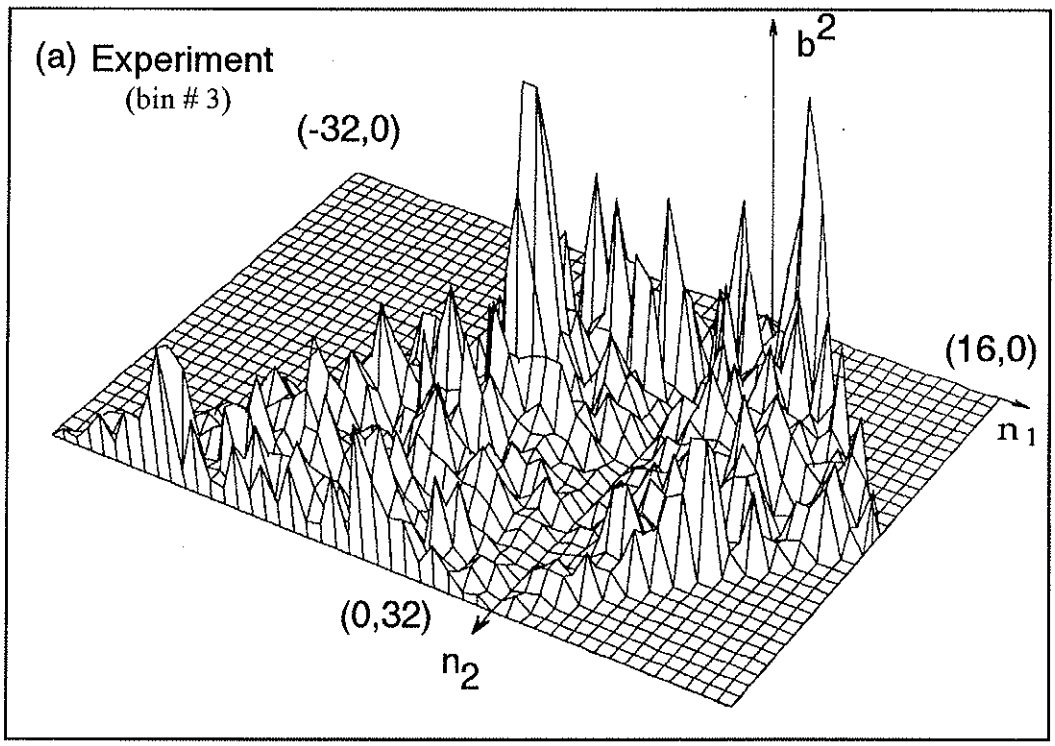

Figure V-5-25) Bi-coherency at the peak of the sawtooth (bin # 3) shows a broad coupled spectrum. Maximum b^2 is 0.43.

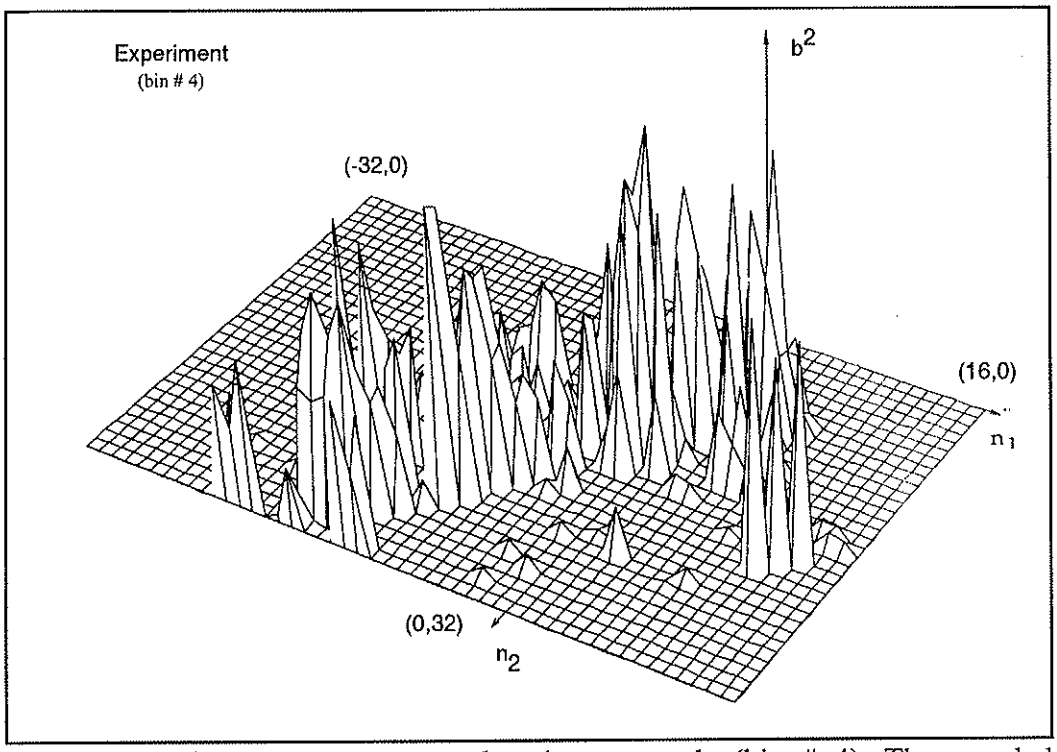

Figure V-5-26) Bi-coherency as relaxation proceeds (bin # 4). The coupled modes exhibit intermediate n-coupling.

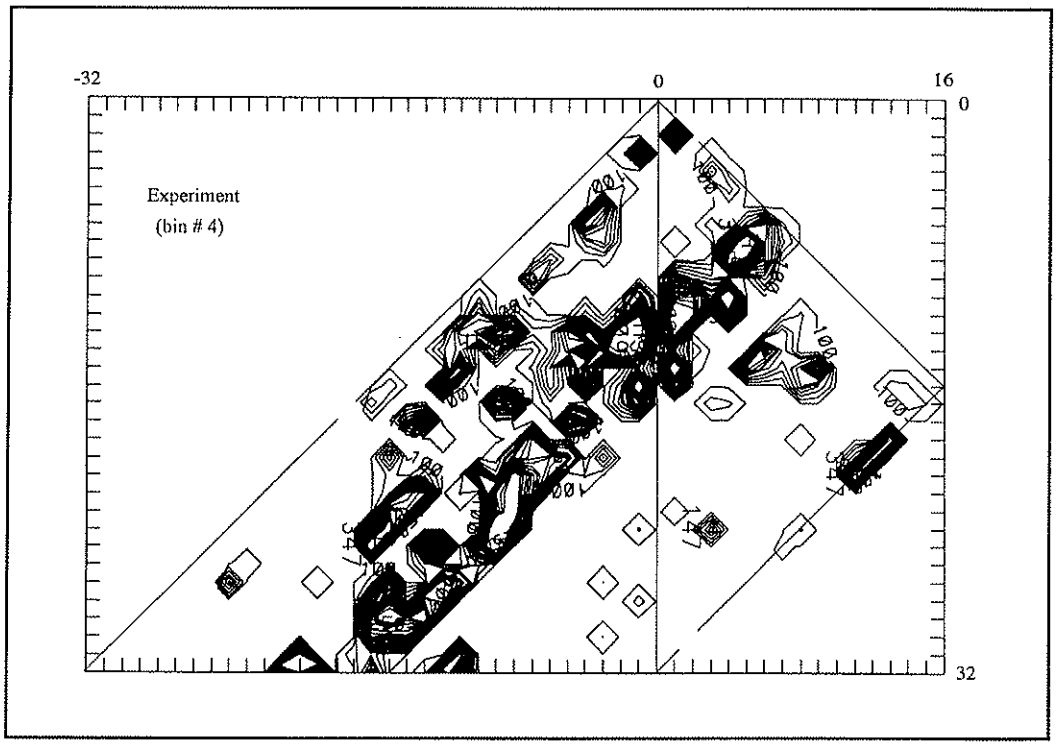

Figure V-5-27) Contour plot of Fig. (V-5-26) clearly shows the mode coupling range. Maximum b^2 is 0.37.

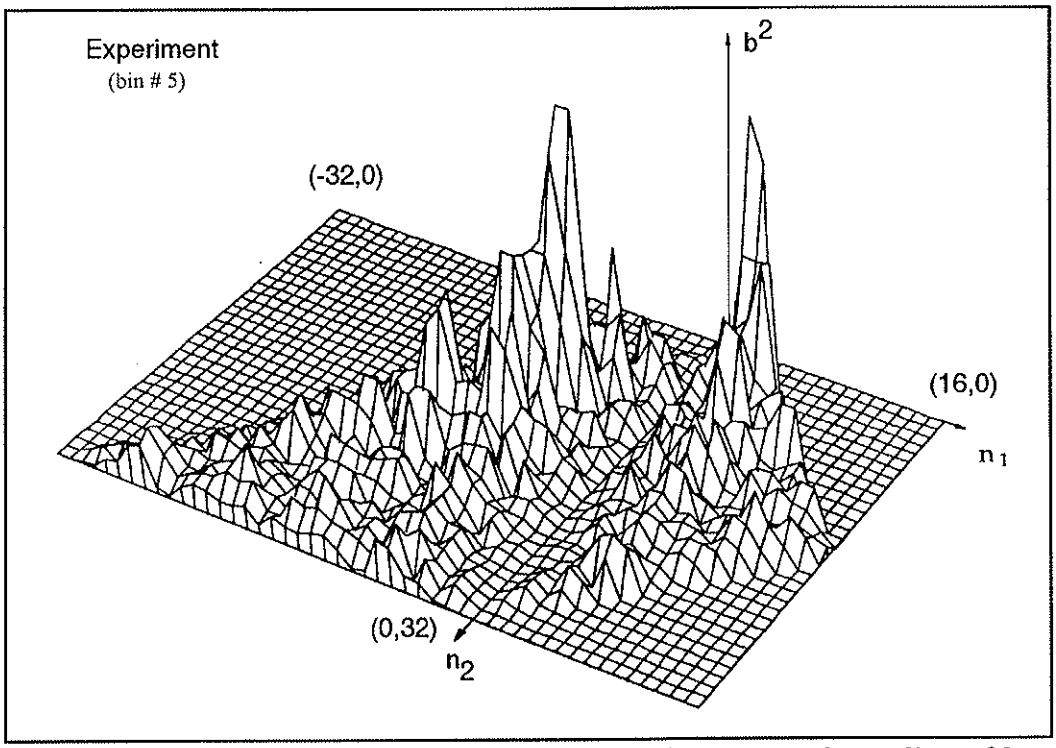

Figure V-5-28) Toroidal bi-coherency at bin # 5. Concentrated coupling of low mode numbers are observed. Maximum b^2 is 0.45.

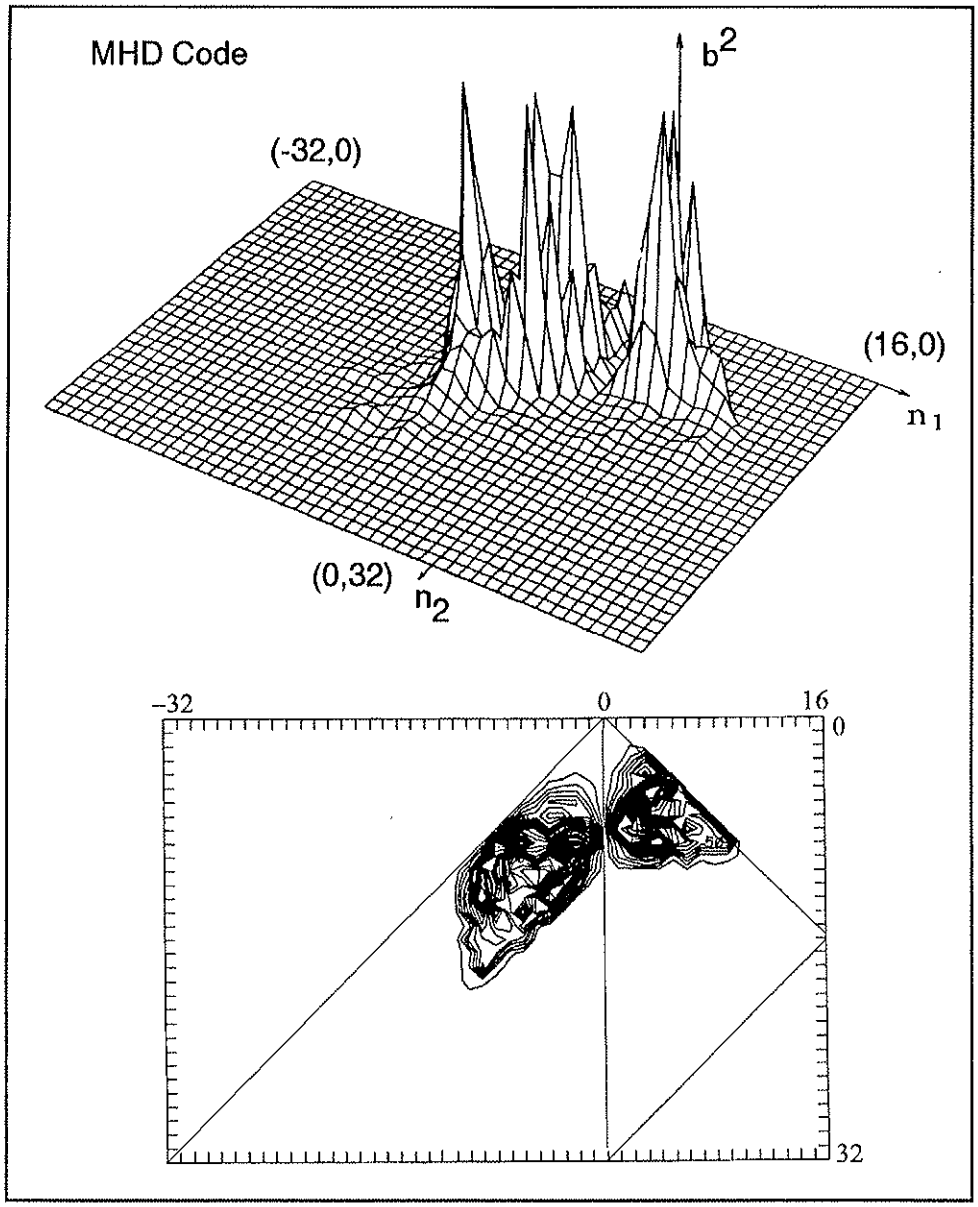

Figure V-5-29) Bi-coherency of MHD code data. We observe "similar" characteristics as bin # 5 of the experiment. Maximum b^2 is 0.61.

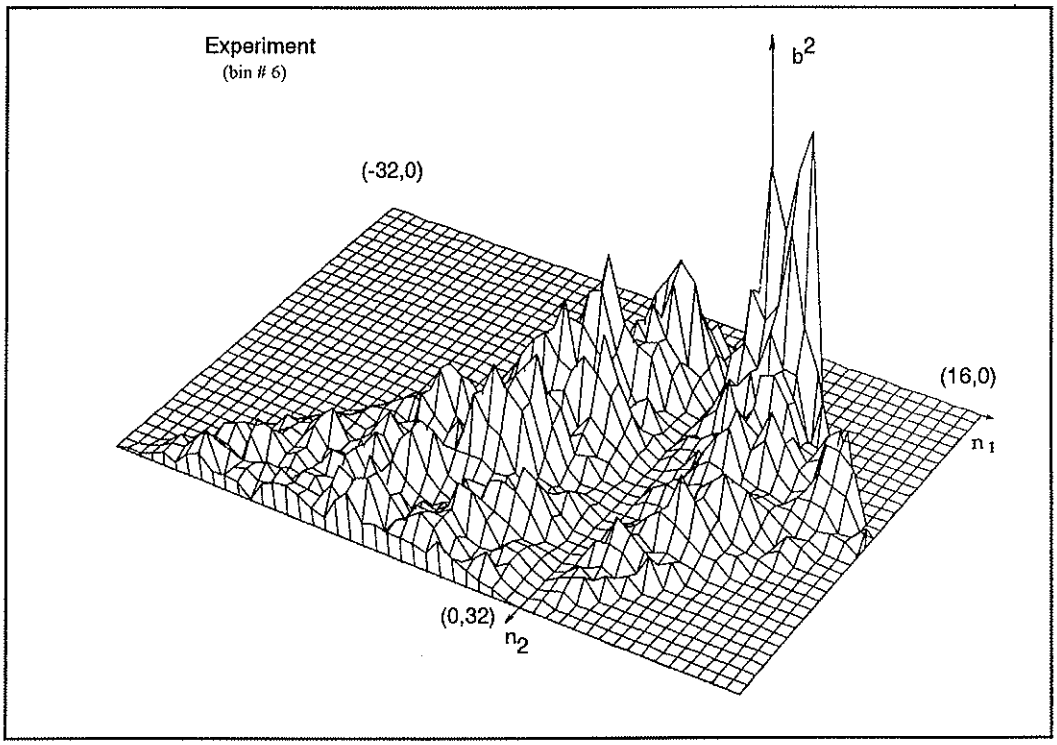

Figure V-5-30) Bi-coherency at zero slope of sawtooth formation. We observe order unity mode coupling. Maximum b^2 is 0.45.

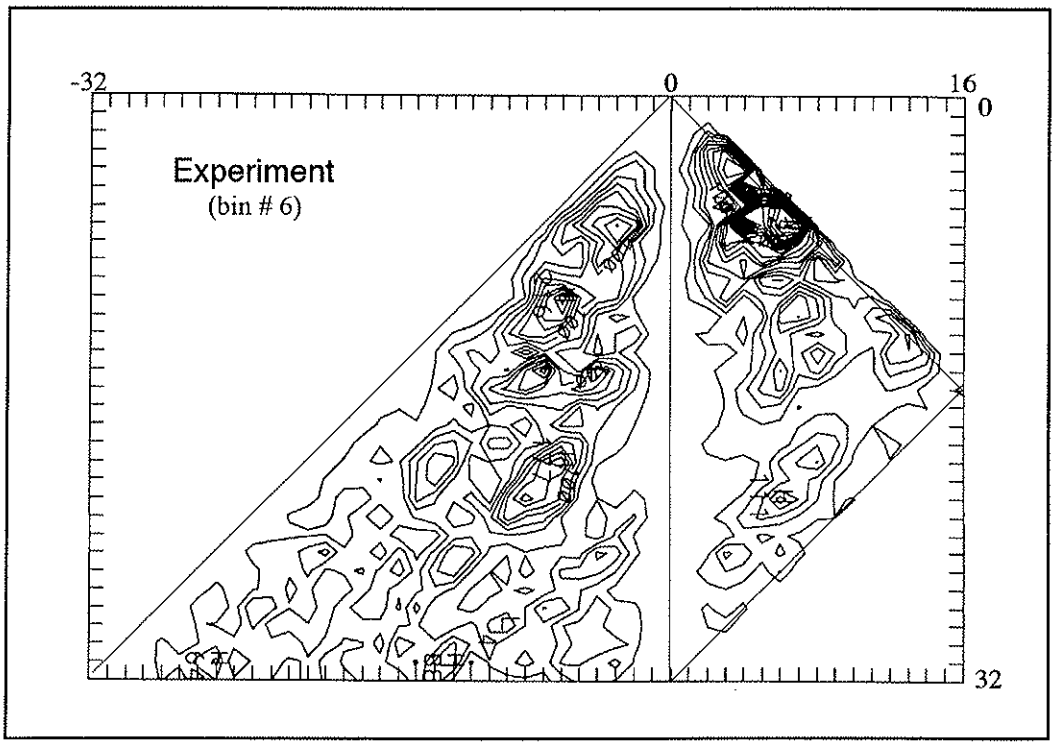

Figure V-5-31) Contour plot of Fig. (V-5-30) shows n-coupling of order unity.

V-6) Experimental Measurement of Transfer Functions and Energy Cascading

In this section the initial results of energy cascading associated with three-wave toroidal mode coupling are presented. I have applied the method described in Chapter IV to study the nonlinear evolution of the toroidal magnetic fluctuation spectra at the edge plasma of the MST reversed field pinch. Magnetic fluctuation data at 64 equally spaced toroidal locations have been used to calculate the n-spectra. The growth rate and coupling coefficient of the toroidal mode spectra have been computed.

The amplitude variation due to nonlinear coupling may be expressed in terms of the measured power spectra and the bispectrum at three different times. The purpose of this section is to model the time evolution of the toroidal mode spectra as a simple system described by a set of sources ("input," initial n-spectra), the response ("output," subsequent n-spectra) and transfer functions ("black box"). We can model the "black box" by an appropriate network, consisting of linear and quadratic nonlinear terms, as described in Section IV-5. To test the validity of the computed linear and quadratic transfer functions, I have applied the computed transfer functions to the second n-spectra to predict the third toroidal mode spectra. Subsequently, the modeled spectra is compared to the measured n-spectra.

Spatial Fourier transforms of 1200 ensembles (400 shots 3 consecutive data records are used to compute the transfer functions. The " input " magnetic fluctuations **b** (ϕ , t_o), the " output-one " **b** (ϕ , t_1), and " output-two " **b** (ϕ , t_2) are used to form the experimental n-spectra (Figures V-6-1 and V-6-2). The 160 microsecond time difference between t_o and t_1 is chosen such that the nonlinearities stay small. The cross-coherency (i.e. spatial phase) between modes at t_o and t_1, which represent the coherent fractional power of the "output" with respect to the "input" is shown in Fig. V-6-3. The linear transfer function shown in Fig. V-6-4 can account for the high coherency between the "input" and "output" at moderate toroidal modes, n ~5-10 (i.e. they are not driven by other modes in this case). Ritz et al. have applied this method to estimate the temporal evolution of frequency spectra, whereas I am applying his method in the spatial Fourier domain. The transfer functions describing the temporal evolution of toroidal mode spectra due to a linear mechanism (growth rate, dispersion) and due to three wave coupling are given below.

The linear transfer function is

$$L_p = \frac{\langle Y_p X_p^* \rangle - \sum_{p_1 \geq p_2} Q_p^{p_1,p_2} \langle X_p^* X_{p_1} X_{p_2} \rangle - \langle \epsilon_p X_p^* \rangle}{X_p X_p^*}$$

and quadratic transfer function is

$$Q_p^{p_1 p_2} = \frac{\langle Y_p X_{p_1}{}^* X_{p_2}{}^* \rangle - L_p \langle X_p X_{p_1}^* X_{p_2}^* \rangle - \langle \epsilon_p X_{p_1}{}^* X_{p_2}{}^* \rangle}{\langle |X_{p_1} X_{p_2}|^2 \rangle}$$

as described in Chapter (IV) where Y_p is spatial Fourier transform of the "output", **b** (ϕ , t_1) and X_p is the spatial Fourier transform of the "input", **b** (ϕ , t_o).

The second term in the above two equations can be interpreted as corrections due to the nonlinear characteristic of the input magnetic fluctuation n-spectrum. Figure V-6-4 presents the computed linear transfer function. The quadratic transfer function is given in Figure V-6-5.

To test the validity of the computed transfer function computation, I have carried out a computer modeling of the toroidal mode spectrum at time slice (3). This time is chosen to be equal to the time between the input and output-one, (160 microseconds). I have then applied the computed linear and quadratic transfer functions to the non-Gaussian "output-one" to model the "output-two". The results are shown in Figure V-6-6. Actual n-spectra measured at time slice (3) are shown in Fig. V-6-7.

Although the predicted low mode numbers were in good agreement with the

experimental results, the prediction of the high mode numbers have been difficult (~ 40% error). This error can be substantially reduced if the number of realizations is increased to greater than 3000, and (or) the number of coils increased from 64 to 128 or 256 (improved modal resolution). Note, the n-spectra has been determined from the 1-D array. Short wavelength (high mode numbers) are multi-helices and could contribute to the mismatch of the model and experiment.

In summary, I have demonstrated the usefulness of the estimation of the linear and nonlinear transfer functions to predict the time evolution of the edge toroidal mode spectra.

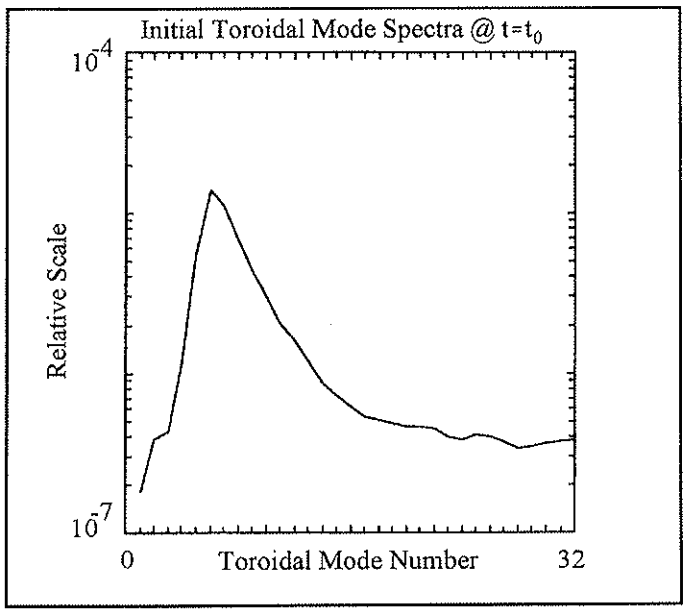

Figure V-6-1) Initial toroidal mode spectrum at t_o (arbitrary time during the flat top) is shown.

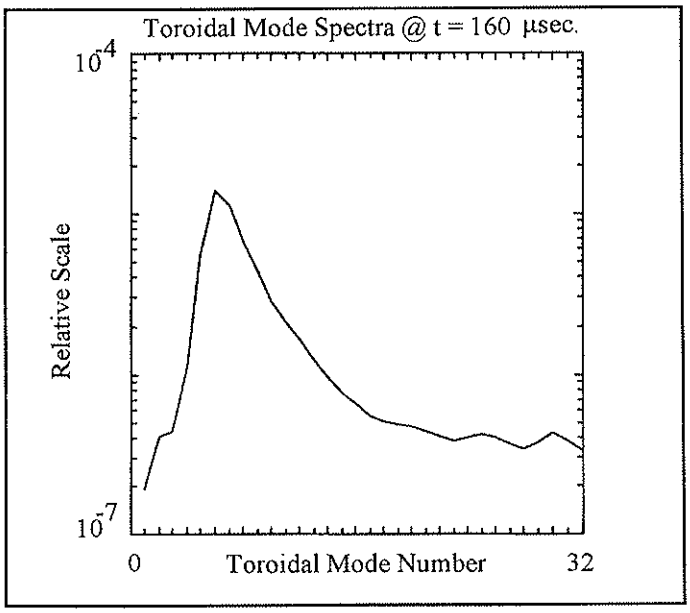

Figure V-6-2) Toroidal mode spectrum at $t_1 = t_o +$ 160 μsec is shown.

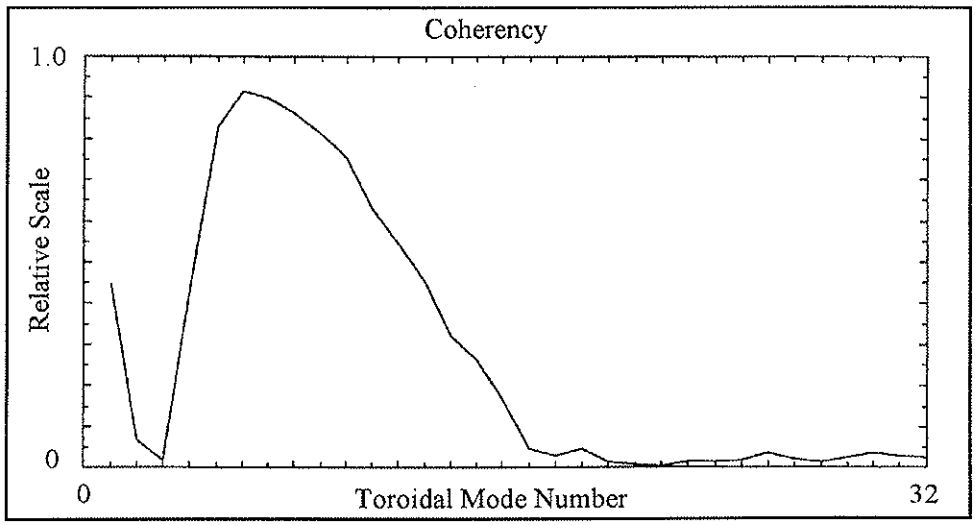

Figure V-6-3) Spatial cross-coherency of "input" and "output-1" reveals that high coherence modes (n ~ 5-8) persist during 160 μsec interval.

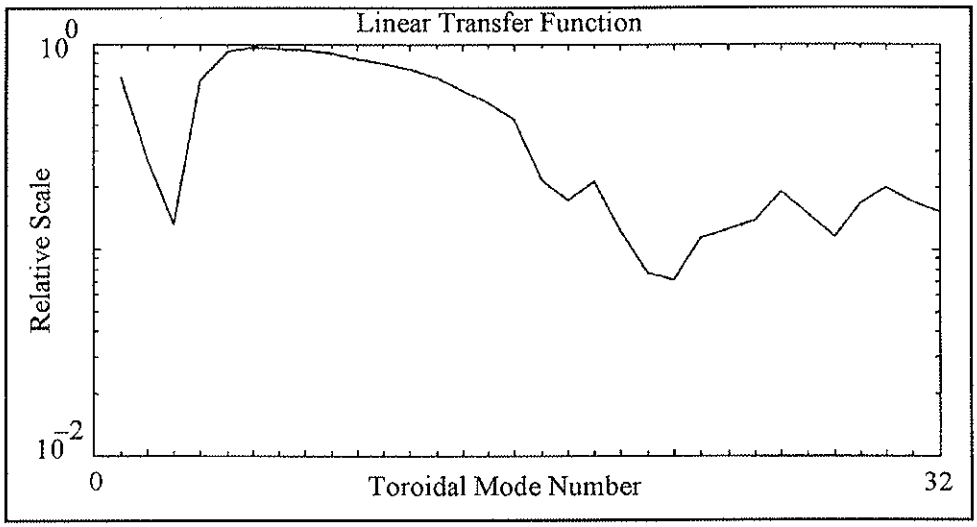

Figure V-6-4) Computed Linear transfer function shows that the time evolution of n ~ 5-8 modes can be modeled by a linear system.

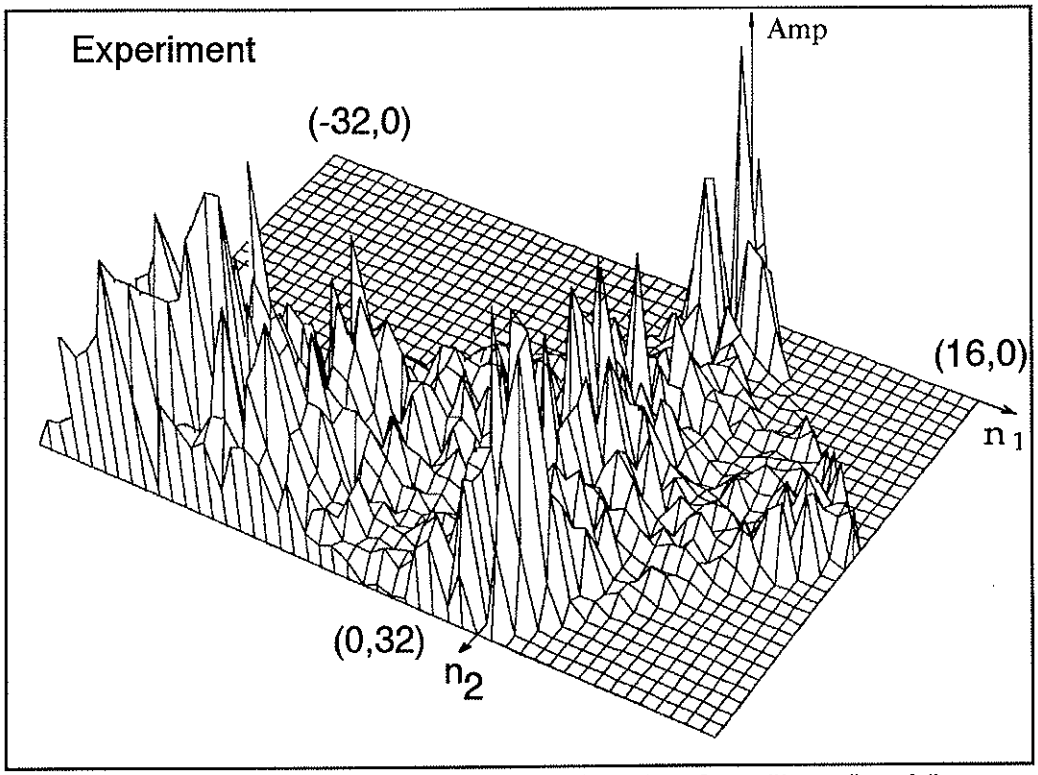

Figure V-6-5) Computed quadratic transfer function from "input" and "output-1."

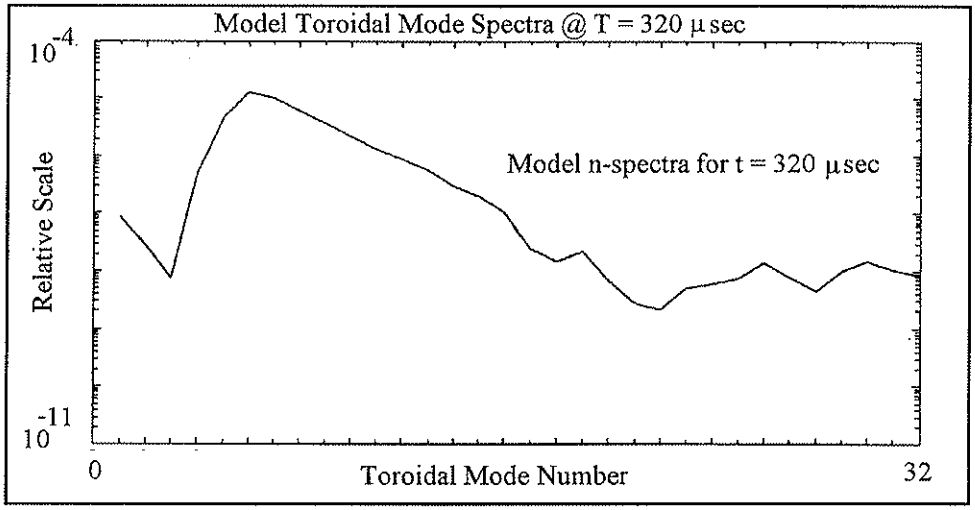

Figure V-6-6) Modeled toroidal mode spectra by applying the linear and quadratic transfer functions to "output-1."

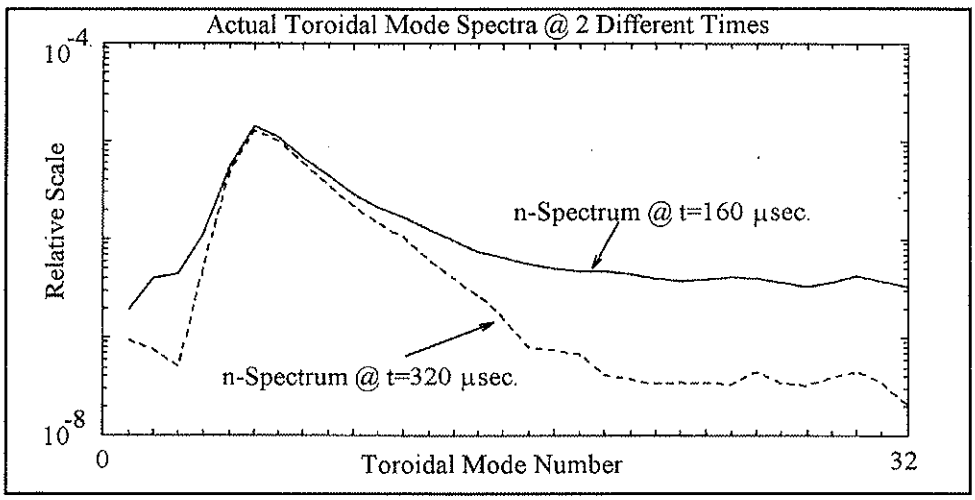

Figure V-6-7) Actual toroidal mode spectrum of "output-1" and "output-2." Rapid change in time evolution of high mode numbers are observed.

V-7) Correlation of Magnetic and Electrostatic Fluctuations

In this section, the detailed results of the cross correlation measurement of the magnetic fluctuations with ion saturation current fluctuations are given. I will show the differences in the mode number structure of the electrostatic versus the radial magnetic fluctuations at low frequencies.

To the extent that magnetic field lines are frozen into the plasma, a fluctuating radial density convection is accompanied by radial magnetic fluctuations. As described in Chapter III, I have constructed a multi-purpose movable forked probe which can simultaneously measure ion saturation current fluctuations (J_{satl}) and radial magnetic fluctuations (b_r) at almost the same location (~ 0.5 cm separation). Ion saturation current fluctuations are taken to be a reasonable measure of density fluctuations. Magnetic and electrostatic data were taken at 7 cm from the conducting wall where the error fields from the port hole are small. The measured cross-correlation between two spatially separated radial coils, $<b_r , b_r>$, as well as two fluctuating ion saturation current $<J_{satl} , J_{satl}>$ are high, but the correlation between electrostatic and magnetic fluctuations, $<J_{satl} , b_r>$ are only slight, (Figure V-7-1). The coherence (γ^2) between b_r and J_{satl} peaks near the tearing mode frequencies. Thus, a significant fraction of the measured electrostatic fluctuations may arise from

sources other than radial convection with the magnetic field. The correlations in the radial magnetic turbulence are distinct from those of the electrostatic turbulence. Thus, the character of electrostatic turbulence remains almost completely undetermined by the magnetic fluctuation measurements presented in this thesis and other experiments are necessary to determine the underlying physics.

The two-point correlation method discussed in Chapter IV has been used to estimate the power weighted toroidal mode number spectrum of electrostatic fluctuations. The forked probe was aligned in the direction of equilibrium toroidal field to simultaneously measure the spatial turbulent time signals. In comparison to the toroidal magnetic mode structure, the electrostatic n-spectrum is broadband and turbulent. Typical power spectra, shown in Figure V-7-2 peak at low frequencies and thereafter fall monotonically with frequency. At low frequencies ($f \leq 50$ kHz), electrostatic toroidal mode number spectra with a width $\Delta n = 80$ is shown in Figure V-7-3. This is in contrast to radial magnetic field fluctuations n-spectra, which are dominated by a tearing mode peak at $n \sim 2R/a \sim 6$ and $\Delta n \leq 10$.

At higher frequencies (50 kHz $\leq f \leq$ 250 kHz), the electrostatic n-spectra broadens even further to $\Delta n = 160$ (Fig. V-5-4). The n spectrum for the ion saturation current shifts to the electron drift direction, peaking at $n \sim 40$. While toroidal magnetic field fluctuations also show a similar shift in this frequency band,

the width of the spectrum is significantly smaller (see Fig. V-4-3 and V-4-4).

The poloidal mode spectra for ion saturation fluctuations at low frequencies is much narrower (not shown here). The spectrum again broadens with frequency (50 kHz $\leq f \leq$ 250 kHz), to a width $\Delta m \sim 10$ (Fig. V-5-5). While poloidal electrostatic fluctuations show some general similarities to poloidal magnetic fluctuations, the spectrum is still broader.

In summary, I have measured the toroidal and poloidal mode spectra for electrostatic signals from a multi-purpose forked probe. The spectra are broad and centered at m = 1, n = 0, although some shift exists at higher frequencies for the toroidal spectra. This is in contrast to magnetic fluctuation spectra. The correlation between electrostatic and radial magnetic fluctuations is found to be small. Phase coherence between electrostatic and magnetic fluctuations does not exist. For example the cross bi-spectrum $\langle b(\omega_1)\, b(\omega_2)\, J_{satl}(\omega_3)\rangle$ is zero, (same is true for

$\langle J_{satl}(\omega_1)\, J_{satl}(\omega_2)\, b(\omega_3)\rangle \approx 0$). We can safely speculate that measured nonlinear mode coupling of the previous sections are purely wave-wave.

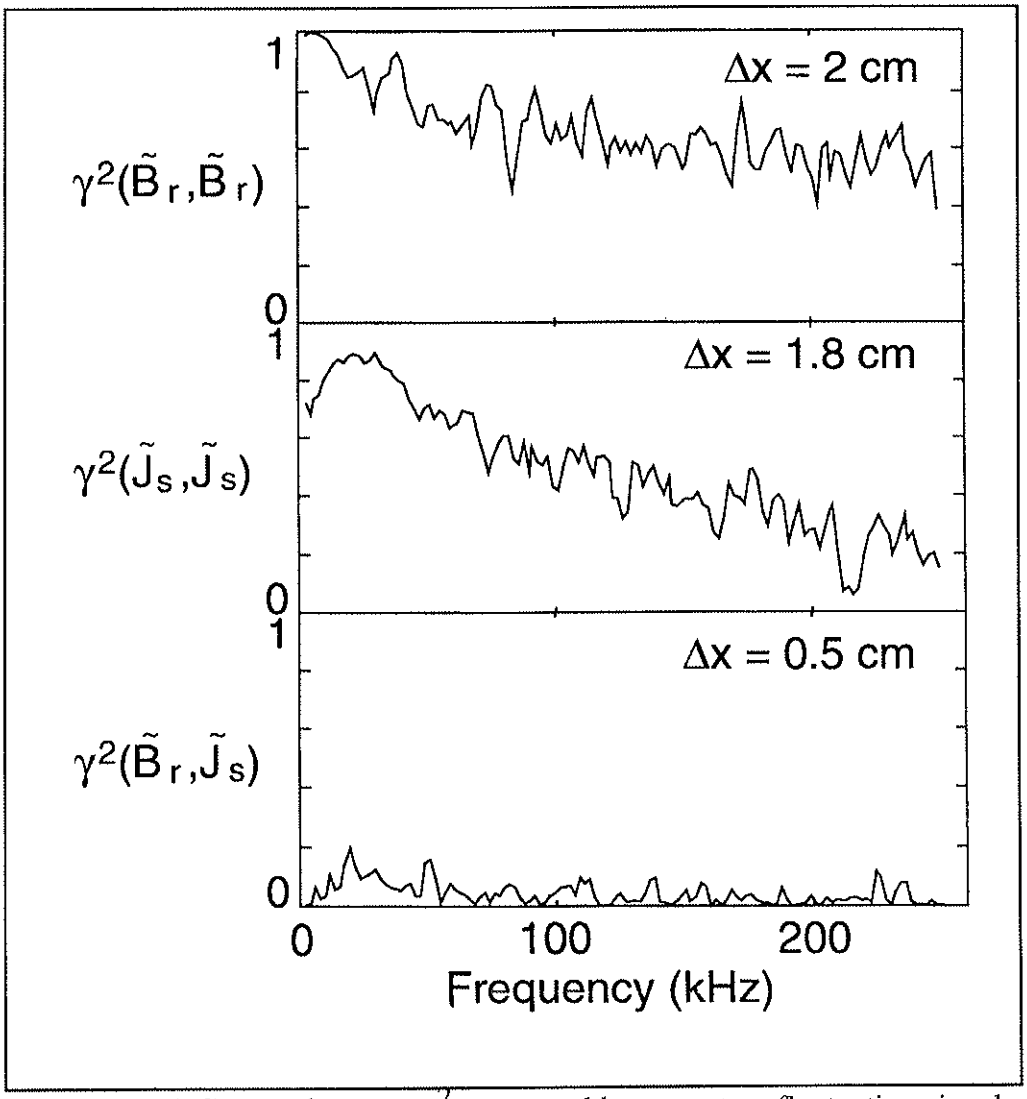

Figure V-7-1) Cross coherence, γ^2, measured between two fluctuating signals, magnetic (top), electrostatic (middle), and J_{sat1} and b_r, (bottom).

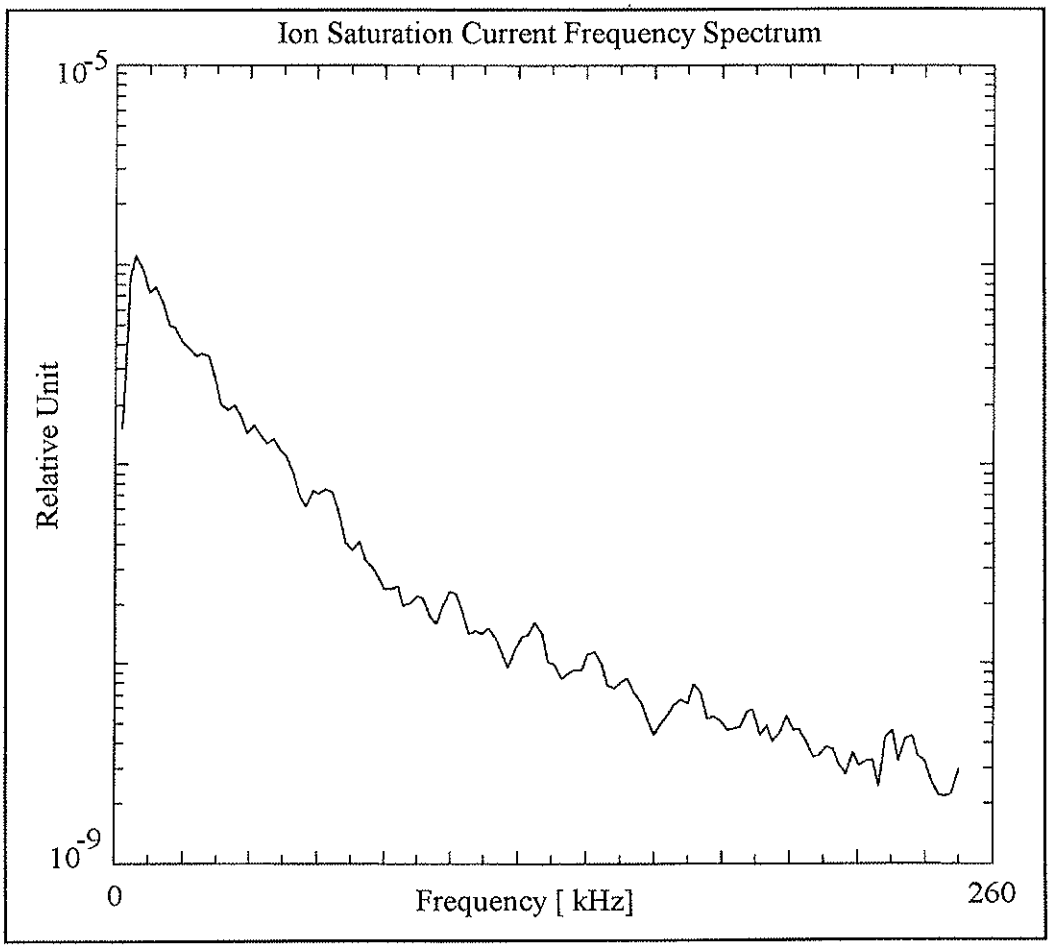

Figure V-7-2) Typical ion saturation current frequency spectrum. Monotonic decay with frequency is observed.

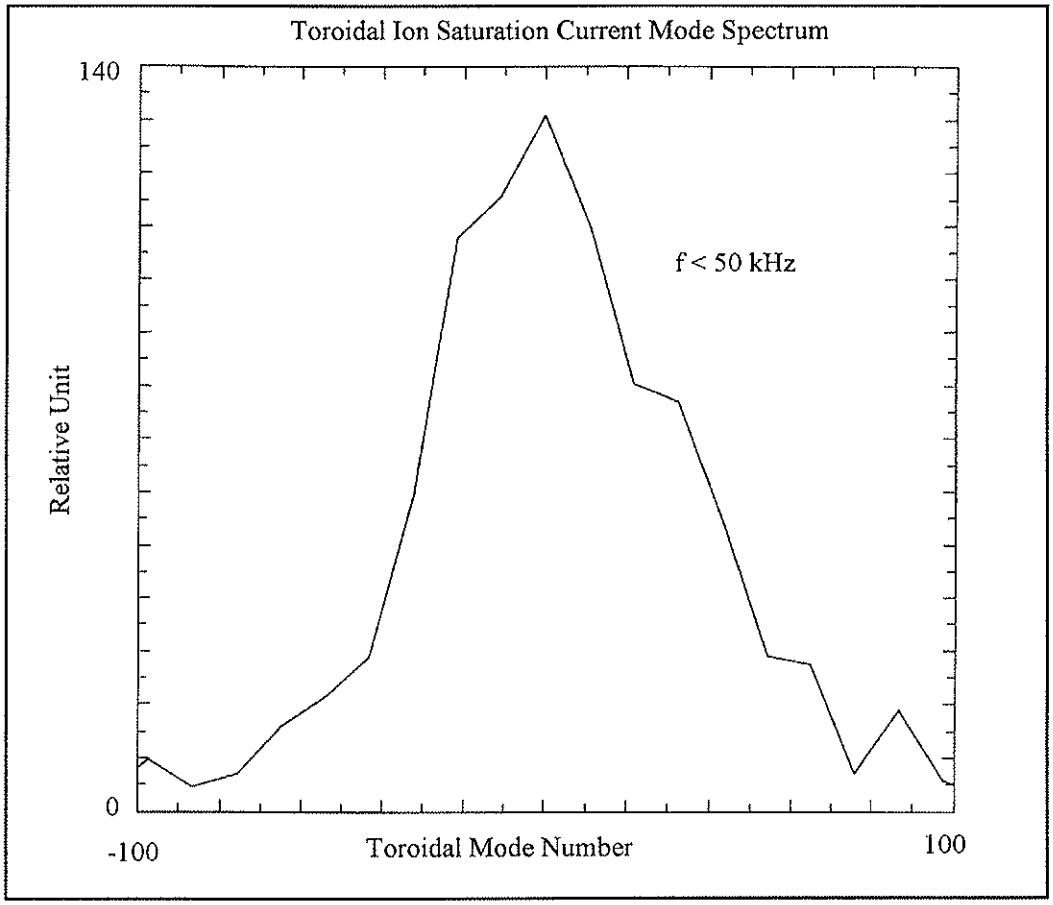

Figure V-7-3) Toroidal n-spectrum of ion saturation current is broader than the magnetic n-spectrum (f < 50 kHz).

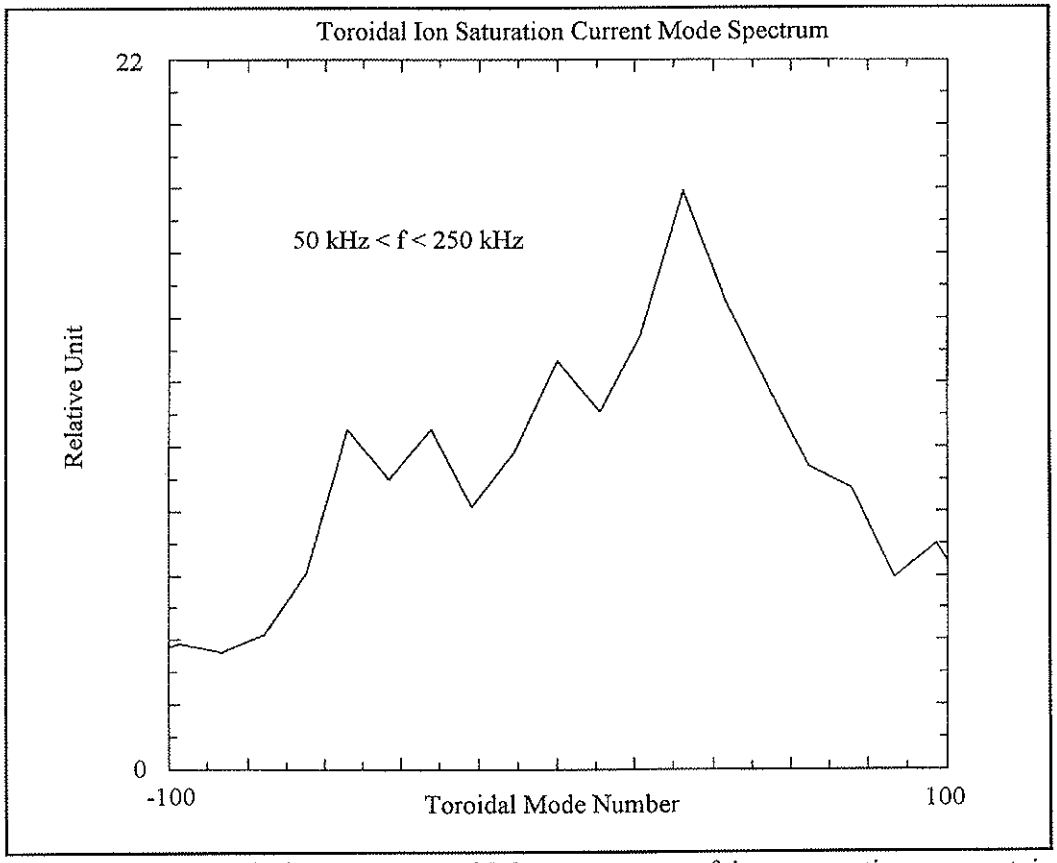

Figure V-7-4) High frequency toroidal n-spectrum of ion saturation current is broader than the magnetic n-spectrum. A shift in peak spectrum is observed

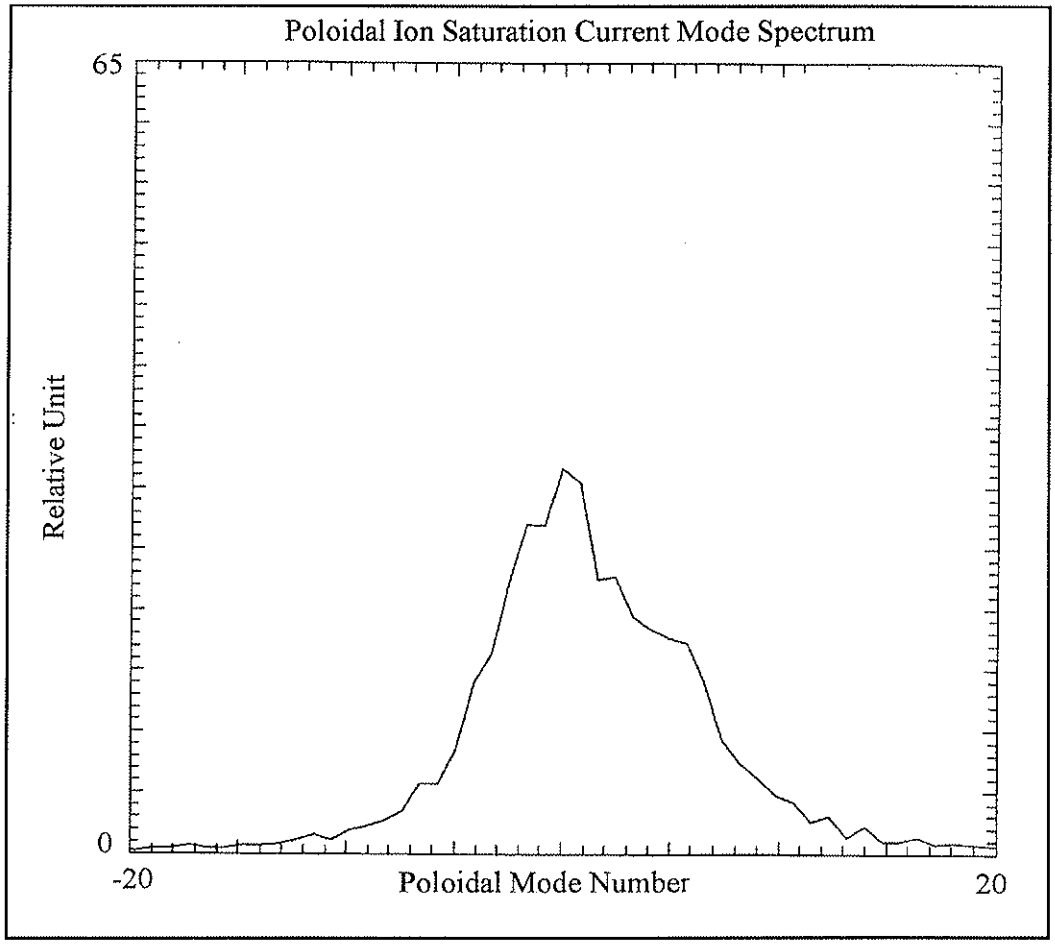

Figure V-7-5) High frequency poloidal m-spectrum of ion saturation current is broader than magnetic m-spectrum (50 kHz <f < 250 kHz). No shift in spectrum is observed

5-8) Effect of Material Limiter and Impurities on Edge Magnetic Fluctuations and Mode Number Spectra

This section presents the results of added impurities (argon doping) and material limiter (graphite paddle) insertion into MST plasmas on edge magnetic fluctuations and mode spectra.

From the detailed edge magnetic fluctuation measurements presented in the previous sections we have observed oscillations, identified as MHD tearing modes (m=1, n=5-8), ordinarily phase-locked to one another and rotating with respect to the laboratory frame (Figure V-8-1). We have also observed sawteeth oscillations. These sawteeth oscillations increase plasma-wall interactions, resulting in confinement degradation accompanied by slowing down of the rotating phase-locked helical modes. Figure V-8-2 and V-8-3 show the dominant rotating modes. These modes slow down after each sawtooth crash for a period depending on the level to which impurities have been added to the plasma. Occasionally, the rotating disturbance becomes stationary (Figure V-8-4) or "locked" in the laboratory frame, magnetic field errors grow, and the discharges shorten. The purpose of this experiment is to model the plasma-wall interactions via added impurities and to model the field errors by the insertion of a conducting limiter into the plasma to produce a non-axisymmetric current profile.

We[1] have increased the argon concentration in the hydrogen plasma to 3.75%. We observe that the rotating coherent modes slow down by a factor ~2 (Figure V-8-5). These rotating modes lock to the wall when the argon impurities are increased to 8% (Figure V-8-6). The percentage of impurities depends strongly on the plasma and on the conducting wall conditions. We have successfully demonstrated that added impurities slow down the phase-locked modes similar to the sawtooth crash phase (both should be avoided). We have observed that the sawtooth crash modifies the current density profile and shifts the plasma inward (see section V-4), generating a sudden radial field error at the poloidal gap [31]. At times coincident with the sawtooth crash, the rotating, phase-locked structure becomes stationary at the poloidal gap.

Next, we examine the effect of a graphite paddle inserted 12 cm (in 4 cm steps) into the plasma, through a 4.5" port at $\phi=138^{O}$ and $\theta=20^{O}$ as a controlled form of generating external field errors since it produces a nonaxial current profile.

For almost the same plasma currents at all limiter insertion positions, we have a found 25% reduction in central electron temperature, 70% reduction in the energy confinement time. Also, the ohmic power dissipation is increased by 90%, the oxygen

---

[1] This experiment is the result of cooperation among Saeed Assadi (edge magnetic fluctuation measurements), Daniel Den-Hartog (impurity diagnostics and electron temperature measurements) and M. Stoneking (electron energy analyzer measurement).

impurity is increased 3 fold, and the single-turn loop voltage has increased by 100%. The reversal parameter and pinch parameter are kept constant. Figure (V-8-7) shows the raw poloidal magnetic fluctuations. We observe a significant reduction in the magnetic fluctuation power. Figures (V-8-8)-(V-8-10) show the frequency spectrum when the limiter is inserted by 4, 8, and 12 cm into the plasma. The power level is reduced by an order of magnitude at each step. At 4 cm the frequencies of the phase-locked modes increase. Simultaneously, the toroidal mode spectrum (Figure V-8-11) shows significant development of external modes, resonant outside the reversal surface (negative n means external in this section). At 8 cm limiter insertion, the frequency spectrum is an order of magnitude smaller than for the 4 cm case, but its respective toroidal mode spectrum has larger external modes than internal modes with a broader toroidal k-spectrum (Figure V-8-12). The normalized cross correlation function among the 64 toroidal fixed array clearly show mode locking to the conducting wall in the vicinity of the limiter position (Figure V-8-13). When the limiter is pushed 12 cm into the plasma, all internal modes lock to the wall (Figure V-8-14). The power spectrum becomes monotonic.

In summary, we have successfully manipulated the rotational speed of the phase-locked mode. The toroidal mode spectrum shifts from internally resonant modes to external "kink" type. Discharges degrade and mode locking occurs at the

largest field error, which is at the limiter location.

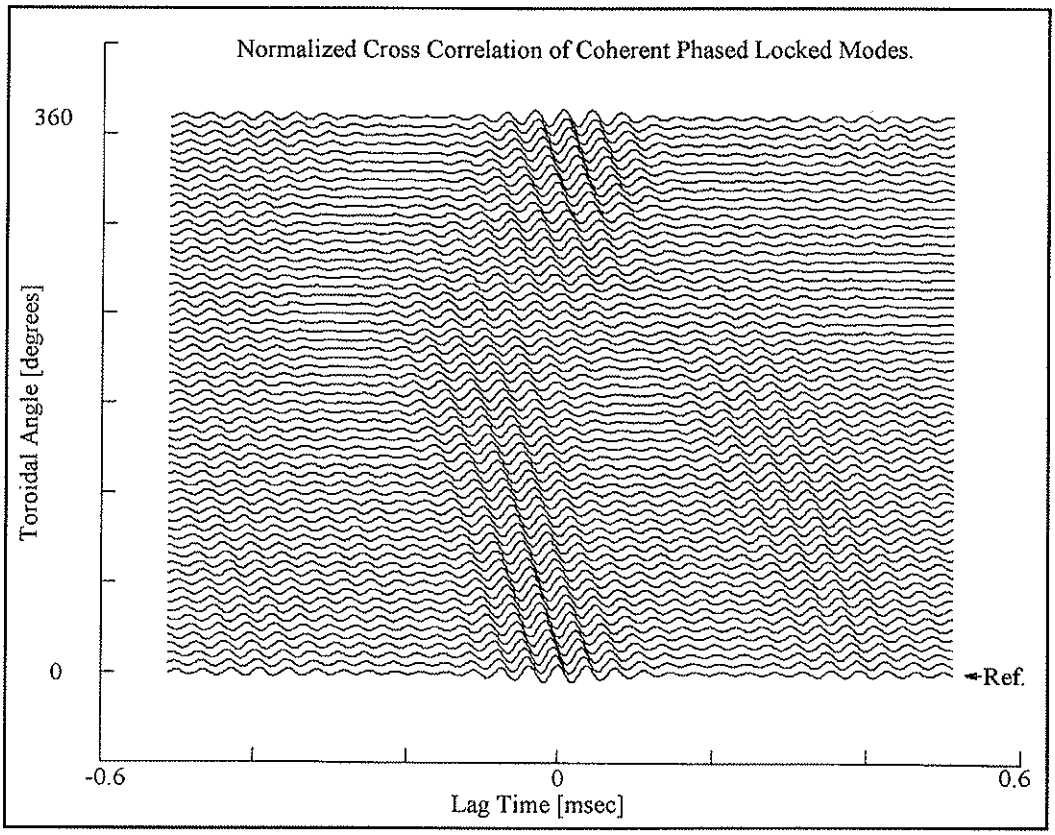

Figure V-8-1) Normalized cross correlation of "normal" discharges exhibit phased-locked tearing modes rotating in the direction of the ion diamagnetic current.

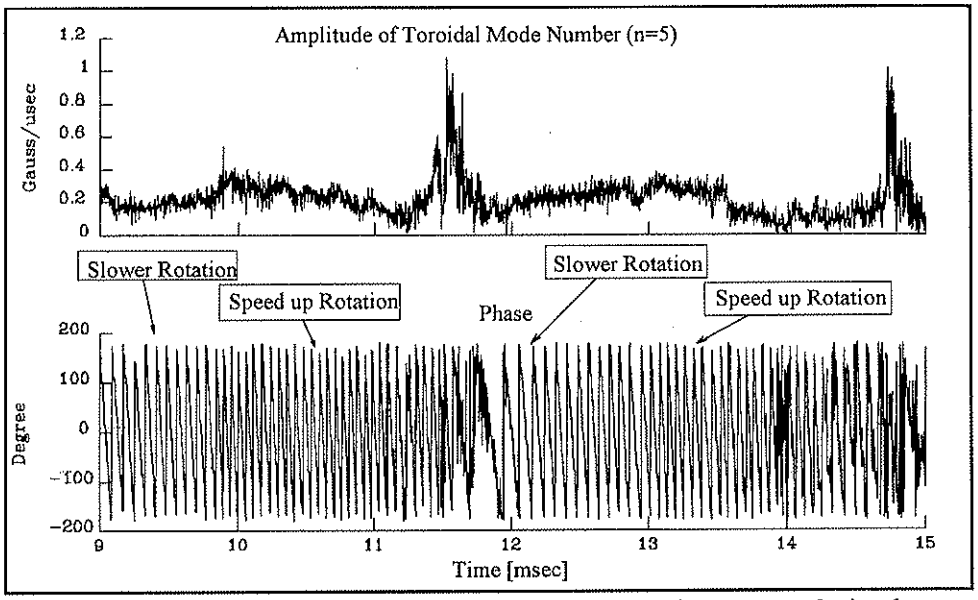

Figure V-8-2) Amplitude and phase of the n = 5 coherent mode is shown. The n=5 mode slows down for some period after each sawtooth crash.

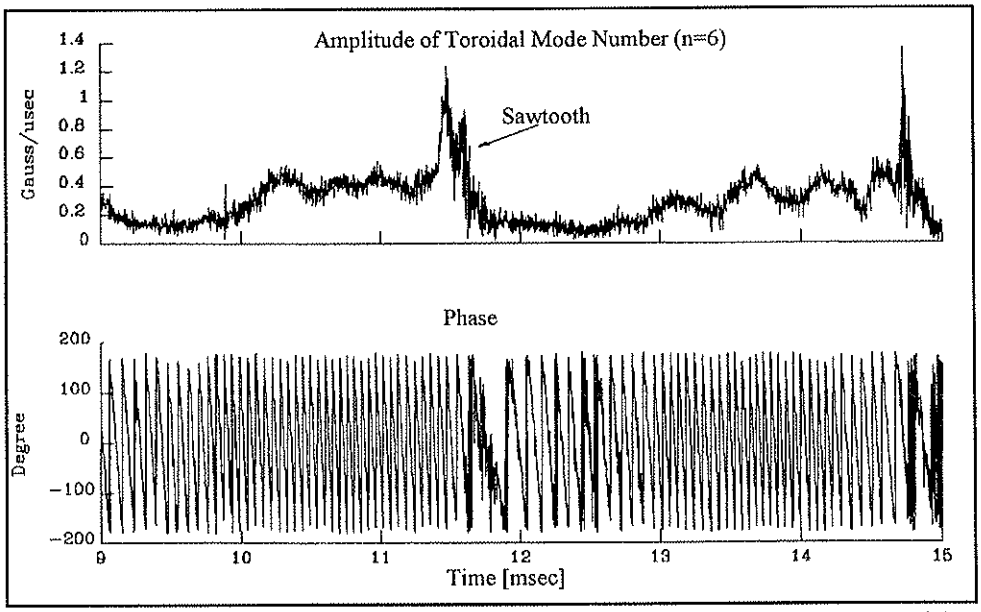

Figure V-8-3) Amplitude and phase of n = 6 is shown. Added impurities after each sawtooth crash slows the coherent modes for some period of time.

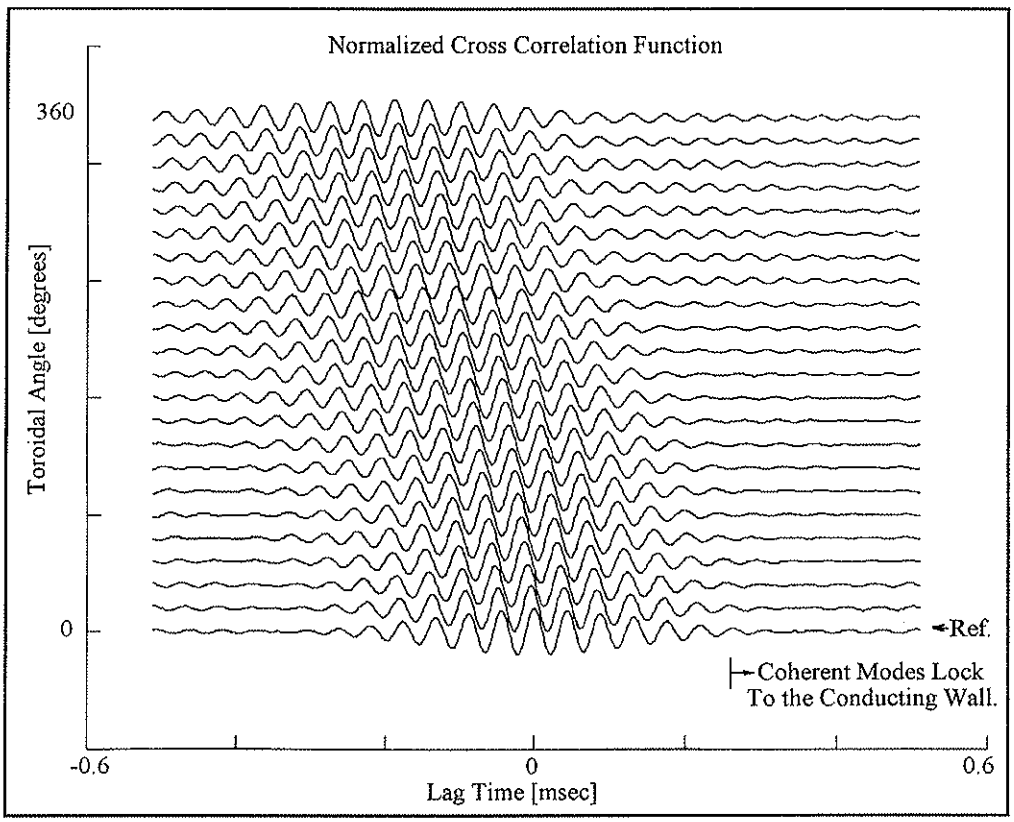

Figure V-8-4) Cross-correlation of edge toroidal magnetic fluctuations show "locking" of phase-locked tearing modes to the conducting wall due to either large field errors or high impurities.

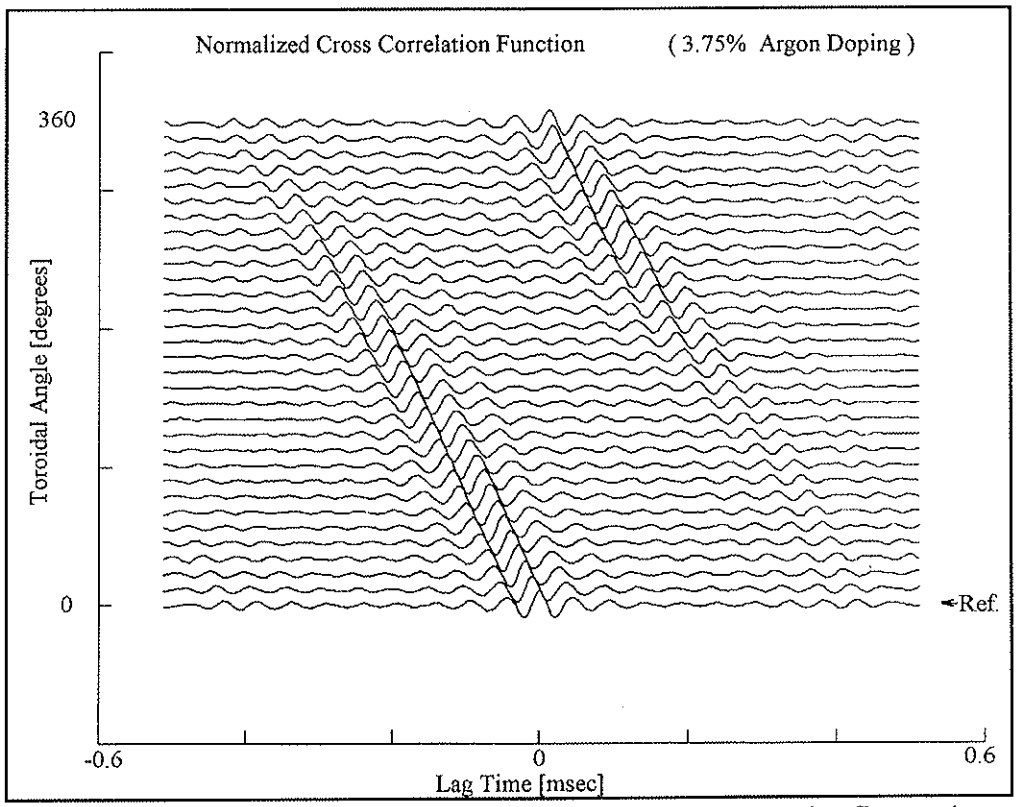

Figure V-8-5) Toroidal cross-correlation of edge magnetic fluctuations. Coherent modes exhibit "slowing down" when impurities (3.75% argon doping) are added to hydrogen plasmas.

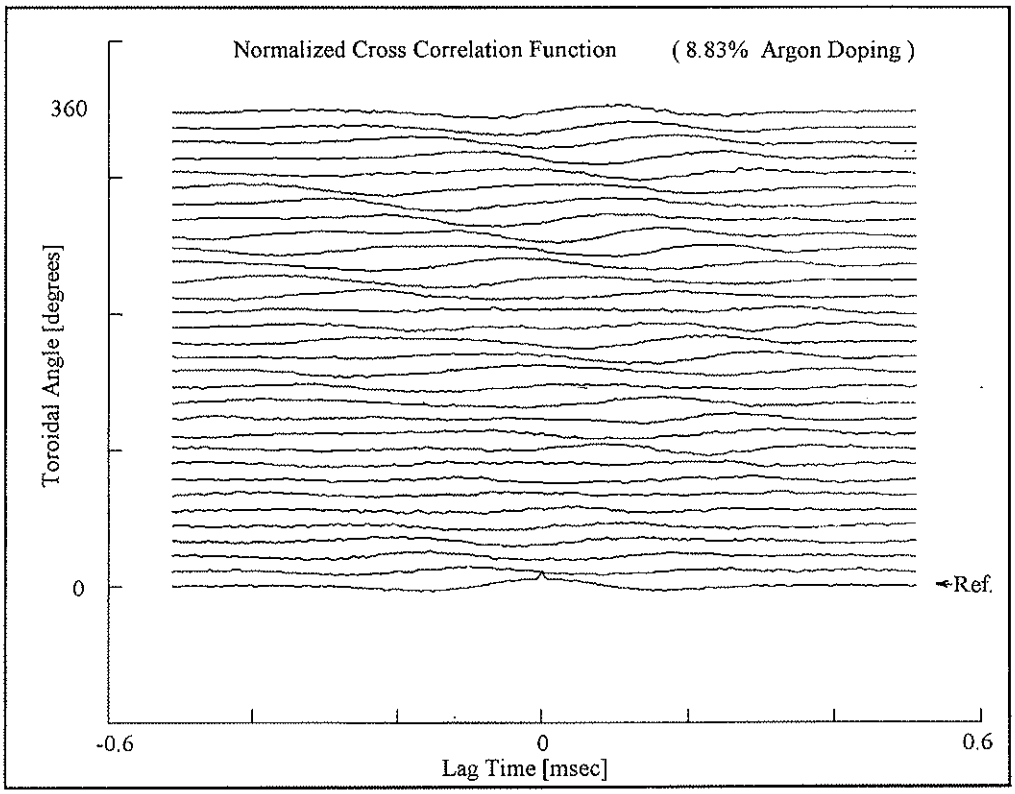

Figure V-8-6) Toroidal cross-correlation of edge magnetic fluctuations. Phase-locked coherent modes are locked to the conducting wall after 8% impurity concentration.

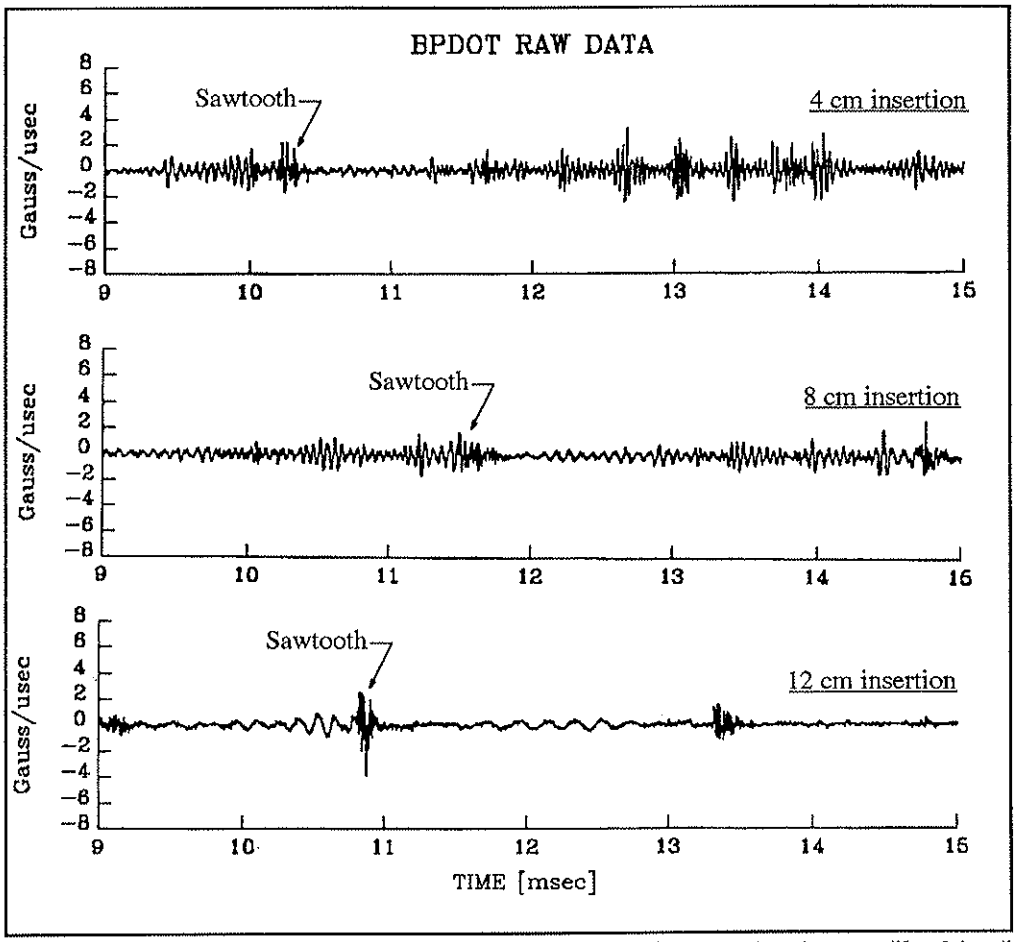

Figure V-8-7) Raw magnetic fluctuation signals show reduction or "locking" of oscillations, as a conducting limiter is inserted into the plasma.

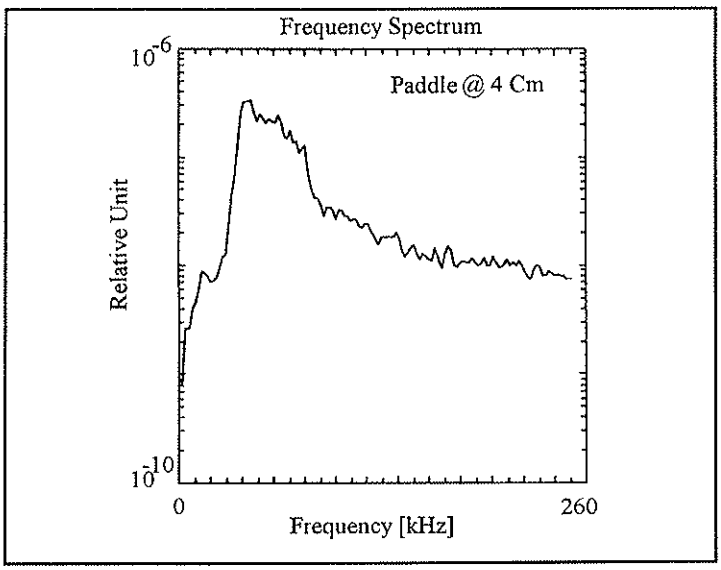

Figure V-8-8) Frequency spectrum of magnetic fluctuations when material limiter is at **4 cm** insertion.The coherent modes shift to higher frequencies.

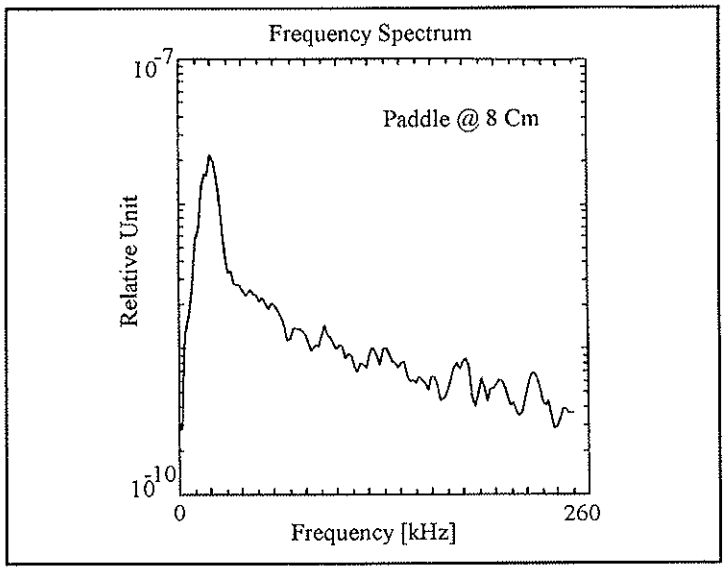

Figure V-8-9) Frequency spectrum when limiter is at **8 cm** insertion. The amplitude is decreased and the frequency is reduced.

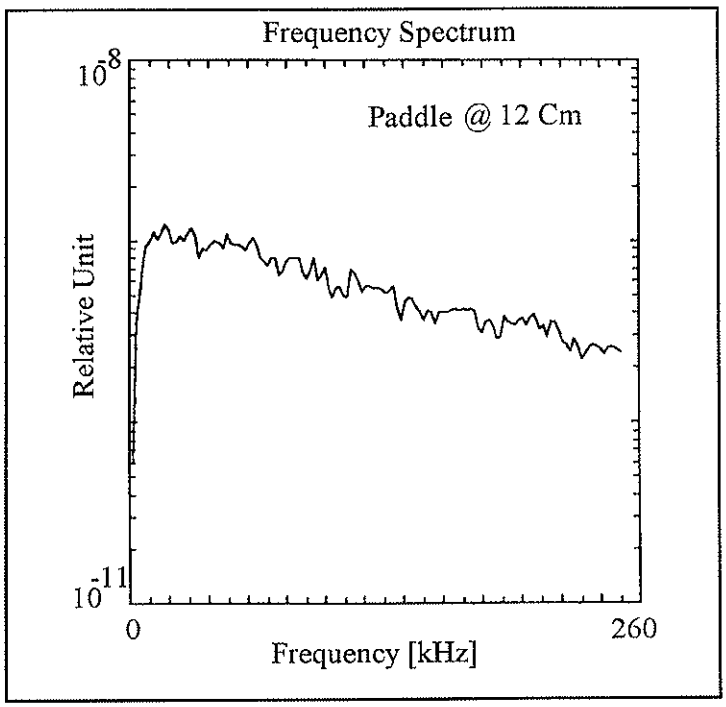

Figure V-8-10) Frequency spectrum after **12 cm** limiter insertion. The modes are locked and a monotonic frequency spectrum is observed.

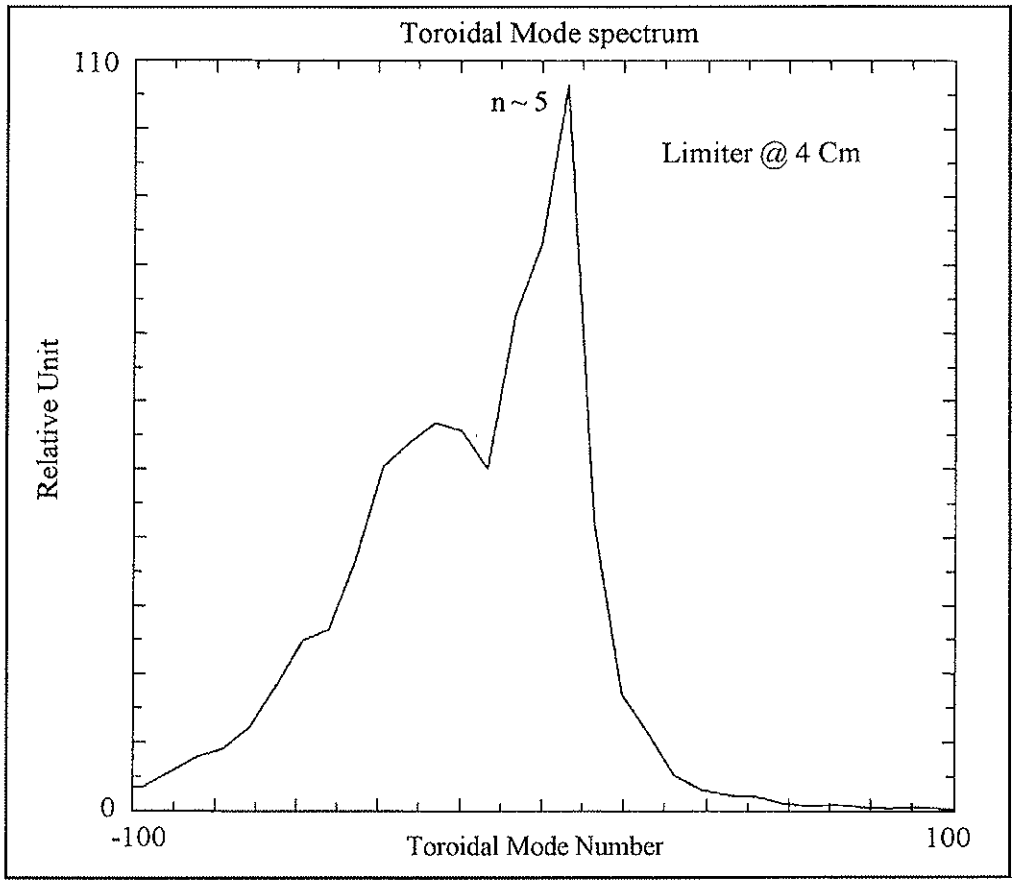

Figure V-8-11) The effect of a material limiter on toroidal mode spectra. We observe the formation of external modes as the limiter is inserted into the plasma.

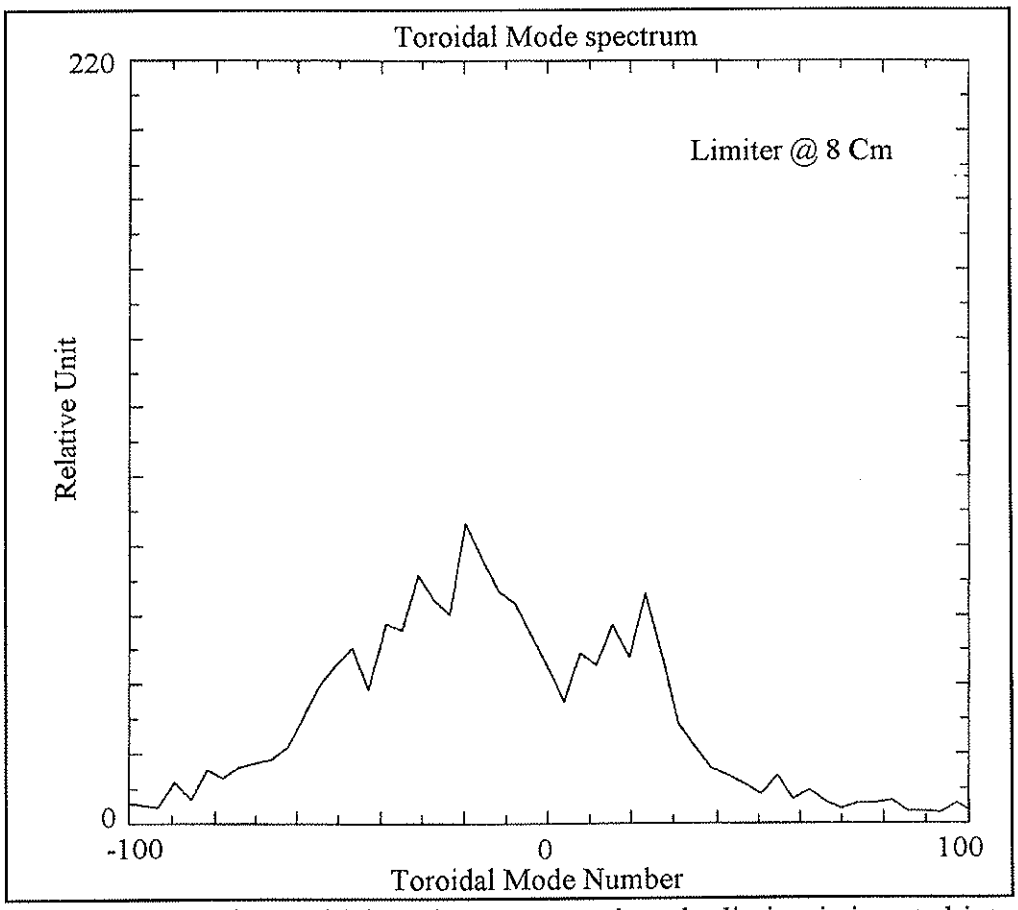

Figure V-8-12) The toroidal mode spectrum when the limiter is inserted into the plasma by **8 cm**. We observe mode locking to the conducting wall.

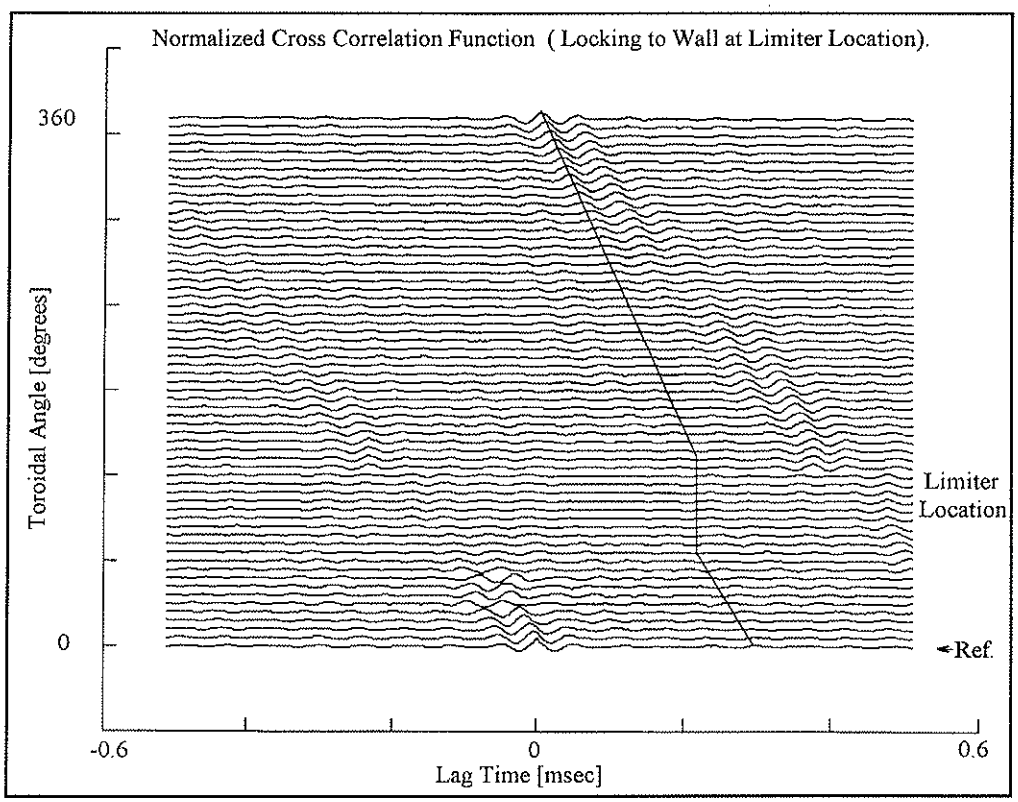

Figure V-8-13) Normalized cross-correlation of 64 toroidal coils. Mode locking in the vicinity of the limiter has occurred.The limiter is at **8 cm.**

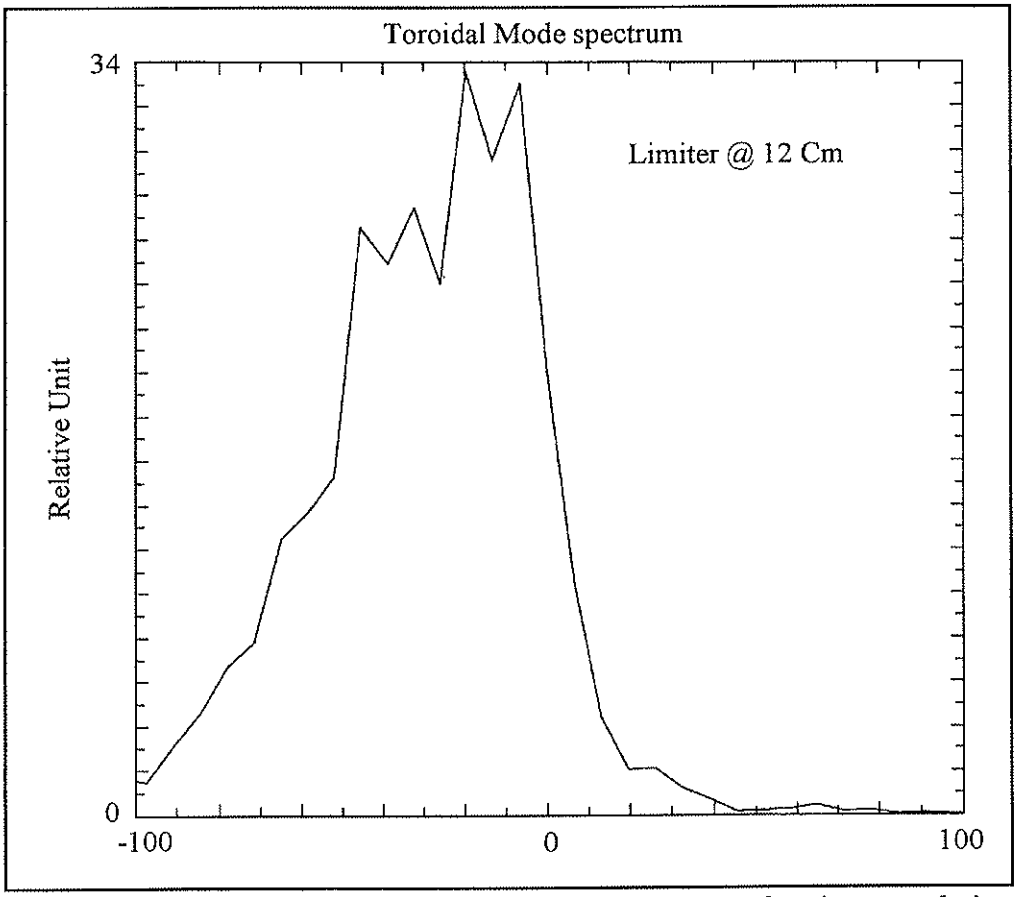

Figure V-8-14) The toroidal mode spectrum from a 2-point correlation analysis is shown. All modes are external and amplitudes are small.

References

1) K. Kato, and E. Kawasaki, Oscillations in a Magnetic Field, J. Phys. Soc. Japan **20**, 1521 (1965).

2) R.A. Stern, Harmonic Generation and frequency mixing at Plasma Resonance, Phys. Rev. Lett. **14,** 538 (1965).

3) R.A. Stern, Interaction of Resonant Plasma Oscillations in a Low-Pressure Hg. Discharges, Appl. Phys. Lett. **4**, 80 (1964).

4) S. Assadi, et.al. presented at U.S./Japan Workshop on Fluctuations in RFP and ULQ Plasma (1990).

5) A.F. Almagri, Ph.D. Thesis, University of Wisconsin-Madison (1990).

6) A.F. Almagri, S. Assadi, S.C. Prager, J.S. Sarff, D.W. Kerst, Locked Modes and Magnetic Field Errors in MST, submitted for publication (1992).

7) D.C. Robinson, M.G. Rusbridge, and P.A.H. Saunder, Plasma Physics **10**, 1005 (1968).

8) P.L. Taylor, R.J. LaHaye, P.S. Lee, M.J. Schaffer, and T. Tamano, Plasma Behavior in OHTE (1984) GA-Report.

9) V. Antoni and S. Ortolani Plasma Physics **25**, 799 (1983).

10) H.A.B. Bodin, et al., "results from HBTX1A Reversed Field Pinch Experiment", Plasma Physics and Controlled Nuclear Fusion Research (9th INT Conf. Baltimore,

1982), Vol. **1,** IAEA, Vienna ,641, (1983).

11) R.G. Watt and R.A. Nebel, Physics Fluids **26**, 1168 (1983).

12) T.C. Hender, D.C. Robinson, 9th Int. Conf. in Plasma Physics & Controlled Nuclear Fusion Research, Baltimore, **III**, 417, (1983).

13) H.R. Strauss, Phys. Fluids **29**, 3008 (1986).

14) Z.G. An, et al., 11th Conf. on Plasma Physics and Controlled Nuclear Fusion Research, **II,** 663, (1987).

15) R.A. Nebel, et al., Phys. Fluids B**1**, 1671 (1989).

16) R. LaHaye, et al., Phys. Fluids **21**, 1452 (1984).

17) D.C. Robinson, Plasma Phys. **13**, 439 (1971).

18) D.C. Robinson, Nuclear Fusion, **18**, 939 (1978).

19) I.H. Hutchinson, et. al., Nuclear Fusion, Vol. **24,** No.1, 59 (1984).

20) T. Tamano, W.D. Bard, C. Chu, Y. Kondoh, R.J. Lahaye, P.S. Lee, M. Saito, M.J. Schaffer, and P.L. Taylor, Phys. Rev. Lett.,**59,** 1444 (1987).

21) T. Tamano, General Atomics Inc., San Diego, Ca., Report. GA-A18972.

22) R.L. Lahaye, T. Tamano, R.J. Lee, "Magnetic Fluctuation Measurements in the thin Sell OHTE Device Operating as a Reversed Field Pinch", Rep. GA-A18970.

23) K. Hattori, Y. Hirano, T. Shimada, Y. Yagi, Y. Maejima, I. Hirota, and K. Ogawa, MHD Phenomena in TPE-1RM15 RFP. U.S./Japan Workshop on Fluctuations

in RFP and ULQ Plasma.

24) K. Kusano, T. Tamano, and T. Sato, Simulation Study of Nonlinear Dynamics in Reversed Field Pinch Configuration, IAEA Proceeding 1990.

25) D.D. Schnack, S. Ortolani, "Computational Modeling of the Effect of a Resistive Shell on the RFX Reversed Field Pinch", Nuclear Fusion, **30**, No. 2, (1990).

26) D.D. Schnack, D.C. Barnes, Z. Mikic, D.S. Harned, and E.J. Caramana, J. Compt. Phys. **70**, 330 (1987).

27) R.B. Watt, and R.A. Nebel, Phys. Fluids **B1**, 153 (1989).

28) K. Hattori, et. al., Phys. Fluids B, 3111 (1991).

29) J.A. Holmes, B.A., Carreras, P.H., Diamond, and V.E. Lynch, Phys. Fluids **31**, 1166 (1988).

30) K. Hattori, et. al., Phys. Fluids B **3,** 3111 (1991).

31) Almagri, A. Ph.D.Thesis , University of Wisconsin-Madison (1991).

Chapter VI

Summary and Conclusions

The thesis addressed a range of issues. We present a brief summary of our results in this section.

We have directly measured three-wave nonlinear coupling of magnetic fluctuations which are identified in this thesis as tearing fluctuations. There is good agreement between the measurements of the k-space couplings and predictions of nonlinear MHD computation. We find that the dominant poloidal mode coupling in the experiment involves two $|m| = 1$ modes coupling to an $|m| = 2$ mode. Toroidal mode coupling is much broader, involving tens of modes. These measurements add credibility to the nonlinear MHD theory used to describe magnetic reconnection in tokamaks and RFPs.

During the crash phase of a sawtooth oscillation (which is not modelled by the MHD computation employed here) the nonlinear couplings are strongly enhanced, simultaneous with broadening of the mode spectra. This is consistent with nonlinear coupling being the source of generation of spectral broadening during a crash

(although bi-spectral analysis does not indicate causality). The data reported here are the first example of measurements of k-space coupling of fluctuation spectra. Measurement of nonlinear interactions, by the technique used here and extensions thereof, are essential for an adequate understanding of the nonlinear plasma physics intrinsic to confined plasmas.

We have modeled the temporal evolution of toroidal mode spectrum as a summation of second and third order moments. Calculated linear (growth rate, L_k) and quadratic (wave-wave coupling , Q_k) transfer functions are used to estimate the "future" n-spectrum. Comparison of measured and modelled n-spectra are similar in the low toroidal mode numbers and are promising for the prediction of small scale wavenumber evolutions.

Correlations of electrostatic fluctuations with radial magnetic fluctuations within a radial separation of 1/2 cm are non-zero, but small ($\gamma^2 \sim 0.2$). Thus, a significant fraction of the measured electrostatic fluctuations may arise from sources other than radial convection with the magnetic field. Hence, specification of magnetic turbulence properties in no way determines those of electrostatic fluctuations.

We have studied the phase-locking of tearing modes and sawtooth oscillations via nonlinear *k*-coupling throughout this thesis. Altering their characteristics could help in finding ways to eliminate them. We have successfully manipulated the

rotational speed of the phased-locked modes by adding impurities and modelled the sawtooth-generated impulsive field errors by a retractable conducting limiter. Further research in this area is in order.

The parallel (poloidal) correlation length has been measured by placing an array of sensors on the inside edge of MST. The values found are similar to those found in other RFPs. For f ~ 35 kHz, L_p (~ $L_{||}$) is of the order of one half the circumference for coherent m=1 helical modes. For higher frequencies the values are smaller. The transverse (toroidal) correlation length is found to be much shorter. Hence, we have utilized the closely-spaced dense-array sensors, (to improve the certainty of the measurement would require consistent coherence between the coils as frequency and spacing increases). This has been achieved by simultaneously measuring the signals of multi-toroidal sensors. The measured toroidal correlation length is L_T ~ 20 cm for f ~ 35 kHz and reduces to ~ 6 cm at 120 kHz, hence, broadening of the n-spectrum as frequency increases is estimated (we have verified this broadening by other methods).

We have measured toroidal and poloidal mode number spectra using extensive arrays of coils by applying three different methods. We have found that low frequency magnetic fluctuations are consistent with the global tearing instabilities predicted by MHD codes (m = 1 and n ~ 2 R/a ~ 6). These coherent modes are phased

locked to one another forming a localized disturbance rotating in ion diamagnetic current direction. High frequency magnetic fluctuations are broadband and locally resonant. The calculated helical "association" spectrum are similar to global helical tearing instabilities predicted by the MHD code.

We have successfully measured edge magnetic fluctuations using hundreds of magnetic sensing coils around the device. Despite the uniqueness and size of the MST device, there is no evidence to indicate that the general attributes of magnetic turbulence measured in MST are in any way significantly different from those found in the other devices to date (e.g., low frequency fluctuations tend to decrease with plasma current, with an exception of no observable correlation between toroidal magnetic fluctuations and Lundquist number in MST from a limited data). This implies that the results presented in this thesis may be considered fully relevant to the study of any other RFP. The goal of this work has been to measure the edge magnetic fluctuations on an RFP plasma device, such as the Madison Symmetric Torus (MST), by including the quadratic nonlinearities in the magnetic fluctuations. Given the complex physics of the RFP, certain approximations were made in representing the modal structure. Some of these assumptions were rather restrictive, and any prediction based on them must be kept in proper perspective. In general, however, the experimental results presented here illustrate excellent agreement with the resistive

MHD model of plasma turbulence and many methods have been implemented to alleviate any restrictions of a given method.